



NISTIR 5958

Smoke Plume Trajectory from In Situ Burning of Crude Oil in Alaska --- Field Experiments and Modeling of Complex Terrain

Kevin B. McGrattan
Howard R. Baum
William D. Walton
Javier Trelles

QC
100
.U56
NO.5958
1997



United States Department of Commerce
National Institute of Standards and Technology

Smoke Plume Trajectory from In Situ Burning of Crude Oil in Alaska --- Field Experiments and Modeling of Complex Terrain

Kevin B. McGrattan
Howard R. Baum
William D. Walton
Javier Trelles

January 1997



U.S. Department of Commerce
Michael Kantor, *Secretary*
National Institute of Standards and Technology
Arati Prabhakar, *Director*



U.S. Department of the Interior
Bruce Babbitt, *Secretary*
Minerals Management Service
Thomas R. Fry, *Director*



**Alaska Department of
Environmental Conservation**
Michele Brown, *Commissioner*
Division of Spill Prevention and Response
Kurt Fredriksson, *Director*

Smoke Plume Trajectory from *In Situ* Burning of Crude Oil in Alaska Field Experiments and Modeling of Complex Terrain

Kevin B. McGrattan, Howard R. Baum, William D. Walton and Javier Trelles
National Institute of Standards and Technology
Gaithersburg, Maryland 20899

Abstract

A combination of numerical modeling and large scale experimentation has yielded a tremendous amount of information about the structure, trajectory and composition of smoke plumes from large crude oil fires. The model, ALOFT (A Large Outdoor Fire plume Trajectory), is based on the fundamental conservation equations that govern the introduction of hot gases and particulate matter from a large fire into the atmosphere. Two forms of the Navier-Stokes equations are solved numerically — one to describe the plume rise in the first kilometer, the other to describe the plume transport over tens of kilometers of complex terrain. Each form of the governing equations resolves the flow field at different length scales. Particulate matter, or any non-reacting combustion product, is represented by Lagrangian particles that are advected by the fire-induced flow field. Background atmospheric motion is described in terms of the angular fluctuation of the prevailing wind, and represented by random perturbations to the mean particle paths. Results of the model are compared with three sets of field experiments. Estimates are made of distances from the fire where ground level concentrations of the combustion products fall below regulatory threshold levels.

Executive Summary

A combination of numerical modeling and large scale experimentation has yielded a tremendous amount of information about the structure, trajectory and composition of smoke plumes from large crude oil fires. The model, ALOFT (A Large Outdoor Fire plume Trajectory), is based on the fundamental conservation equations that govern the introduction of hot gases and particulate matter into the atmosphere. Some major results of the ALOFT modeling effort and the experimental burns can be summarized as follows:

1. The results of the original plume modeling study, Reference [1], remain valid for flat terrain applications. "Flat" in this context refers to terrain that does not vary in height by more than about 10% of the expected plume height. Thus, for a single burn consuming up to about 1,000 barrels per hour in wind speeds less than 12 m/s (23 knots), the maximum ground level extent of the region where the concentration of PM-10 particulate would be in excess of $150 \mu\text{g}/\text{m}^3$ (hour-averaged) is roughly 5 km (3.0 miles) over flat terrain.
2. The ALOFT model has been extended to accommodate scenarios involving both flat and complex terrain, and the conclusions of Reference [1] have been expanded. The maximum extent of the region where the hour-averaged, ground level PM-10 particulate concentration would be in excess of $150 \mu\text{g}/\text{m}^3$ downwind of a burn consuming 1,000 barrels per hour can be as low as 1 km for a scenario with flat terrain and nearly adiabatic lapse rates, and as high as 20 km for a scenario where the terrain height extends above the mixing layer. More refined predictions for intermediate cases are included in the report. Also included are simple formulae for modifying the maximum ground level distances to accommodate changes in air quality thresholds and combustion product emission factors.
3. The uncertainty of ALOFT model predictions is largely a function of the uncertainty in the meteorological conditions and fire emission rates. The factor of safety of 2 that had been applied to the downwind distance predictions as an estimate of uncertainty for the original flat terrain modeling results has been replaced by more appropriate ways of assessing uncertainty, and these will be presented in the report.
4. The ventilation factor, which is the product of the wind speed and mixing layer depth used to characterize the dispersive potential of the atmosphere, is a reasonably good indicator of expected ground level concentration of smoke or combustion products from a large burn. This is true of both flat and complex terrain.
5. Smoke particulate is by far the most likely combustion product of crude oil burning to exceed ambient air quality standards at ground level beyond a few hundred meters from the fire.
6. Peak concentrations of ground level smoke particulate for the 1993 Newfoundland Offshore Burn Experiment, the 1994 Alaska Clean Seas Burning of Emulsions experiment, and the 1994 diesel fuel burns in Mobile, Alabama, never exceeded $100 \mu\text{g}/\text{m}^3$ beyond a few hundred meters from the fires, and in most cases were well below that level.

Contents

1	Introduction	1
2	Description of the ALOFT Model	3
2.1	Historical Background	3
2.2	Development of the ALOFT model	3
2.3	ALOFT Compared to Other Dispersion Models	5
3	The Fire and its Emissions	7
3.1	Heat Release Rate	7
3.2	Particulate Emissions	8
3.3	Particulate Size	11
3.4	Other Emissions	12
4	The Smoke Plume	15
4.1	The Boussinesq Approximation	15
4.2	Scaling Laws for the Three-Dimensional Equations (ALOFT-CT)	17
4.3	Scaling Laws for the Two-Dimensional Equations (ALOFT-FT)	18
4.4	Atmospheric Turbulence	20
4.5	Flat Terrain Correlations	24
5	Validation Experiments for ALOFT-FT	29
5.1	The Newfoundland Offshore Burn Experiment (NOBE)	29
5.2	Alaska Clean Seas Burning of Emulsions Experiment	33
5.3	Mesoscale Diesel Fuel Burns, Mobile, Alabama	37
5.4	Discussion of Field Experiments	46
6	ALOFT Applications in Alaska	50
6.1	Outline of the Solution Procedure	50
6.2	Single Burn, Single Sounding, Various Locations	52
6.2.1	North Slope, Atigun Pass and Fairbanks	53
6.2.2	Port Valdez	58
6.2.3	Prince William Sound	58
6.2.4	Cook Inlet	61
6.3	Single Burn, Various Soundings, Single Location	61
6.4	Multiple Burns, Various Soundings, Various Locations	68
6.5	Ground Level Distance Estimates for Complex Terrain	70
7	Conclusions	77
8	Acknowledgements	79
9	References	80
	Appendices	84

A	Description of ALOFT Model Input Parameters	84
A.1	Burn Input Parameters	84
A.2	Meteorological Input Parameters	86
A.3	Numerical Grid Parameters	87
A.4	Processing Results	88
A.5	Forecast Systems Laboratory (FSL) sounding format	88
B	Numerical Method	90
B.1	ALOFT-FT Algorithm (Plume Rise Calculation for ALOFT-CT)	90
B.1.1	The Energy Equation	90
B.1.2	The Momentum Equations	91
B.1.3	The Incompressibility Condition	93
B.1.4	Particle Tracking	94
B.2	ALOFT-CT Wind Field Calculation	94
B.2.1	The Energy Equation	95
B.2.2	The Momentum Equations	96
B.2.3	The Incompressibility Condition	97
B.2.4	Particle Tracking	98
C	Additional Results and Flat Terrain Wind Speed/Lapse Rate Charts	100

List of Figures

1	Near-field simultaneous measurements of particulate and CO ₂ at the 1994 Alaska Clean Seas emulsion burns.	9
2	Near-field simultaneous measurements of particulate and CO ₂ at the 1994 Mobile diesel fuel burn.	10
3	Electron micrograph of a smoke particle from a 3 m crude oil fire.	12
4	Three dimensional view of a computed smoke plume in the first few kilometers of its development.	21
5	A view of the plume from below.	21
6	Photograph taken from about 200 m downwind of the Newfoundland Offshore Burn Experiment (NOBE) showing the two large counter-rotating vortices which characterize the structure of the rising smoke plume.	22
7	Correlated ALOFT-FT results for an 820 MW fire and typical overland wind fluctuations.	25
8	Average temperature lapse rate versus mixing layer depth for a variety of soundings in Alaska.	28
9	Photograph of the Newfoundland Offshore Burn Experiment showing the shift of the wind at about 120 m off the surface.	29
10	Cross sectional slices of the simulated smoke plume from the second NOBE burn. .	31
11	Cross sectional slices of the actual smoke plume from the second NOBE burn. . . .	32
12	Lidar measurement of plume centerline of the second burn taken from University of Washington airplane.	33
13	Aerial photograph taken of the second ACS burn, Prudhoe Bay, September, 1994. .	34
14	ALOFT predictions of ground level particulate concentrations along side the actual time-averaged RAM data for the three ACS Emulsion Burns.	36
15	Ground level particulate concentration about 1 km directly downwind of the second ACS burn.	37
16	Downwind view of the simulated smoke plume from the second ACS emulsion burn, Prudhoe Bay, September, 1994.	38
17	Photograph of a diesel fuel burn at the US Coast Guard Fire and Safety Test Detachment, Mobile, Alabama.	39
18	ALOFT predictions of maximum ground level particulate concentration for the Mobile burn series of October, 1994.	40
19	Cross-plume flight paths for burn 2.	42
20	Cross-plume flight paths for burn 3.	43
21	Lidar images of the plume cross section for the morning burn of October 26, 1994, Mobile Bay.	44
22	Lidar images of the plume cross section for the afternoon burn of October 26, 1994, Mobile Bay.	45
23	ALOFT predictions of ground level particulate concentration for the morning burn of October 26, 1994, in Mobile Bay.	47
24	ALOFT predictions of ground level particulate concentration for the afternoon burn of October 26, 1994, in Mobile Bay.	48

25	Three-dimensional view of simulated smoke plume originating off Bligh Island, Prince William Sound.	51
26	Footprint of simulated smoke plume originating at Pump Station No. 1, Prudhoe Bay.	54
27	Footprint of simulated smoke plume originating at Pump Station 4, near Atigun Pass.	55
28	Footprint of simulated smoke plume originating at just a few kilometers south of Atigun Pass.	56
29	Footprint of simulated smoke plume originating near the Trans-Alaska Pipeline just east of Fairbanks.	57
30	Footprint of simulated smoke plume originating off Valdez Marine Terminal.	59
31	Footprint of simulated smoke plume originating in the Valdez Narrows.	60
32	Footprint of simulated smoke plume originating off Bligh Island.	62
33	Footprint of simulated smoke plume originating off Knowles Head.	63
34	Footprint of simulated smoke plume originating off Zaikof Point.	64
35	Footprint of simulated smoke plume originating off Bligh Reef.	65
36	Footprint of simulated smoke plume originating at Otter Creek on the Kenai Peninsula.	66
37	Footprint of simulated smoke plume originating off Harriet Point on the western shore of Cook Inlet.	67
38	Three-dimensional views of smoke plumes originating in the Valdez Narrows.	69
39	Footprint of simulated smoke plume from a single large fire originating near Pump Station 1, Prudhoe Bay.	71
40	Footprint of simulated smoke plume from 10 fires originating near Pump Station 1, Prudhoe Bay.	72
41	Footprint of simulated smoke plume from 10 fires originating near Pump Station 1, Prudhoe Bay.	73
42	Correlated ALOFT-FT results for a fire generating 1,336 MW with typical overland wind fluctuations.	101
43	Correlated ALOFT-FT results for a fire generating 2672 MW with typical overland wind fluctuations.	102
44	Correlated ALOFT-FT results for a fire generating 668 MW with typical overland wind fluctuations.	103
45	Footprint of simulated smoke plume originating in the Valdez Narrows.	104
46	Footprint of simulated smoke plume originating in the Valdez Narrows.	105
47	Footprint of simulated smoke plume originating in the Valdez Narrows.	106
48	Footprint of simulated smoke plume originating in the Valdez Narrows.	107
49	Footprint of simulated smoke plume originating in the Valdez Narrows.	108
50	Footprint of simulated smoke plume originating in the Valdez Narrows.	109
51	Footprint of simulated smoke plume originating in the Valdez Narrows.	110
52	Footprint of simulated smoke plume originating in the Valdez Narrows.	111
53	Footprint of simulated smoke plume originating in the Valdez Narrows.	112
54	Footprint of simulated smoke plume originating in the Valdez Narrows.	113
55	Footprint of simulated smoke plume originating in the Valdez Narrows.	114
56	Footprint of simulated smoke plume originating in the Valdez Narrows.	115

57	Footprint of simulated smoke plume originating at the Trans-Alaska Pipeline just west of Fairbanks.	116
58	Footprint of simulated smoke plume originating at the Trans-Alaska Pipeline just west of Fairbanks.	117
59	Footprint of simulated smoke plume originating at the Trans-Alaska Pipeline just west of Fairbanks.	118
60	Footprint of simulated smoke plume originating at the Trans-Alaska Pipeline just west of Fairbanks.	119
61	Footprint of simulated smoke plume originating at the Trans-Alaska Pipeline just west of Fairbanks.	120
62	Footprint of simulated smoke plume originating at the Trans-Alaska Pipeline just west of Fairbanks.	121
63	Footprint of six smoke plumes originating at the Valdez Marine Terminal.	122
64	Footprint of six smoke plumes originating at the Valdez Marine Terminal.	123
65	Footprint of six smoke plumes originating at the Valdez Marine Terminal.	124
66	Footprint of six smoke plumes originating at the Valdez Marine Terminal.	125
67	Footprint of six smoke plumes originating at the Valdez Marine Terminal.	126
68	Footprint of six smoke plumes originating at the Valdez Marine Terminal.	127

List of Tables

1	Emission factors and cumulative mass fraction for several particulate sizes.	11
2	US EPA National Ambient Air Quality Standards (NAAQS), Alaska State Regulatory Standards for Concentrations of Contaminants in the Ambient Air, plus relevant Occupational Safety and Health Administration (OSHA) Permissible Exposure Limits (PEL).	13
3	Emission factors for the major combustion products from the Newfoundland Off-shore Burn Experiment.	14
4	Threshold levels for several combustion products compared with the equivalent levels of PM-10 particulate.	15
5	ALOFT Default Dispersion Parameters.	23
6	Key to Pasquill Stability Categories.	23
7	Summary of the ACS Mesoscale Emulsion Burns.	35
8	Summary of the Mobile Burn Series, October, 1994.	38
9	Distance from a fire consuming 1,000 bbl/h beyond which the hour-averaged ground level concentration of PM-10 falls below $150 \mu\text{g}/\text{m}^3$	75
10	Burning characteristics of several heavy hydrocarbon fuels.	86
11	ALOFT Default Dispersion Parameters.	87

1 Introduction

There is growing interest in the environmental consequences of large fires, mostly because the transport of combustion products by a windblown smoke plume can distribute potentially hazardous materials over a wide area. Pools of burning oil and other petroleum products are of particular concern due to the vast flow of these materials through the global economy and because of the fragility of the environment in many regions where oil is extracted or transported. The present work is part of a larger study of a closely related issue, the feasibility of cleaning up oil spills through burning [2].

Several regions of the United States, Canada and Europe are presently evaluating the feasibility of using burning as a remediation tool for large oil spills. In particular, the Alaska Regional Response Team (ARRT) has been working over the past decade to develop procedures and guidelines to facilitate the decision process regarding emergency *in situ* burning of crude oil [3]. As part of their effort to assess the impact of smoke plumes from *in situ* burning on nearby populations, the ARRT and the Alaska Department of Environmental Conservation (ADEC) established a Cooperative Research and Development Agreement (CRADA) with the National Institute of Standards and Technology (NIST) in 1993. Phase I of this project was completed in 1993, and the results have been documented in References [1, 4]. Briefly, laboratory-scale experiments were conducted to determine the heat release rate and smoke yield from two types of Alaskan crude oils, Alaska North Slope (ANS) and Cook Inlet. These experiments were used to determine the input parameters for the ALOFT (A Large Outdoor Fire plume Trajectory) model¹. The version of the model used in this study is now referred to as ALOFT-FT (Flat Terrain). It predicts the concentration of combustion products over relatively² flat terrain downwind of a single large fire. In processing the results of the model, special attention was given to the downwind and lateral extent of ground-level particulate concentrations in excess of $150 \mu\text{g}/\text{m}^3$ averaged over one hour. No formal guidance is available concerning safe levels of short-term exposure to particulate emissions from oil fires. $150 \mu\text{g}/\text{m}^3$ averaged over 24 hours is the upper level established under air quality control regulations in Alaska³. For meteorological conditions typical of the northern and southern coasts of Alaska, the calculations showed that hour-averaged particulate concentrations found at the ground downwind of a single continuous burn of a boomful of oil would not exceed $150 \mu\text{g}/\text{m}^3$ beyond 5 km.

In a follow-up report [5], measurements from two recent mesoscale burn experiments were compared with ALOFT-FT predictions. The first experiment, the Newfoundland Offshore Burn Experiment (NOBE), was conducted by Environment Canada in August, 1993. The second, the Burning of Emulsions Test, was conducted by Alaska Clean Seas (ACS) in September, 1994. For each series of burns, ALOFT-FT was run for the recorded meteorological and burn conditions, and the results were compared with data collected in the field. This analysis, plus a similar comparison with measurements taken at a recent series of burns at the US Coast Guard Fire and Safety Detachment in Mobile, Alabama, are included in this report. For all three large scale field exper-

¹In previous reports the ALOFT model was referred to as the Large Eddy Simulation (LES) model of smoke transport. This title was used during the development of ALOFT because the methodology had been borrowed from an enclosure fire model of the same name.

²Relatively flat in this case means that the variation in altitude of the terrain over which the plume lofts is no more than about 10% of the plume rise height.

³Title 18, Alaska Administrative Code, Chapter 50, Section 20 (AAC 50.020) Ambient Air Quality Standards.

iments, the agreement between model and experiment is very favorable, and greatly increases the confidence in the numerical model.

The purpose of this report is to both assess the conclusions of the original study [1] in light of the recent field experiments, and to extend the applicability of the ALOFT model to scenarios involving complex terrain and multiple burns. The extension of the model to incorporate changes in terrain elevation justifies the original decision to solve the fundamental equations of motion that govern the transport of the smoke and hot gases from the fires. The increased complexity of the problem makes it more difficult to apply conventional empirical models because the amount of field data with which to calibrate an empirical model to account for arbitrary terrain is very limited, plus the built-in assumptions of such a model are too simplistic to describe the plume as it is transported over a complex landscape. Because the ALOFT model solves the fundamental conservation equations that describe the plume structure and trajectory rather than relying on simplistic assumptions, it is a very flexible tool that can be adapted with confidence to increasingly complicated scenarios.

2 Description of the ALOFT Model

2.1 Historical Background

Buoyant windblown plumes have been studied since the early 1960s. A summary of the early work together with a useful bibliography is given by Turner [6]. For summaries of more recent work see Turner [7] and Wilson [8], as well as actual "User's Guides" for some of the more popular models [9, 10, 11, 12]. Virtually all the models described in these works are integral models, where the profiles of physical quantities in cross-sectional planes perpendicular to the wind direction are assumed, together with simple laws relating entrainment into the plume to macroscopic features used to describe its evolution. A great many of the models in use for air quality assessment simply use Gaussian profiles of pollutant density. However, the plume structures actually observed are often too complex to be described in terms of a few simple parameters. This is especially true of plumes lofting over complex terrain.

Most of the assumptions required by integral models can be removed by taking advantage of the enormous advances in computational fluid dynamics that have occurred since most of these models were developed. Of course, large scale computations of atmospheric phenomena can still overwhelm even the fastest computing platforms, but by applying some reasonable approximations to the equations governing the fluid flow, it is possible to reduce the size of the computations to fit onto a reasonably priced personal computer. One particularly useful approximation for the wind-blown plume problem is to assume that the component of the fluid velocity in the direction of the ambient wind is literally the wind speed. The neglect of streamwise perturbations to the ambient wind is an old idea in aerodynamics, where it has been used to study aircraft wake dynamics since the 1930s [13]. Once this approximation is made, the plume (or wake) can be studied as a two-dimensional, time-dependent entity. The large scale structure of the plume can then be determined in detail at moderate computational cost.

This approach was first used to study the settling of a smoke plume in an unstratified atmosphere by Ghoniem *et al.* [14]. This study was performed using Lagrangian vortex dynamics techniques. The main emphasis was on the mixing process as it affected the plume structure. The ALOFT model takes a similar approach, but it uses finite-difference methods to determine the large scale mixing, combined with a Lagrangian description of the transport of the smoke and other pollutants. The effect of sub-grid scale velocity fluctuations on the dispersion of the smoke is accounted for explicitly, and the ambient temperature profile is subject only to the constraint that it is stable over the altitudes occupied by the plume.

2.2 Development of the ALOFT model

The ALOFT model consists of the conservation equations of mass, momentum and energy that describe the steady-state convective transport of heated gases introduced into the atmosphere by a steadily burning fire. The fire itself is not modeled; the smoke plume is the main interest. The fire is represented as a source of heat and smoke, but not necessarily as a point source. Only the overall fuel consumption and heat release rates per unit burn area, plus the fuel-specific emission factors for the combustion products of interest, need be specified. This information is all derived from experimental measurements. The local meteorological conditions that must be provided are the wind speed, the magnitude of the fluctuation of the wind from the prevailing direction, and

the temperature stratification of the atmosphere. Because the model is based on the fundamental conservation equations and does not rely on empirical correlation to describe the plume rise and dispersion, additional physical phenomena can be included in the model if necessary.

The development of the ALOFT model began in the early 1990s. The original intent of the effort was to solve a simplified form of the equations of motion that govern the the introduction of smoke and hot gases from a large fire into the atmosphere. It was assumed that the smoke plume was blown by a non-zero wind over relatively flat terrain (*i.e.*, the sea surface or a flat coastal area). This version of the model is now referred to as ALOFT-FT (Flat Terrain) [15, 16]. The flat terrain assumption is crucial, for it leads to the assumption that the windward component of the flow of smoke and hot gases from the fire *is* the prevailing wind, and the numerical problem is reduced to solving for the fire-induced components of velocity and temperature in a plane perpendicular to the prevailing wind. From a computational point of view, this simplifies the problem tremendously and allows for well-resolved computations of the plume dynamics as it rises and levels off in the atmosphere. High resolution in this case refers to the fact that motion on length scales of 5 to 10 m is captured directly.

The uniform wind assumption is no longer valid when the plume is to be tracked over complex terrain. Many regions in Alaska where burning might occur are characterized by complex terrain. In the region near Valdez, mountains rise several thousand meters within a few kilometers of the shore. The ALOFT-CT (Complex Terrain) model was developed to extend the applicability of the model to handle complex terrain and multiple fires. With this new capability, more realistic, site-specific scenarios can be evaluated. ALOFT-CT still makes use of the plume rise methodology employed by ALOFT-FT because the original simplification of the governing equations can be exploited to compute the rise of the plume until its stabilization height is reached. Then, the three-dimensional governing equations can be solved to provide a wind field over the complex terrain. The Lagrangian particles that represent the smoke particulate⁴ are introduced into the atmosphere by the ALOFT-FT plume rise calculation, and are then transported through the ALOFT-CT three-dimensional flow field.

The computational requirements necessary to generate a full three-dimensional wind field are greater than those required by the flat terrain calculation. Whereas the ALOFT-FT calculations require 10 to 15 minutes of CPU time and roughly 10 megabytes of memory on current generation workstations, ALOFT-CT calculations require two to three times as much CPU time and roughly 32 megabytes of memory. Of course, the requirements demanded by either version of the model depend on the desired resolution of the spatial grid. The numbers cited here are typical for simulations performed in the present study.

An obvious question to ask is why not use the three-dimensional algorithm of ALOFT-CT to compute the plume rise, and eliminate the need to use two algorithms? The answer has to do with spatial resolution. The spatial resolution of the fully three-dimensional ALOFT-CT algorithm is on the order of hundreds of meters because the overall domains of interest are tens of kilometers on a side and several kilometers high. Gridding this volume requires hundreds of thousands of computational cells, depending on how the mesh is arranged. This is the limit of most desktop workstations. Finer grid resolution would require too much time to make the many calculations

⁴Throughout this report smoke particulate will be used as an indicator of plume concentration. Any other combustion product can be analyzed simply by determining the ratio of its emission factor to that of the smoke particulate and multiplying the particulate concentration by that ratio. The emission factor is the ratio of the mass of the particular combustion product to the mass of fuel consumed, usually expressed in units of grams/kilogram.

necessary to consider the wide variety of burn and terrain types. Thus, with a spatial resolution on the order of 100 m, it is not possible to resolve an individual smoke plume as it rises into the atmosphere with the ALOFT-CT algorithm. However, the finer resolution of the ALOFT-FT plume rise algorithm can be exploited to describe the rise and stabilization of the plume, after which the wind field generated by ALOFT-CT can be used to track the Lagrangian particles representing smoke particulate further downwind.

It should be mentioned here that the type of calculation performed by ALOFT-CT is similar to that of several numerical models used by the meteorological community to predict atmospheric phenomena on local or regional scales [17]. The type of model generally depends on the length and time scales of the phenomena of interest. These scales can vary from kilometers to hundreds of kilometers, and from minutes to days. These models include a vast array of features describing wind fields, cloud formation, precipitation, storms, and a variety of other effects. The complexity of the numerical algorithms, however, makes them difficult to adapt to the problem of smoke dispersal from a large fire, specifically because of the resolution limitations in the vicinity of the fire itself. The consolidation of the highly resolved smoke plume generated by ALOFT-FT with the large scale wind field over complex terrain generated by ALOFT-CT is a unique blend of medium-scale and large-scale hydrodynamics that eliminates much of the need for empirical inputs to predict plume-rise heights and other meteorological and geographical effects.

2.3 ALOFT Compared to Other Dispersion Models

The ALOFT model differs from most of the atmospheric dispersion models in use today because it is a *deterministic* rather than an *empirical* model. The approach is to solve the equations governing the flow rather than to rely on empirical formulae that approximate the extent of the dispersion. Empirical models typically assume the pollutant is Gaussian-distributed in the plane perpendicular to the direction of the prevailing wind. The parameters defining the distribution are estimated from experiments. However, Gaussian models are inappropriate for two reasons: (1) the characteristics of the “source” are different from the smokestacks that are usually assumed by such models, and (2) the size of the source is well beyond those considered in industrial applications and thus outside of the experimental parameter range used to calibrate the models.

The rise of a smoke plume from a large fire is governed by the complicated mixing of the hot combustion products with the surrounding air, a process known as entrainment. The extent to which the hot gases are cooled and diluted by the entrained air determines how high the plume will rise. The fires considered in this study generate hundreds of megawatts of energy, and the smoke plumes can rise a few hundred meters to a few kilometers into the atmosphere, depending on the temperature stratification. Often, conventional dispersion models characterize the source in terms of an exit velocity and temperature. Even if a characteristic velocity and temperature of the hot gases near the fire could be ascertained, there is no way to accurately determine the ultimate height to which the plume will rise unless a calculation is performed that explicitly accounts for the mixing processes. This is especially true of atmospheres exhibiting non-linear temperature profiles and features such as temperature inversions.

The ALOFT model exploits the tremendous power of modern computers to solve a simplified version of the Navier-Stokes equations that govern the convective mixing processes. These equations express the conservation laws of mass, momentum and energy of the hot combustion gases as they mix with the atmosphere. Because of the fundamental nature of the governing equations,

far fewer empirical parameters need be input by the user. Ultimately, this simplification will prove to be the most beneficial improvement offered by this direct approach. As the problems of atmospheric dispersion become increasingly complicated by the addition of more physical phenomena, the number of empirical model input parameters will increase tremendously, but the amount of available field data will remain limited due to the difficulty of conducting such experiments. Indeed, this is why numerical models were developed in the first place. With a lack of good data to calibrate empirical models, especially in cases involving complex terrain, the direct approach of solving the fundamental equations of motion has become more attractive.

In the short term however, there is certainly a need for fast, robust numerical models that can run on most any computer. The US Environmental Protection Agency maintains a collection of dispersion models that are available free of charge. Often these “guideline” models are compared with developing models as a first means of assessing their validity. Of the available models, the ISCST3 (Industrial Short Complex, Short Term) [9], CTDMPPLUS (Complex Terrain Dispersion Model PPlus algorithms for Unstable Situations) [11], or the CALPUFF model [10] might be considered as tools to assess the impact of *in situ* burning. The ISCST3 model is a popular Gaussian model designed to predict short-term (hours, days), short-range (1 to 10 km) concentrations of pollutants from industrial sources. The related model CTDMPPLUS considers more complex terrain. These models are less appropriate for oil burning because its size and characteristics fall outside of the parameter space for which the Gaussian models were designed and calibrated. The major shortcoming is the handling of the plume rise from large, open burns. If the plume rise is not calculated correctly, huge errors in downwind concentration can result. In the case of smokestack emissions, the plume does not rise appreciably high, reducing the uncertainty of the results. For this type of problem, the Gaussian models can be expected to give a reasonable answer. However, if the plume originates in a pool fire with little initial velocity, the dynamics of the fire-induced flow field must be included in the simulation. Simple empirical expressions, such as the those described by Briggs [18], often include entrainment parameters calibrated for different source characteristics, but these usually do not encompass the regime of large, buoyancy-dominated plumes such as those produced by burning large amounts of a liquid fuel.

The CALPUFF model is an improvement over the standard Gaussian models for the open burning problem because of its flexibility of design. Its principle feature is its ability to track “puffs” of pollutants through a temporally and spatially changing atmosphere. This idea is also used in the ALOFT model. The difference between CALPUFF and ALOFT lies in the description of the plume rise and the wind field over complex terrain. The CALPUFF model uses empirical plume rise formulae and simplified rules to track the pollutants over terrain features such as hills and mountains. ALOFT describes these processes using the fundamental equations of motion. Of course, the trade-off is that the CALPUFF model is fast and runs on most computers, whereas the ALOFT model requires more computational power (at least for the wind field calculation). This restriction will fall away in the coming years with faster computers. In fact, the calculations included in this report were performed on a Silicon Graphics R4000 workstation. This machine is several years old as of this writing, and is comparable in speeds to the current generation of Intel Pentium processors. Indeed, its speed is surpassed by the Pentium Pro series. Run times on the order of half an hour are typical for the Silicon Graphics machine, with a memory usage of about 32 megabytes.

3 The Fire and its Emissions

Before embarking on a detailed description of the ALOFT model algorithm, it is necessary to describe how the model characterizes the fire and its emissions. The ALOFT model does not model the fire itself, but rather the smoke plume generated by the fire. Thus, only the overall heat release rate and the emission factors for the combustion products of interest need be specified. Dozens of large scale experimental burns of crude and diesel fuels have been conducted by NIST over the past decade at the US Coast Guard Fire and Safety Detachment in Mobile, Alabama [19, 20]. In addition, Environment Canada [22], Alaska Clean Seas [35], and several other organizations both in North America and Europe have conducted large scale burns of heavy hydrocarbon fuels. Based on these and smaller scale laboratory experiments, a data set is now available that contains the burning characteristics of a variety of hydrocarbon fuels on water. Of most importance to the modeling effort are the measurements of heat release rate and smoke yield (the fraction of the fuel mass converted to smoke particulate). As will be discussed in this section, smoke is by far the most likely combustion product to violate air quality standards, thus the modeling results are usually expressed in terms of particulate concentration.

Generally speaking, the heat release rate from a large scale burn of a heavy hydrocarbon fuel is about 2 megawatts per square meter of burning surface. Likewise, the smoke yield varies from 10 to 15%, depending on the fuel type and burn conditions. Given the much greater uncertainties in meteorological conditions, the accuracy of the burning properties is sufficient for modeling. Indeed, the differences in heat release rates and product emissions from the various hydrocarbon fuels studied are relatively small and allow conclusions to be drawn based on the combined properties of the fuels.

3.1 Heat Release Rate

Typically, the “size” of a fire is described in terms of its energy release rate. The fire expected from a typical *in situ* burn application would be on the order of hundreds of megawatts. There are various approaches to measuring the heat release rate of such a large fire, details of which can be found in Reference [19]. Measurements taken at large scale experiments over the past twenty years have led to the development of a data base of burning characteristics for medium to heavy hydrocarbon liquid fuels. For the fuels of most interest to this study (crude oils and diesel fuels), the heat release rates are similar. To convey this information to the numerical model, it is easiest to simply input the area of burning surface, which is proportional to the burning rate, hence the heat release rate, of the fire. Usually, the heat release rate from a large fire of a heavy hydrocarbon fuel on water is about 2 megawatts per square meter. Of course this value depends on the extent of emulsification, weathering, water temperature, *etc.* Appendix A includes values for several fuels under the best of conditions. Modification of these values in consideration of less than ideal conditions is still a subject of much study.

The ALOFT model assumes that the fire is burning steadily. However, in practice, burning, especially for emulsified and weathered heavy liquid fuels on water, is not steady. During the Alaska Clean Seas (ACS) emulsion burn experiments in September 1994, observers noted that the burn of a 50%/50% water/oil emulsion did not burn steadily. Rather, the area of burning surface fluctuated from small, isolated patches to the entire boom area 8 or 9 times over the course of the burn. How does the numerical model handle this type of burning behavior? Because the ALOFT

model predicts time-averaged plume concentrations, it requires the time-averaged burning rate of the fire. This is usually obtained by measuring the amount of fuel consumed, multiplying this by the heat of combustion of the oil and dividing by the time of the burn⁵

$$\text{Total Heat Release Rate (MW)} = \frac{\text{Mass of oil (kg)} \times \text{Total Heat of Combustion (MJ/kg)}}{\text{Burn time (s)}}$$

This time-averaged heat release rate is consistent with all of the other time-averaged ALOFT model inputs. The ground-level sampling results validated the predictions of the ALOFT model for the pulsing fire [5]. If one wanted to account for the pulsations of the fire directly, a fully three-dimensional, time-dependent calculation would have to be performed involving over ten million computational cells for the equivalent spatial resolution of the ALOFT-FT model. This is clearly beyond the means of most if not all available computers, and would yield very little new information or increased accuracy.

3.2 Particulate Emissions

Most guidelines for *in situ* burning target PM-10 smoke particulate as the combustion product most likely to cause a health concern to populations downwind of a burn. PM-10 refers to particulate matter less than 10 μm in diameter. Particle size will be discussed further below. The ALOFT model generally uses PM-10 smoke particulate as a tracer for all other pollutants. If one knows the concentration of smoke particulate downwind, then one can calculate the concentration of all other non-reacting combustion products by way of their relative emission factors. Similar techniques, using experimental measurements of smoke particulate and CO_2 , are crucial in determining the amount of smoke generated by a large fire. For large, open burns a practical method for determining the emission factor for smoke particulate is based on carbon balance principles [21]. The emission factor for particulate is expressed as the product of the measured fraction of carbon in the fuel, multiplied by the ratio of the measured carbon in the smoke to the total carbon mass in the combustion products (CO , CO_2 and smoke aerosols). These quantities are determined by sampling the smoke above the fire, measuring the CO and CO_2 concentrations, and collecting and weighing the smoke particulate. Throughout the analysis, the assumption is made that in the portion of the combustion product flow from which samples are drawn, both the smoke particulate and gaseous combustion products have been transported together from the combustion zone and their concentrations have been equally diluted by entrained air.

It has been proposed, however, that this assumption is invalid [22]. The basis of the argument is that CO_2 , because it is heavier than air (molecular weight 44 versus 29 for air), forms its own plume entirely separate from the smoke plume. This hypothesis contradicts the most basic premise of modern combustion science, and there is no experimental validation for the claim. One of the simplest experiments to perform to justify the carbon balance method is to simultaneously measure the particulate and CO_2 concentrations both inside and outside of the smoke plume. A consistent correlation between the two indicates that indeed the particulate and CO_2 , along with all the other combustion products, are transported and diluted together. Near-field sampling of smoke particulate and CO_2 was conducted by NIST at the ACS emulsion burns, September, 1994,

⁵Note the use of the units MW (megawatts) and MJ (megajoules). A joule is a unit of energy whose counterpart in the English system is a BTU (British Thermal Unit). A watt is a measure of heat released per unit time, and is equivalent to a joule per second. The letter M denotes one million.

and at a set of Mobile diesel fuel burns in October, 1994 [5]. Similar measurements were made by a team from the University of Washington at the Newfoundland Offshore Burn Experiment (NOBE) [23, 24]. In each instance, simultaneous measurements of CO₂ and smoke particulate were made; the NIST measurements near the fire at ground-level; the University of Washington measurements aboard an aircraft flying in and out of the plume. For the NIST measurements, a RAM (real-time aerosol monitor) unit for particulate and a highly sensitive nondispersive infrared CO₂ analyzer were placed together at various locations within a radius of about 10 m from the burn pit. Figure 1 shows values of the two quantities during the first ACS burn. The curves reflect

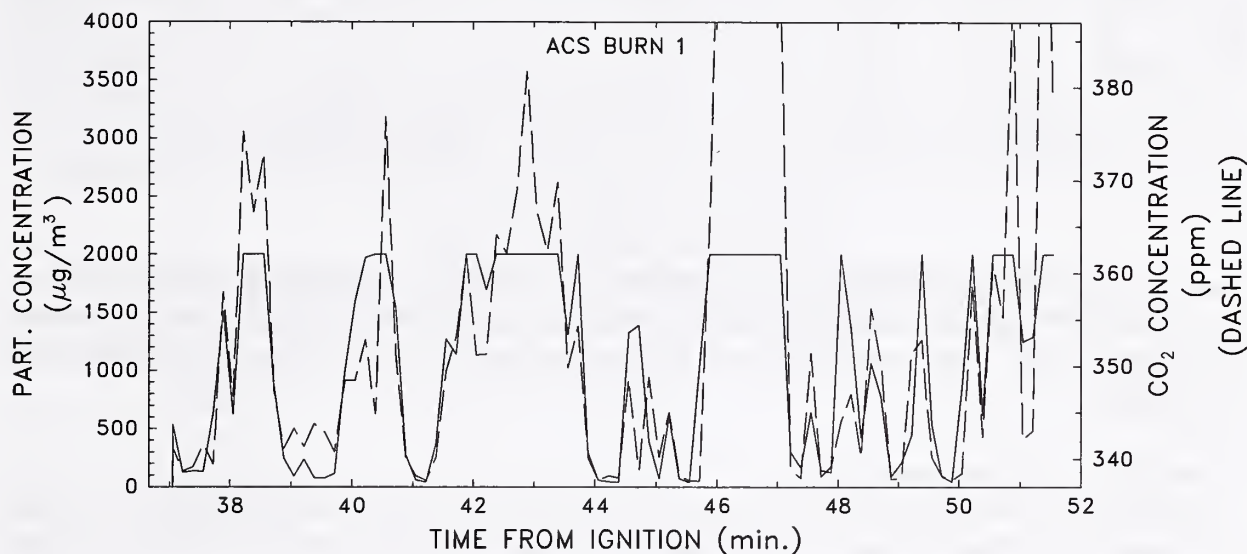


Figure 1: Near-field simultaneous measurements of particulate (solid line) and CO₂ (dashed line) at the 1994 Alaska Clean Seas emulsion burns (See Section 5.2). The location of the instruments for this time sequence was about 5 m downwind of the fire, just below the berm of the pit. The scale ratio of the left and right axes is 80 to 1. The flattened peaks of the particulate curve are due to the fact that the RAM (real-time aerosol monitor) has reached its upper range of 2,000 µg/m³.

a ratio of 80 µg/m³ particulate for every ppm (part per million) excess CO₂. This same ratio was also found by the University of Washington team at the Newfoundland burn in the plume several kilometers downwind of the fire. The ratio corresponds to a smoke yield of about 11%, based on the carbon balance method. Figure 2 shows a result of a similar exercise for diesel fuel conducted at the October, 1994, series of mesoscale burns at the US Coast Guard Fire and Safety Detachment, Mobile, Alabama. Although diesel fuel rather than crude oil was burned, the results are very similar. In fact, the data is plotted with the same scaling ratio as that for the Alaska burn. As before, the presence of excess CO₂ correlated very closely with both the presence and quantity of particulate recorded throughout the test.

The University of Washington team found a similar correlation between CO₂ and particulate in the plume several kilometers downwind of the second NOBE burn. In addition, the smoke yield they derived for PM-3.5 particulate (only particles less than 3.5 µm in size were sampled) was 8.7%. The NIST particle size distribution measurements at NOBE indicate that about 70% of the particulate mass was PM-3.5. Thus the University of Washington smoke yield result extrapolates

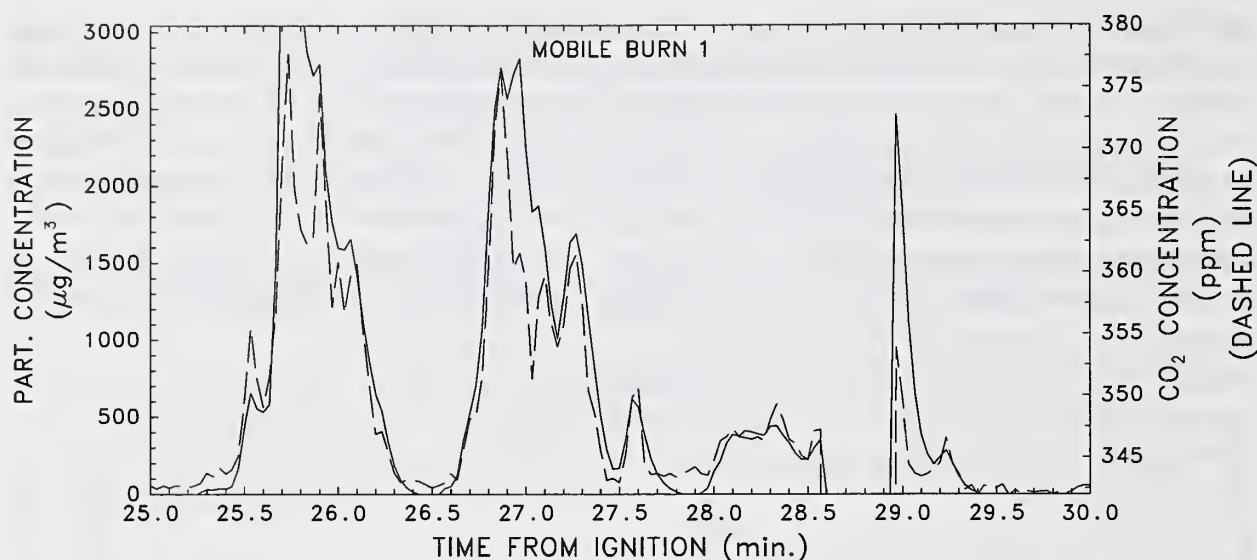


Figure 2: Near-field simultaneous measurements of particulate (solid line) and CO₂ (dashed line) at the 1994 Mobile diesel fuel burn (See Section 5.3). The location of the instruments for this time sequence was about 15 m downwind of the fire. The scale ratio of the left and right axes is 80 to 1.

to roughly 12% for total particulate.

The results from the NIST and University of Washington experiments clearly show that when and where CO₂ is detected there is also particulate. In fact, the ratio of particulate to CO₂ indicates a smoke yield on the order of 10 to 12%. There is no evidence of a CO₂ plume separate from the visually obvious smoke plume as reported in Reference [22]. Furthermore, the ratio of excess CO₂ to particulate was found to be about the same both near the fire (ACS and Mobile experiments) and far downwind (NOBE), indicating that the smoke particulate and CO₂ travel together for large distances from the fire. This finding supports the carbon balance method as the appropriate technique for determining smoke yield, which for crude oils and heavy refined fuels is consistently in the range of 10 to 15%.

Often the results of smoke yields measurements from the Kuwait oil field fires following the Gulf War in 1991, are thought to apply to *in situ* burning of oil spills. They do not. Researchers at the Kuwait fires concluded that the smoke yield from these fires was on the order of 1 or 2%. However, the nature of most of the fires was very different from *in situ* burning. The Kuwaiti fires were mostly *jet* fires as opposed to pool fires. Jet fires inherently burn more efficiently than pool fires due to the enhanced mixing of fuel and air brought about by the violent ejection of oil from the damaged well head. A discussion of the measurements and the discrepancy between the types of fires can be found in Reference [25].

3.3 Particulate Size

Particulate size is an important health consideration and also impacts the dynamics of smoke settling. Particulates having an aerodynamic effective diameter⁶ less than 10 μm are considered respirable and may be drawn into the lungs with normal breathing. In general, small particle sizes are less likely to settle out of the plume and can be expected to be carried much further from the burn site than larger particles⁷. The analysis of the smoke from several burn experiments reveals that 70 to 90% of the particulate mass is associated with particles less than 10 μm in size. This type of analysis is performed by drawing a sample of the smoke through a series of cascade impactors, each of which filters out particles of increasing effective diameter. The results indicate the fraction of the total particulate mass associated with particles of different sizes. Table 1 presents the emission factors for various particulate sizes. These results are based on several large scale burns of Louisiana crude [20], the Newfoundland offshore burns of Alberta Sweet Mixed Blend [23, 26], and some laboratory scale burns of Alaska North Slope (ANS) and Cook Inlet crudes [1]. A more discerning

Particulate Size Distribution		
Particulate Size (μm)	Emission Factor (g/kg)	Cumulative Mass (%)
Total Particulate	150	100
PM-10	130	87
PM-5	100	67
PM-3.5	87	58
PM-2.5	82	55
PM-1.0	75	50

Table 1: Emission factors and cumulative mass fraction for several particulate sizes. The cumulative mass fraction is the percentage of the total particulate mass associated with particles whose effective diameters are less than or equal to the given PM value. These results are based on several large scale burns of Louisiana crude [20], the Newfoundland offshore burns of Alberta Sweet Mixed Blend [23, 26], and some laboratory scale burns of Alaska North Slope and Cook Inlet crudes [1].

selection of particulate size raises the issues of accuracy and interpretation. Smoke particles are not spherically shaped, but rather complicated amalgamations of smaller particles. Figure 3 shows the structure of a smoke particle as viewed through an electron microscope. Clearly, the “size” of a given particle is subject to some interpretation. Measurements with a cascade impactor are subject to an appreciable uncertainty due to the possible breakdown of these particles into their more fundamental components. Plus, it has been observed that the size distribution is somewhat related to the fire size [27]. The particulate size distribution presented in Table 1 is characteristic of smoke from a fire that is at least 10 m in diameter.

⁶The aerodynamic effective diameter of a particle is defined as the diameter of an equivalent smooth spherical particle with a density of 1 g/cm³ that has the same settling velocity in air.

⁷For a smoke particle with an aerodynamic effective diameter of 10 μm , its settling velocity in still air would be on the order of a millimeter per second, based on a simple Stokes flow analysis. Thus, in a few hours the particle might be expected to settle 10 or 20 m in the absence of precipitation. For the length and time scales of the problem, this is a negligible amount.

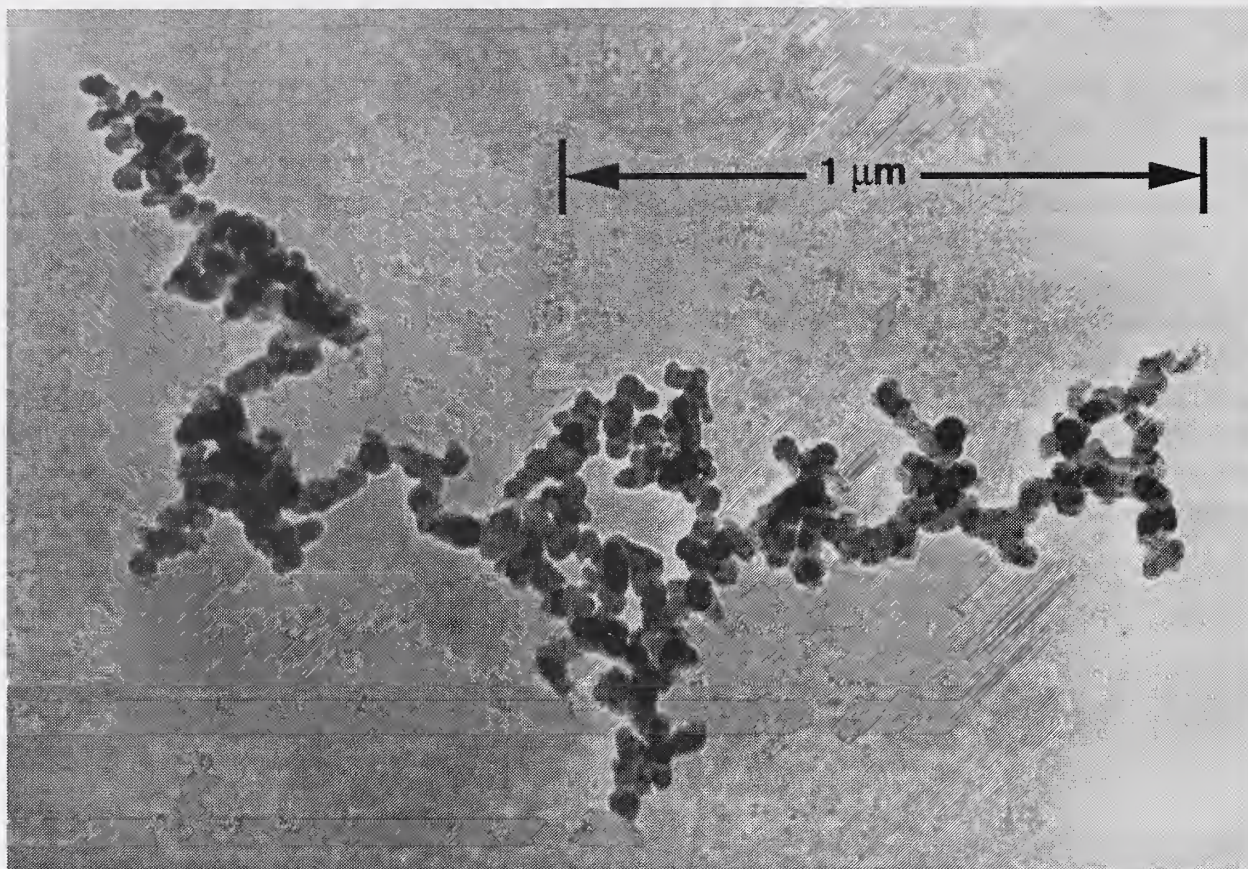


Figure 3: Electron micrograph of a smoke particle from a 3 m crude oil fire.

The particulate concentrations predicted by the ALOFT model can easily be adjusted to accommodate any new PM standard. The emission factor for the particulate size of concern can be input during the post-processing phase of the calculation. The computation of the fire-induced flow field is not affected by the choice of pollutant since it is assumed that the pollutant is passive and does not settle out of the plume during the period of time being simulated (a few hours). For the calculations presented in this report, PM-10 particulate is used as the pollutant “tracker”. Predictions of the downwind concentration of any other combustion product can be made assuming that its emission factor is known.

3.4 Other Emissions

There has been much discussion over the past few years about the relative importance of the health hazards posed by the various combustion products from a burn of crude oil. Listed in Table 2 are the National Ambient Air Quality Standards (NAAQS) established by the US Environmental Protection Agency, the corresponding Alaska state regulations, plus some relevant work place standards established by the Occupational Safety and Health Administration (OSHA). Note that the Alaska State Regulatory Standards for Concentrations of Contaminants in the Ambient Air closely follow the national standards.

The University of Washington team that sampled the smoke plumes from Newfoundland Off-

Pertinent Air Quality Standards					
Contaminant (units)	Averaging Periods				
	Annual	24 hour	8 hour	3 hour	1 hour
National Ambient Air Quality Standards (NAAQS)					
PM-10 ($\mu\text{g}/\text{m}^3$)	50	150	—	—	—
CO (ppm)	—	—	9	—	35
SO ₂ (ppm)	0.03	0.14	—	—	—
NO ₂ (ppm)	0.053	—	—	—	—
O ₃ (ppm)	—	—	—	—	0.12
Lead ($\mu\text{g}/\text{m}^3$)	1.5	—	—	—	—
Alaska State Regulatory Standards					
PM-10 ($\mu\text{g}/\text{m}^3$)	50	150	—	—	—
CO (mg/m^3)	—	—	10	—	40
Sulfur Oxides ($\mu\text{g}/\text{m}^3$)	80	365	—	1,300	—
NO ₂ ($\mu\text{g}/\text{m}^3$)	100	—	—	—	—
OSHA Permissible Exposure Limits (PEL)					
CO ₂ (ppm)	—	—	10,000	—	—
PAH ($\mu\text{g}/\text{m}^3$)	—	—	200	—	—
Benzene (in VOC) (ppm)	—	—	1	—	—

Table 2: US EPA National Ambient Air Quality Standards (NAAQS), Alaska State Regulatory Standards for Concentrations of Contaminants in the Ambient Air, plus relevant eight hour Permissible Exposure Limits (PEL) established by the Occupational Safety and Health Administration (OSHA). Note that values written in units of mass per volume (*i.e.* $\mu\text{g}/\text{m}^3$ or mg/m^3) can be converted to volume fractions (often expressed in units of parts per million or ppm), according to the formula

$$[\text{volume fraction}] \equiv \frac{[\text{mass/volume (gm}/\text{m}^3)]}{44.619 m_p}$$

where 44.619 is the number of moles of an ideal gas that occupy 1 m^3 at standard temperature and pressure (273.15°K and 1 atm), and m_p is the molecular weight of the combustion product (gm/mole).

shore Burn Experiment (NOBE) sampled not only the smoke particulate and CO₂, but several other important combustion gases, as well. Table 3 contains the emission factors for the major combustion products of concern. If it is assumed that the combustion products from an *in situ* burn of crude oil are well-mixed and non-reacting over time periods of roughly several hours, and that the emission factors cited in Table 3 are fairly typical, then one can conclude based on the analysis to follow that smoke particulate is the combustion product of most concern from a regulatory standpoint.

The 24 hour standard for PM-10 particulate is 150 $\mu\text{g}/\text{m}^3$. Table 3 lists the emission factor for PM-10 as 130 g/kg, slightly less than the emission factor of 150 g/kg for total particulate.

Emission Factors for the Major Products of Combustion		
Combustion Product	Emission Factor (g/kg)	Emission Rate kg/h
CO ₂	2,810	75,900
Total Particulate, Ref. [26]	150	4,050
PM-10 Particulate, (Interpolated)	130	3,510
PM-3.5 Particulate	87	2,350
CO	30	810
SO ₂ (ANS crude)	3 (25)	81
VOC	5	132
Polynuclear Aromatic Hydrocarbons (PAH)	~0.1	~2.7
NO _x	~1	~27

Table 3: Emission factors for the major combustion products from the Newfoundland Off-shore Burn Experiment [23]. The oil burned was Alberta Sweet Mixed Blend. Note that the emission factor for PM-10 is an interpolation based on the measurements of total particulate, PM-3.5, and the particulate size distribution. Also note the inclusion of a second emission factor for SO₂ corresponding to the more “sour” Alaska North Slope (ANS) crude. The emission factors for the other combustion products are not expected to change significantly from one type of heavy hydrocarbon fuel to another.

Assuming the combustion products in the smoke plume are found in amounts proportional to their emission factors one can calculate the expected PM-10 concentration corresponding to the the threshold concentration of any other combustion product. For example, consider carbon monoxide, CO. At its one-hour threshold level of 40 mg/m³ (40,000 µg/m³), the PM-10 concentration would be 173 mg/m³ (173,000 µg/m³). This result is obtained by noting from Table 3 that for every 30 g of CO produced by the fire, 130 g of PM-10 are produced. Thus, one would expect to find 130/30 times as much PM-10 as CO at a given location in the smoke plume. Table 4 summarizes this exercise for the combustion products of interest. Note that sulfur dioxide SO₂ is a distant second to particulate in terms of potential for air quality standard violation⁸. Table 4 simply states that if the concentration of any of the combustion products besides particulate were to approach its regulatory standard, the PM-10 concentration at the same location would be almost two orders of magnitude greater than its standard. Clearly, this indicates that particulate is the combustion product on which to concentrate when performing the numerical simulations.

⁸The emission factor for SO₂ at the NOBE burn was reported by the University of Washington team to be 3 g/kg, based on the assumption that all of the sulfur in the fuel is converted to SO₂ on burning. The mass concentration of sulfur in the original oil was measured to be 0.0015. SO₂ is exactly half sulfur by mass, thus for every kilogram of oil burned 3 grams of SO₂ were generated. The sulfur content of samples of Cook Inlet and ANS crude was determined to be 0.0019 and 0.0127, respectively [1]. Thus, the emission factors for SO₂ from the burning of each are 3.8 and 25.4 g/kg, respectively.

Contaminant	Threshold Concentration ($\mu\text{g}/\text{m}^3$)	Equivalent PM-10 Concentration ($\mu\text{g}/\text{m}^3$)
SO ₂ (from ANS crude)	1,300 (3 h)	6,800
NO ₂	100 (Annual)	13,000
CO	40,000 (1 h)	173,000
PAH	200 (8 h)	260,000
CO ₂	12,260,000 (8 h)	650,000

Table 4: Threshold levels for several combustion products compared with the equivalent levels of PM-10 particulate. For example, if CO were found at a concentration of 40,000 $\mu\text{g}/\text{m}^3$, then the particulate concentration in that same location would be about 173,000 $\mu\text{g}/\text{m}^3$.

4 The Smoke Plume

All versions of the ALOFT model consist of the discretized equations of motion that govern the introduction of heat, smoke particulate and other combustion products into the atmosphere. As seen from the previous section, these fire-related quantities are obtained from laboratory and field experiments. The role of the equations introduced in this section is to track the rise and dispersion of the pollutants in the atmosphere over distances ranging from hundreds of meters to tens of kilometers. This wide range of length scales necessitates several different treatments of the governing equations so that phenomena associated with the various stages of plume development are captured. This is what is meant by the term “spatial resolution,” and it frequently enters the discussion of the numerical algorithms designed to solve the governing equations in approximate form. This section outlines the simplification of the equations meant to make their solution tractable on modern computer workstations, and in some cases, personal computers. Two forms of the equations will be derived. The first set is an approximation based on a uni-directional wind field and is used by ALOFT-FT to compute the plume rise and downwind transport over flat terrain. This algorithm is also used by ALOFT-CT to calculate just the plume rise. The second form of the equations is fully three-dimensional, and used by ALOFT-CT to generate a wind field over the complex terrain. Details of the actual computational algorithms are found in Appendix B.

4.1 The Boussinesq Approximation

The introduction of smoke and hot gases from a large fire into the atmosphere can be described by conservation equations of mass, momentum and energy that govern the temperature, pressure, density, and velocity of the air.

Conservation of mass

$$\frac{\partial \rho}{\partial t} + \nabla \cdot \rho \mathbf{u} = 0 \quad (1)$$

Conservation of momentum

$$\rho \left(\frac{\partial \mathbf{u}}{\partial t} + (\mathbf{u} \cdot \nabla) \mathbf{u} \right) + \nabla p - \rho \mathbf{g} = \nabla \cdot \boldsymbol{\sigma} \quad (2)$$

Conservation of energy

$$\rho c_p \left(\frac{\partial T}{\partial t} + \mathbf{u} \cdot \nabla T \right) - \frac{dp}{dt} = \dot{q} + \nabla \cdot k \nabla T \quad (3)$$

Equation of state

$$p = \rho \mathcal{R} T \quad (4)$$

Here, all symbols have their usual fluid dynamical meaning: ρ is the density, \mathbf{u} the velocity vector (u, v, w), p the pressure, \mathbf{g} the gravity vector, c_p the constant-pressure specific heat, T the temperature, k the thermal conductivity, t the time, \dot{q} the prescribed volumetric heat release rate, \mathcal{R} the gas constant equal to the difference of the specific heats ($\mathcal{R} = c_p - c_v$), and σ the standard stress tensor for compressible fluids.

These equations must be simplified to make the numerical computations tractable. Both ALOFT-FT and ALOFT-CT make use of a technique known as the Boussinesq approximation, which asserts that the fluid is essentially incompressible, but allows for buoyancy-driven flow due to the difference in temperature between the hot gases of the smoke plume and the surrounding atmosphere. A rigorous justification of the approximation is given by Panofsky and Dutton [28], and a brief description is given here. First, it is assumed that the pressure may be divided into a hydrostatic term and a fire/terrain-induced perturbation term

$$p(\mathbf{x}, t) = p_0(z) + \tilde{p}(\mathbf{x}, t) \quad (5)$$

where the Cartesian coordinate system is represented by the vector $\mathbf{x} = (x, y, z)$ with z the vertical coordinate. Likewise, the temperature and density fields are decomposed

$$T(\mathbf{x}, t) = T_0(z) + \tilde{T}(\mathbf{x}, t) \quad ; \quad \rho(\mathbf{x}, t) = \rho_0(z) + \tilde{\rho}(\mathbf{x}, t) \quad (6)$$

The ambient pressure and density are related through the hydrostatic condition

$$\frac{dp_0}{dz} = -\rho_0 g \quad (7)$$

The variations in ambient quantities T_0 , p_0 and ρ_0 are also assumed to be small compared with their sea-level values. This limits the validity of the model to the lowest few kilometers of the atmosphere. The most important consequence of the Boussinesq form of the equations is that the convective derivative $dp/dt = \partial p/\partial t + \mathbf{u} \cdot \nabla p$ in Eq. (3) is approximated by $w dp_0/dz$ to eliminate acoustic waves from the solution. This greatly facilitates the numerical solution of the equations because the time step is not limited by the sound speed. Now, the Boussinesq form of the governing equations are written

Conservation of mass (incompressibility)

$$\nabla \cdot \mathbf{u} = 0 \quad (8)$$

Conservation of momentum

$$\rho_0 \left(\frac{\partial \mathbf{u}}{\partial t} + (\mathbf{u} \cdot \nabla) \mathbf{u} \right) + \nabla \tilde{p} - \tilde{\rho} \mathbf{g} = \mu \nabla^2 \mathbf{u} \quad (9)$$

Conservation of energy

$$\rho_0 c_p \left(\frac{\partial \tilde{T}}{\partial t} + \mathbf{u} \cdot \nabla \tilde{T} \right) - \left(\frac{dp_0}{dz} - \rho_0 c_p \frac{dT_0}{dz} \right) w = \dot{q} + k \nabla^2 \tilde{T} \quad (10)$$

Equation of state

$$\frac{\rho - \rho_0}{\rho_0} = -\frac{T - T_0}{T_0} \quad (11)$$

Notice that the dissipation terms have been simplified by assuming that the coefficients of viscosity μ and thermal conductivity k are constant. The role of these dissipative terms will be discussed below.

4.2 Scaling Laws for the Three-Dimensional Equations (ALOFT-CT)

The Boussinesq form of the governing equations is used both to generate a wind field over the complex terrain and to compute the plume rise. In both cases the equations are nondimensionalized to facilitate their numerical solution. However, the scalings used are different in each case. For the plume rise, the scalings are based on the heat output of the fire. This scaling will be discussed in the next section. For the wind field calculation, the scaling is based on the thermal stability of the atmosphere, as defined by the Brunt-Väisälä frequency N , which is related to the background temperature $T_0(z)$

$$\frac{N^2}{g} = \frac{1}{T_0} \left(\frac{dT_0}{dz} + \frac{g}{c_p} \right) \quad (12)$$

This quantity is used to establish the characteristic length scale

$$H = \frac{U_0}{N_0} \quad (13)$$

where U_0 is the wind speed at an altitude where the plume is expected to loft, and N_0 is the Brunt-Väisälä frequency characteristic of the lower atmosphere.

Applying these scalings to the Boussinesq form of the governing equations described in the previous section yields a relatively simple set of equations to solve numerically. The asterisk applied to the variables indicate that they have been nondimensionalized as follows

$$\begin{aligned} (x, y, z) &= H(x^*, y^*, z^*) & \tilde{p} &= \rho_0 U_0^2 \tilde{p}^* \\ t &= H t^* / U_0 & N^2 &= N_0^2 N^{2*} \\ (u, v, w) &= U_0(u^*, v^*, w^*) & \tilde{T} &= U_0^2 T_0 \tilde{T}^* / (g H) \end{aligned}$$

Conservation of mass (incompressibility)

$$\frac{\partial u^*}{\partial x^*} + \frac{\partial v^*}{\partial y^*} + \frac{\partial w^*}{\partial z^*} = 0 \quad (14)$$

Conservation of momentum

$$\frac{\partial u^*}{\partial t^*} + u^* \frac{\partial u^*}{\partial x^*} + v^* \frac{\partial u^*}{\partial y^*} + w^* \frac{\partial u^*}{\partial z^*} + \frac{\partial \tilde{p}^*}{\partial x^*} = \frac{1}{\text{Re}} \left(\frac{\partial^2 u^*}{\partial x^{*2}} + \frac{\partial^2 u^*}{\partial y^{*2}} + \frac{\partial^2 u^*}{\partial z^{*2}} \right) \quad (15)$$

$$\frac{\partial v^*}{\partial t^*} + u^* \frac{\partial v^*}{\partial x^*} + v^* \frac{\partial v^*}{\partial y^*} + w^* \frac{\partial v^*}{\partial z^*} + \frac{\partial \tilde{p}^*}{\partial y^*} = \frac{1}{\text{Re}} \left(\frac{\partial^2 v^*}{\partial x^{*2}} + \frac{\partial^2 v^*}{\partial y^{*2}} + \frac{\partial^2 v^*}{\partial z^{*2}} \right) \quad (16)$$

$$\frac{\partial w^*}{\partial t^*} + u^* \frac{\partial w^*}{\partial x^*} + v^* \frac{\partial w^*}{\partial y^*} + w^* \frac{\partial w^*}{\partial z^*} + \frac{\partial \tilde{p}^*}{\partial z^*} - \tilde{T}^* = \frac{1}{\text{Re}} \left(\frac{\partial^2 w^*}{\partial x^{*2}} + \frac{\partial^2 w^*}{\partial y^{*2}} + \frac{\partial^2 w^*}{\partial z^{*2}} \right) \quad (17)$$

Conservation of energy

$$\frac{\partial \tilde{T}^*}{\partial t^*} + u^* \frac{\partial \tilde{T}^*}{\partial x^*} + v^* \frac{\partial \tilde{T}^*}{\partial y^*} + w^* \frac{\partial \tilde{T}^*}{\partial z^*} + N^{2*} w^* = \frac{1}{\text{Re Pr}} \left(\frac{\partial^2 \tilde{T}^*}{\partial x^{*2}} + \frac{\partial^2 \tilde{T}^*}{\partial y^{*2}} + \frac{\partial^2 \tilde{T}^*}{\partial z^{*2}} \right) \quad (18)$$

The Reynolds number $\text{Re} = \rho_0 U_0 H / \mu$ and the Prandtl number $\text{Pr} = \mu c_p / k$ nondimensionalize the “eddy” viscosity and thermal conductivity μ and k . The term “eddy” implies that these coefficients do not take on their molecular values, but rather serve as sinks of kinetic and thermal energy that actually result from unresolvable, sub-grid scale dissipative processes. In practice, they are used to set the dynamic range of length scales employed in the simulation, and they stabilize the numerical algorithm. They also permit solutions with vortex separation from the terrain boundaries.

4.3 Scaling Laws for the Two-Dimensional Equations (ALOFT-FT)

Equations (14)–(18) are solved to establish a wind field over the complex terrain. This wind field is regarded as the background flow, into which the hot gases from the fire are introduced. The equations governing the hot plume are also based on the Boussinesq form of the fundamental equations, but the solution methodology is different in that it exploits the assumption that the wind field within a radius of about 1 km from the fire is relatively uni-directional and blowing at a speed of at least 1 or 2 m/s. It is also assumed that the terrain is fairly flat in the vicinity of the fire. These assumptions are the basis for the ALOFT-FT model. Through a technique sometimes referred to as *parabolization*, the time-dependent terms of the governing equations are removed, the windward component of velocity is assumed constant, and the windward spatial coordinate is replaced by a temporal coordinate. After a suitable nondimensionalization, the three-dimensional, steady-state system of equations becomes a two-dimensional, time-dependent system. It can now be characterized as an initial value problem in which the solution is initially prescribed in a plane perpendicular to the direction of the prevailing wind. This initial plane is taken to be a few fire diameters downwind of the fire. These simplified equations resolve the plume rise down to a length scale of about 5 to 10 m, sufficient to capture the entrainment of air into the smoke plume. Because of the high spatial resolution afforded by the simplification, these equations are used to describe the plume rise in both ALOFT-FT and ALOFT-CT.

The parabolization of the governing equations is brought about by assuming that the prevailing wind speed and direction are relatively steady and aligned with the positive x -axis. The crosswind velocity components (v, w) lie in a plane (y, z) normal to the direction (x) of the uniform ambient

wind whose speed is U_0 . The only information about the fire required is the overall *convective*⁹ heat release rate Q and the particulate mass flux M . The initial temperature distribution in the plume cross section is assumed to be Gaussian and satisfy the following integral

$$\int_{-\infty}^{\infty} \int_0^{\infty} \rho_0 c_p U_0 \tilde{T} dz dy = Q \quad (19)$$

The particulate distribution is initialized similarly and satisfies the integral

$$\int_{-\infty}^{\infty} \int_0^{\infty} \rho_p U_0 dz dy = M \quad (20)$$

where ρ_p is the density of the particulate matter. The particulate matter is considered a passive scalar and thus has no effect on the hydrodynamic calculation. It is represented by Lagrangian particles that are advected by the flow field.

The scaling of the Boussinesq form of the governing equations is based on the strength of the fire. The length scale is given by

$$L = \left(\frac{Qg}{c_p T_{\infty} \rho_{\infty} U_0 N_0^2} \right)^{\frac{1}{3}} \quad (21)$$

where the subscript “ ∞ ” refers to ground level, ambient conditions, and N_0 is the Brunt-Väisälä frequency characteristic of the lower atmosphere. The length scale L roughly corresponds to the plume height. The windward spatial coordinate x is replaced by a temporal coordinate

$$t^* = \frac{N_0}{U_0} x \quad (22)$$

The characteristic velocity of the air in the crosswind plane is given by

$$V = N_0 L \quad (23)$$

The characteristic length L and velocity V are used to define dimensionless crosswind spatial coordinates (y^*, z^*) and velocities (v^*, w^*) as follows:

$$(y, z) = fL(y^*, z^*) \quad ; \quad (v, w) = fV(v^*, w^*) \quad (24)$$

The factor f is an adjustable scale factor that ensures that the plume height does not exceed the height of the computational domain, fL . The non-dimensional temperature perturbation \tilde{T}^* is defined

$$\tilde{T} = \frac{fQ}{c_p \rho_{\infty} U_0 L^2} \tilde{T}^* \quad (25)$$

Finally, the turbulent Reynolds and Prandtl numbers are:

$$\text{Re} = \frac{f^2 \rho_{\infty} V L}{\mu} \quad ; \quad \text{Pr} = \frac{\mu c_p}{k} \quad (26)$$

⁹About 10% of the total energy released by the fire is in the form of thermal radiation, and is not accounted for by the model. The low radiative loss is a consequence of the high smoke loading, which provides an absorbing “sheath” around the strongly radiating gaseous combustion products [27].

The dimensionless form of the conservation laws are now given as

Conservation of mass (incompressibility)

$$\frac{\partial v^*}{\partial y^*} + \frac{\partial w^*}{\partial z^*} = 0 \quad (27)$$

Conservation of momentum

$$\frac{\partial v^*}{\partial t^*} + v^* \frac{\partial v^*}{\partial y^*} + w^* \frac{\partial v^*}{\partial z^*} + \frac{\partial \tilde{p}^*}{\partial y^*} = \frac{1}{\text{Re}} \left(\frac{\partial^2 v^*}{\partial y^{*2}} + \frac{\partial^2 v^*}{\partial z^{*2}} \right) \quad (28)$$

$$\frac{\partial w^*}{\partial t^*} + v^* \frac{\partial w^*}{\partial y^*} + w^* \frac{\partial w^*}{\partial z^*} + \frac{\partial \tilde{p}^*}{\partial z^*} - \tilde{T}^* = \frac{1}{\text{Re}} \left(\frac{\partial^2 w^*}{\partial y^{*2}} + \frac{\partial^2 w^*}{\partial z^{*2}} \right) \quad (29)$$

Conservation of energy

$$\frac{\partial \tilde{T}^*}{\partial t^*} + v^* \frac{\partial \tilde{T}^*}{\partial y^*} + w^* \frac{\partial \tilde{T}^*}{\partial z^*} + N^{*2} w^* = \frac{1}{\text{Re Pr}} \left(\frac{\partial^2 \tilde{T}^*}{\partial y^{*2}} + \frac{\partial^2 \tilde{T}^*}{\partial z^{*2}} \right) \quad (30)$$

subject to the initial conditions

$$v^*(y^*, z^*, t = 0) = w^*(y^*, z^*, t = 0) = 0 \quad (31)$$

$$\int_{-\infty}^{\infty} \int_0^{\infty} \tilde{T}^*(y^*, z^*, t = 0) dy^* dz^* = 1/f^3 \quad (32)$$

Initially, the crosswind velocity components v and w are assumed to be zero, although this assumption is not restrictive. No-flux, free-slip boundary conditions are prescribed at the ground, consistent with the assumed uniformity of the prevailing wind and the resolution limits of the calculation. Details of the numerical method applied to these equations are given in Appendix B.

Figures 4 and 5 show the results of a sample computation, illustrating the position of the initial slice and the extent of the computational domain. The plume is visualized by interpolating the particle locations onto the computational grid, and then plotting the isosurface on which the particulate density is zero. Figure 5 shows the plume from underneath, illustrating the structure of the large, counter-rotating vortices that are generated by the rising plume. This vortex structure is a dominant feature of the rising plume, and governs the rate at which fresh air is mixed in with the hot combustion products. Figure 6 is a photograph taken about 100 m downwind of the Newfoundland Offshore Burn Experiment, and it shows clearly the development of the two vortices. An excellent discussion of these structures is given in Reference [29].

4.4 Atmospheric Turbulence

The solutions to both forms of the Boussinesq equations described in the previous two sections may be regarded as “time-averaged”. This is certainly the case with the parabolized equations where the time-dependent terms are explicitly removed. For the three-dimensional, time-dependent equations described in Section 4.2, the spatial resolution of the calculations is coarse and the wind fluctuations are not explicitly built into the boundary conditions. Instead, the trajectories of the Lagrangian particles used to represent the smoke particulate are randomly perturbed from their

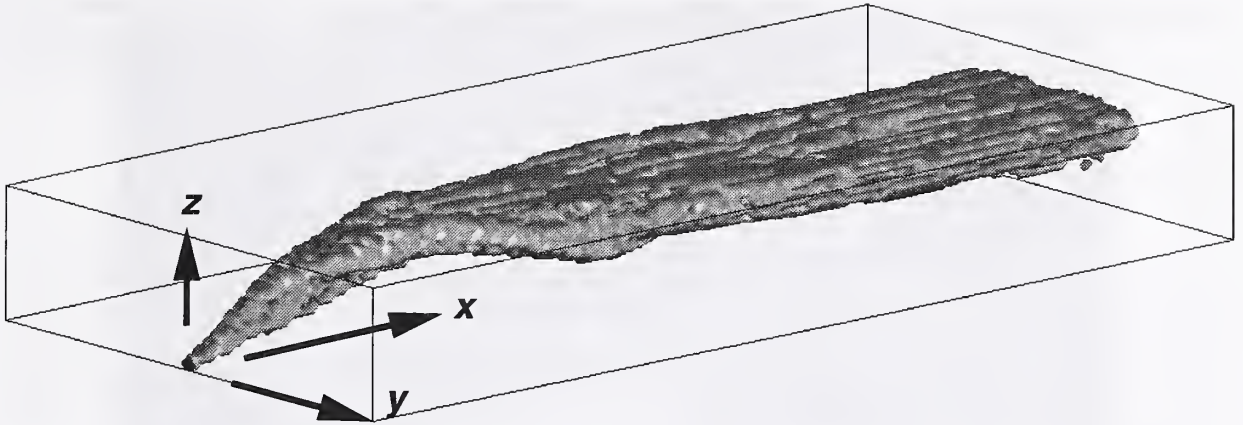


Figure 4: Three dimensional view of a computed smoke plume in the first few kilometers of its development. The height of the viewbox is 1 km, the length 8 km, and the crosswind length 4 km. The wind speed is 6 m/s. The computation is initialized by prescribing the temperature and particulate distribution in the plane spanned by the y and z coordinates. Then the plume is constructed as the initial plane is swept downwind.

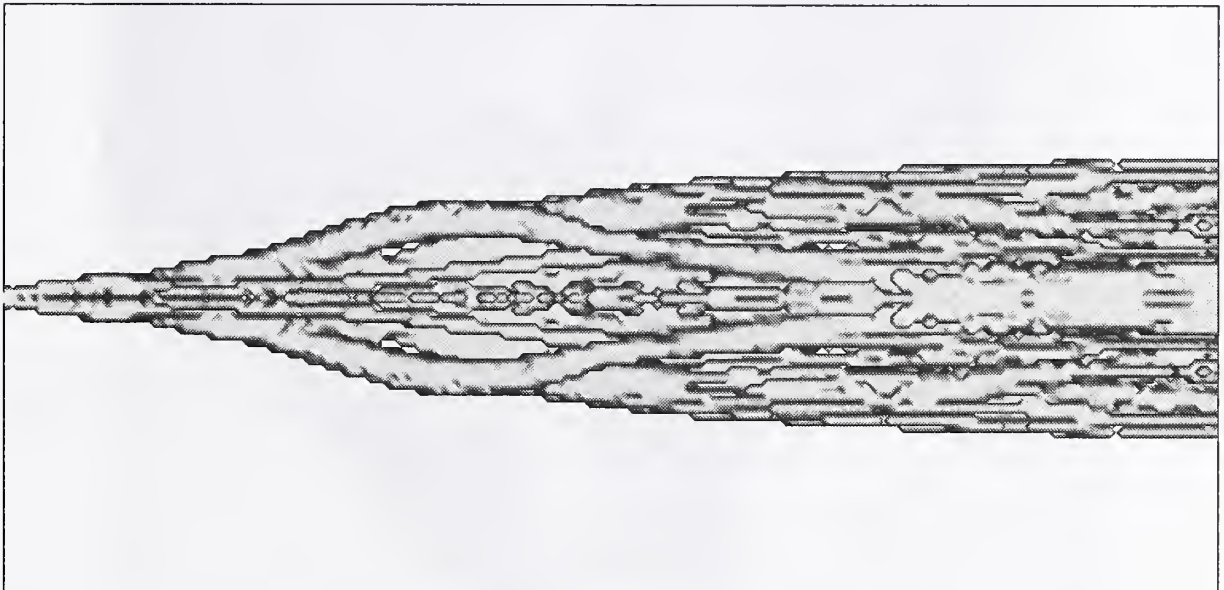


Figure 5: A view of the plume from below. Note the separation and reconnection of the two large counter-rotating vortices.

mean paths in order to mimic the spatial and temporal fluctuations of the wind and the underlying turbulence. Specifically, the motion of each particle is governed by the mean wind field (u, v, w) plus a perturbation velocity field (u', v', w') that represents the random temporal and spatial variations of the ambient wind. For simplicity, it will be assumed that the wind direction is aligned with the velocity component u , even though the numerical algorithm does not require the wind to be aligned with the x coordinate. Most meteorological texts adhere to the convention that v and w are perpendicular to the direction of the prevailing wind. Indeed, this is the case for the



Figure 6: Photograph taken from about 200 m downwind of the Newfoundland Offshore Burn Experiment (NOBE) showing the two large counter-rotating vortices which characterize the structure of the rising smoke plume.

two-dimensional form of the equations. The perturbation velocity components are derived from the recursive relations

$$u'(t + \delta t) = R_u(\delta t) u'(t) + u'' \quad ; \quad R_u(\delta t) = e^{-\delta t/\tau_u} \quad (33)$$

$$v'(t + \delta t) = R_v(\delta t) v'(t) + v'' \quad ; \quad R_v(\delta t) = e^{-\delta t/\tau_v} \quad (34)$$

$$w'(t + \delta t) = R_w(\delta t) w'(t) + w'' \quad ; \quad R_w(\delta t) = e^{-\delta t/\tau_w} \quad (35)$$

The double-primed terms are random variables with Gaussian distributions whose variances are that of the perturbation velocities multiplied by $(1 - R_u^2)$, $(1 - R_v^2)$ and $(1 - R_w^2)$, respectively, ensuring that the variance of the each velocity component will not change from one time step to another. The variance of v' and w' are denoted in the literature as σ_v^2 and σ_w^2 , respectively. The fluctuation of the windward velocity component u can be associated with wind gusts. The functions R_u , R_v and R_w are Lagrangian correlation coefficients, taken as exponentials. The parameter τ is indicative of the period of atmospheric fluctuations. Appropriate values for various meteorological conditions are given by Draxler [30]. Generally speaking, τ is on the order of several minutes. The default values of these constants are given in Table 5.

	Marine	Coastal	Mountain
σ_u (m/s)	0.2	0.4	0.4
σ_v (m/s)	0.5	1.2	1.2
σ_w (m/s)	0.4	1.0	1.0
τ_u (s)	300	300	300
τ_v (s)	300	300	300
τ_w (s)	100	100	100

Table 5: ALOFT Default Dispersion Parameters [10, 30, 12]

A popular classification scheme for defining the turbulence of the atmosphere is given by Pasquill [31]. Table 6 summarizes the various “stability categories”. Corresponding to each stabil-

Surface Wind m/s	Day			Night	
	Incoming Solar Radiation			Cloud Cover	
	Strong	Moderate	Slight	Low	High
<2	A	A-B	B		
2-3	A-B	B	C	E	F
3-5	B	B-C	C	D	E
5-6	C	C-D	D	D	D
>6	C	D	D	D	D

Table 6: Key to Pasquill Stability Categories [31]

ity category are values for the standard deviation of the prevailing wind direction in the horizontal and vertical directions. Reference [32] contains a discussion of these parameters and methods of evaluating them. The following are suggested values for $\sigma_\theta = \sigma_v/U_0$ corresponding to the Pasquill

Stability Categories A–F: 25° , 20° , 15° , 10° , 5° , and 2.5° , respectively. The values of $\sigma_\phi = \sigma_w/U_0$ are taken to be roughly two-thirds of the respective values of σ_θ . These values may be interpreted as averaged over a time period of 10 minutes to an hour. Notice that the values of σ_v and σ_w given in Table 5 roughly correspond to the angular fluctuations corresponding to the Pasquill stability categories when the wind speed is taken into account.

Usually, the smoke plume resides mainly in what is referred to as the planetary boundary layer (PBL). Sometimes this region is also called the mixing layer, although the precise definitions of these terms varies depending on the specific application. For the discussion to follow, the boundary or mixing layer is that part of the troposphere that is directly influenced by the presence of the earth's surface. The depth of this layer can vary from roughly fifty meters to several thousand meters. Within it, the interaction of the complex terrain, solar heating and surface friction creates a turbulent wind field, to which the solution of the above equations may be considered a time-average. The values of the wind fluctuation parameters given above are appropriate within this mixing layer. However, it often happens that the smoke plume, due to the tremendous thermal buoyancy, will penetrate the top of the mixing layer. When this happens, the plume is subject to far less turbulent motion because the air currents are more representative of the free atmosphere. As a result, the magnitude of the wind fluctuations used in the model are reduced for those particles that penetrate the top of the mixing layer. More discussion of this can be found in Appendix A.

Finally, it should be noted that the model of atmospheric turbulence discussed in this section is relatively simple. There exist in the literature more elaborate models, and the user is directed to any number of references that provide correlations based on various other observed conditions [28, 31, 32, 10, 12]. The best source of wind fluctuation parameters is an anemometer, but this type of data is often hard to come by for a given region and a given set of atmospheric conditions.

4.5 Flat Terrain Correlations

The scalings employed in Section 4.3 reduce the time-dependent, three-dimensional Navier-Stokes equations to a nondimensionalized, two-dimensional initial value problem that, when solved, yields a steady state plume lofting over flat terrain. These scalings can be exploited once again to produce a set of correlations that summarize the results of the model for a wide range of meteorological conditions. The only complication stems from the fact that the reduction to the nondimensional set of equations (27)–(30) does not account for the imposition of atmospheric turbulence described in Section 4.4. If only the equations that govern the fire-induced flow were being considered, then a single solution could be redimensionalized to yield a family of solutions parameterized by the fire's heat release and smoke generation rates, the average temperature lapse rate of the atmosphere, and the wind speed. However, the fact that the fluctuations of the wind are not necessarily correlated with any of these parameters means that several dimensionless solutions of the governing equations need to be generated to account for various levels of atmospheric turbulence that may occur for any particular set of fire size, lapse rate and wind speed.

To make this discussion more clear, consider the diagram presented in Figure 7. The wind speed and average lapse rate have been chosen as the two independent variables because they essentially define the meteorology. The specific fire size chosen represents a single burn of North Slope crude typical of what one might expect during an actual spill. For each pair of wind speed and lapse rate, the three sets of contours reveal the predicted maximum ground level concentration (short dashes), the distance downwind of the fire that it would occur (solid lines), and the farthest

FLAT TERRAIN, GROUND LEVEL PARTICULATE CONCENTRATION
FOR VARIOUS METEOROLOGICAL CONDITIONS

BURN SIZE 820 MW

SMOKE GENERATION RATE 2.8 kg/s

LATERAL VELOCITY STANDARD DEVIATION 1.2 m/s

VERTICAL VELOCITY STANDARD DEVIATION 1.0 m/s

CRITICAL CONCENTRATION $150 \mu\text{g}/\text{m}^3$

SOLID LINES INDICATE DOWNWIND DISTANCE (km); SHORT DASHES MAXIMUM CONCENTRATION ($\mu\text{g}/\text{m}^3$); LONG DASHES EXTENT OF CRITICAL CONCENTRATION (km)

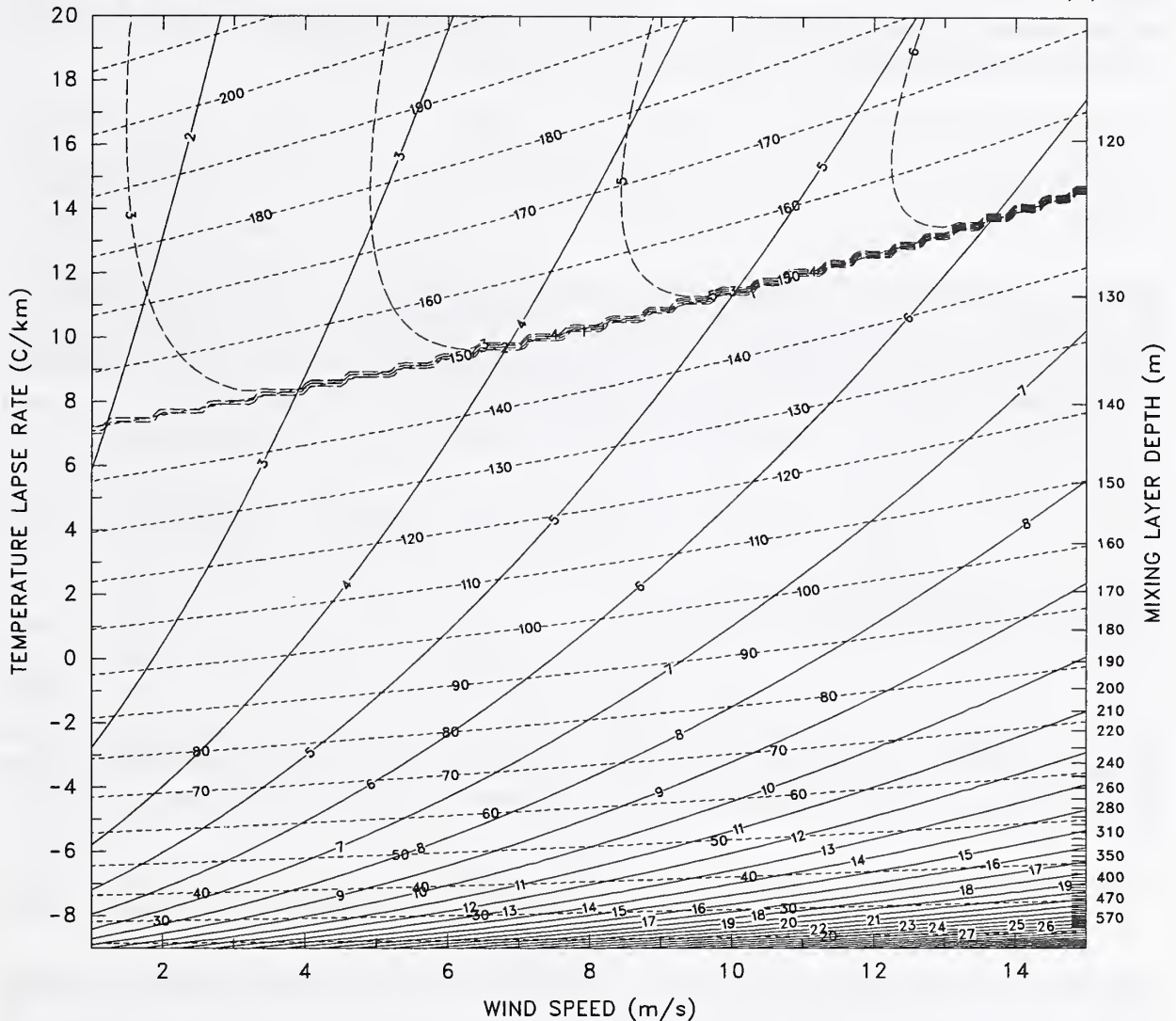


Figure 7: Correlated ALOFT-FT results for an 820 MW fire and typical overland wind fluctuations. The thick, somewhat jagged line represents the $150 \mu\text{g}/\text{m}^3$ threshold (ground level, hour-averaged). Note that the term lapse rate applied to the vertical temperature profile is equivalent to dT_0/dz . Often in the meteorological literature, the lapse rate is defined $-dT_0/dz$.

distance downwind one could expect to find a concentration of a certain critical value (long dashes). In this case, the critical value is $150 \mu\text{g}/\text{m}^3$. Notice that the long dashes may only be found on that part of the diagram where the maximum concentration exceeds the critical value. The thick, somewhat jagged curve (or set of curves) separates the diagram into areas where the critical concentration is expected at the ground and where it is not.

These diagrams can easily be generated for different fire sizes and levels of atmospheric turbulence, as well as for different values of the critical concentration. For a given value of the wind speed U_0 (m/s), temperature lapse rate Γ ($^\circ\text{C}/\text{m}$), heat release rate¹⁰ Q (W), mass generation rate of any combustion product of interest¹¹ M ($\mu\text{g}/\text{s}$), the standard deviation of the lateral wind direction σ_θ (degrees), and the ground temperature T_∞ (K) compute the following:

$$\begin{aligned}\sigma_v &= U_0 \sin(\sigma_\theta) \\ U_{eq} &= \left(\frac{1.2}{\sigma_v}\right) U_0\end{aligned}$$

The term U_{eq} represents an equivalent wind speed used in lieu of the actual wind speed to account for the difference in wind fluctuation between that which is observed and that for which the calibration calculations were performed. Values of heat release and mass generation rate for particulate as a function of the fire area for various fuels are given in Table 10 in Appendix A.

An estimate of the maximum ground level concentration is given by the expression

$$\rho_{max} = \frac{M}{Q^{2/3}} \left(\frac{U_0}{U_{eq}}\right)^{\frac{2}{3}} \left(\frac{\Gamma - \Gamma_{ad}}{T_\infty}\right)^{\frac{2}{3}} (31.6 - 0.480 U_{eq}) \quad \left(\frac{\mu\text{g}}{\text{m}^3}\right) \quad (36)$$

This maximum concentration will be reached

$$x_{max} = \sqrt{\frac{T_\infty}{\Gamma - \Gamma_{ad}}} (11.6 + 3.11 U_{eq}) \quad (\text{m}) \quad (37)$$

downwind of the fire. Note that the dry adiabatic lapse rate Γ_{ad} is $-0.0097 \text{ }^\circ\text{C}/\text{m}$. If the maximum concentration ρ_{max} exceeds the given critical concentration ρ_c , then the expression

$$x_c = x_{max} + 23.2 \sqrt{\frac{-T_\infty \ln\left(\frac{\rho_c}{\rho_{max}}\right)}{\Gamma - \Gamma_{ad}}} \quad (\text{m}) \quad (38)$$

provides an estimate of how far downwind one would expect to find ground level concentrations in excess of the critical concentration ρ_c .

These correlations yield time-averaged predictions of ground level concentration over time periods consistent with the determination of the wind fluctuations. In other words, if the standard deviation of the lateral wind direction is based on an hour-average, then the predicted concentration is taken as an hour-average. Also, it is assumed that the vertical mixing is unlimited, that is, the

¹⁰The heat release rate can be calculated by multiplying the burn area by the heat release rate per unit area for the given fuel, found in Table 10. For the flat terrain correlations, express the heat release rate in units of watts.

¹¹The mass generation rate of a given combustion product is obtained by multiplying the burn area by the burning rate per unit area (Table 10) by the emission factor expressed in terms of grams of product per gram of fuel burned. Express the result in units of micrograms per second.

wind fluctuations are applied at all altitudes. These assumptions are intended to render predictions that are likely to over-estimate ground level concentration. This built in conservative bias is only true for the simplified correlations discussed in this section.

Also, in many instances, the situation of interest will be where a plume from an offshore burn is blown onshore. The magnitude of the wind fluctuations will roughly double when the plume reaches the shore. To account for this, one may define an equivalent offshore distance d_{eq} which is related to the actual offshore distance d through the relation

$$d_{eq} = \frac{\sigma_{w,\text{marine}}}{\sigma_{w,\text{coastal}}} d \quad (39)$$

Usually, $\sigma_{w,\text{marine}}$ is about 0.5 m/s, whereas $\sigma_{w,\text{land}}$ is about 1.0 m/s. A good rule of thumb is to take d_{eq} as half the distance to the shore along the direction parallel to the prevailing wind. After defining the equivalent offshore distance, then the above formulae, applied with coastal values of the wind fluctuations, can be used to estimate the distance from the burn beyond which the concentration will fall below a preset value.

If the lapse rate Γ is not readily available, then a rough correlation between lapse rate and mixing layer depth¹² can be employed. This correlation is based on an examination of about 1,000 soundings at various stations in Alaska, at various times of the day and seasons of the year. Figure 8 presents a comparison of the average lapse rate and mixing layer depth for the soundings, plus a best fit curve¹³. The mixing layer depth is a useful quantity because it is often easier to determine the mixing layer depth than the lapse rate. Even though from a modeling standpoint the lapse rate is a more useful quantity, the mixing layer depth is often the only quantity available. This is especially true in Alaska, where the dispersive potential of the atmosphere is often characterized in terms of the "ventilation factor." This quantity is the product of the mixing layer depth and wind speed, and usually expressed in units of m²/s. In Figure 7, it is easily seen that the meteorological conditions that yield higher ground level concentrations correspond to low ventilation factors (upper left), whereas lower ground level concentrations correspond to relatively high ventilation factors (lower right). Of course, a single value of the ventilation factor corresponds to a family of meteorological conditions, thus if the ventilation factor is to be used to make a prediction, either the wind speed or mixing layer depth must be estimated or measured so that a single point on the chart can be determined.

¹²The mixing layer depth is determined from the vertical profile of the virtual potential temperature θ_v , which is defined as follows

$$\theta_v = T(p_0/p)^{0.286} (1 + 0.61 r)$$

where T is the temperature (K), p the pressure, p_0 the surface pressure, and r the mixing ratio of water vapor (g/g). The mixing ratio is found from the dew point temperature T_d using Tetens' formula [33]

$$r = (380/p) \exp(17.27(T_d - 273.15)/(T_d - 35.86))$$

The top of the mixing layer usually is reached at an altitude where the virtual potential temperature begins to increase with height. This often occurs near the cloud base.

¹³The relationship between lapse rate and mixing layer depth is approximately given by the following formula

$$h = 75 + \frac{1200}{\Gamma - 10.5}$$

where h is the mixing layer depth in meters and Γ is the lapse rate in °C/km.

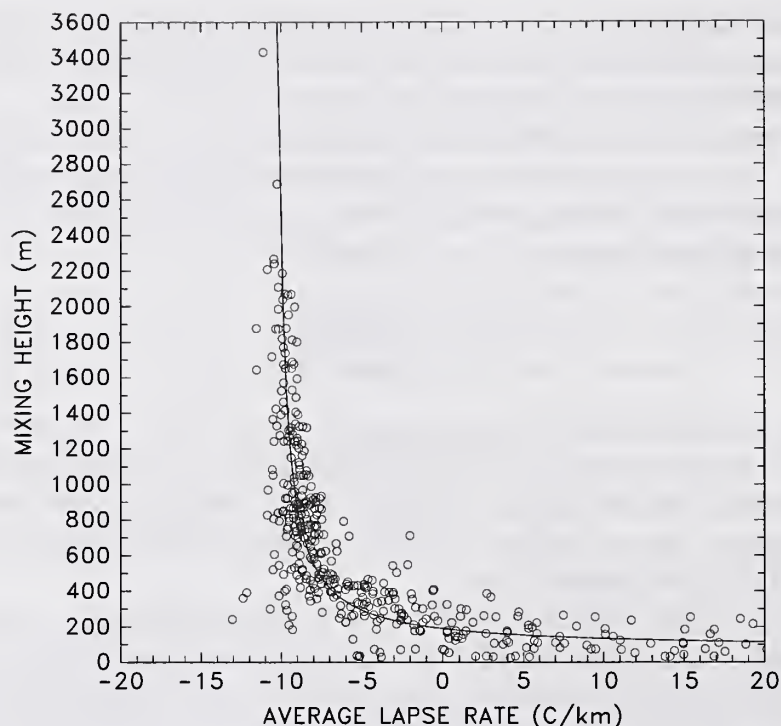


Figure 8: Average temperature lapse rate versus mixing layer depth for several hundred randomly chosen soundings in Alaska. These soundings were extracted from the NOAA radiosonde data base [34]. More information about the sounding data is included in Appendix A.

One additional benefit of the diagram shown in Figure 7 is that it presents the user with a better appreciation of the uncertainty inherent in any model prediction. It is easy to see from the diagram to what extent uncertainties in the wind speed and lapse rate can yield uncertainties in ground level concentrations. This is especially true if the wind speed and lapse rate fall on the diagram near the critical concentration curve. On one side of the curve, the model predicts that the critical concentration will never be observed at ground level, whereas the other side of the curve yields a prediction where not only is the critical concentration observed at ground level, but at a considerable distance from the fire, perhaps past some established “safe distance.” In this example, the critical concentration is found at the ground when the atmosphere is very stable (*i.e.* the temperature increases by at least 8 degrees (C) per kilometer near the ground). Under these conditions, the plume will be relatively close to the ground, and slight changes in atmospheric conditions can easily change the ground level concentration.

5 Validation Experiments for ALOFT-FT

Following the original study [1] in which ALOFT-FT was applied to the problem of *in situ* burning over relatively flat coastal regions of Alaska, the model predictions were compared with measurements taken at three recent field experiments. The following sections document the comparisons. It should be pointed out that the experimental data was used to assess the accuracy of the model predictions. The data was *not* used to calibrate the model. This is an important distinction, and it points out the difference between a deterministic and an empirical model.

5.1 The Newfoundland Offshore Burn Experiment (NOBE)



Figure 9: Photograph of the Newfoundland Offshore Burn Experiment showing the shift of the wind at about 120 m off the surface.

The Newfoundland Offshore Burn Experiment (NOBE) provided an enormous amount of data regarding *in situ* burning of oil at sea. The experiment consisted of two burns of crude oil conducted off the coast of St. John's, Newfoundland on August 12, 1993. Most of the sampling of the chemical species produced by the burning was done relatively close to the fire. However, the University of Washington's Cloud and Aerosol Research Group performed airborne measurements of the smoke plume from the two burns at distances up to 20 km downwind of the fire. Of particular importance to the present study are the lidar (Light Detection and Ranging) measurements of the plume cross section, and the real-time monitoring of the CO₂ level in the plume.

Lidar measurements were performed during the second burn. For this burn, it was reported that 28.9 m³ (182 bbl)¹⁴ of Alberta Sweet Mixed Blend crude oil of density 843.7 kg/m³ was burned in 1.3 hours [22]. Even though substantial fluctuations in burning rate were observed, for the purposes of modeling the plume it was assumed that the burning rate was constant at 5.2 kg/s. Based on previous work with Louisiana crude [19], the effective heat of combustion of the oil was assumed to be 42,000 kJ/kg, even though a different oil was used for the experiment¹⁵. The smoke yield for the burn was measured by the team from NIST to be approximately 15% [20], and the fraction of the total heat release lost from the flame as radiation through the dense smoke plume was assumed to be 10% [27]. Thus, the *convective* heat release rate for the model run was about 200 MW and the particulate production rate was 0.78 kg/s. Atmospheric temperature soundings taken from the University of Washington airplane [24] and from the NIST tethered blimp [20] show a temperature inversion from about 100 to 175 m in altitude, accompanied by a shift of roughly 30 to 40 degrees in the direction of the wind. This shift in the wind can be seen in the photograph presented in Figure 9. The wind speed at the ground was about 5 to 6 m/s, increasing to about 8 m/s a few hundred meters up.

Figure 10 displays time-averaged cross sections of the simulated plume at downwind locations comparable to those at which lidar measurements were made from the University of Washington aircraft (See Figure 11). The shift in the wind direction at about 120 m in altitude dramatically increases the lateral width of the plume, spreading the smoke over a 2 km wide path. This spreading is seen in both the simulated and the actual plume cross sections. There is qualitative and quantitative¹⁶ agreement between the two for a distance of about 6 km from the fire. This assessment is based mainly on the height and lateral extent of the simulated plume in comparison to the lidar images. It should be emphasized that the lidar images reflect the instantaneous plume cross section, whereas the simulated cross sections represent a time-averaged picture.

Beyond 6 km from the fire the numerical model does not predict the additional lofting of the plume shown by a lidar trace along the approximate plume centerline (Figure 12). The model correctly predicts the initial rise height of 200 m, but after about 6 km, the plume gradually rises to a height of about 600 m. The centerline of the simulated plume reaches a height of about 250 m, but does not exhibit this gradual rise. It is unclear exactly why it occurs. It has been speculated that this lofting might be due to the heat generated by the absorption of sunlight by the smoke particulate. Another explanation is the possible presence of local convective cells in the path of the plume. These updrafts occur over small areas and cannot be predicted from the meteorology of the entire region. In any case, this example points out the limitation of any predictive dispersion or meteorological model. Large scale patterns and trends can be predicted, but small scale details cannot.

In addition to lidar measurements, the University of Washington airplane made a number of other measurements. Of interest to this study are measurements of CO₂. Plume particulate concentrations may be derived either by quantifying lidar cross section data as shown above, or by measuring the excess CO₂ and backing out the particulate concentration based on the smoke yield and the elemental carbon mass fraction of the fuel. Direct measurements of excess CO₂ made while

¹⁴A very common unit in the petroleum industry is a barrel (bbl), equivalent to 42 gallons (U.S.) or 0.159 m³. Throughout this report, volume of oil will be expressed in terms of barrels to conform with common practice.

¹⁵The heat of combustion is based on laboratory tests of a number of crude oils.

¹⁶This quantification is based on an analysis of the scattering characteristics of the individual smoke particles. Details of the analysis may be found in Reference [24].

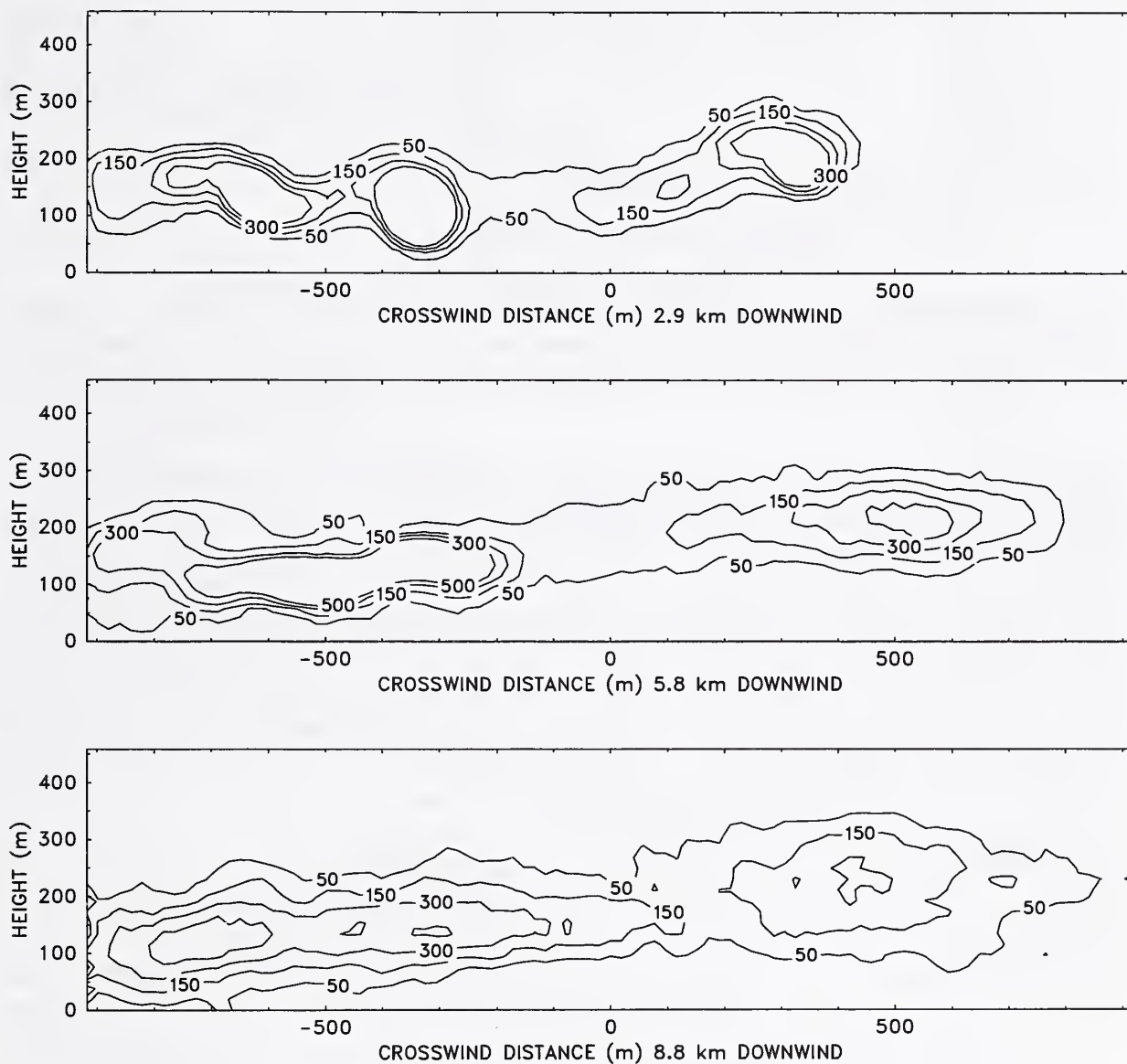


Figure 10: Time-averaged cross sectional slices of the simulated smoke plume from the second NOBE burn. Shown are particulate concentration contours of 50, 150, 300, and 500 $\mu\text{g}/\text{m}^3$ at three locations downwind corresponding to where lidar measurements were taken. The vertical length scale indicates height above sea level, while the horizontal scale indicates the distance from the assumed plume centerline.

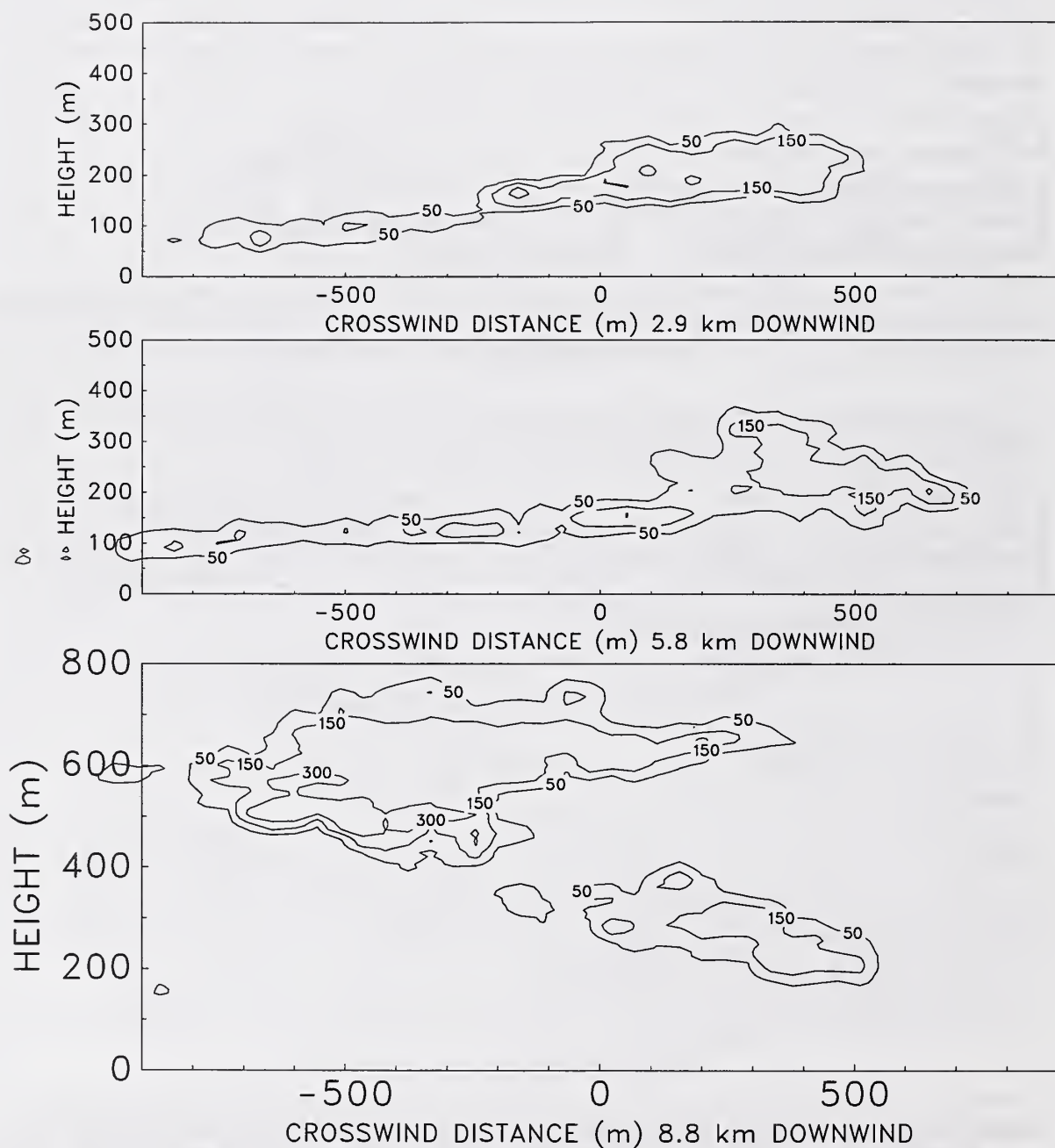


Figure 11: Instantaneous cross sectional slices of the actual smoke plume from the second NOBE burn, courtesy of the University of Washington Cloud and Aerosol Research Group. Shown are contours of particulate concentration at 50, 150 and 300 $\mu\text{g}/\text{m}^3$. The crosswind scale indicates relative distances, and the origin was chosen to compare with the simulation.

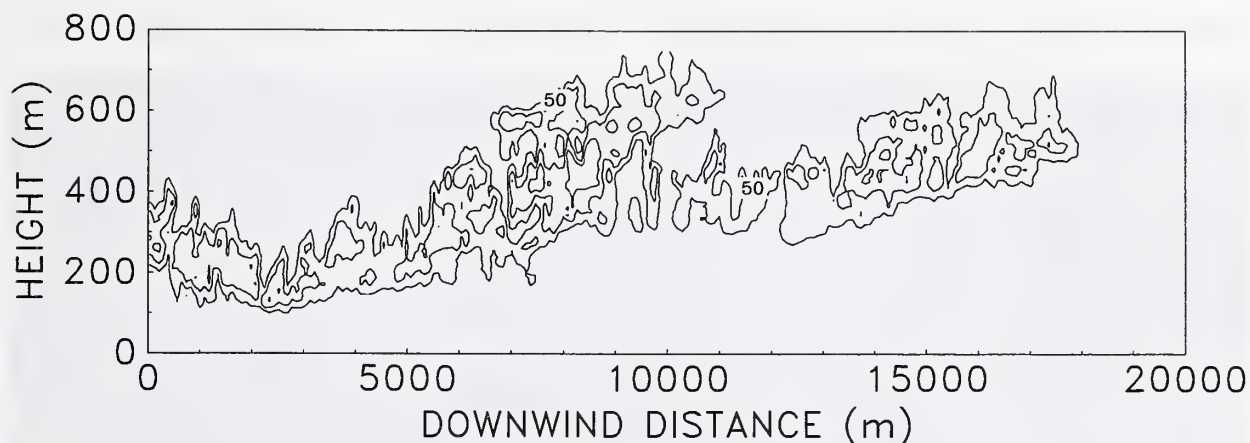


Figure 12: Lidar measurement of plume centerline of the second burn taken from University of Washington airplane. Note that the horizontal and vertical length scales are very different. In actuality, the plume shown is a long, slender object. Also, the origin of the plot is about 0.9 km from the actual fire.

flying the airplane along the centerline of the plume have been used to estimate the concentration of particulate matter. Taking the smoke yield to be 15% (from the NIST tethered blimp) and the elemental carbon mass fraction of the fuel to be 0.8664 ; it is estimated that 1 ppm excess CO_2 corresponds to a particulate concentration of $103 \mu\text{g}/\text{m}^3$. Direct measurements of excess CO_2 from the airplane show volume fractions decreasing to about 1.5 ppm (the equivalent of $150 \mu\text{g}/\text{m}^3$ particulate) by about 16 km downwind of the burn. The quantified lidar images are consistent with this finding. The model calculation predicts that concentrations in excess of $150 \mu\text{g}/\text{m}^3$ extend slightly farther than 20 km downwind. The discrepancy in the two estimates is not surprising, given the enhanced plume dispersion of the experiment due to the unexpected lofting. Also, the comparison is being made based on only one pass of the airplane along the plume centerline, which may not account for the maximum concentration. Indeed, the model predicts, and visual sightings confirm, the existence of counter-rotating vortices which are generated by the fire and which entrain a substantial fraction of the particulate. Thus, it is not necessarily true that the maximum concentration of particulate would be found along the centerline of the plume. *In situ* measurements of the plume cannot account for its complex structure, and thus a better means of measuring particulate concentration would be through the use of integrated techniques, such as the lidar measurements discussed above.

5.2 Alaska Clean Seas Burning of Emulsions Experiment

In early September 1994, Alaska Clean Seas conducted at its Fire Training Ground in Prudhoe Bay, Alaska, three mesoscale burns to determine the feasibility of burning emulsified oil [35]. Figure 13 shows an aerial view of the second burn. At the request of the Alaska office of the US Environmental Protection Agency, the EPA's Emergency Response Team (EPA/ERT) came to Prudhoe Bay with 12 real-time aerosol monitors (RAMs). These instruments use a light scattering

technique to measure particulate concentrations¹⁷. The twelve instruments were set out on meter



Figure 13: Aerial photograph taken of the second ACS burn, Prudhoe Bay, September, 1994.

high tripods, spread out in rows of three or four, at distances ranging from 1 to 5 km from the burn site. The deployment strategy varied from burn to burn, depending on the weather conditions and the terrain over which the plume was expected to loft. The instruments were set to sample every second, and then log the 5 second average. Global positioning instruments recorded the locations of the individual devices.

Table 7 summarizes the three mesoscale emulsion burns. Each burn consisted of burning an oil mixture within the confines of a fire-resistant circular boom which floated in a pit filled with water. The boom diameter was roughly 9 m, and the rectangular pit was roughly 20 m by 30 m. The first and third burns consumed emulsions of salt water and 17.4% evaporated Alaska North Slope crude. Emulsion breakers were applied to these mixtures. The second burn consumed fresh ANS crude. To compute the average heat release rate for the burns, the mass of oil consumed (Oil Mass \times Removal Efficiency) was multiplied by a total heat of combustion of 42,000 kJ/kg, and then divided by the number of seconds needed to consume the oil. As an input to the ALOFT model, an estimate is made that 90% of the total heat release rate may be considered the *convective* heat

¹⁷The real-time aerosol monitors (RAMs) were equipped with an air intake separator to eliminate particulate larger than 10 μm in size.

	Burn 1	Burn 2	Burn 3
Date	Sept. 8	Sept. 10	Sept. 11
Volume of Emulsion (m ³)	7.7	12.2	16.6
Percent Oil	50%	100%	60%
Oil Mass (kg)	3,768	1,0827	6,545
Oil Removal Efficiency	97.3%	98.4%	96.7%
Burn Time (minutes)	47	40	45
Estimated Heat Release Rate (MW)	55	186	98
Estimated Particulate Mass Flux (kg/s)	0.15	0.51	0.27

Table 7: Summary of the ACS Mesoscale Emulsion Burns.

release rate, that is, 90% of the heat from the fire is lofted into the plume. The remaining 10% of the heat released is assumed to be radiated away, and plays no role in the model. The particulate mass flux was determined by multiplying the mass of oil consumed by the measured smoke yield of ANS crude (11.6%), divided by the burn time.

Atmospheric temperatures, wind speeds and wind directions were measured with a weather station suspended from a small tethered blimp, deployed just after the burns were completed. However, the wind speed for the second burn was too high to use the blimp, and the temperature profile was taken from a helicopter, the wind speed and direction estimated from the flight log of the airplane and ground weather stations.

The first burn lasted about 47 minutes, during which time the area of burning surface varied from practically zero to the full area of the boom plus spillover. In all, 9 “pulses” of several minutes in duration occurred. Due to the unsteady burning, the downwind instruments detected a number of “hits” due to the fact that the smoke generated when the fire was small was not lofted very high. The first plot of Figure 14 summarizes the model simulation of Burn 1, showing the model prediction of ground level particulate concentration versus the actual measurements made in the field. The field measurements were averaged over the time of the burn. Neither the model predictions nor the RAM data is uniform in space or in time, due in part to random fluctuations in wind direction, convective cells which are not accounted for in the model, small terrain effects, and unsteady burning of the fuel (See Figure 15 for a typical time history of particulate readings). Nevertheless, the time-averaged model predictions and field measurements agree to within the uncertainty of the measured fire and meteorological conditions,¹⁸ showing particulate concentrations ranging from 0 to 80 $\mu\text{g}/\text{m}^3$ along the narrow path over which the plume is lofted. In addition to ground level instruments, a small airplane was hired to fly in the vicinity of the plume and record plume positions at various times, as well as to photograph the burn site and the plume. According to flight track data, the plume top rose to a height of about 550 to 600 m, in agreement with model predictions.

The second burn was conducted for two reasons. First, it provided a control with which to compare the two emulsion burns. Second, it served as a test case to compare to the numerical model since the smoke yield and heat release rate from a large pool fire of unweathered, unemulsified oil are relatively well known from previous laboratory and mesoscale experiments [1], [19]. The

¹⁸To assess the accuracy of the computed results, the model was run several times with input parameters varying over their uncertainty intervals. The measured concentrations, with the exception of a few stray points, all fell within the range of concentrations established by the parameter sensitivity study.

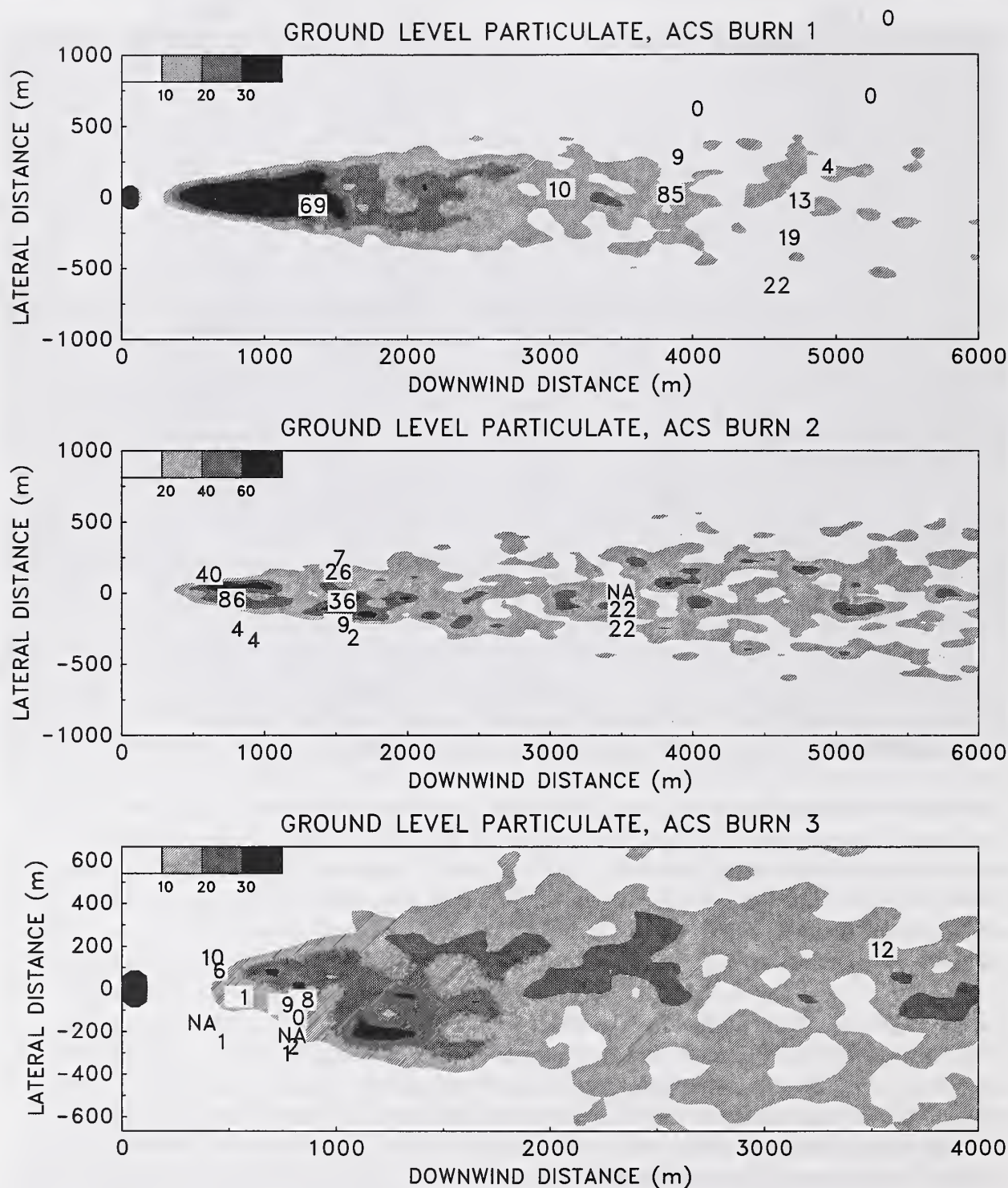


Figure 14: ALOFT predictions of ground level particulate concentrations (shaded contours) along side the actual time-averaged RAM data for the three ACS Emulsion Burns. All concentrations are given in units of $\mu\text{g}/\text{m}^3$.

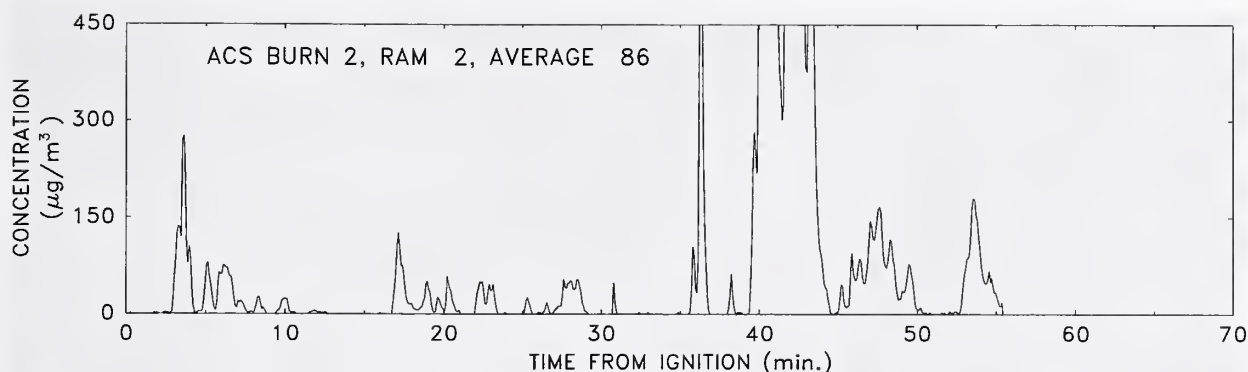


Figure 15: Ground level particulate concentration about 1 km directly downwind of the second ACS burn, as recorded by a real-time aerosol monitor (RAM). The concentrations are given in units of $\mu\text{g}/\text{m}^3$.

second plot of Figure 14 summarizes the model prediction versus field measurements for Burn 2. Of particular interest in this burn was the presence of a thermal inversion at about 300 m. This inversion layer restricted the plume to a maximum height of about 400 m, and again this altitude was verified by the accompanying flight track recorder from the airplane. The wind variability was less than that recorded for the first or the third burn, yielding a plume which retained its basic shape and structure for about 10 km. Figure 16 presents a downwind view of the simulated smoke plume.

Even though the fuel for the third burn resembled that of the first, the burn was much steadier than the first. This probably was due to a slight modification in the application of the emulsion breaker. In any event, weather conditions on the day of the third burn (September 11) were so foggy that the helicopter, which had been used on previous days to place instruments in the field, was grounded. The wind was from the north, blowing directly over a river bed, but shifting about 10° per hour. Because of the bad terrain and visibility, it was decided to deploy the instruments in the near field, all within a kilometer of the pit except for one which was sent with a monitor further afield. The third plot of Figure 14 summarizes the numerical prediction and field measurements from the third burn.

5.3 Mesoscale Diesel Fuel Burns, Mobile, Alabama

Three mesoscale burns of number 2 diesel fuel were conducted by NIST at the US Coast Guard Fire and Safety Test Detachment facility on Little Sand Island in Mobile Bay, Alabama in October, 1994 [36]. The burns were conducted in a 15.2 m square by 0.61 m deep steel burn pan. Water filled about 0.5 m of the pan, and diesel fuel was added to fill the rest. The number 2 diesel fuel was obtained from a commercial vendor. Figure 17 is a photograph of one of the burns. Table 8 summarizes the relevant information for each burn. Note that the first burn was conducted with a fire resistant boom forming one edge of the burn area, thus its burn area is slightly smaller than the second two burns. This is the reason for the slightly longer burn time and slightly lower heat release rate. The smoke yield for number 2 diesel had been measured at a previous burn series in Mobile to be about 14% [20].

Only ground level meteorological information was available from two stations on the island.

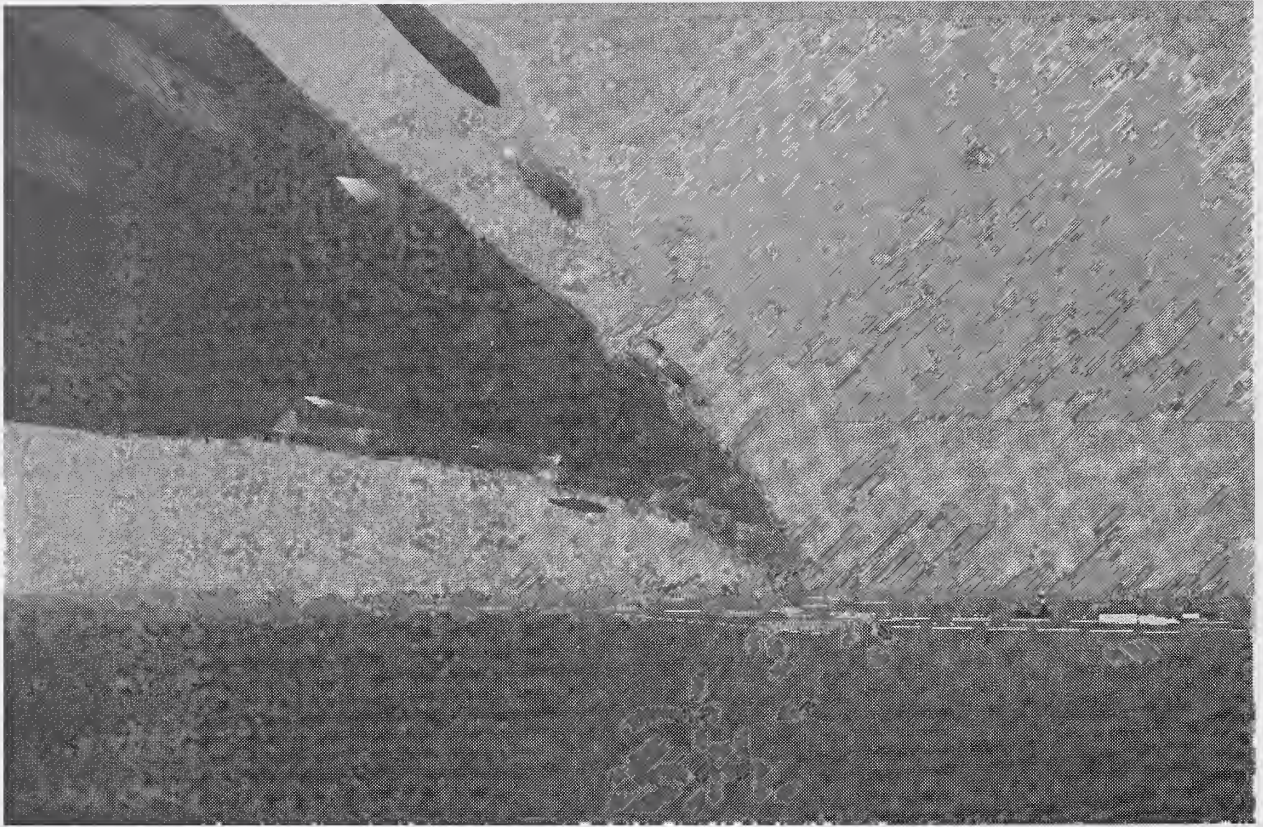


Figure 16: Downwind view of the simulated smoke plume from the second ACS emulsion burn, Prudhoe Bay, September, 1994.

	Burn 1	Burn 2	Burn 3
Date	Oct. 23	Oct. 26	Oct. 26
Burn Area (m ²)	199	231	231
Fuel Volume (bbl)	107	107	107
Burn Time (min)	19	15	15
Burning Rate (bbl/h)	338	428	428
Total Heat Release Rate (MW)	484	602	598
Particulate Mass Flux (kg/s)	1.75	2.18	2.18
Ground Wind Speed (m/s)	1.6±0.8	5.1±1.7	4.7±1.5
Mixing Layer Depth (m)	2,000	450	700

Table 8: Summary of the Mobile Burn Series, October, 1994.

The wind speeds and fluctuations during the burn of October 23 correspond to Pasquill stability class A or B, while the conditions of October 26 correspond to class C. The mixing layer depths were determined from the analysis of lidar data that will be described below. Because of the limited amount of meteorological information, it is certainly appropriate to make use of the type of diagram introduced in Section 4.5. Figure 18 presents flat terrain predictions for the entire range of possible wind speeds and lapse rates/mixing layer depths, so that the conditions observed during



Figure 17: Photograph of a diesel fuel burn at the US Coast Guard Fire and Safety Test Detachment, Mobile, Alabama.

this particular burn series can be put into some perspective. The burn size used is that of burns 2 and 3, but as noted before, the difference in burn sizes between burn 1 and burns 2 and 3 does not change the diagram appreciably. Following is a description of each burn, plus an analysis of the predicted and measured plume concentrations.

The first burn was ignited in the afternoon on the 23rd of October. The winds were calm (1 to 2 m/s), and as a result the smoke plume rose 2 km into the atmosphere and mixed into a cloud layer. There was no mixing of the plume down to the ground. The combination of wind speed and mixing layer depth for this burn lies at the very fringe of the parameter space for which the ALOFT model was designed. Looking at the diagram shown in Figure 18, the meteorological conditions correspond to the extreme lower left hand corner. The lapse rate is very nearly adiabatic, leading to a high plume rise. In this case, the plume rises until it reaches the cloud layer, at which point the atmosphere stabilizes.

The meteorological conditions on the day the second and third burns were conducted were within the parameter space for which the ALOFT model was designed. On this day, the wind was blowing from the north, and the smoke plumes from both burns lofted over the western shore of Mobile Bay and out into the Gulf of Mexico. A team from SRI, International, of Menlo Park, California, performed airborne lidar measurements of the smoke plumes [37]. The instrument was flown above the smoke plume, generating cross-sectional images of the plume in vertical planes *perpendicular* to the direction of the wind at various distances downwind of the fire. Figures 19

FLAT TERRAIN, GROUND LEVEL PARTICULATE CONCENTRATION FOR VARIOUS METEOROLOGICAL CONDITIONS

BURN SIZE 540 MW

SMOKE GENERATION RATE 2.2 kg/s

LATERAL VELOCITY STANDARD DEVIATION 1.2 m/s

VERTICAL VELOCITY STANDARD DEVIATION 1.0 m/s

CRITICAL CONCENTRATION $150 \mu\text{g}/\text{m}^3$

SOLID LINES INDICATE DOWNWIND DISTANCE (km); SHORT DASHES MAXIMUM CONCENTRATION ($\mu\text{g}/\text{m}^3$); LONG DASHES EXTENT OF CRITICAL CONCENTRATION (km)

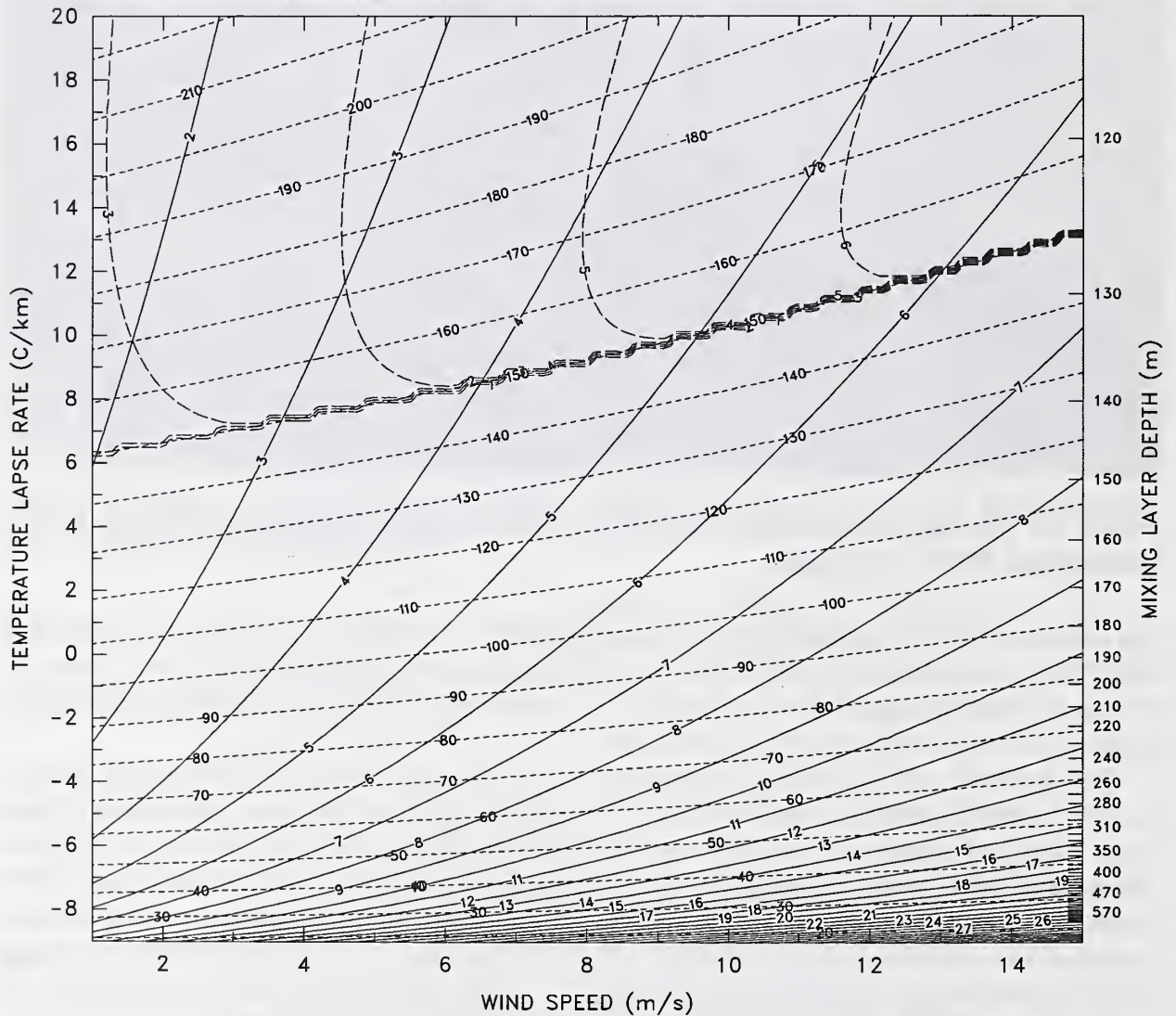


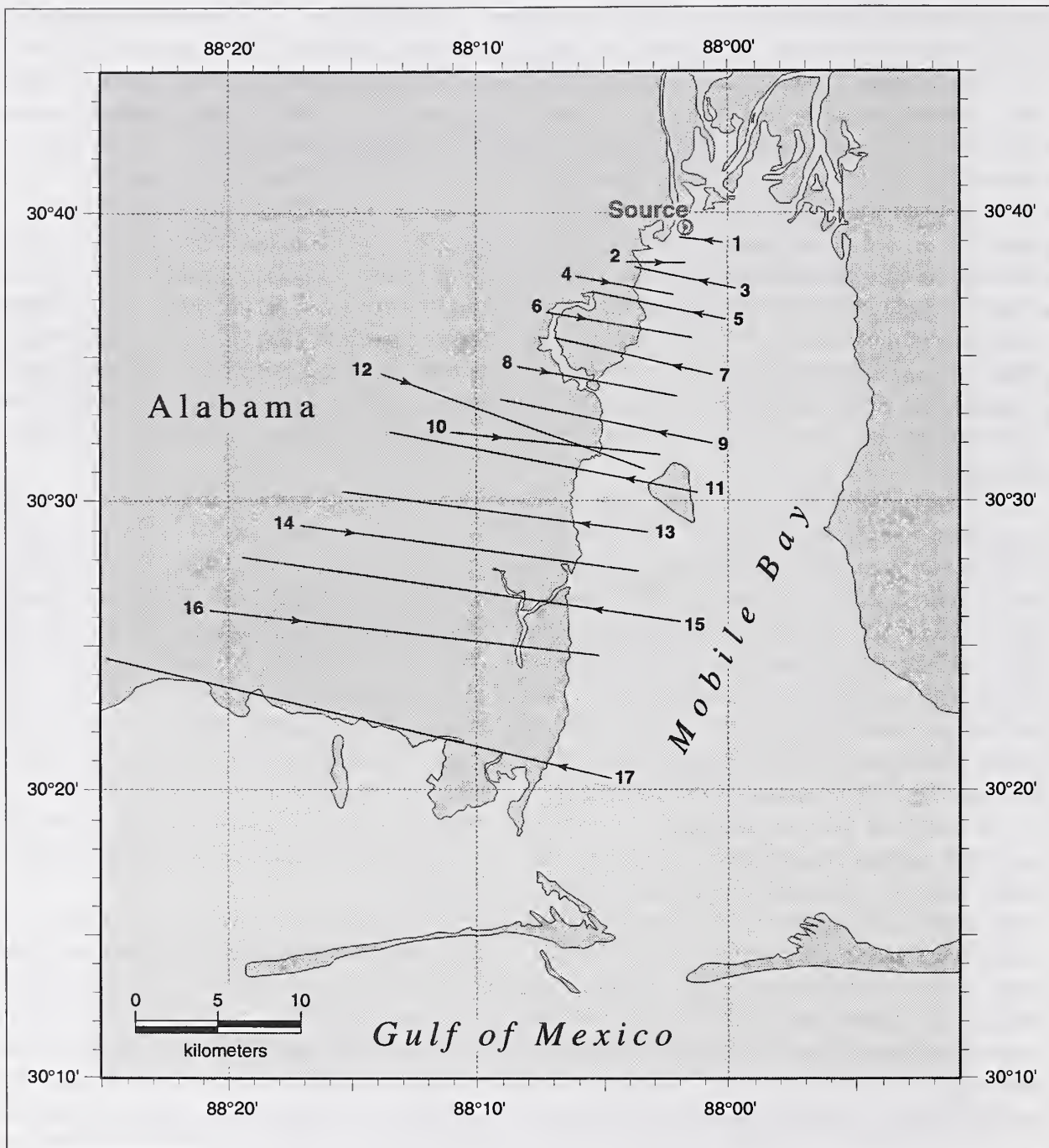
Figure 18: ALOFT predictions of maximum ground level particulate concentration (dashed lines) and the distance downwind where this concentration is expected (solid lines) for the Mobile burn series of October, 1994.

and 20 show the flight path of the aircraft in relation to the burn site. The lidar was operated at a pulse rate of 10 Hz with each pulse producing backscatter profiles at wavelengths of 0.53 and 1.06 μm . Figures 21 and 22 present the lidar images for roughly the first 10 km from the burn site. Clearly visible in each sequence of images is the top of the mixing layer, which separates the earth's turbulent boundary layer below from the free atmosphere above. The mixing layer is characterized by turbulent motion generated by surface friction and vertical heat transfer from the warm ground to the cooler air above. For the morning burn, the depth of the mixing layer was about 450 m, and in the afternoon it had risen to about 700 m. Although a temperature sounding could not be obtained on that day, it is clear from the lidar images of the smoke plume that the top of the mixing layer at both times of the day corresponded to a shift in wind direction, and probably a temperature inversion. The wind was blowing out of the north at ground level, but apparently shifted to become northeasterly above the mixing layer top. This wind shear is very noticeable due to the fact that most of the smoke particulate is concentrated in that narrow band. The smoke that mixes down to the surface does so at the interface between land and water, in a process known as fumigation.

These two burns also provide an opportunity to demonstrate the use of the flat terrain wind speed/lapse rate charts introduced in Section 4.5. The diagram shown in Figure 18 shows expected maximum ground level concentrations of particulate plus the distances from the fire where these concentrations would be expected. The observed mixing layer depths and estimated wind speeds lead to predictions from the diagram in agreement with the quantified lidar data. For burn 2, for winds estimated to be between 6 and 8 m/s at the top of the mixing layer (450 m), the maximum time-averaged, ground level concentration is predicted to be about 35 $\mu\text{g}/\text{m}^3$, located about 12 km downwind of the fire. For burn 3, with similar winds a mixing layer depth of 700 m, the maximum ground level concentration is predicted to be about 25 $\mu\text{g}/\text{m}^3$, located about 20 km downwind of the fire. The degree of uncertainty in these predictions, at least in regard to meteorological uncertainty, can be discerned from the diagram. For example, the distances downwind of the fire where the predicted maxima are expected to be found vary considerably with mixing layer depth and wind speed. The maxima themselves are subject to less uncertainty.

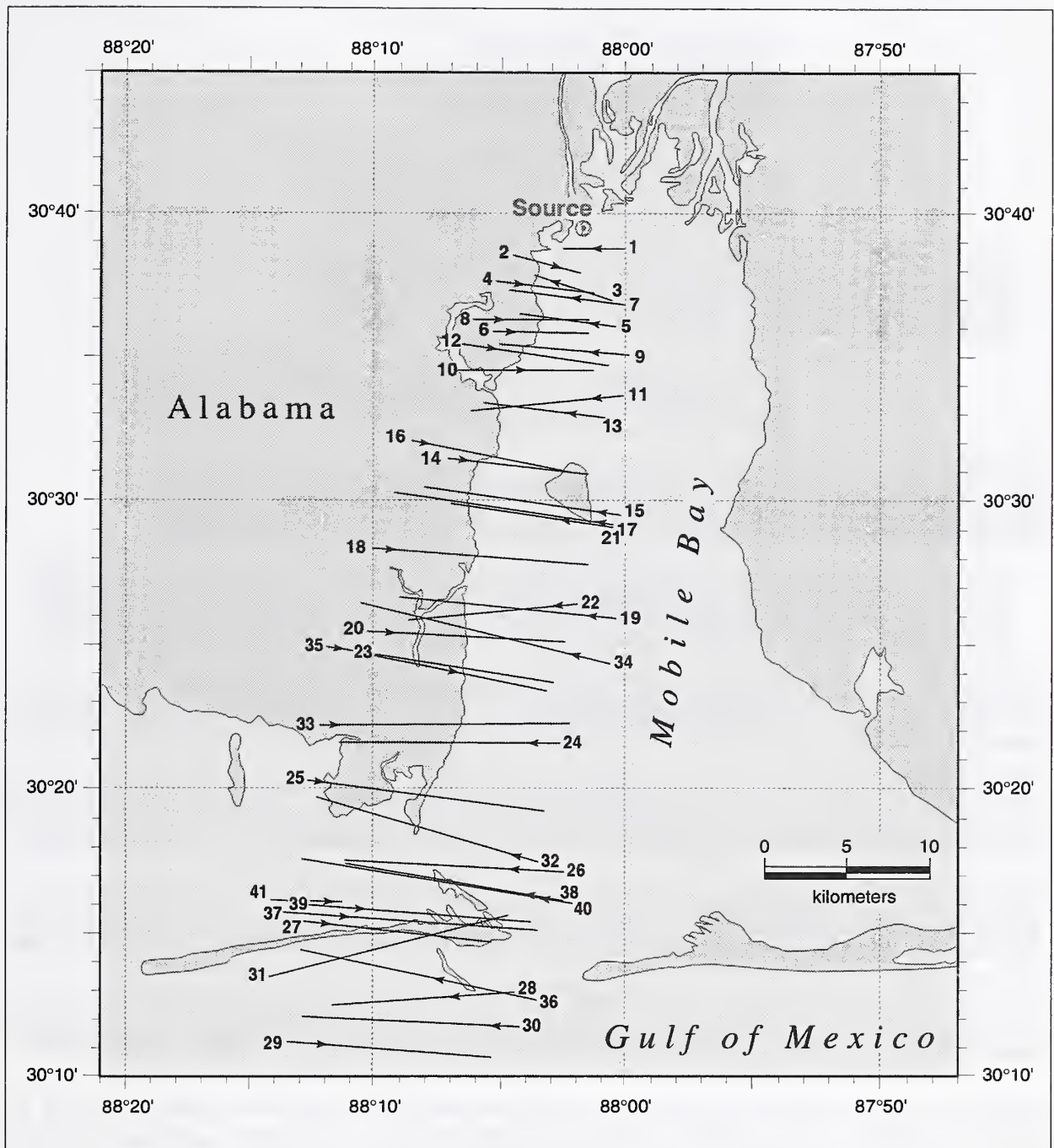
In addition to comparing the quantified lidar data with predictions easily obtained from a flat terrain wind speed/lapse rate chart, the ALOFT model was run to simulate the second and third burn using a non-linear temperature profile. The ground level concentration predicted by the calculations is lower than that predicted by the linear profile correlations. The reason for the difference is that the plume in the non-linear case penetrates the inversion layer, and there is less mixing of the particulate back to the surface. The linear correlations do not account for this effect. Indeed, the unlimited vertical mixing assumption made in deriving the linear correlation is the main reason for its conservative bias (see Section 4.5). Figures 23 and 24 summarize the ground level prediction of smoke particulate concentration from the model, along with the maximum values of the lidar measurements for each pass of the aircraft above the plume¹⁹. The model prediction of the location of the peak concentration for burn 2 agrees well with the lidar measurement. For burn 3, the model appears to overpredict the distance of peak concentration. In both cases, the magnitude of the ground level concentration is in agreement with the lidar measurements. Again, "agreement" infers that the model prediction is within the uncertainty range established by the uncertainty of

¹⁹The particulate concentrations are derived from the lidar signatures by assuming constant backscatter-to-density and extinction-to-density ratios. The latter quantity was derived by the University of Washington team for their analysis of the Newfoundland lidar data [24].



6539fr/14

Figure 19: Cross-plume flight paths for burn 2. Path numbers are placed at the start of the flight path.



6539fr/f2

Figure 20: Cross-plume flight paths for burn 3. Path numbers are placed at the start of the flight path.

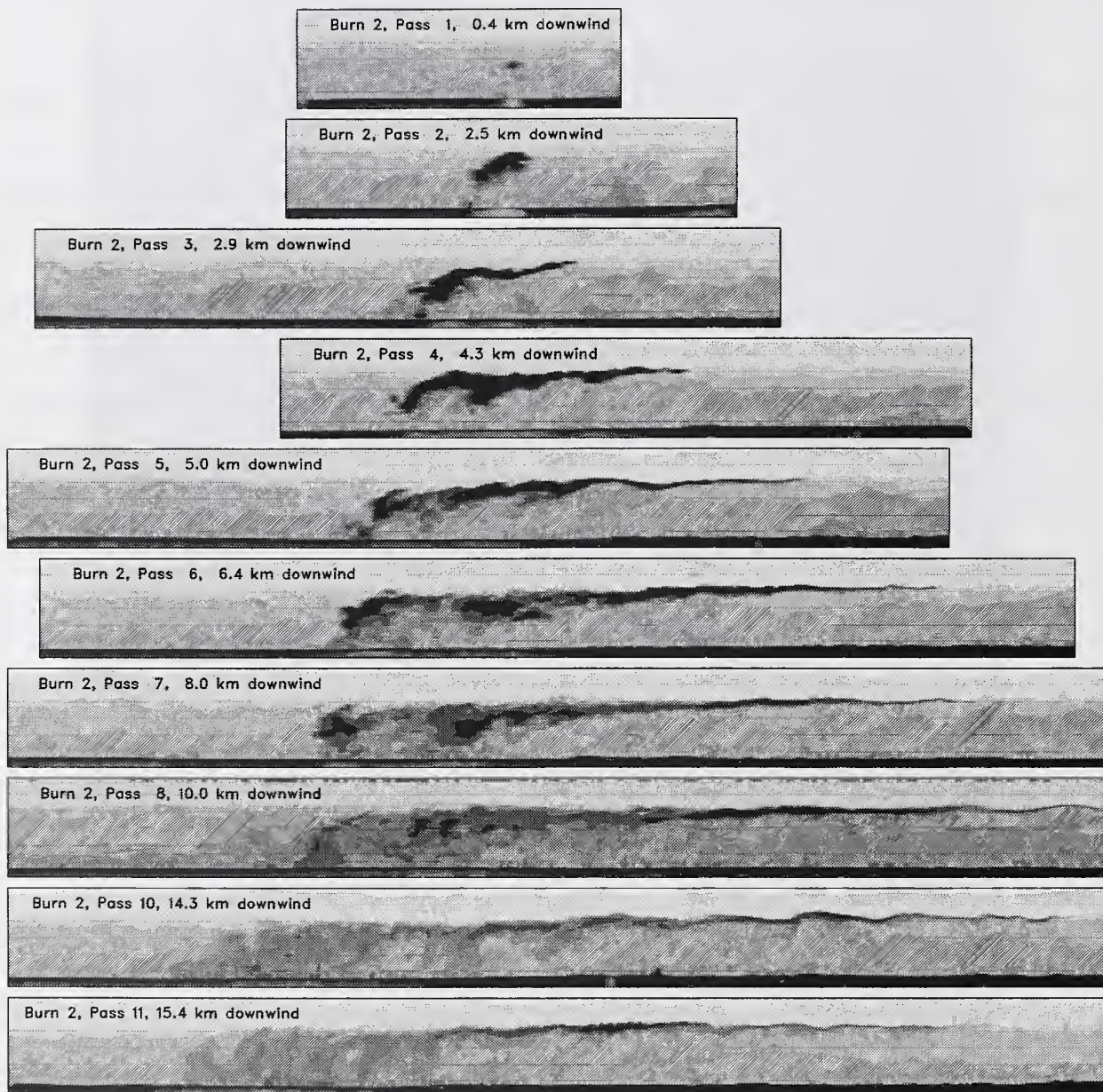


Figure 21: Lidar images of perpendicular plume cross sections for the morning burn of October 26, 1994, Mobile Bay. The grayscale indicates total particulate concentration. The horizontal and vertical lengths are identically scaled, and the height of each frame is 900 m. Note that background particulate and aerosol levels are represented by the horizontal layers extending the width of the frame.

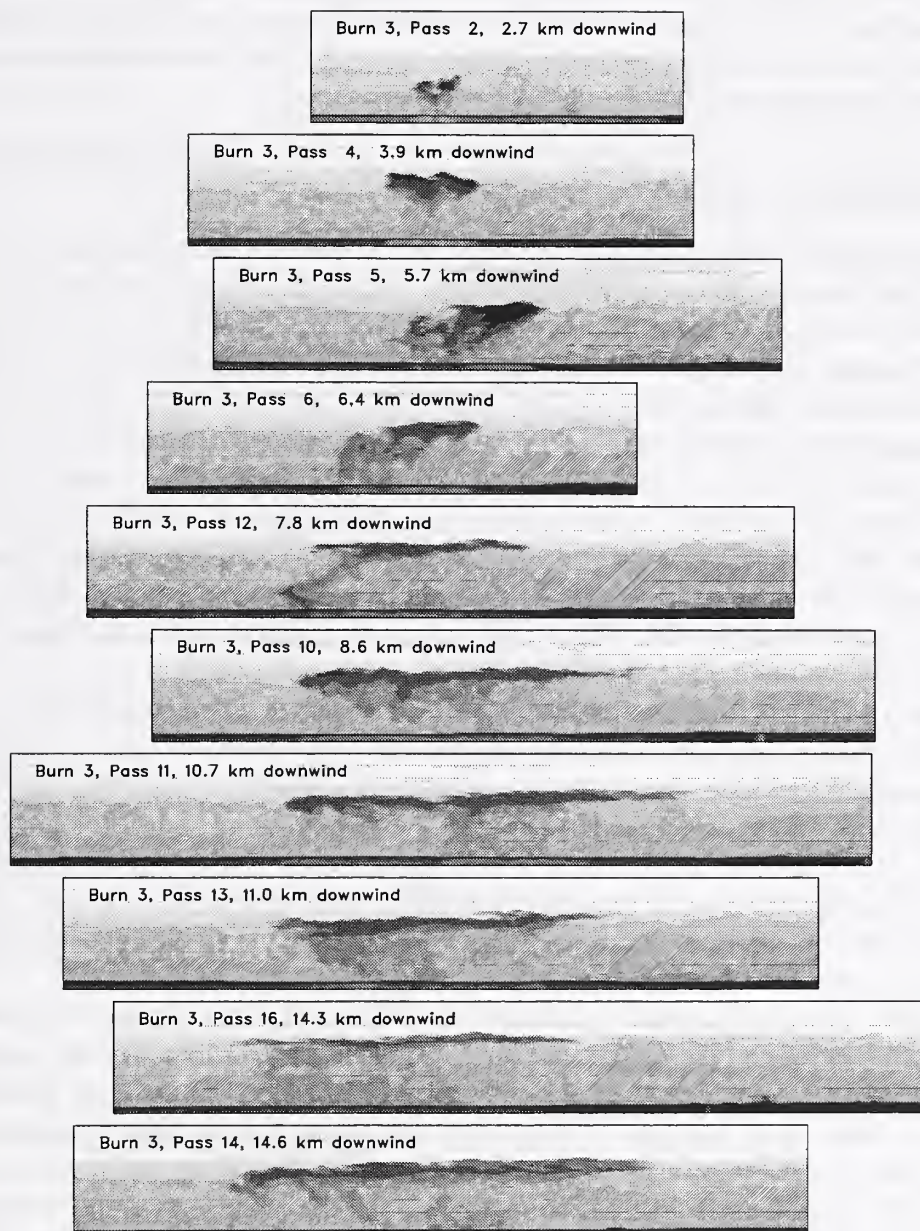


Figure 22: Lidar images of perpendicular plume cross sections for the afternoon burn of October 26, 1994, Mobile Bay. The grayscale indicates total particulate concentration. The horizontal and vertical lengths are identically scaled; the vertical dimension is 1,350 m. Note that background particulate and aerosol levels are represented by the horizontal layers extending the width of the frame.

the meteorological and fire conditions, plus the uncertainty of the lidar quantification.

As in the analysis of the Newfoundland data, it is impossible to replicate with the *steady-state* model every meteorological detail reflected in the *instantaneous* lidar measurements. Instead, it is assumed that the wind fluctuation and vertical convective motion are random processes. In this way, the plume structure and the local meteorology can be described in sufficient detail to produce predictions in the neighborhood of the measured concentrations.

5.4 Discussion of Field Experiments

Small and large scale experiments play two key roles in the modeling process. First, measurements of the fires furnish the heat release rate and emission factors for the combustion products. The model does not predict these quantities. Second, the experimentally measured downwind concentrations of smoke particulate can be compared against the model predictions to determine their accuracy and to assess whether new physical phenomena should be included in the model, such as radiative heating, unsteady burning, and smaller-scale atmospheric motion. The decision to include or exclude these effects is based on how well the model performs in comparison to the results of the experiments. For the three experiments discussed in this report – NOBE, the ACS Emulsion Burns, and the Mobile burns – none of the observed secondary effects was important enough to merit a change of the numerical algorithm. It should be noted that the large scale experiments are *not* used to calibrate the model. That is, the processes governing the entrainment, mixing and dispersion of combustion products do not rely on empirical parameters.

The results of the experiments presented here increase the confidence in the numerical predictions of plume structure, trajectory and composition. The comparison of predicted versus measured particulate concentration is very encouraging, given the uncertainties in the fire and weather characterization. In fact, the model predictions were based on very limited meteorological information – wind speed, wind variation and temperature stratification only. This is important for two reasons. First, local meteorological data for regions of interest is often very limited. Second, if the numerical model is to be used effectively for a wide variety of conditions, it must not depend on empirical input parameters tuned for a particular situation.

As far as the field measurement techniques are concerned, these experiments have provided a wealth of information on how to monitor emissions from large burns. Unlike conventional air monitoring where the source, such as a power plant, is expected to generate pollutants over a long period of time, an *in situ* burn will typically last a few hours. High volume samplers are difficult to position and cannot collect enough particulate in that short period of time, hence the need for reliable, portable real-time aerosol monitors. For the purpose of model verification, lidar measurements have the most potential because they can capture the overall plume structure rather than sparse points. The drawbacks of the lidar are that it is expensive, and the measurements are difficult to quantify.

Of all the experiments discussed within this paper, the smoke plumes from the Mobile burns, although of short duration, are most representative of those that can be expected from an actual *in situ* burn for two reasons. First the burning rate of 400 bbl/h is probably a reasonable rate to expect from an actual burn. It has been estimated that a 150 m (500 ft) fire boom towed in a U-shape configuration could easily provide enough oil area to sustain a burn eliminating about 715 bbl/h [38]. Second, the experiments were conducted in a coastal environment, thus the atmospheric conditions represented by the lidar images are very typical of what one can expect in the event of a near-shore

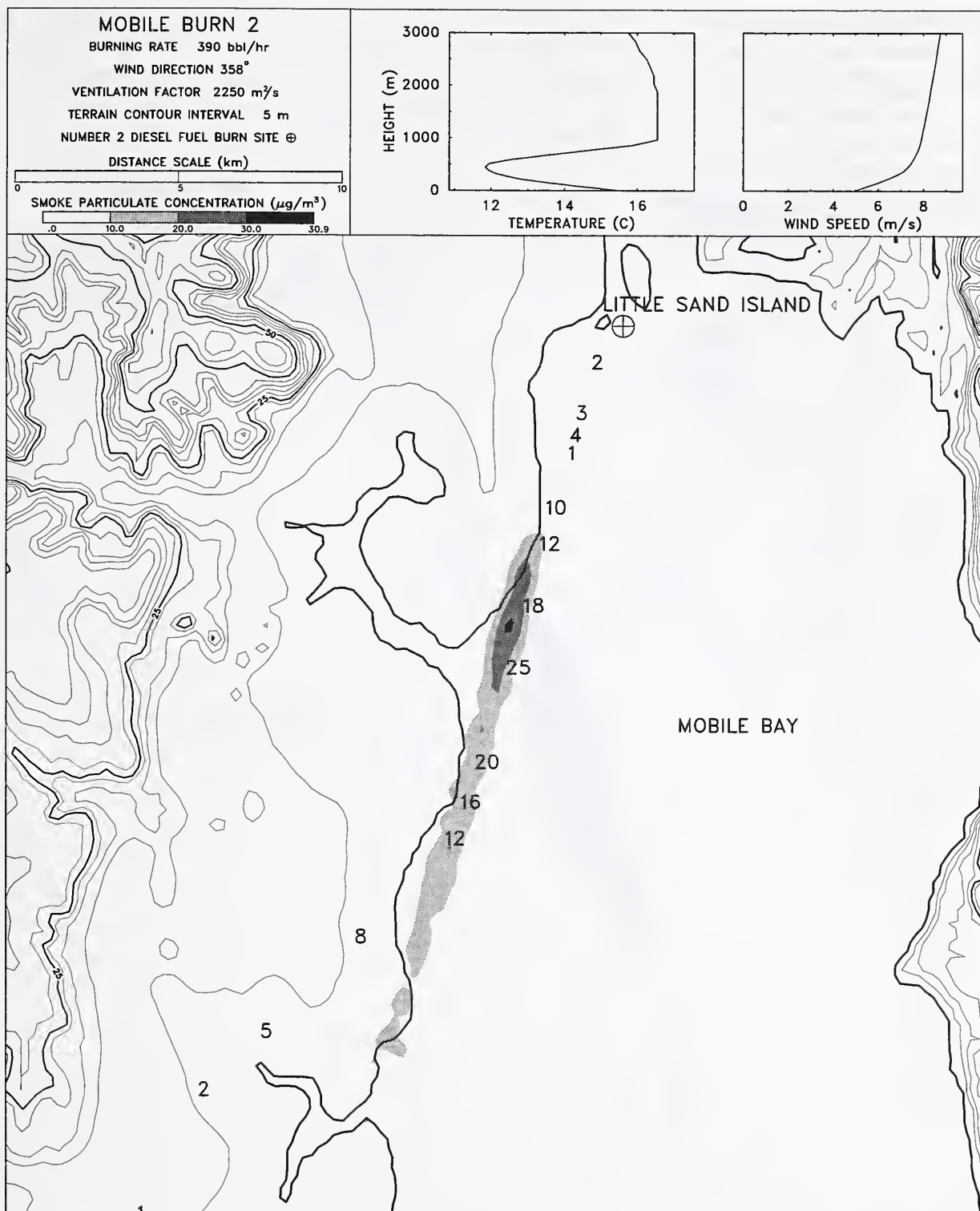


Figure 23: ALOFT predictions of ground level particulate concentration for the morning burn of October 26, 1994, in Mobile Bay. The shaded contours represent model predictions, the numbers represent near ground peak values ($\mu\text{g}/\text{m}^3$) of the quantified lidar signatures for each pass of the aircraft. The ventilation factor is the depth of the mixing layer multiplied by the wind speed, and is used as a rough indicator of atmospheric stability.

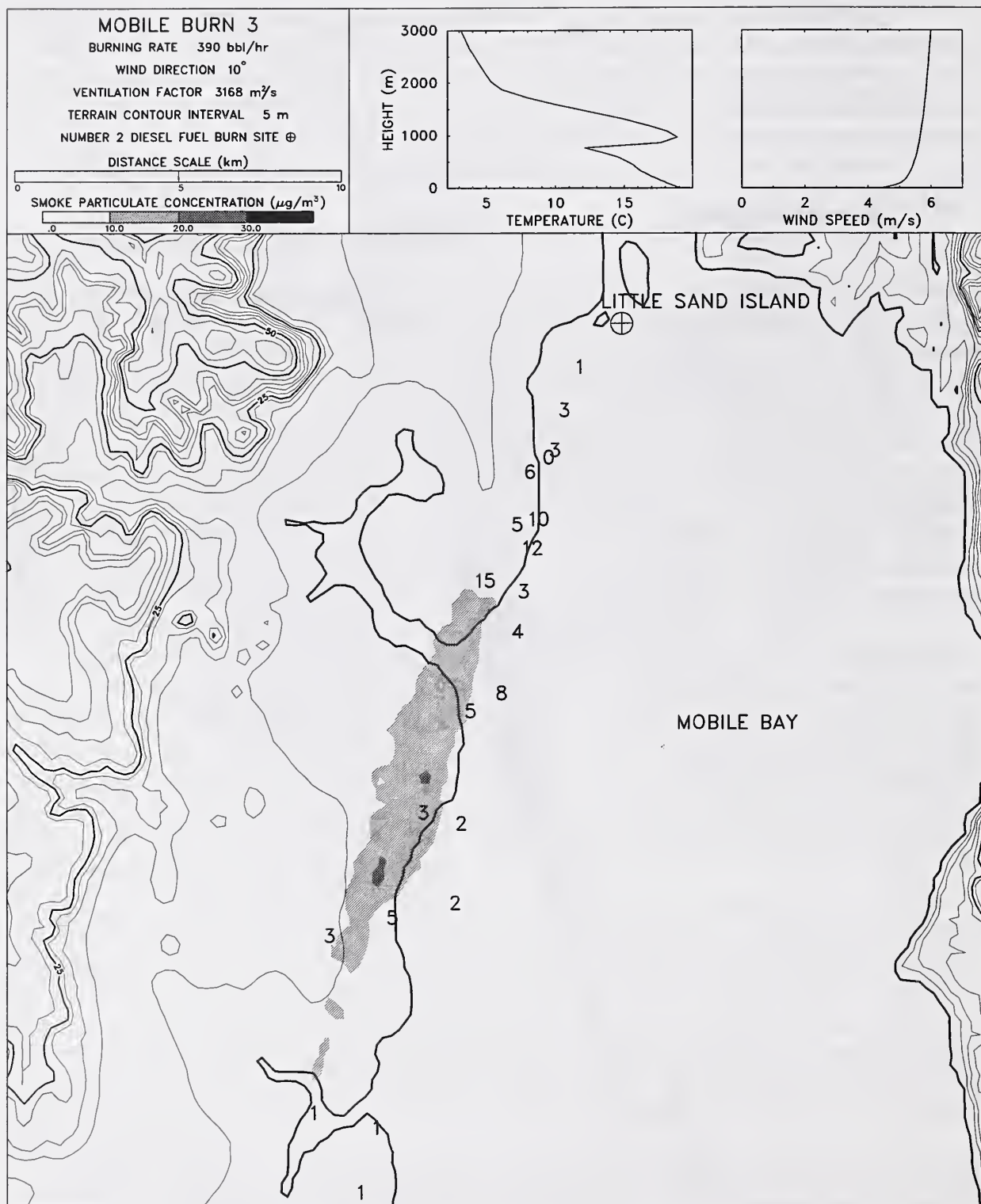


Figure 24: ALOFT predictions of ground level particulate concentration for the afternoon burn of October 26, 1994, in Mobile Bay. The shaded contours represent model predictions, the numbers represent near ground peak values ($\mu\text{g}/\text{m}^3$) of the quantified lidar signatures for each pass of the aircraft. The ventilation factor is the depth of the mixing layer multiplied by the wind speed, and is used as a rough indicator of atmospheric stability.

in situ burn. The results of both the modeling effort and the lidar measurements showed that even though an inversion layer was present, the plume penetrated it, and as a result less smoke was mixed back to the surface. The plume will not always penetrate an inversion layer, and in those instances ground level concentrations could be higher.

In summary, peak concentrations of ground level smoke particulate for all the burns discussed above never exceeded $100 \mu\text{g}/\text{m}^3$ (averaged over the time of the burn) beyond a few hundred meters from the fire, and in most cases were well below that level. It should be emphasized, however, that these experiments were conducted in reasonably good weather conditions, and in each instance, complex terrain was not a factor. The issue of terrain and multiple burns shall be taken up in the next section.

6 ALOFT Applications in Alaska

This section describes the application of the ALOFT model to specific areas of Alaska. In all cases, the complex terrain version ALOFT-CT shall be used, even though in certain cases the flat terrain ALOFT-FT could have been used as well. The complex terrain version of the model should be used if the terrain downwind of the fire is expected to vary by more than about 10% of the expected lofting height of the plume (or roughly the depth of the mixing layer).

Following the presentation of various plume trajectory simulations, the results will be generalized so that estimates can be made of the distance from a fire where the ground level concentration is expected to fall below air quality threshold limits. This distance is primarily a function of the terrain height over which the plume is expected to loft, and the depth of the mixing layer. A simple formula has been developed to allow the ground level distances to be modified to accommodate changing regulatory limits, particulate sizes, multiple burns, and off shore/on shore plume trajectories.

6.1 Outline of the Solution Procedure

The original application of the ALOFT model to the problem of *in situ* burning in Alaska, documented in References [1, 4], considered the rise and dispersion of a smoke plume from a single burn over water and/or flat coastal areas. The improvements made to the model now enable site-specific simulations of one or more burns. These additional features of complex terrain and multiple plumes greatly increase the applicability of the ALOFT model, but also increase the number of possible burn scenarios. Obviously, it is impossible to consider every mile of Alaskan coastline under every possible weather condition. Thus the strategy adopted in this report will be to first consider several of the many spill response drills conducted in Alaska over the past decade. The location and meteorological conditions of the sites are used as input to the model. For the purpose of consistency, each simulation involves the same size fire. The fuel is ANS crude, burning at a rate of 1,000 bbl/h. The area of the fire necessary to consume this much oil is about 760 m², the total energy output of the fire is about 1,340 MW, and the smoke production rate is 4.5 kg/s. It will be assumed that the oil is contained in a single boom, and one plume is generated. Following these examples, scenarios will be presented that involve variations of the standard test burn scenario to test the sensitivity of the model to changes in the more important input parameters, including a discussion of multiple fires.

All of the simulations discussed in the following pages employ the same basic methodology. Each numerical simulation of an *in situ* burn consists of a near-field calculation required to compute the plume rise (ALOFT-FT plume rise algorithm), then a far-field calculation that generates a wind field through which the smoke particulate, represented by Lagrangian particles, is advected (ALOFT-CT wind field algorithm). Figure 25 presents a three-dimensional view of the results of a typical simulation. A smoke plume originating near Bligh Island, Prince William Sound is shown blowing towards Port Valdez. Over water, the wind fluctuations are generally smaller than those over land, and this is reflected in a more cohesive plume over the water. As the plume approaches the shore, there is more scattering of the particulate due to the increase in the atmospheric turbulence. Depending on the height of the plume above the sea surface, there is the possibility of increased ground level concentration due to what is called fumigation. This occurs when the elevated smoke plume which originates in stable air offshore meets the terrestrial mixing layer formed

by the warmer land surface.

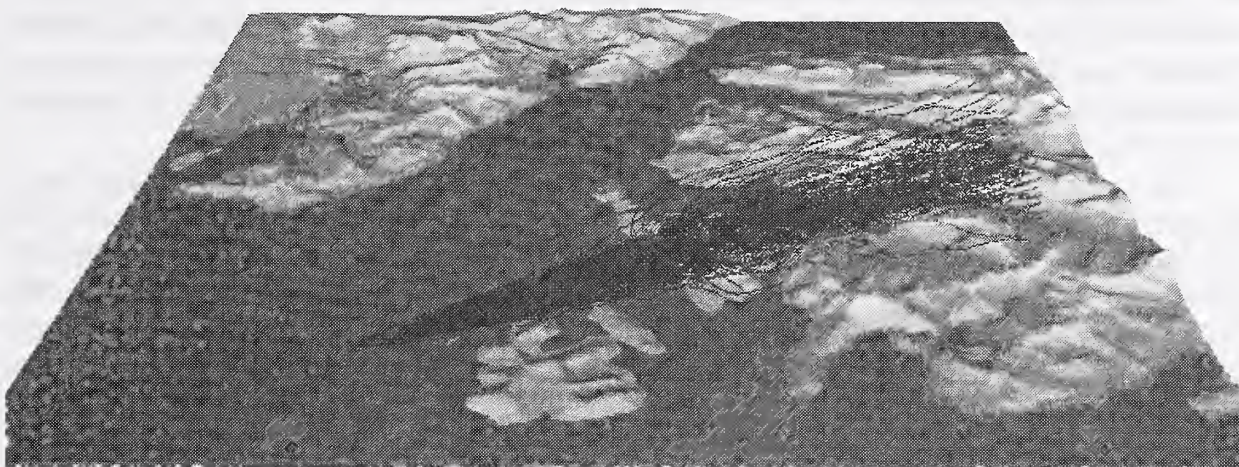


Figure 25: Three-dimensional view of simulated smoke plume originating off Bligh Island, Prince William Sound. Note the increased scattering of the particulate over the land due to the increased wind fluctuations.

To extract more quantitative information from each calculation, a single figure is generated following the completion of the run, showing the near-ground concentration of smoke particulate (hour-averaged) and wind field. The legend at the top of the map displays the sounding information used for the simulation, the distance scale, the ventilation factor, the prevailing wind direction, and the rate at which the oil is burning. The ventilation factor is the product of the wind speed and the mixing layer depth of the atmosphere. The mixing layer depth refers to the height of the planetary boundary layer (PBL) which is the region of the atmosphere adjacent to the earth's surface characterized by continuous and vigorous turbulence. Its upper edge is sometimes well defined by a temperature inversion, but in other cases, it is less clearly defined, especially in the presence of large, active cumulus clouds [39]. The ventilation factor provides a rough measure of the level of turbulence in the atmosphere. The higher the value, the more "dispersive" the atmosphere. The ground-level particulate concentration is presented using gray scale contours. Here, ground-level concentration refers to a spatial average spanning the height (about 40 m) and width (about 200 m) of a ground-level numerical grid cell, and a temporal average over a time period of about one hour. The wind fields shown in the figures correspond to an altitude of about 40 m off the ground, thus the trajectory of the smoke plume (indicated roughly by its ground level "footprint") does not necessarily follow the wind field shown because the plumes in general loft much higher than 40 m into the atmosphere.

Temperature and wind speed profiles are taken from a data base of radiosonde soundings [40, 34]. The particular sounding used in the first set of simulations to follow corresponds to afternoon conditions in Anchorage in the month of April. This sounding was chosen because it is typical of coastal regions in Alaska, and it includes a temperature inversion at about 400 m. Given a wind speed of about 5 m/s, the ventilation factor for this particular set of weather conditions is about 2,000 m²/s, indicative of a moderate level of atmospheric turbulence. In terms of the Pasquill stability categories listed in Table 6, these conditions are indicative of a class C or D, depending on the level of incoming solar radiation. Applying the default dispersion parameters listed in Table 5,

the lateral fluctuation of the prevailing wind direction over land is about 13° (standard deviation of a Gaussian distribution), and about 6° over water. The vertical fluctuations are 11° and 5° , respectively. It is assumed that the temperature profile included in the sounding applies to both the land and sea. None of these assumptions is demanded by the numerical methodology, which can accommodate spatially and temporally varying meteorological conditions, but rather by the desire to simplify the analysis and limit the parameter space explored in the study.

The wind velocity profile of the sounding, *i.e.*, the wind speed and direction as a function of altitude, is usually over-ridden by a typical exponentially increasing wind profile. The reason that the actual wind speed data from the sounding is not used is because wind speed and direction information in a single sounding for low altitudes is very much a function of the particular area in which the sounding is taken. The intent of using actual sounding data is not necessarily to mimic exact conditions of one particular day, but rather to extract typical conditions of the area at some time of the year. Also, the wind profile is only used as a boundary condition for the ALOFT-CT wind field generation routine. The complex wind field generated by solving the governing equations is influenced not only by the prevailing wind speed and direction, but most importantly by the regional terrain.

The complex wind pattern plays a major role in dispersing the pollutants from the fire. This effect is referred to as “mechanical dispersion.” The other major player can be regarded as “turbulent dispersion.” Turbulence is introduced into the numerical model by way of Lagrangian particles that are transported by the wind field. Mechanical dispersion is a natural consequence of the fact that the particles are scattered as the flow weaves through the mountains and valleys. Turbulent dispersion, however, is introduced by randomly perturbing the particle trajectories to mimic the effect of the spatially and temporally varying atmosphere. This issue is discussed in Section 4.4 and in Appendix A. The dispersion parameters chosen for the simulations to follow correspond to the default values given in Table 5.

The terrain data required by the model is extracted from a 3 arc second database maintained by the US Geological Survey, EROS Data Center²⁰. In Alaska, 3 arc seconds is equivalent to roughly 100 m, and this is sufficient resolution for the simulations performed because the horizontal grid spacing varies from 200 to 400 m. The spacing in the vertical varies from about 40 m at the ground to several hundred meters at an altitude of about 5 km.

6.2 Single Burn, Single Sounding, Various Locations

As a starting point for the investigation of complex terrain and its effect on smoke plume dispersion, several simulations based on spill response drills conducted in Alaska over the past decade were performed, and the results are presented on the following pages. Only the location of the scenarios have been used here, the burn size and meteorological conditions are not changed from one case to another. The meteorological conditions represent fairly typical afternoon conditions along the southern coast of Alaska during the spring, summer or fall. These conditions are less typical, and occur in other parts of Alaska, even in winter time. The fuel for the burns is ANS crude, burning at a rate of 1,000 bbl/h. The area of the fire necessary to support this burning rate is about 760 m², the total energy output of the fire is about 1,350 MW, and the smoke production rate is 4.5 kg/s.

²⁰The Earth Resources Observation Systems (EROS) Data Center, located in Sioux Falls, South Dakota, is a data management, systems development, and research field center of the US Geological Survey's National Mapping Division. One of the Center's activities is to maintain an on-line data base of digitized maps.

It will be assumed that the oil is contained in a single boom, and one plume is generated. The area of burning oil represents an upper bound for a single boom of length 150 to 300 m (500 to 1,000 ft). Allen and Ferek [38] estimate that a fire-resistant boom of conventional length could easily accommodate burning at a rate of about 700 bbl/h. Thus 1,000 bbl/h is certainly within the capability of a single boom. Following is a region by region description of the plume simulations.

6.2.1 North Slope, Atigun Pass and Fairbanks

Before embarking on regions of complex terrain, it is useful to simulate a burn at Pump Station 1 near Deadhorse at Prudhoe Bay because the terrain there can be considered flat. The results of this simulation will serve as a benchmark to compare the results from the more mountainous areas inland and along the southern coast. For this reason, the April sounding from Anchorage is used here, and in the simulations to follow. Ultimately, the goal is to develop simple rules to estimate ground-level concentrations over complex terrain based solely on flat terrain simulations.

Figure 26 summarizes the results of the calculation. The very flat terrain, which varies from about 20 to 40 m above sea level for the area shown, has little effect on the overall wind field. The ALOFT-FT plume rise and dispersion methodology would have been sufficient to describe the plume here. The plume rises about 500 m into the atmosphere, a level established by a temperature inversion.

A more interesting simulation is summarized in Figure 27. Now it is assumed that the same fire is burning at Pump Station 4 along the Atigun River just south of Galbraith Lake and about 30 km north of Atigun Pass. The northeast winds push the plume towards the west bank of the river valley, increasing ground-level concentrations as the terrain height approaches 2,000 m. The river valley channels much of the smoke plume due south, and winds blowing over the high western terrain push the plume down as it impinges on the split in the valley formed by James Dalton Mountain. The smoke plume then splits and rounds the mountain on either side. This is probably the best example of how complex terrain can influence the dispersion of a large smoke plume. It is important to note that higher than normal (*i.e.* compared with a flat terrain case) concentrations are found at higher terrain elevations, where one would expect, but also at elevations comparable to that of the fire due to the complicated interaction of the wind field and the terrain features. It is not unusual for smoke particulate to become trapped within a depression, such as a valley, with the result being that the concentration continues to increase as long as the burn continues and more smoke is supplied to the depression.

A similar example is shown in Figure 28. Here the fire is just south of Atigun Pass, with the winds blowing out of the southwest. The smoke follows very closely the Atigun River valley, along the Dalton Highway. This raises another issue concerning smoke particulate – visibility. Although concentrations on the order of a few hundred micrograms per cubic meter do not obscure vision at short distances, they can be seen clearly when the smoke plume is aligned with the line of sight, as in the case here.

The Trans-Alaska Pipeline passes just to the east of Fairbanks. A response drill scenario here often involves the spilling of ANS crude into one of the many creeks that pass under the pipeline. Figure 29 shows the footprint from the single standard burn under the same meteorological conditions as the simulations of the previous section. The wind is blowing from the south towards the hilly region northeast of the city.

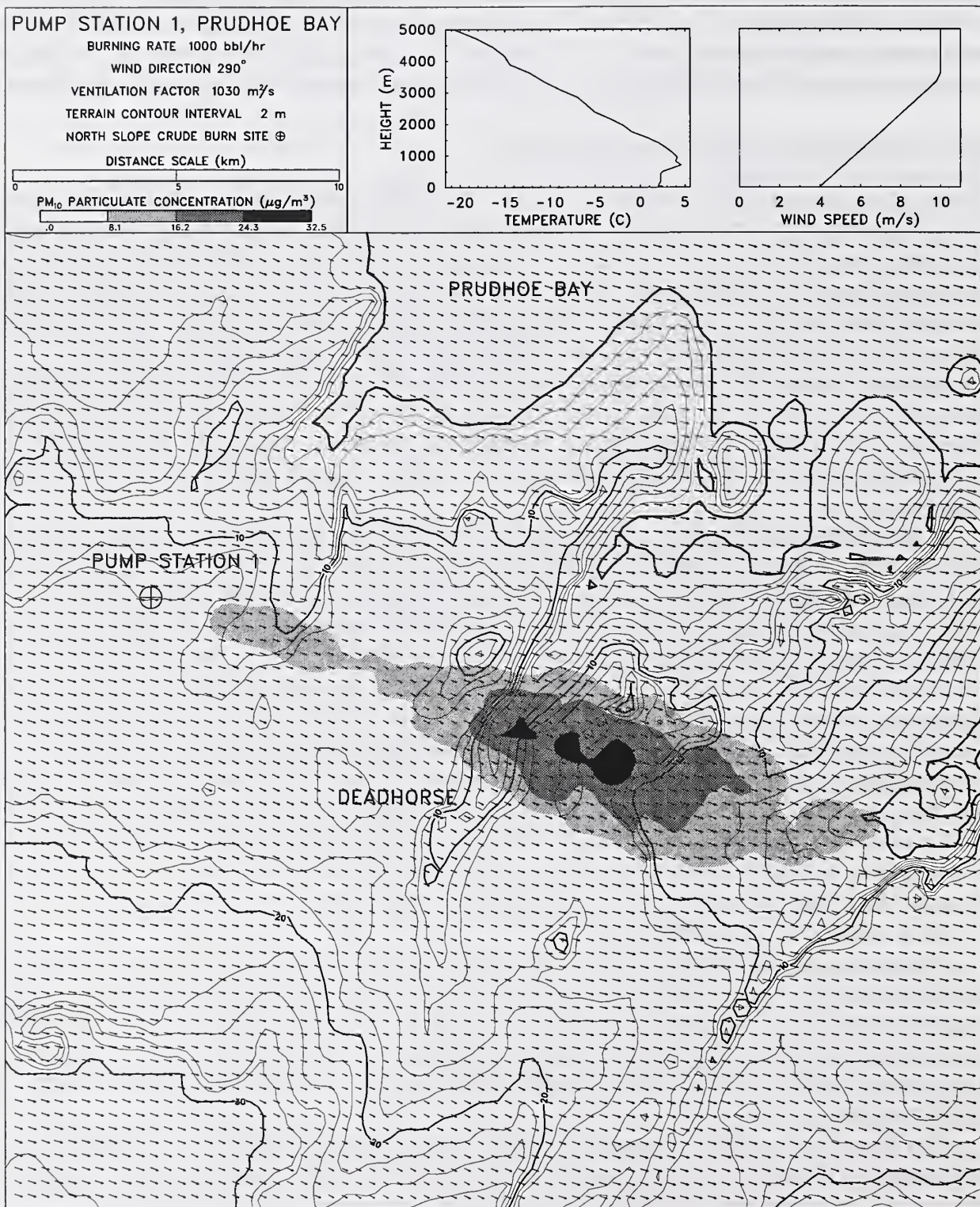


Figure 26: Footprint of simulated smoke plume originating at Pump Station 1, Prudhoe Bay.

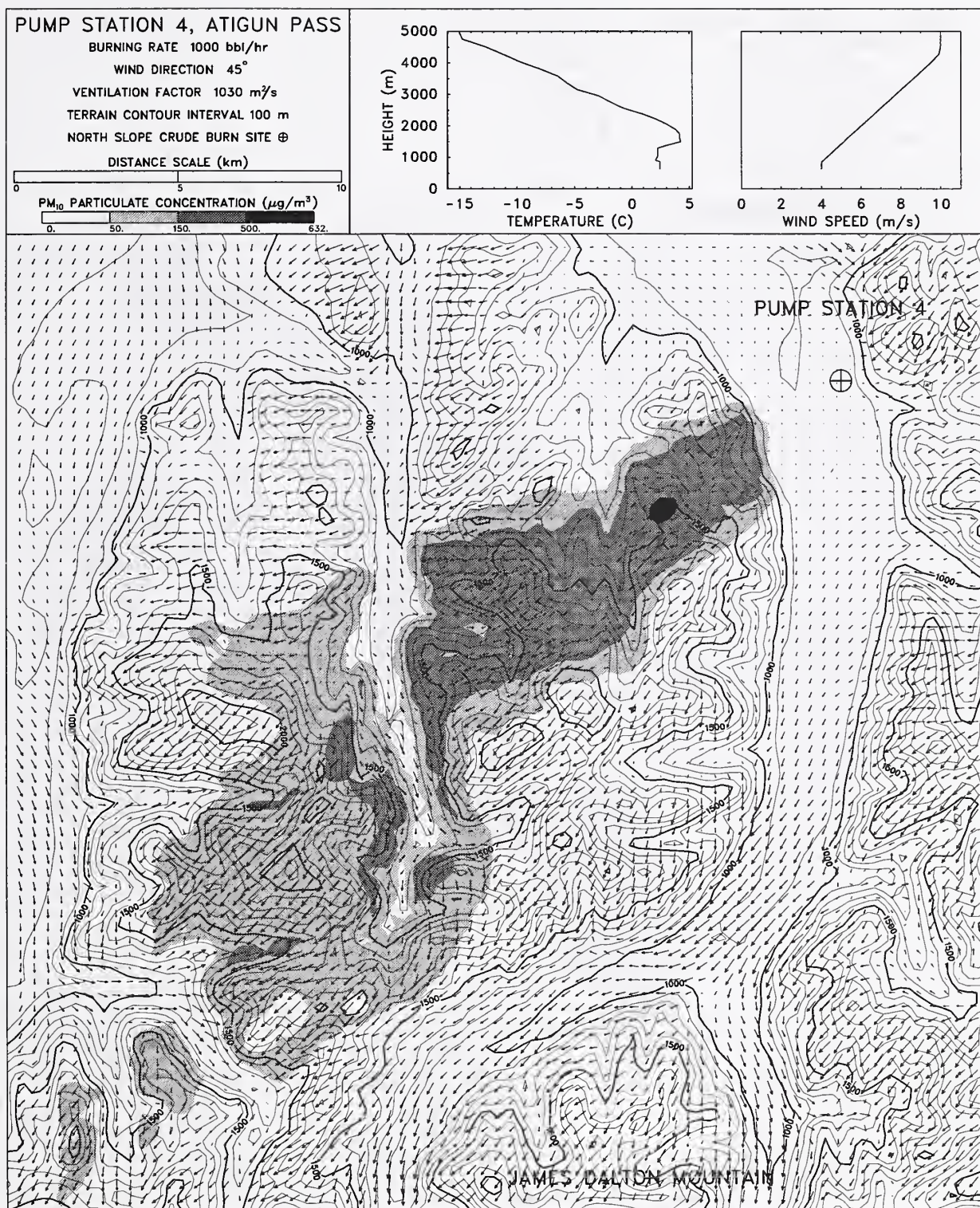


Figure 27: Footprint of simulated smoke plume originating at Pump Station 4, near Atigun Pass.

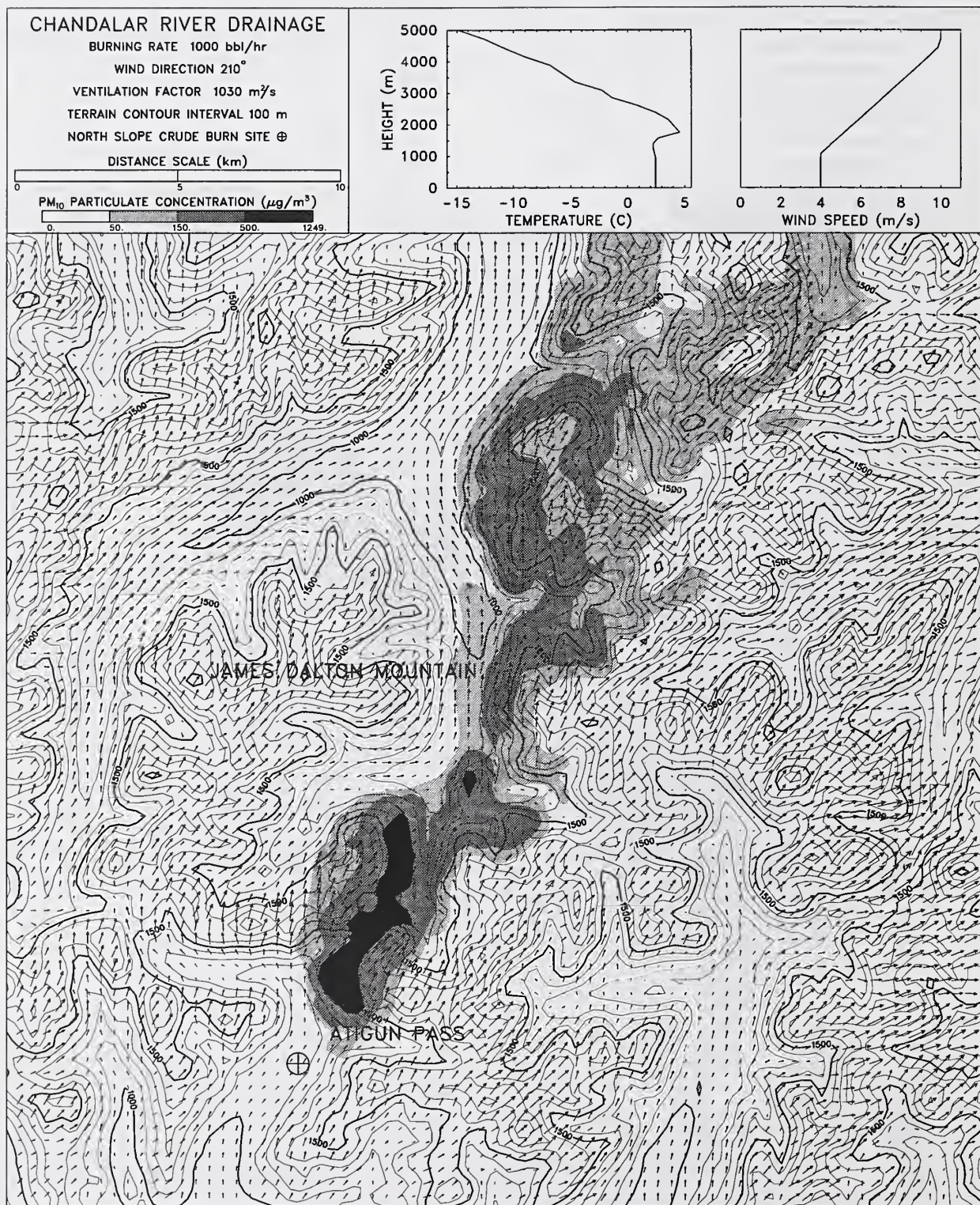


Figure 28: Footprint of simulated smoke plume originating at just a few kilometers south of Atigun Pass.

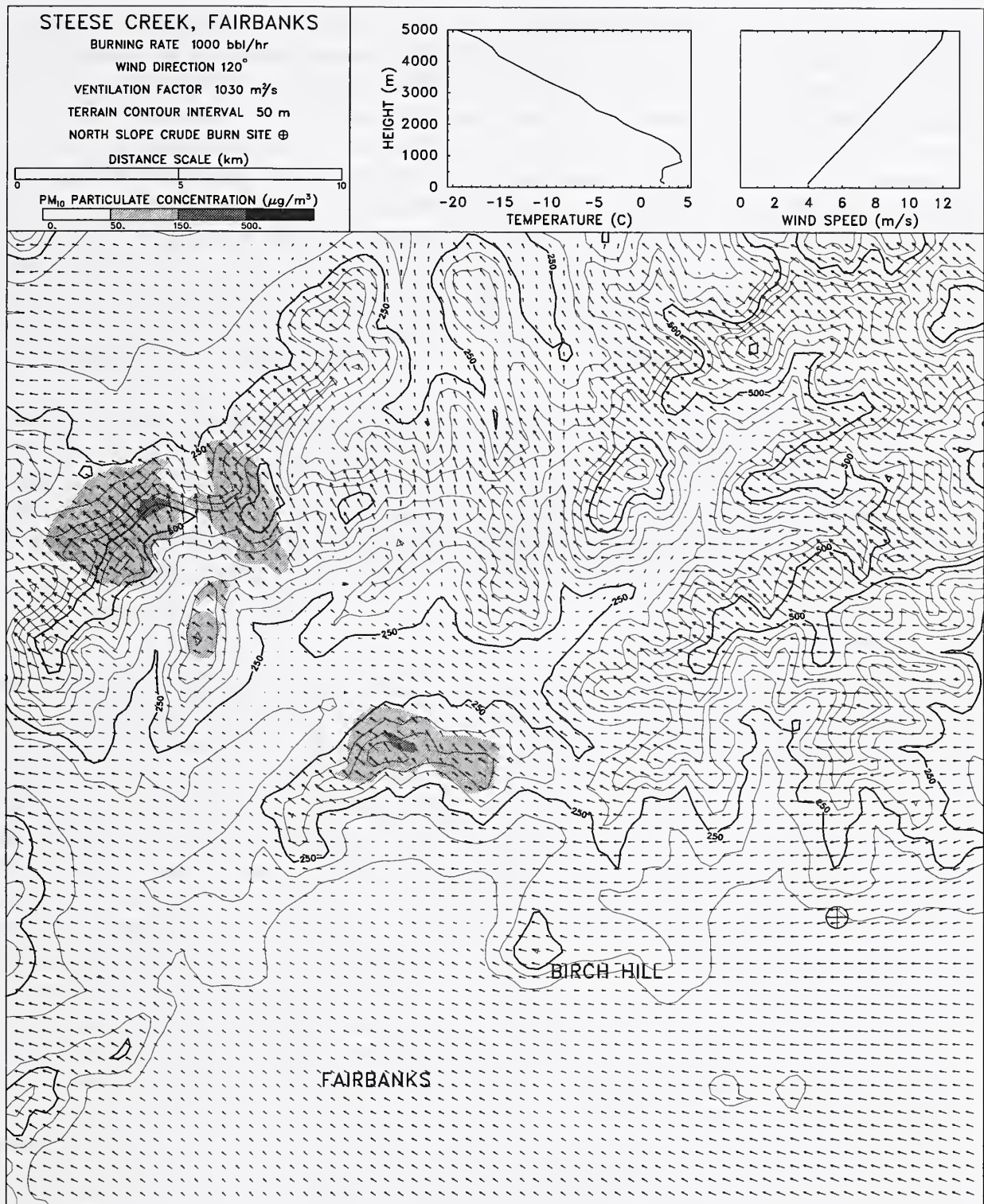


Figure 29: Footprint of simulated smoke plume originating near the Trans-Alaska Pipeline just east of Fairbanks.

6.2.2 Port Valdez

An area of concern where an oil spill might occur is at the point where the Valdez Arm narrows to form the entrance to Port Valdez, known as the Valdez Narrows, and along the southern coast of Port Valdez where the Trans-Alaska Pipeline terminates at the Valdez Marine Terminal. Port Valdez is surrounded by very steep terrain, and even if the prevailing wind direction is known, it is very difficult to predict the local wind field. Consider the simulation summarized in Figure 30. It is assumed that spilled oil in the waters just off the Valdez Marine Terminal is burning at the same rate as the previous simulations – 1,000 bbl/h. The winds are blowing out of the northeast. As in the case of the burn at Pump Station 4, the steep terrain surrounding the port channels the smoke plume towards the west. It appears from the figure that the wind at the location of the burn is blowing in the northwesterly direction, but this is misleading. The wind field shown is at an altitude of about 40 m, whereas the plume rises to a height of about 500 m. At this altitude, the plume is transported by the prevailing winds towards the Valdez Narrows, the entrance to Port Valdez.

A similar footprint is shown in Figure 31, where now the fire is located in the Valdez Narrows. The Valdez Arm forms a channel that traps much of the smoke plume in a swath that hugs the western shoreline. A phenomenon known as fumigation occurs at such a land-water interface, where increased vertical convective motion increases the mixing of plume constituents to the ground. This motion is highly unpredictable due to its localized nature. The numerical model accounts for it with higher diffusion coefficients corresponding to the land as opposed to the water.

6.2.3 Prince William Sound

Moving from Port Valdez out into Prince William Sound, the simulation of the standard test burn becomes more tractable because the wind fields are more easily predicted in the larger area. The first scenario supposes the burn to take place where the tanker Exxon Valdez went aground off Bligh Island on March 24, 1989 (60° 50' 9" N, 146° 53' 45" W). This simulation does not reflect the weather conditions at the time of the accident, however. The prevailing winds are out of the southwest, blowing the plume directly towards the shore. Figure 32 shows the footprint of the smoke plume in the area south of Port Valdez. The ground-level concentrations shown in the figure are lower than those of Port Valdez because now the plume originates in a larger body of water, rises to its level of neutral buoyancy at about 500 m, and is transported by the prevailing winds over land at a sufficiently high altitude that it is less affected by the low level, terrain-induced wind field. As expected, appreciable concentrations are only found at higher altitudes. This pattern is repeated for simulations of burns off Knowles Head (Figure 33) and Zaikof Point (Figure 34).

Of course, the wind direction is not always towards shore, and it is informative to conduct a simulation for a case where the prevailing wind is away from the shore. Figure 35 presents the results of a simulation in which the burn is placed at the same location as in Figure 32, just off Bligh Reef, but now the winds are out of the northeast. This wind direction was observed during the early stages of the Exxon Valdez accident. Notice that no concentration in excess of 50 $\mu\text{g}/\text{m}^3$ is predicted near the water surface. Similar conditions and results were obtained by the University of Washington team flying a lidar-equipped aircraft over the smoke plume at the Newfoundland Offshore Burn Experiment in 1993 [24, 22]. They report that *no* smoke mixed down to the surface, which can be interpreted more precisely as *no measurable* smoke mixed down to the surface.

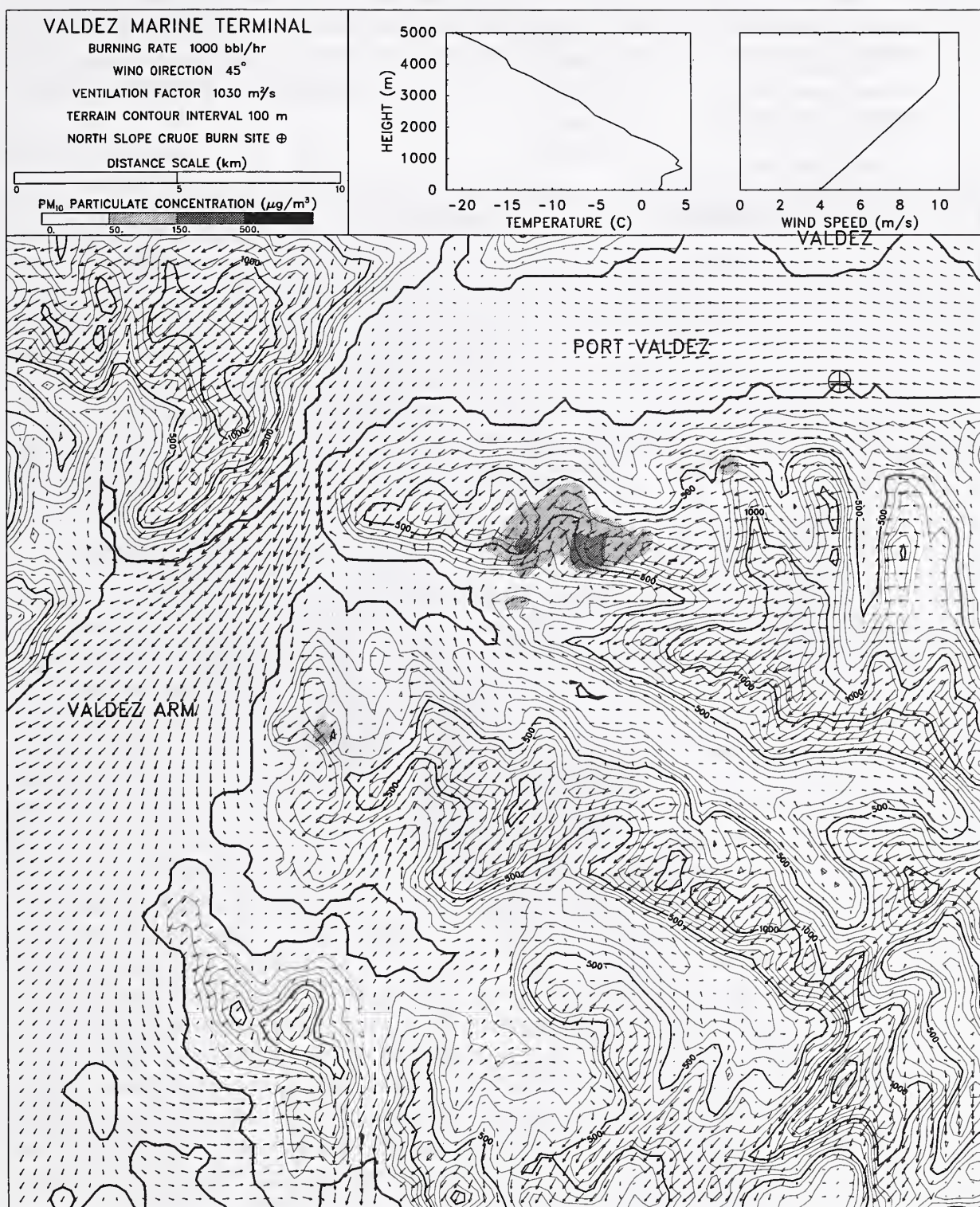


Figure 30: Footprint of simulated smoke plume originating off Valdez Marine Terminal.

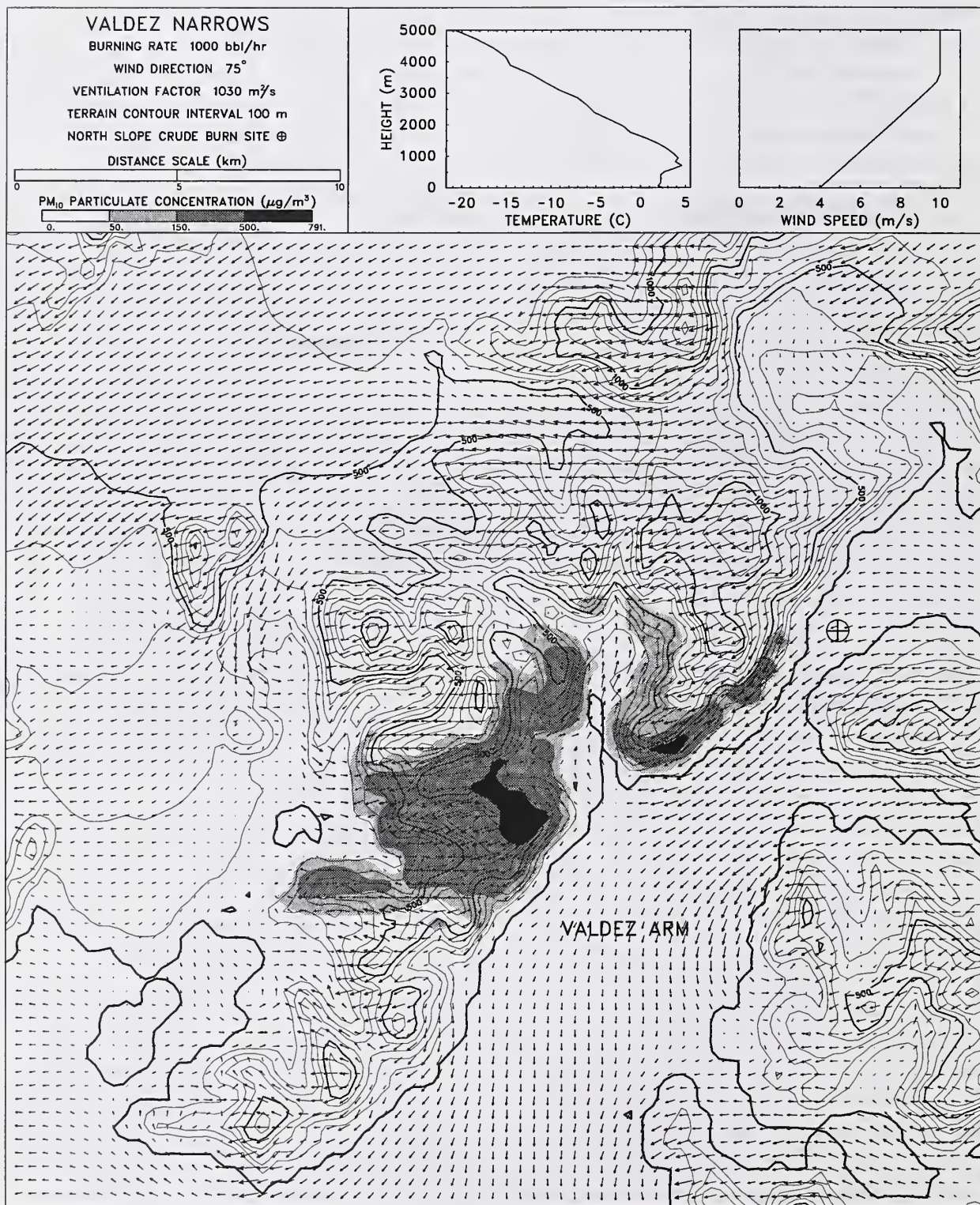


Figure 31: Footprint of simulated smoke plume originating in the Valdez Narrows.

The Bligh Reef simulation can also be compared to the North Slope simulation reported in Figure 26. The difference in the two simulations is due to the different diffusion coefficients and temperature profiles used over land and over water. In general, there is less vertical mixing over water and ice covered seas than over land due to the difference in surface characteristics and thermally-induced vertical convection.

6.2.4 Cook Inlet

The terrain surrounding Cook Inlet is not as mountainous as Prince William Sound or Port Valdez, but there are certainly regions of comparable terrain gradients. The area comprising the Kenai National Wildlife Refuge is relatively flat compared to the plume lofting heights expected of the large burns. An example of a burn in this region is shown in Figure 36. As in the example for Deadhorse, Prudhoe Bay, the flat terrain version of the ALOFT model, or even the flat terrain wind speed/lapse rate charts could be used in this region.

A more challenging example is shown in Figure 37. The burn takes place off Harriet Point on the western shore of Cook Inlet with the winds blowing inland. As in previous onshore examples, increased vertical mixing in addition to rising terrain heights yield higher ground level concentrations than would normally be expected over water.

6.3 Single Burn, Various Soundings, Single Location

To further explore the interaction of complex terrain with different meteorological conditions, a single location was selected as a test site for simulating a single burn (1,000 bbl/h) subject to about a dozen different atmospheric soundings. The location chosen is Valdez Narrows, and the winds were fixed to blow from the northeast. Figures 45–56 included in Appendix C summarize the results. Note that the figures are presented in order of increasing ventilation factor.

To put these cases into some perspective, consider the three-dimensional views of two simulations of smoke plumes originating in the Valdez Narrows, shown in Figure 38. The great difference in the plume trajectories, and the ground level concentration footprints as well, is due to the difference in meteorological conditions. The temperature lapse rate in the first case is very nearly adiabatic and the Brunt-Väisälä frequency is very small. This essentially rids the atmosphere of the effects of the density stratification which for more stable atmospheres tends to suppress vertical motion induced by terrain obstacles. Thus, in the first case where the atmosphere is neutrally stratified, the terrain plays less of a role in the plume's trajectory. Contrast this with the bottom figure. Here the atmosphere is very stable, and the Brunt-Väisälä frequency is relatively large. Now, vertical motion is severely suppressed, forcing the air flow to go around rather than over the terrain obstacles. Indeed the plume winds its way through the various passageways between the larger mountain peaks, leading to greater concentrations near the surface. An excellent description of stratified flow past three-dimensional obstacles is given by Smolarkiewicz and Rotunno in References [41, 42]. They characterize the tendency of the fluid to go around rather than over an obstacle in terms of a Froude number²¹ given as $Fr = U_0 / (N_0 h)$, where U_0 is the prevailing wind speed, N_0 is the characteristic Brunt-Väisälä frequency, and h is the characteristic height of the terrain obstacle(s). Low values of this parameter (less than 0.5) yield flows characterized by small vertical displacements and the appearance of stagnation regions on both the windward and leeward

²¹Froude numbers represent the ratio of inertial forces to gravitational forces in buoyancy-driven flows.

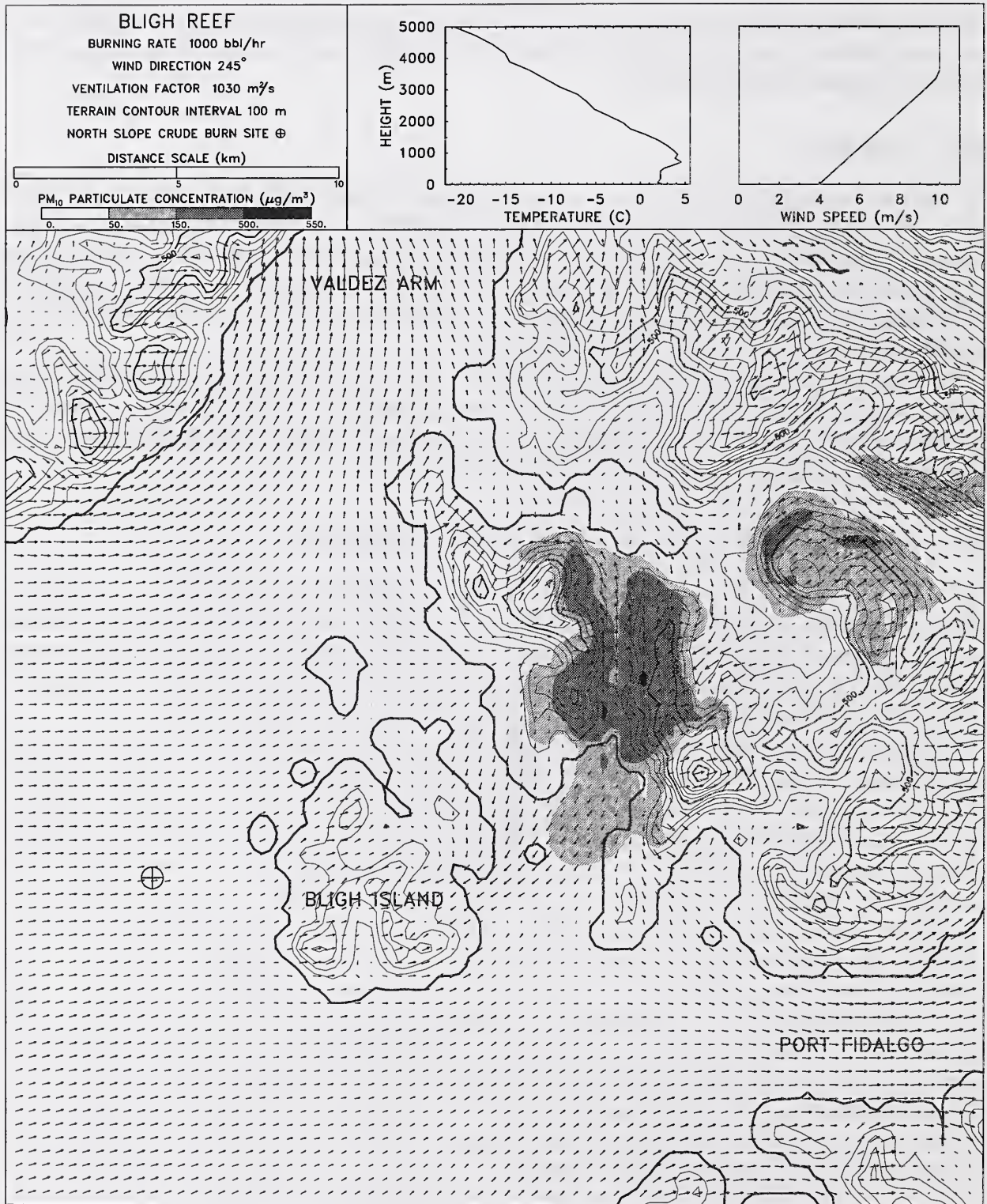


Figure 32: Footprint of simulated smoke plume originating off Bligh Island.

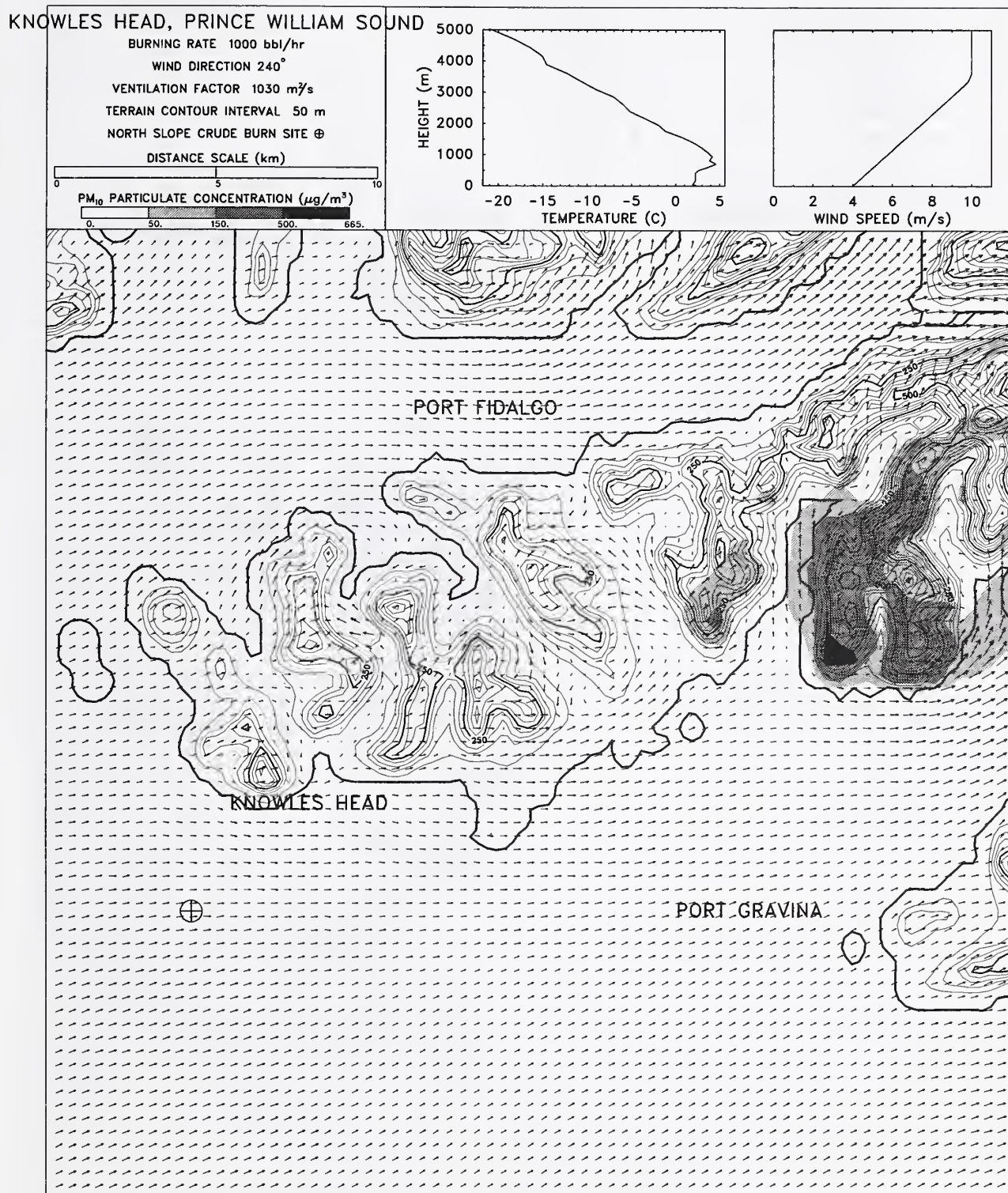


Figure 33: Footprint of simulated smoke plume originating off Knowles Head.

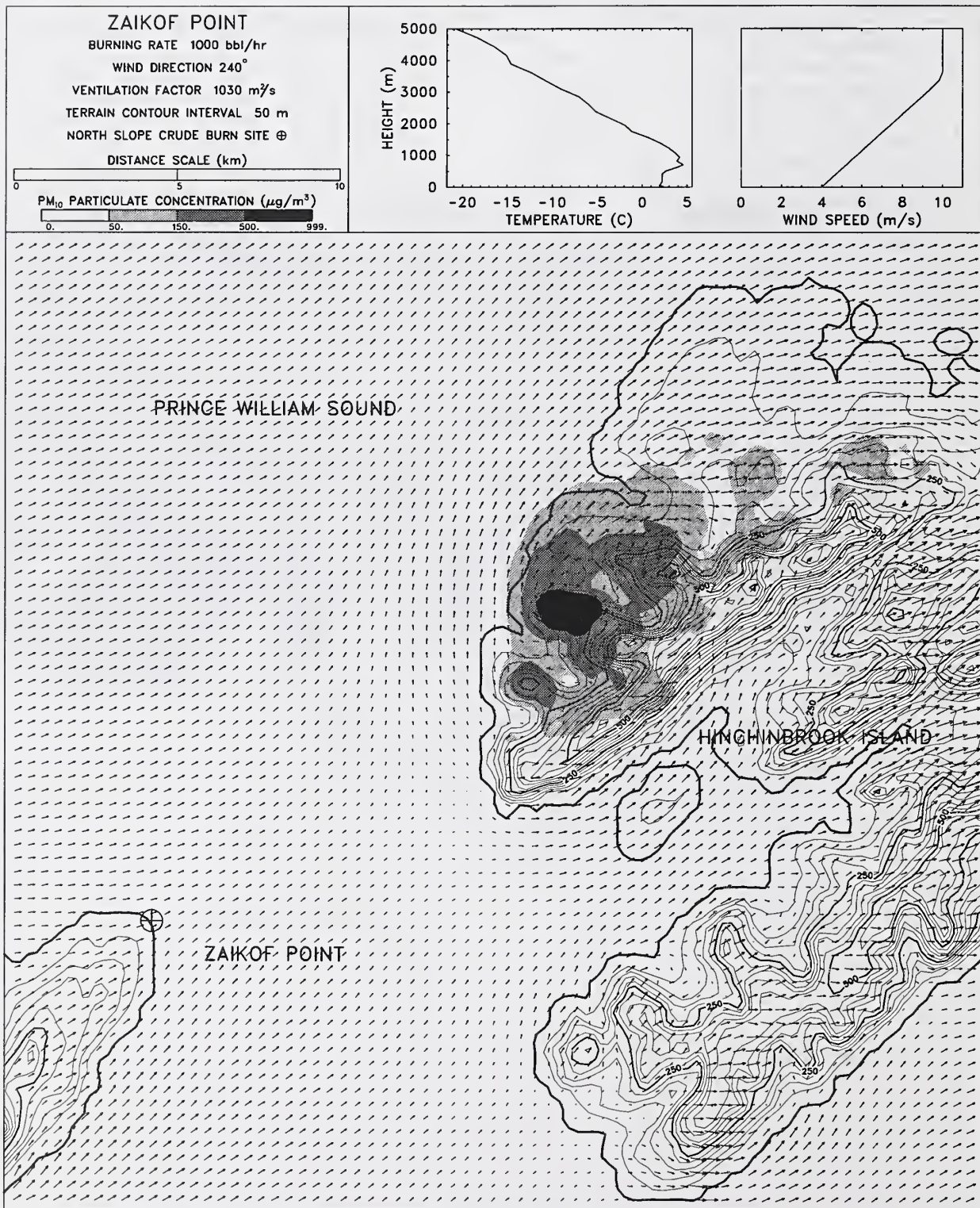


Figure 34: Footprint of simulated smoke plume originating off Zaikof Point.

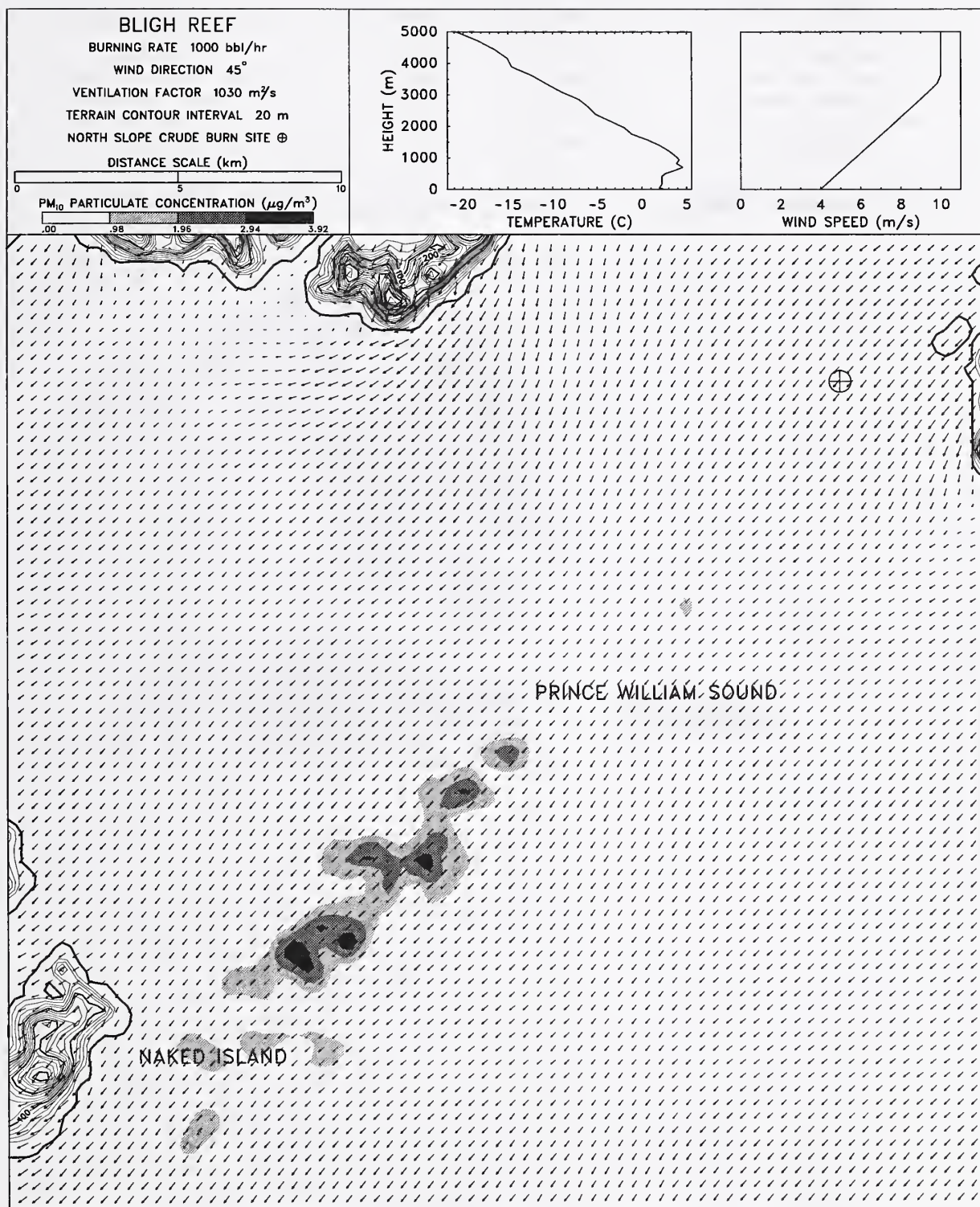


Figure 35: Footprint of simulated smoke plume originating off Bligh Reef.

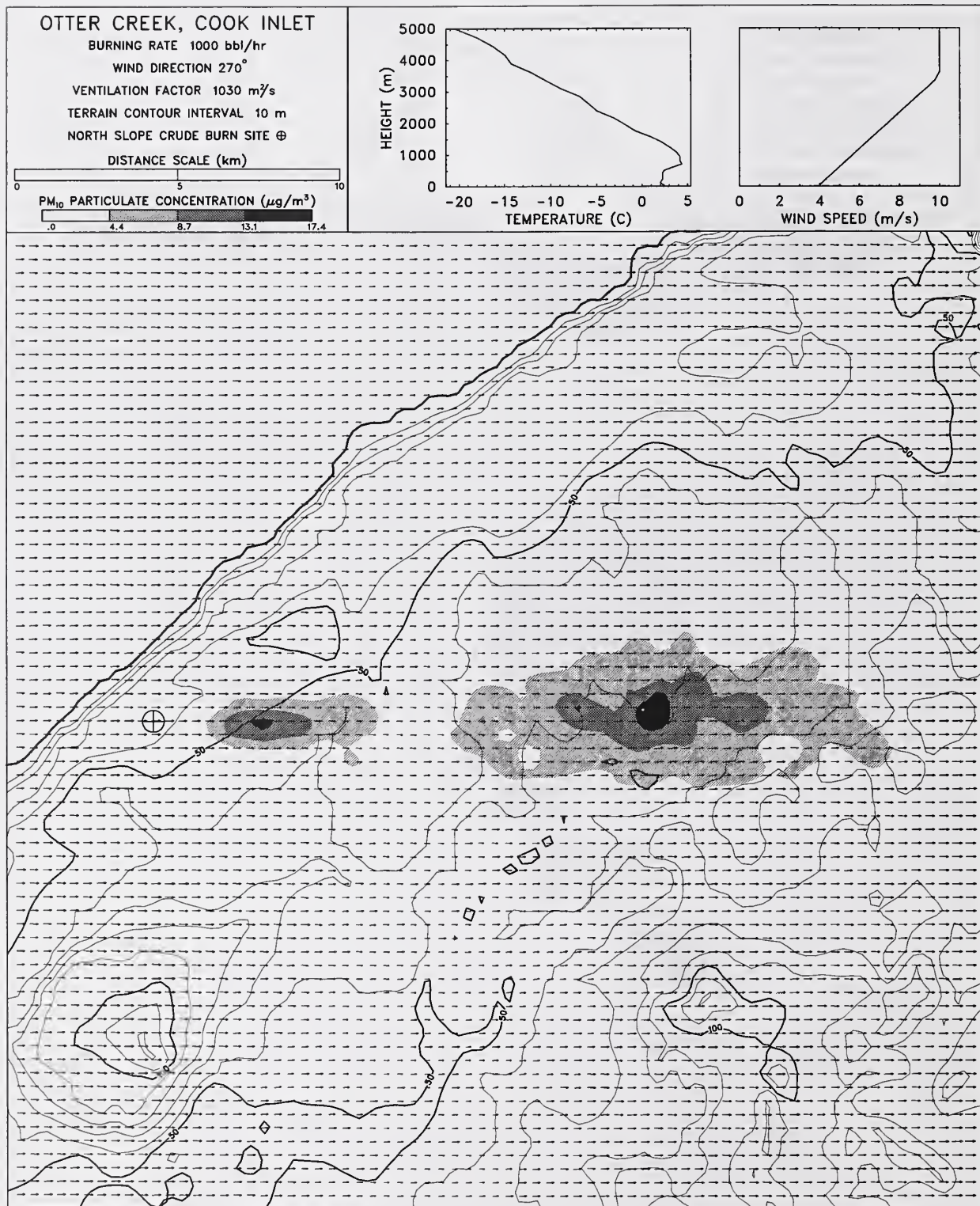


Figure 36: Footprint of simulated smoke plume originating at Otter Creek on the Kenai Peninsula.

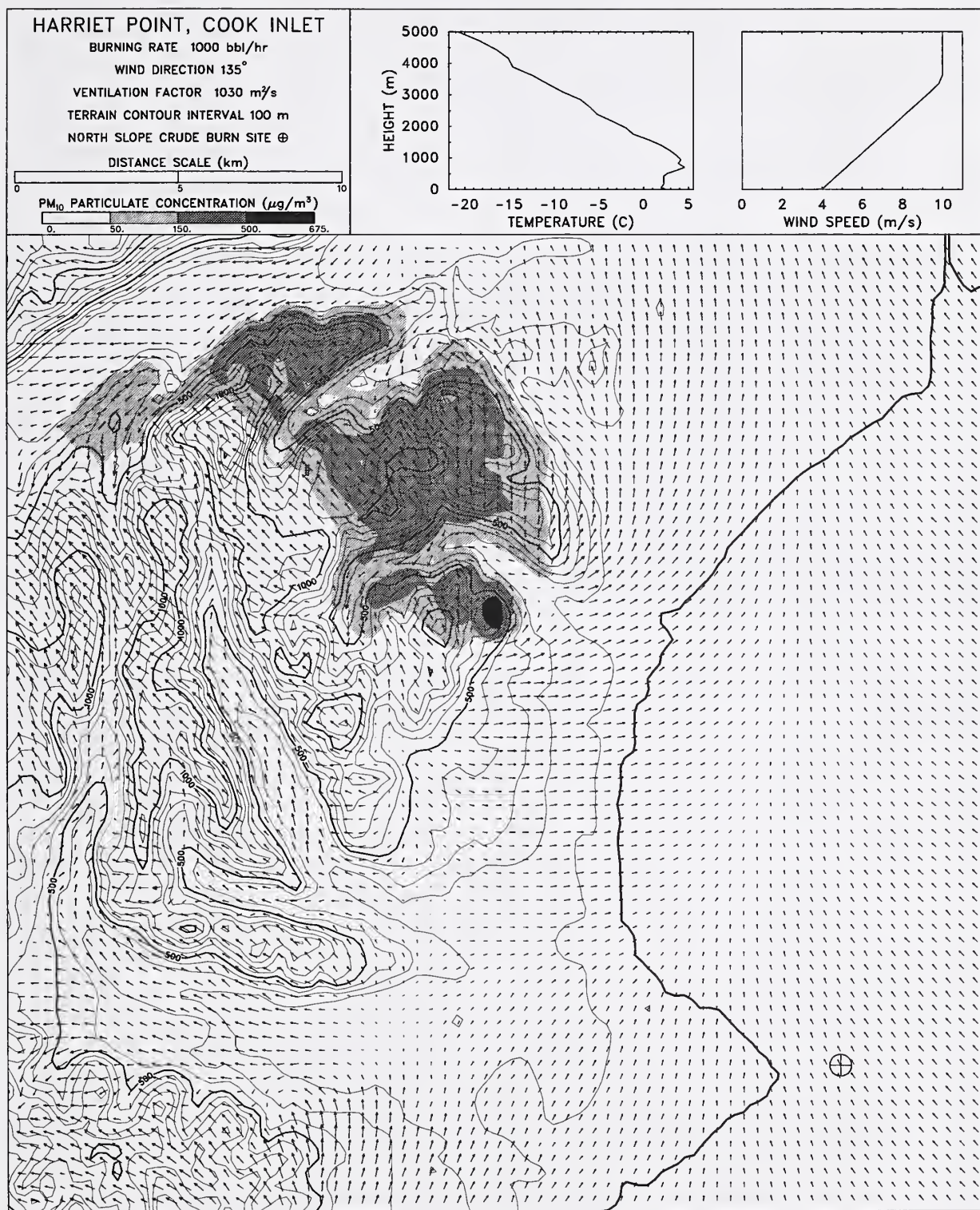


Figure 37: Footprint of simulated smoke plume originating off Harriet Point on the western shore of Cook Inlet.

sides of the obstacle. High values of the Froude number yield flows that tend to pass over, rather than around, mountainous terrain. Not surprisingly, high values of the Froude number correspond to high values of the ventilation factor, and low Froude numbers correspond to low ventilation factors. Thus, as a rough measure of the impact of terrain on flat terrain plume calculations, the ventilation factor is important.

6.4 Multiple Burns, Various Soundings, Various Locations

Thus far, the only *in situ* burn scenarios that have been considered are those in which there is a single patch of burning oil. The term “multiple burns” has two meanings: one refers to the deliberate separation of oil into more than one towed booms, the other refers to the break up of a large (probably unconfined) burning patch into separate fires. The more likely scenario is the first where individual teams attacking an oil slick simultaneously boom off separate patches of the slick and proceed to burn the oil. It is assumed that the distance between any two fires is at least 100 m in the crosswind direction. In this case, as far as the plume modeling is concerned, these fire plumes can be regarded as independent to a first approximation, and the downwind footprint is merely a superposition of the individual footprints. Thus, if three burns of comparable size are being conducted sufficiently far apart, the concentration one might expect to find at some point downwind would be three times as high as for a single burn. The smoke generation rate for three burns is triple that of one burn, whereas the heat release rate that dictates the plume rise of any individual plume does not change. Essentially, the fact that there are three burns as opposed to one does not dramatically change the plume structure of any so long as the plumes are sufficiently far apart.

If the fires are closer together, whether because a large burning patch breaks up or because towed booms are brought close together, there will be some interaction of the plumes. As before, the smoke generation rate will simply be the sum of the rates of each individual plume, but the trajectory of each plume will be influenced by its neighbors. Both the flat and complex terrain versions of the ALOFT model include the capability to track more than one smoke plume, and the interaction of the plumes is explicitly calculated. In the case where separate patches of oil are confined in separate towed booms and burned, it is easy to designate the fires in terms of the size and location of the individual burn areas. However, in the case of large unconfined fire breaking up into smaller fires, it is more difficult to designate the fires because it is not well understood at what point a fire will become so large that it no longer generates a single plume or breaks up into multiple fires. It has been assumed throughout this report that a single burning patch of oil produces a single smoke plume. Certainly for a patch confined within a boom of typical length (150 – 300 m or 500 – 1,000 ft), this is the case, but a question remains about what will result from the burning of a larger patch of oil, whether it be confined by broken ice, a small lake, stream or other terrain depression, or whether it is unconfined, for example, a spreading slick on a large body of water. There have been a number of examples over the years of *in situ* burning of spilled fuels on land. Most of these efforts were not reported, and certainly very little measurements were taken. A case study of one is given in Reference [45]. As for the burning of unconfined slicks at sea, there is much less experimental or anecdotal information. Its feasibility has been demonstrated by Guénette and Sveum at SINTEF in Norway [46] in a series of tests in which an initially confined patch of oil was ignited and then allowed to spread. The experiments demonstrated a “wind herding” effect, by which the spreading of the oil is reduced by the fire-induced flow field. In order for this technique

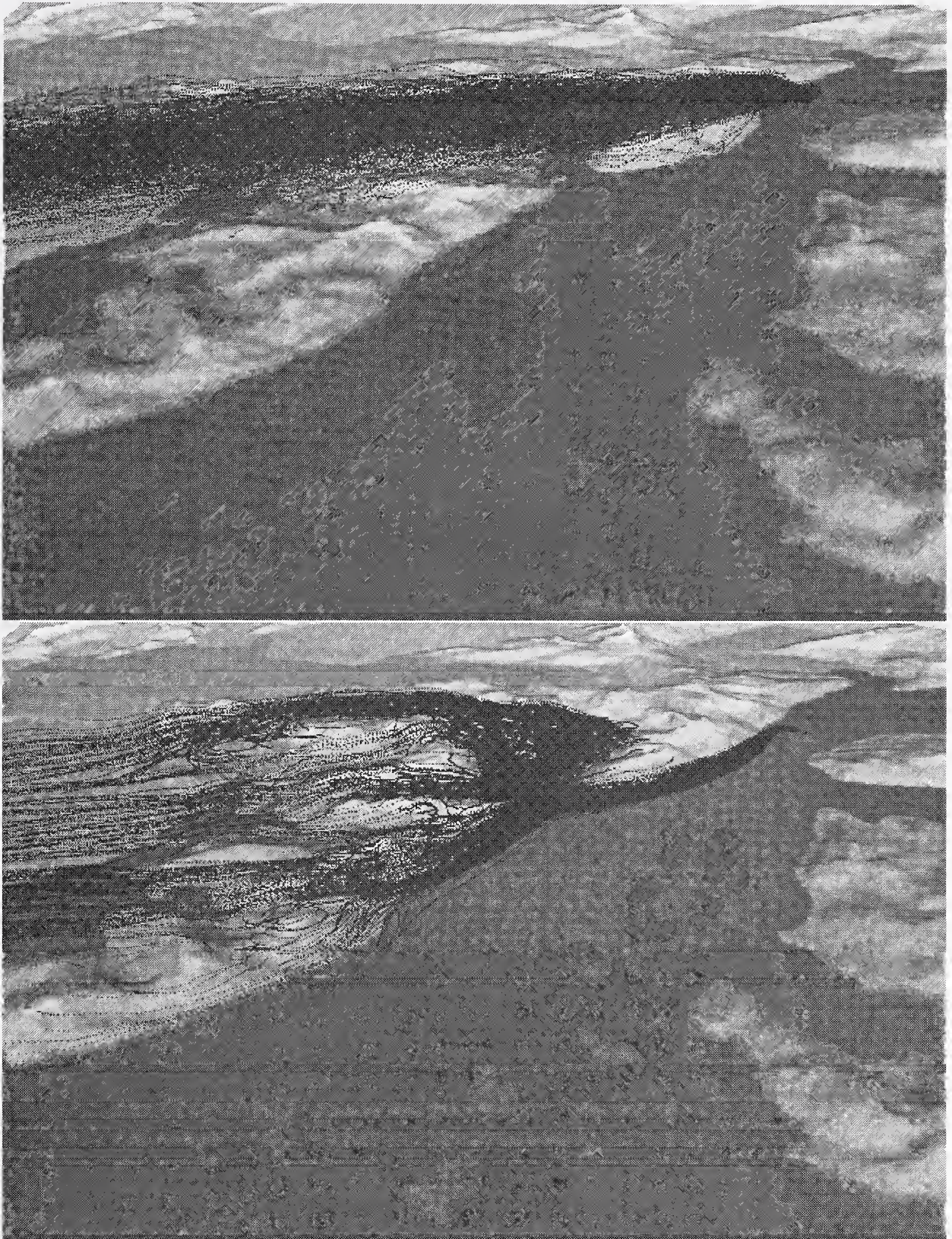


Figure 38: Three-dimensional views of smoke plumes originating in the Valdez Narrows. The top plume represents a case where the Froude number, $U_0/(N_0 h)$, is large. The bottom figure is for a case where the Froude number is small.

to be used, burning would have to commence very shortly after the spill, or as the oil spills from the vessel, so that a sufficient thickness of oil would be maintained (>1 mm). A particularly interesting test involved the burning of 8 m^3 of oil initially confined in a 10 m diameter ring. The burning area increased to about 850 m^2 before the slick thickness decreased and the area receded. It was observed that one plume was generated by the burning patch when at its greatest width, but the patch split into two towards the end of the burn as the slick thickness neared the extinction point.

Based on these experiments, plus the Newfoundland Offshore Burn Experiment, it is reasonable to expect that a roughly circular patch of oil of area less than $1,000\text{ m}^2$ ($10,000\text{ ft}^2$) will generate a single plume when burned. It is assumed here that the area represents regions of a slick that are at least a millimeter in thickness. For burn areas greater than $1,000\text{ m}^2$, it is less clear whether the slick will split into separate burning regions. Certainly sea conditions, local slick thickness, and the local wind field will have a tremendous influence on the burning characteristics. From a modeling perspective, there are two strategies to handle an unconfined burn whose area exceeds $1,000\text{ m}^2$. Either the fire can be prescribed in terms of a single burning area, or the fire can be broken up into separate areas. If the fire is broken into separate patches, then the distance between the patches also becomes a factor. Consider a case in which oil is spilled near Pump Station 1 forming a roughly circular pool whose area is $7,600\text{ m}^2$. If this pool were ignited, the fire would consume about $10,000\text{ bbl/h}$. To model this scenario, one can designate a single burn area of $7,600\text{ m}^2$, or multiple areas whose combined total is $7,600\text{ m}^2$. Figure 39 shows the downwind footprint from a single burn consuming $10,000\text{ bbl/h}$. Figure 40 shows the footprint from 10 separate fires each consuming $1,000\text{ bbl/h}$, with each fire separated by about 50 m. Figure 41 shows the footprint from 10 separate fires each consuming $1,000\text{ bbl/h}$, with each fire separated by about 150 m. The footprints from the single fire case and the case where the fires are relatively close together are not dramatically different. The footprint from the fires spaced more widely apart, however, shows a substantial increase in ground level concentration. The reason for the difference is not apparent from the figures. In the case of the single fire, the plume rises higher than those in the multiple fire cases. As the separation between the fires increases, the interaction between the plumes decreases until such a point where the plumes are independent of each other. This distance is on the order of 100 m. When the plumes are effectively independent, the downwind footprint can then be considered as merely a superposition of the footprints from the individual fires, with concentrations at each location being the sum of those from the separate fires. The ground level concentration from the superposition of independent fires is greater than the concentration from a single fire consuming the equivalent amount of oil. In the next section, as part of an overall strategy for predicting distances from fires where the particulate concentration falls below a given level of concern, the issue of multiple fires will be discussed in a more quantitative manner.

6.5 Ground Level Distance Estimates for Complex Terrain

The introduction of complex terrain into an atmospheric dispersion model certainly enhances its applicability and usefulness, but at the same time increases the variety of burn scenarios to consider. For the simulations of burns in Alaska described above, it is clear that generalizations are not easy to make concerning the introduction of complex terrain into the problem. For many cases, particularly for plumes originating over relatively open waters, it is possible to estimate increased ground level concentrations on elevated terrain near the coast over which the plume is lofted based on flat terrain simulations. However, for cases where the plume originates in an area surrounded

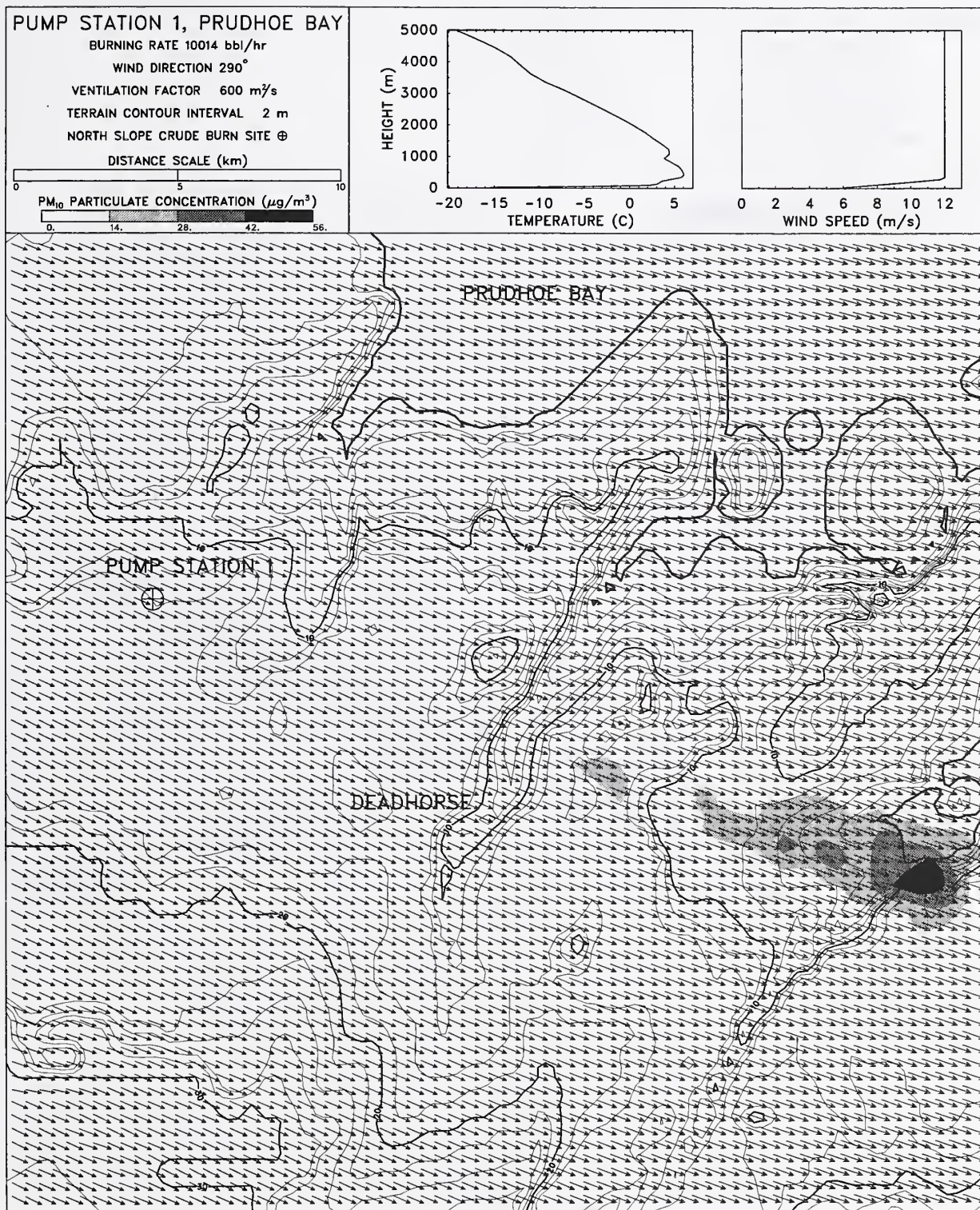


Figure 39: Footprint of simulated smoke plume from a single large fire originating at Pump Station 1, Prudhoe Bay. The fire consumes 10,000 bbl/h.

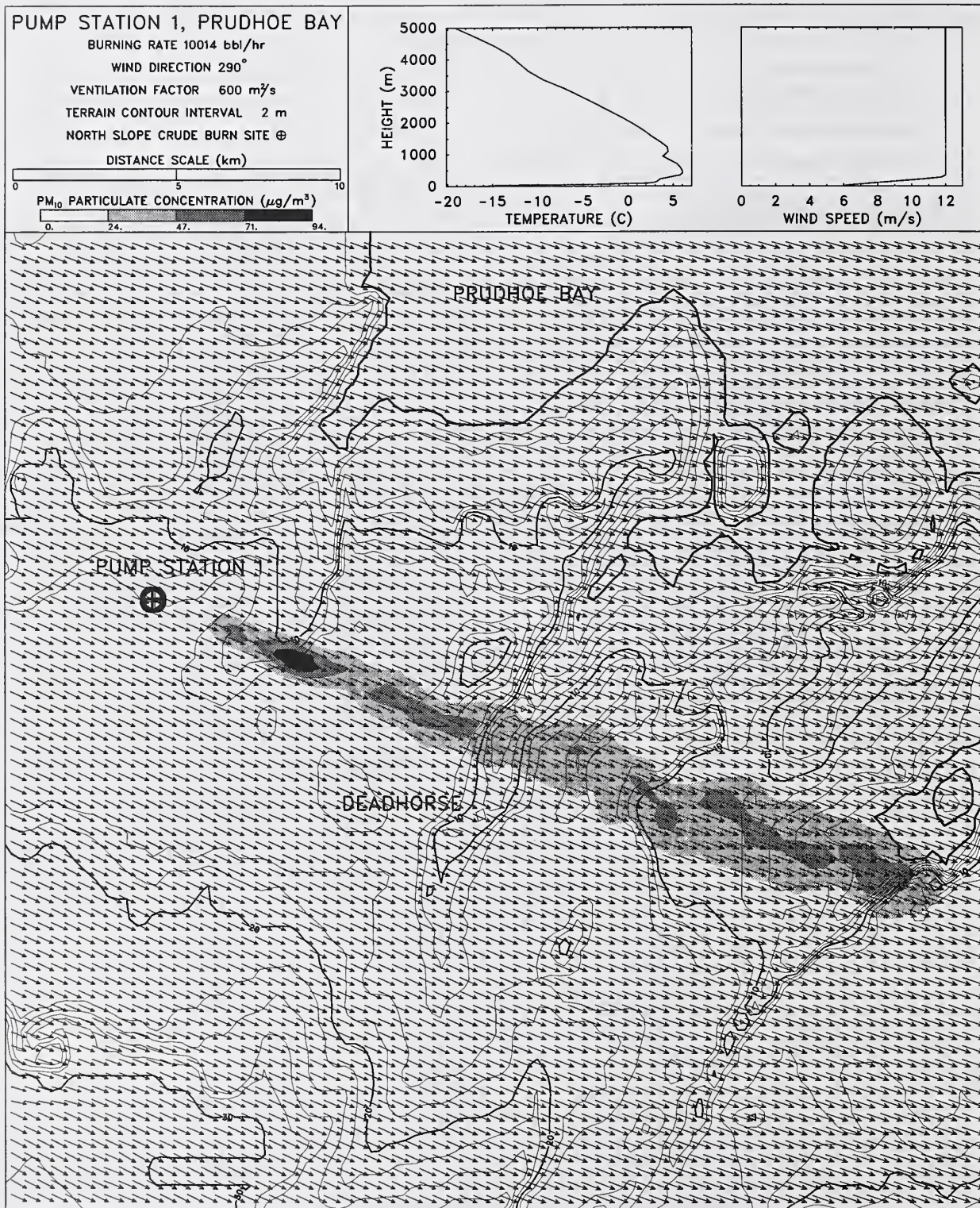


Figure 40: Footprint of simulated smoke plume from 10 fires originating at Pump Station 1, Prudhoe Bay. Each fire consumes 1,000 bbl/h. The fires are separated by about 50 m.

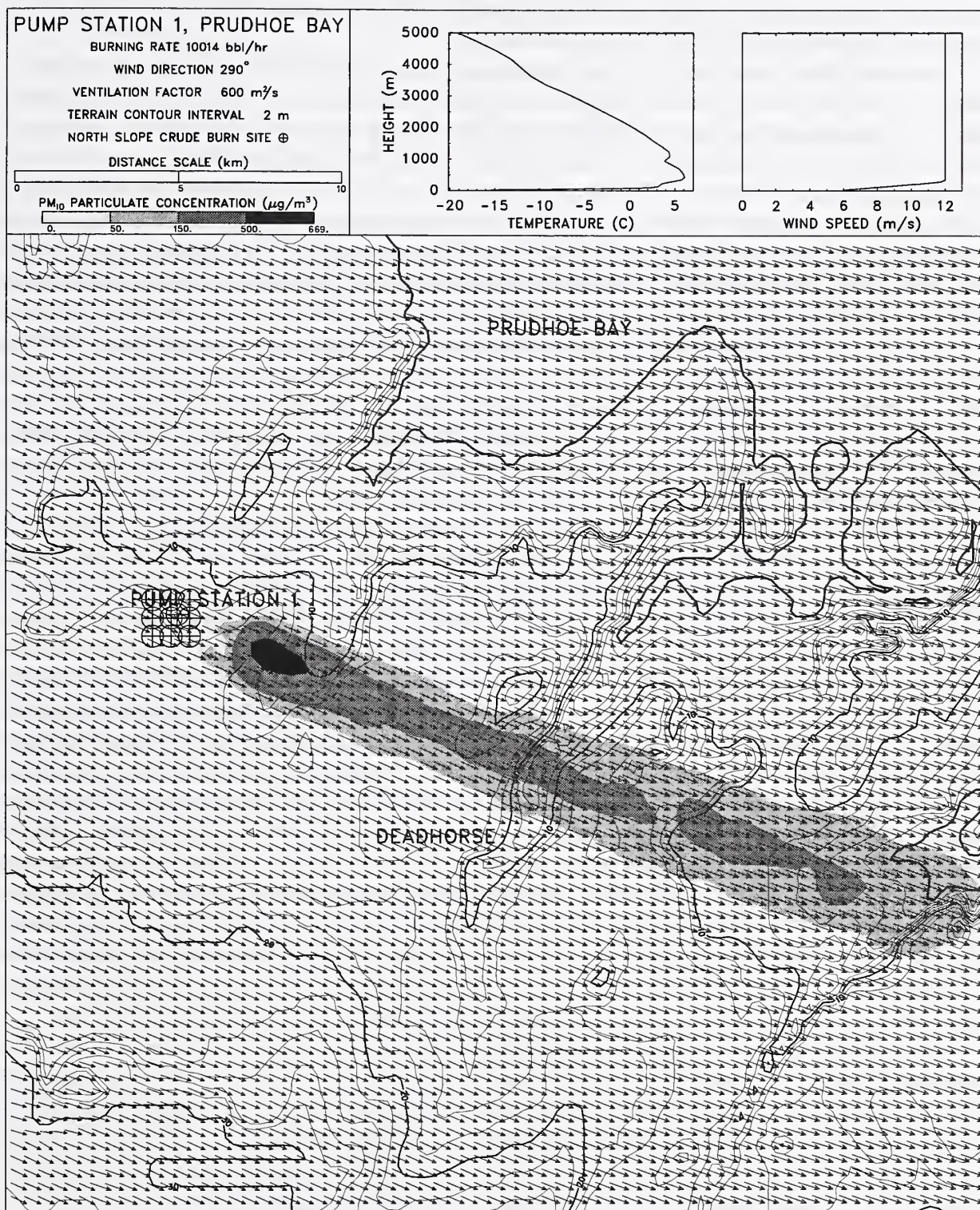


Figure 41: Footprint of simulated smoke plume from 10 fires originating at Pump Station 1, Prudhoe Bay. Each fire consumes 1,000 bbl/h. The fires are separated by about 150 m.

by steeply rising terrain and carved by glaciers and inlets, it is more difficult to make an estimate of ground level concentration based on flat terrain results. These situations certainly justify the more intensive computations required to make predictions.

The calculations described in the previous sections can be used to estimate the distance from a fire beyond which ground level concentrations of combustion products fall below regulatory thresholds. The combustion product most likely to violate ambient air quality standards is particulate, and the guideline recommended for *in situ* burning is $150 \mu\text{g}/\text{m}^3$ (PM-10) averaged over one hour. The distance beyond which the PM-10 concentration falls below this threshold depends mainly on the terrain height and the mixing layer depth, with wind speed the next most important factor. In addition, the region where one might expect to find concentrations in excess of $150 \mu\text{g}/\text{m}^3$ is not necessarily narrow as in the case of ground level footprints generated by plumes lofting over relatively flat terrain. Consequently, both the overall shape and extent of the region need to be characterized. A reasonable approach is to idealize the shape of the region as a sector²² of the circle whose center is the fire itself. Thus a distance and an angle define the region where ground level concentrations exceed the threshold value. Roughly speaking, both the radius and the angle of the sector decrease as the ventilation factor increases. The sector angle decreases because the plume tends to go over, rather than around, terrain obstacles as the ventilation factor (and the similarly defined Froude number) increases.

Taking all the simulations performed to date with the complex terrain version of the ALOFT model, some conservative estimates of maximum distance can be made. In addition, flat terrain plume simulations can be analyzed to determine the extent of concentrations exceeding $150 \mu\text{g}/\text{m}^3$ not only at ground level but throughout the entire plume. The idea behind this approach is that the distance downwind of a plume lofting over flat terrain where the maximum concentration anywhere within the plume no longer exceeds the threshold value can be used as a conservative estimate for the distance where the concentration no longer exceeds the threshold at comparable elevations in cases of complex terrain. For the 1,000 bbl/h fire used in many of the simulations above, depending on the level of turbulence in the atmosphere, flat terrain calculations show the maximum hour-averaged $150 \mu\text{g}/\text{m}^3$ PM-10 concentration in the plume (not just near the ground) extending anywhere from 10 to 20 km from the fire when lofted over land. When lofted over water, this distance extends to about 30 km. This sets the upper bound on ground level concentration, regardless of the terrain height. This upper bound is inherently conservative because it does not take into account the increased dispersion of the plume as it interacts with the complex terrain. As can be seen in Figure 38, a low ceiling height in the presence of relatively high mountains forces the smoke flow around rather than over the terrain obstacles, which brings the smoke closer to the ground but also breaks up the plume more effectively than the atmospheric turbulence would on its own.

Both the flat terrain and complex terrain simulations can be summarized in terms of the distance beyond which the PM-10 concentration falls below regulatory thresholds. The two most important factors determining this distance are the terrain height and the mixing layer depth *relative* to the elevation of the burn site. Taking the 1,000 bbl/h burn as an upper limit for a single fire, 130 g/kg as the particulate emission factor, and $150 \mu\text{g}/\text{m}^3$ as the hour-averaged concentration threshold, Table 9 lists the maximum distance as a function of terrain height and mixing layer depth. The mixing layer depth is loosely correlated with the temperature lapse rate, and the wind speeds considered were in the range from 1 to 12 m/s. Note that the first row of the table corresponds to

²²The sector of a circle is the region bounded by two radii and the included arc.

Terrain Height (m)	Mixing Layer Depth (m)				
	0–100	100–250	250–500	500–1,000	> 1,000
0–25 (“Flat Terrain”)	5	4	3	2	1
25–250	10	8	6	4	3
250–500	15	12	10	8	5
> 500	20	17	15	12	10

Table 9: Distance from a fire consuming 1,000 bbl/h beyond which the hour-averaged ground level concentration of PM-10 falls below $150 \mu\text{g}/\text{m}^3$. These distances are expressed in units of kilometers (1 mi \approx 1.61 km). Terrain Height and Mixing Layer Depth are relative to the altitude of the burn site. Modifications to these distances to account for different fire sizes and PM standards can be made according to the formula given by Eq. (40).

relatively flat terrain. The maximum distance estimates can be modified to account for changes in the fire size, emission factor, concentration threshold, offshore burns, and multiple burns. If the given burn scenario calls for something other than a single fire on land consuming 1,000 bbl/h, and the ground level particulate criteria is something other than $150 \mu\text{g}/\text{m}^3$ of PM-10, then the distance from Table 9, D_{table} , should be modified according to the following formula

$$D = D_{\text{table}} + 7 \ln \left[(\# \text{ of burns}) \frac{150}{\rho_c} \frac{\text{EF}}{130} \left(\frac{\text{BR}}{1,000} \right)^{\frac{1}{3}} \right] + (d - d_{eq}) \text{ km} \quad (40)$$

The expression “(# of burns)” refers to independently burning patches of oil separated by at least 100 m. Superposition of ground level concentration is applied in these cases. The critical hour-averaged concentration ρ_c should be expressed in units of $\mu\text{g}/\text{m}^3$. The emission factor EF should be expressed in units of g/kg. Emission factors for various PM sizes can be found in Table 1. The value 130 g/kg is for PM-10. The Burning Rate BR is expressed in units of bbl/h *per fire*. It is assumed that in the case of multiple burns, all the fires are of comparable size. Note that the Burning Rate, BR, can be expressed in terms of the burn area, burning rate or heat release rate as long as the value of the denominator (here given as 1,000 bbl/h) is given in equivalent units. The distance $d - d_{eq}$ accounts for the case where a plume originates offshore and is subject to less atmospheric turbulence over water. The distance d is the actual distance the plume travels over the water, and d_{eq} is given as

$$d_{eq} = \frac{\sigma_{w,\text{marine}}}{\sigma_{w,\text{coastal}}} d \quad (41)$$

and represents an equivalent distance where the plume would be subjected to coastal rather than marine atmospheric conditions. The magnitude of the vertical wind fluctuation offshore is roughly half that of land, thus a good rule of thumb is to assume that the equivalent offshore distance, d_{eq} , is about half the actual distance, d (See Section 4.4 for more details).

Note that the distance given by (40) may be negative, in which case the distance from Table 9 would be reduced. However, this distance should never be reduced inside of a kilometer from the fire because of the unpredictable, transient nature of the near field environment that is not accounted for by the quasi-steady state model. This includes low traveling smoke due to fire ignition and extinction.

The discussion of multiple burns in the previous section can be made more quantitative with the use of the correction term in Eq. 40. Consider again a very large slick of oil which, if ignited, could support a fire consuming about 10,000 bbl/h. Its area would be about 7,600 m². The correction term to the distance listed in Table 9 depends on whether or not the slick burns as one big fire or as smaller fires separated by at least 100 m. Suppose, the slick was broken up into 10 smaller patches, with the burning rate of each patch being 1,000 bbl/h. The correction term in this case would be $7 \ln 10 \approx 16$ km, that is, a distance of 16 km should be added to the Table 9 estimate. However, if the slick was burned as a single fire, the correction term would be $7 \ln 10^{\frac{1}{3}} \approx 5$. This result is due to the fact that the increased particulate matter generated by increasing the burning rate of a single fire is offset by the fact that the plume will rise higher into the atmosphere. Breaking up a larger fire into smaller ones leads to higher ground level concentrations downwind because the same amount of particulate matter is being injected into the atmosphere at lower altitudes due to the increased mixing of the smaller plumes with the surrounding air. A forest fire differs from an *in situ* burn for exactly this reason — a forest fire of comparable total smoke generation rate to an *in situ* burn will exhibit higher ground level smoke concentrations because the source fires are typically spread over a wider area. Needless to say, the strategy for *in situ* burning should be to create as large a fire or fires as possible so that the combustion products rise as high as possible into the atmosphere.

7 Conclusions

The strategy from the beginning of the development of the ALOFT model has been to work from the fundamental conservation equations that describe the introduction of hot gases and particulate matter into the atmosphere. The justification for this approach is manifested by the extremely complicated flow simulations of smoke dispersal over the rugged terrain of Alaska. There simply is no other way to simulate these flow patterns except by solving the fundamental equations of fluid mechanics. Empirical correlations become hopelessly awkward to apply as the number of degrees of freedom in the problem increases with the introduction of realistic meteorology and terrain. Fortunately, the rapid development of relatively inexpensive, powerful computers has made it possible to compute the solution to the equations of motion that govern the transport of pollutants in the lower atmosphere at a resolution that is comparable to that of the underlying terrain data.

A combination of numerical modeling and small and large scale experiments has yielded a tremendous amount of information about the structure, trajectory and composition of smoke plumes from large crude oil fires. The results of both the ALOFT modeling effort and the series of large scale experimental burns can be summarized as follows:

1. The results of the original plume modeling study, summarized in Table 9 of Reference [1], remain valid for flat terrain applications. "Flat" in this context refers to terrain that does not vary in height by more than about 10% of the expected plume height. Thus, for a single burn consuming up to about 1,000 bbl/h in wind speeds less than 12 m/s (23 knots), the maximum ground level extent of particulate concentration in excess of $150 \mu\text{g}/\text{m}^3$ (hour-averaged) is 5 km (3.0 miles) over flat terrain. This distance is considerably less for typical daytime conditions, and simple correlations of ALOFT results (see Section 4.5) can be used to produce more refined distance estimates given a knowledge of the wind speed, ceiling height and burn size.
2. The uncertainty of ALOFT model predictions is largely a function of the uncertainty in the meteorological conditions and fire emission rates. The factor of safety of 2 that had been applied to the downwind distance predictions of the original flat terrain modeling effort (Reference [1]) should no longer be used as a means to incorporate model uncertainty. For cases involving flat terrain, a more rigorous estimation of uncertainty can be made using the flat terrain lapse rate/wind speed diagrams introduced in Section 4.5. These simple charts readily convey the sensitivity of model results to variations in the input parameters. The most important parameter is the lapse rate, which is roughly correlated with the mixing height. The latter quantity, along with the terrain height, has been used to extend the generalized flat terrain results to situations involving complex terrain.
3. The ventilation factor, which is the product of the wind speed and mixing layer depth used to characterize the dispersive potential of the atmosphere, is a reasonably good indicator of expected ground level concentration of smoke or combustion products from a large burn. This is true of both flat and complex terrain. In the case of flat terrain, the ALOFT correlations show clearly the relationship between ground level concentrations and ventilation factor. In the case of complex terrain, the ventilation factor is similar to the Froude number, a nondimensional quantity used by the meteorological community to express the propensity of air currents to flow over, rather than around, terrain obstacles. Low ventilations factors,

like low Froude numbers, indicate conditions more likely to lead to a higher ground level concentration of pollutants.

4. Smoke particulate is by far the most likely combustion product of crude oil burning to exceed ambient air quality standards beyond a few hundred meters from the fire. This is true of both the National Ambient Air Quality Standard (NAAQS) and the Alaska State Regulatory Standards. Presently, the standards apply to PM-10 particulate, but the translation of results for other PM sizes and/or concentrations can easily be made and will not alter the conclusions of this report dramatically. The next likeliest combustion product to violate any air quality standard would be sulfur dioxide (SO_2). Based on the measured ratio of particulate to SO_2 in the smoke, SO_2 will not reach its 3 hour standard until the PM-10 particulate concentration reaches $7,800 \mu\text{g}/\text{m}^3$. ALOFT-predicted maximum hour-averaged, ground level concentrations from a burn consuming 1,000 bbl/h ANS crude never exceeded $2,000 \mu\text{g}/\text{m}^3$ for all the locations and soundings considered.
5. Peak concentrations of ground level smoke particulate for the Newfoundland Offshore Burn Experiment, the Alaska Clean Seas Burning of Emulsions experiment, and the October 1994 diesel fuel burns in Mobile, Alabama, never exceeded $100 \mu\text{g}/\text{m}^3$ beyond a few hundred meters from the fires, and in most cases were well below that level. All these experiments were conducted under reasonably good weather conditions and over relatively flat terrain, and the burns were smaller than burns anticipated in a real *in situ* burning application. However, extrapolating these burns to full scale would not dramatically change the overall results.
6. Simple correlations of ALOFT model results cannot be made for cases involving complex terrain because there are too many degrees of freedom in the problem. The extent of the surface level PM-10 concentration in excess of $150 \mu\text{g}/\text{m}^3$ averaged over several hours can be as much as 20 km from the burn site for a burn consuming 1,000 bbl/h. However, this estimate can be refined based primarily on the relative terrain height and the depth of the mixing layer (see Section 6.5). The distance from a large burn (1,000 bbl/h) can be as low as 1 km for flat terrain and nearly adiabatic lapse rates, and as high as 20 km for terrain elevations extending above the mixing layer.
7. The downwind deposition patterns from the simultaneous burning of multiple patches of oil is very much dependent on the distance between the fires. For lateral distances (perpendicular to the wind direction) of at least 100 m, the plumes may be considered effectively independent, and their individual footprints superimposed. For fires which are closer, the ALOFT model, either the flat terrain or complex terrain version, must be run to assess the interaction of the two rising plumes.

8 Acknowledgements

This work was sponsored by the Alaska Department of Environmental Conservation (ADEC), under the supervision of Larry Dietrick. The ALOFT model and experimental techniques for smoke measurement used in this work were developed in part under funding provided by the Minerals Management Service, US Department of the Interior, under the supervision of Edward Tennyson and Joseph Mullin. The complex terrain version of the ALOFT model has been developed in cooperation with EMCON Alaska, under the supervision of Michael Bronson and David O'Brien.

Additional thanks to Ming Xue at the Center for the Analysis and Prediction of Storms, University of Oklahoma, for advice on the terrain mapping and numerical meteorology; Ron Ferek and John Ross of the University of Washington who provided data from the Newfoundland Offshore Burn Experiment and assisted in its analysis; Nick Glover and Bruce McKenzie of Alaska Clean Seas who invited NIST to participate in the Burning of Emulsions project and provided important logistical support; Phil Campagna and the Emergency Response Team of the US Environmental Protection Agency who gathered particulate data under adverse conditions at Prudhoe Bay; and Nir Barnea and John Whitney of NOAA and Joseph Mullin of MMS who also assisted in the data collection at Prudhoe Bay.

References

- [1] K.B. McGrattan, A.D. Putorti, W.H. Twilley, and D.D. Evans. Smoke Plume Trajectory of In Situ Burning of Crude Oil in Alaska. Technical Report NISTIR 5273, National Institute of Standards and Technology, Gaithersburg, Maryland, October 1993.
- [2] J.A. Raloff. Burning issues. *Science News*, 144:220–223, October 1993.
- [3] J. Whitney, C. Lautenberger, and L. Dietrick. Alaska Regional Response Team In Situ Burn Guidelines and Pre-approvals. In *Proceedings of the 17th Arctic and Marine Oil Spill Program (AMOP) Technical Seminar*, pages 419–437. Environment Canada, Emergencies Science Division, Ottawa, Ontario, Canada, June 1994.
- [4] K.B. McGrattan, H.R. Baum, and R.G. Rehm. Smoke Plume Trajectory of In Situ Burning of Crude Oil in Alaska. In *Proceedings of the 17th Arctic and Marine Oil Spill Program (AMOP) Technical Seminar*, pages 725–734. Environment Canada, Emergencies Science Division, Ottawa, Ontario, Canada, June 1994.
- [5] K.B. McGrattan, W.D. Walton, A.D. Putorti, W.H. Twilley, J. McElroy, and D.D. Evans. Smoke Plume Trajectory of In Situ Burning of Crude Oil in Alaska – Field Experiments. In *Proceedings of the 18th Arctic and Marine Oil Spill Program (AMOP) Technical Seminar*, pages 901–914. Environment Canada, Emergencies Science Division, Ottawa, Ontario, Canada, June 1995.
- [6] J.S. Turner. *Buoyancy Effects in Fluids*. Cambridge University Press, Cambridge, England, 1973.
- [7] J.S. Turner. Proposed pragmatic methods for estimating plume rise and plume penetration through atmospheric layers. *Atmospheric Environment*, 19:1215–1218, 1985.
- [8] R.B. Wilson. Review of development and application of CRSTER and MPTER models. *Atmospheric Environment*, 27B(1):41–57, 1993.
- [9] US Environmental Protection Agency. *User's Guide for the Industrial Source Complex (ISC3) Dispersion Models, Vol. II – Description and Model Algorithms*, September 1995. Publication EPA-454/B-95-003b.
- [10] US Environmental Protection Agency, Office of Air Quality Planning and Standards, Research Triangle Park, North Carolina. *A User's Guide for the CALPUFF Dispersion Model*, July 1995. Publication EPA-454/B-95-006.
- [11] S.G. Perry. *User's Guide to the Complex Terrain Dispersion Model Plus Algorithms for Unstable Situations (CTDMPLUS), Vol. I – Model Description and User's Instructions*. US Environmental Protection Agency, March 1989. Publication PB89 181424.
- [12] D.C. DiCristofaro and S.R. Hanna. *OCD: The Offshore and Coastal Dispersion Model, Volume 1: User's Guide*. Sigma Research Corporation, Westford, Massachusetts, 1989. Report No. A085-1.

- [13] G.K. Batchelor. *An Introduction to Fluid Dynamics*. Cambridge University Press, Cambridge, England, 1967.
- [14] A.F. Ghoniem, X. Zhang, O.M. Knio, H.H. Baum, and R.G. Rehm. Dispersion and deposition of smoke plumes generated from massive fires. *Journal of Hazardous Materials*, 33:275–293, 1993.
- [15] H.R. Baum, K.B. McGrattan, and R.G. Rehm. Simulation of Smoke Plumes from Large Pool Fires. In *Proceedings of the 25th International Symposium on Combustion*, pages 1463–1469. The Combustion Institute, Pittsburgh, PA, August 1994.
- [16] K.B. McGrattan, H.R. Baum, and R.G. Rehm. Numerical simulation of smoke plumes from large oil fires. *Atmospheric Environment*, 30(24):4125–4136, 1996.
- [17] M. Xue, K.K. Droegemeier, V. Wong, A. Shapiro, and K. Brewster. *Advanced Regional Prediction System (ARPS)*. Center for Analysis and Prediction of Storms (CAPS), University of Oklahoma, 1995.
- [18] G.A. Briggs. *Plume Rise Predictions*, pages 59–111. Lectures on Air Pollution and Environmental Impact Analysis. American Meteorology Society, Boston, 1975.
- [19] W.D. Walton. In-situ burning of oil spills: Meso-scale experiments and analysis. In *Proceedings of the 16th Arctic and Marine Oil Spill Program (AMOP) Technical Seminar*, pages 679–734. Environment Canada, Emergencies Science Division, Ottawa, Ontario, Canada, June 1993.
- [20] W.D. Walton. Smoke measurements using a helicopter transported sampling package. In *Proceedings of the 17th Arctic and Marine Oil Spill Program (AMOP) Technical Seminar*, pages 735–764. Environment Canada, Emergencies Science Division, Ottawa, Ontario, Canada, June 1994.
- [21] G.W. Mulholland, V. Henzel, and V. Babrauskas. The effect of scale on smoke emissions. In *Fire Safety Science – Proceedings of the Second International Symposium*, pages 347–357, New York, 1989. Hemisphere Publishing Corporation.
- [22] M.F. Fingas. The Newfoundland Offshore Burn Experiment – NOBE. In *Proceedings of the 1995 International Oil Spill Conference*, pages 123–132. American Petroleum Institute, 1995. Publication 4620.
- [23] J.L. Ross, R. Ferek, and P.V. Hobbes. Particle and gas emissions from an in situ burn of crude oil on the ocean. *Journal of the Air & Waste Management Association*, 46:251–259, 1996.
- [24] J.L. Ross, A.P. Waggoner, P.V. Hobbes, and R. Ferek. Airborne Lidar Measurements of a Smoke Plume Produced by a Controlled Burn of Crude Oil on the Ocean. *Journal of the Air & Waste Management Association*, 46:327–334, 1996.
- [25] K.K. Laursen, R.J. Ferek, V.H. Hobbes, and R.A. Rasmussen. Emission Factors for Particles, Elemental Carbon, and Trace Gases from the Kuwait Oil Fires. *Journal of Geophysical Research*, 97(13), 1992.

- [26] W.D. Walton, W.H. Twilley, J. McElroy, and D.D. Evans. Smoke measurements using a tethered miniblomp at the newfoundland offshore burn experiment. In *Proceedings of the 17th Arctic and Marine Oil Spill Program (AMOP) Technical Seminar*, pages 1083–1098. Environment Canada, Emergencies Science Division, Ottawa, Ontario, Canada, June 1994.
- [27] H. Koseki and G.W. Mulholland. The effect of diameter on the burning of crude oil pool fires. *Fire Technology*, 54, 1991.
- [28] H.A. Panofsky and J.A. Dutton. *Atmospheric Turbulence*. Wiley-Interscience, New York, 1984.
- [29] C.R. Church and J.T. Snow. Intense atmospheric vortices associated with a 1000 mw fire. *Bulletin of the American Meteorological Society*, 61(7), July 1980.
- [30] R.R. Draxler. Determination of atmospheric diffusion parameters. *Atmospheric Environment*, 10:95–105, 1976.
- [31] F.A. Pasquill. *Atmospheric Diffusion*. Halstead Press–Wiley, New York, second edition, 1974.
- [32] D.H. Slade. Meteorology and atomic energy, 1968. Technical report, Air Resources Laboratory, Environmental Science Services Administration, United States Department of Commerce, July 1968. Available through National Technical Information Service (NTIS), Department of Commerce, Publication TID-24190.
- [33] R.B. Stull. *An Introduction to Boundary Layer Meteorology*. Kluwer Academic Publishers, Boston, Massachusetts, 1988.
- [34] Radiosonde Data of North America, 1946 – 1994. CD-ROM data set, August 1995. Produced by the Forecast Systems Laboratory and the National Climatic Data Center, National Oceanographic and Atmospheric Administration.
- [35] Ian Buist. Demulsifiers and Modified Heli-Torch Fuels to Enhance *in situ* Burning of Emulsions. Technical report, S.L. Ross Environmental Research Ltd., Ottawa, Ontario, February 1995. Prepared for Alaska Clean Seas, Anchorage, Alaska.
- [36] W.D. Walton, W.H. Twilley, A.D. Putorti, and R.R. Hiltabrand. Smoke measurements using an advanced helicopter transported sampling package with radio telemetry. In *Proceedings of the 18th Arctic and Marine Oil Spill Program (AMOP) Technical Seminar*, pages 1053–1074. Environment Canada, Emergencies Science Division, Ottawa, Ontario, Canada, June 1995.
- [37] E.E. Uthe, R.D. Kaiser, L. Carr, and B. Bumbaca-Deneen. Airborne lidar characterization of oil-burn effluent plumes. In *Proceedings of the Third Thematic Conference on Remote Sensing for Marine and Coastal Environments*, pages I–453–465, Ann Arbor, Michigan, 1995. Environmental Research Institute of Michigan (ERIM).
- [38] A.A. Allen and R.J. Ferek. Advantages and disadvantages of burning spilled oil. In *Proceedings of the 1993 International Oil Spill Conference*, pages 765–772. American Petroleum Institute, Pub. No. 4580, 1993.

- [39] A. Venkatram and J.C. Wyngaard, editors. *Lectures on Air Pollution Modeling*, chapter 1. American Meteorological Society, Boston, Massachusetts, 1988.
- [40] B.E. Schwartz and M. Govett. A hydrostatically consistent North American Radiosonde Data Base at the Forecast Systems Laboratory, 1946-present. Technical Report NOAA Technical Memorandum ERL FSL-4, Forecast Systems Laboratory, National Oceanographic and Atmospheric Administration, 325 Broadway, Boulder, Colorado, 1995.
- [41] P.K. Smolarkiewicz and R. Rotunno. Low Froude number flow past three-dimensional obstacles. part I: Baroclinically generated lee vortices. *Journal of the Atmospheric Sciences*, 46:1154–1164, 1989.
- [42] P.K. Smolarkiewicz and R. Rotunno. Low Froude number flow past three-dimensional obstacles. part II: Upwind flow reversal zone. *Journal of the Atmospheric Sciences*, 47:1498–1511, 1990.
- [43] H.R. Baum, O.A. Ezekoye, K.B. McGrattan, and R.G. Rehm. Mathematical modeling and computer simulation of fire phenomenon. *Theoretical and Computational Fluid Dynamics*, 6:125–139, 1994.
- [44] K.B. McGrattan, R.G. Rehm, and H.R. Baum. Fire-driven flows in enclosures. *Journal of Computational Physics*, 110(2):285–292, 1994.
- [45] M.E. Moir and B. Erskin. In-Situ Burning of Oil Spills on Land: A Case Study. In *Proceedings of the 17th Arctic and Marine Oil Spill Program (AMOP) Technical Seminar*, pages 651–655. Environment Canada, Emergencies Science Division, Ottawa, Ontario, Canada, June 1994.
- [46] C.C. Guénette and P. Sveum. In-situ burning of uncontained crude oil and emulsions. In *Proceedings of the 18th Arctic and Marine Oil Spill Program (AMOP) Technical Seminar*, pages 997–1010. Environment Canada, Emergencies Science Division, Ottawa, Ontario, Canada, June 1995.
- [47] F. Clare and D. Kennison. *NCAR Graphics Guide to New Utilities, Version 3.00*. National Center for Atmospheric Research, Scientific Computing Division, P.O. Box 3000, Boulder, Colorado 80307-3000, 1989. NCAR/TN-341+STR.
- [48] Green Mountain Software, Boulder, Colorado. *CRAYFISHPAK User's Guide*, 1990.

A Description of ALOFT Model Input Parameters

For a given *in situ* burn scenario, there are three options for making a prediction of the concentration of combustion products downwind using the ALOFT model. The choice depends on the following criteria:

- Flat vs. complex terrain.
- Availability of meteorological information.
- Amount of detail required in the output.

The decision path is relatively simple: If the terrain varies by more than about 10% of the expected plume height, then the terrain cannot be considered “flat”, and the complex terrain version of the ALOFT model (ALOFT-CT) must be used. If the terrain can be considered flat, either a flat terrain (ALOFT-FT) calculation should be performed or the flat terrain lapse rate/wind speed diagrams based on ALOFT-FT can be used. This decision is dictated by the availability of meteorological information and the level of detail required in the output. If the meteorological information is limited to an estimate of the temperature lapse rate and/or an estimate of the mixing layer depth, then the correlations will suffice as long as the required information is limited to ground level maximum concentration and the distance downwind one might expect to find a certain critical concentration. If more detailed meteorological information, like a temperature sounding, is available, then an ALOFT-FT calculation should be performed, yielding more information about the plume height and structure. The obvious advantage of the correlations is that it requires a few simple calculations, or a glance at a pre-computed chart, examples of which are found throughout this report.

The ALOFT model, regardless of version, is narrowly focussed on the problem of smoke and pollutant dispersion from large fires. Because of this, the input list required of the user is relatively short. At present, the ALOFT model is being developed for implementation on both UNIX and PC platforms, but the scope of the model will be limited by the speed and memory of the particular machine. Nevertheless, the input parameters defined below are generally applicable for all versions of the model. These parameters are divided into several groups defining the meteorological conditions, the terrain, the burn conditions and the numerical grid. The specific form of the input will depend on the version of the ALOFT model being used, and the details will accompany the numerical codes. However, suffice it say here that the input list will be limited to about a dozen parameters, most of which pertain to the physical description of the specific problem rather than the numerical algorithm itself. Numerical parameters will be adjustable for those wishing to modify the given default values.

A.1 Burn Input Parameters

The burning rate of the fire is a function of the area of burning surface. The heat release rate and the emission rates of the combustion products are all proportional to the burning rate. These parameters are fuel dependent, and included in a single file that can be expanded to accommodate additional fuels or improved measurements of the properties of the existing fuels. The user need only specify the area of the burning surface (plus the fire’s latitude and longitude for ALOFT-CT).

The heat and smoke generation rates are then calculated based on the characteristics of the fuel included in the data base. A typical entry in the data base is as follows:

NORTH SLOPE CRUDE	Fuel Name
1.76	Heat Release Rate Per Unit Area (MW/m**2)
0.05097	Burning Rate Per Unit Area (kg/s-m**2)
876.	Fuel Density (kg/m**3)
PM10 PARTICULATE	Name of Combustion Product
116. -1.	Emission Factor (g/kg), Molecular Weight
PM2.5 PARTICULATE	.
86. -1.	.
CARBON DIOXIDE	.
2810. 44.	Emission Factor (g/kg), Molecular Weight
CARBON MONOXIDE	.
30. 28.	.
VOC	.
5. -1.	.
SULFUR DIOXIDE	.
25. 64.	.

Heat Release Rate Per Unit Area This is the *convective* heat release rate of the fire per unit area, expressed in units of MW/m². Radiative heat is not considered by the model. For very sooty fires, it is often assumed that about 10% of the total heat release rate is lost to radiation.

Burning Rate Per Unit Area The rate of fuel consumption, expressed in units of kg/s/m².

Fuel Density The density of the unburned fuel in units of kg/m³.

Emission Factors The fraction of the fuel mass converted into whichever combustion product is listed. These are expressed in units of g/kg.

Molecular Weight This is positive if the combustion product is a gas of definable molecular weight. If not, -1 is used to indicate that the concentration should only be reported in terms of its mass density, rather than volume density.

By default, the fuel used in the ALOFT model is Alaska North Slope crude. Other fuel characteristics are listed in Table 10. Notice from this table that the burning characteristics do not vary significantly from fuel to fuel.

Fuel Type	Burning Rate		Heat Release Rate MW/m ²	Smoke Yield g/kg
	kg/s/m ²	bbl/h/ft ²		
Alaska North Slope crude	0.051	0.122	1.76	116
Cook Inlet crude	0.056	0.140	1.94	92
Louisiana crude	0.056	0.140	2.14	120
Alberta Sweet Mixed Blend	0.056	0.140	2.00	150
Number 2 diesel fuel	0.067	0.157	2.34	140

Table 10: Burning characteristics of several heavy hydrocarbon fuels. The values for Louisiana crude and number 2 diesel fuel are based on large scale experiments at the USCG Fire and Safety Test Detachment, Mobile, Alabama. The values for North Slope and Cook Inlet crude are based on 1.2 m pan burns, extrapolated to larger scale [1]. The values for Alberta Sweet Mixed Blend are based on the Newfoundland Offshore Burn Experiment.

A.2 Meteorological Input Parameters

All versions of the ALOFT model make use of a single sounding to describe the vertical stratification of the atmosphere. A convenient method to input this information to the code is through a data format supported by the Forecast Systems Laboratory (FSL) of the National Oceanic and Atmospheric Administration (NOAA) [40]. This laboratory has set up a database of soundings for various locations throughout North America for the years 1946 through 1994, and continues to update the database with more current data. The format for these sounding files is included in at the end of the section. Some of the information contained in the sounding do not apply to the problem. ALOFT-CT utilizes the temperature, wind speed and wind direction profiles, whereas ALOFT-FT only uses the temperature profile. In addition, the user has the ability to override any or all of the sounding profiles by prescribing the following optional parameters:

Wind Speed A constant wind speed (m/s) is required by ALOFT-FT, and optional in ALOFT-CT. In ALOFT-CT, the sounding wind speed profile can be overridden by one of the form

$$u(z) = u_1 \left(\frac{z}{z_1} \right)^p$$

where u_1 is the wind speed at the reference height z_1 , and p is an exponent whose value is on the order of 0.15. For ALOFT-FT, the wind speed ought to be taken at an altitude to which the plume is expected to loft, usually a few hundred meters. Extrapolations of ground level measurements can be made with the above formula.

Lapse Rate A linear lapse rate (°C/m) can override the temperature profile of the sounding.

Wind Direction The prevailing wind direction (degrees) can be specified, overriding the vertical direction profile of the sounding.

Wind Fluctuations These are expressed in terms of the standard deviation of the wind direction from its prevailing direction. Both lateral and vertical deviations are required. These are best obtained with an anemometer whose readings are taken over time periods of the order

of the burn time. The particulate concentrations resulting from the computation can be considered as average values over this time period. Table 11 presents values of the default wind fluctuations.

	Marine	Coastal	Mountain
σ_u (m/s)	0.2	0.4	0.4
σ_v (m/s)	0.5	1.2	1.2
σ_w (m/s)	0.4	1.0	1.0
τ_u (s)	300	300	300
τ_v (s)	300	300	300
τ_w (s)	100	100	100

Table 11: ALOFT Default Dispersion Parameters [10, 30, 12]

A.3 Numerical Grid Parameters

An ALOFT-CT simulation consists of basically two calculations. The first is referred to as the “far-field” calculation and is intended to establish a wind field in the vicinity of the burn. The spatial extent of this calculation is on the order of several tens of kilometers in both the latitudinal and longitudinal directions. The second calculation simulates the plume rise over several kilometers. This calculation is performed with the parabolized equations used in ALOFT-FT. Following is a list of input parameters needed to specify the spatial and temporal bounds of both calculations:

Width of the far-field grid The distance (m) in both the latitudinal and longitudinal directions across the computational grid. It is usually 30,000 to 40,000. Note that this domain is made square for computational convenience.

Height of the far-field grid The altitude (m) of the top of the computational grid. It is usually on the order of 5,000 m.

Height of ground level grid cell of the far-field grid The vertical dimension (m) of the first level of grid cells in the computational grid. The grid is stretched in the vertical direction, allowing for greater spatial resolution at the ground. The lateral dimensions of the cells are uniform.

Grid Dimensions The number of cells in the latitudinal, longitudinal and vertical directions corresponding to the x , y and z axes for the three-dimensional, far-field calculation. For the plume rise calculation, the velocity component along the x -axis (windward direction) is assumed constant, thus only the dimensions for the y - and z -axes (lateral and vertical directions) are needed.

Simulation Time The time in seconds to iterate the time-dependent equations for the far-field calculation. Usually this is on the order of several thousand, *i.e.*, an hour. The plume rise equations are inherently steady-state.

A.4 Processing Results

The details about compilation of the numerical code, computer resources required, *etc.*, will accompany the specific version of the code. The graphical display of results is the most important part of the analysis because the ALOFT model is actually simulating in appreciable detail the plume's interaction with a complex environment. Ground level wind patterns and particulate concentrations cannot be conveyed through a simple chart or table, but rather through a picture. Although most of the numerical algorithm for the ALOFT model was developed at NIST and as a result remains in the public domain, the software required to render the results graphically is not. It is not the intention of NIST to develop on its own these tools, but rather to use either packages that are reasonably priced and widely available, or packages that are not proprietary. The results of the Alaska study presented in this report were produced with NCAR Graphics on a Silicon Graphics UNIX workstation. NCAR Graphics is a product of the Scientific Computing Division of the National Center for Atmospheric Research [47]. This package is relatively inexpensive and used widely in the meteorological as well as many other scientific fields. It is designed primarily for UNIX workstations. Graphical presentation on the PC will depend on the application.

A.5 Forecast Systems Laboratory (FSL) sounding format

The official FSL data format is similar to the format used by the National Severe Storms Forecast Center (NSSFC) in Kansas City. The first 4 lines of the sounding are identification and information lines. All additional lines are data lines. An entry of 32767 indicates that the information is either missing, not reported, or not applicable.

254	HOUR	DAY	MONTH	YEAR	(blank)	(blank)
1	WBAN#	WMO#	LAT	LON	ELEV	RTIME
2	HYDRO	MXWD	TROPL	LINES	TINDEX	SOURCE
3	(blank)	STAID	(blank)	(blank)	SONDE	WSUNITS
9	PRESSURE	HEIGHT	TEMP	DEWPT	WIND DIR	WIND SPD
4						
5						
6						
7						
8						

The integer at the start of each line indicates the function of that particular row of data according to the following codes

254	= indicates a new sounding in the output file
1	= station identification line
2	= sounding checks line
3	= station identifier and other indicators line
4	= mandatory level
5	= significant level
6	= wind level
7	= tropopause level
8	= maximum wind level
9	= surface level

HOUR is the time of report in UTC (Universal Time)

WMO# is the World Meteorological Organization station number
WBAN# is the Weather Bureau, Army, Navy number as assigned by the National Climatic Data Center (NCDC)

LAT is the latitude in degrees and hundredths

LON is the longitude in degrees and hundredths

ELEV is the elevation from station history in meters

RTIME is the actual release time of radiosonde

HYDRO is the pressure of the level to where the sounding passes the hydrostatic check.

MXWD is the pressure of the level having the maximum wind in the sounding. If within the body of the sounding there is no "8" level then MXWN is estimated.

TROPL is the pressure of the level containing the tropopause. If within the body of the sounding there is no "7" level, then TROPL is estimated.

LINES is the number of levels in the sounding, including the 4 identification lines.

TINDEX is an indicator for estimated tropopause. A "7" indicates that sufficient data was available to attempt the estimation; 11 indicates that data terminated and that tropopause is a "suspected" tropopause.

SOURCE 0 = National Climatic Data Center (NCDC)

1 = Atmospheric Environment Service (AES), Canada

2 = National Severe Storms Forecast Center (NSSFC)

3 = GTS or FSL GTS data only

4 = merge of NCDC and GTS data (sources 2,3 merged into sources 0,1)

STAID is the station identification string of 3 capital letters

SONDE is the type of radiosonde code (only reported with GTS data)

10 = VIZ "A" type radiosonde

11 = VIZ "B" type radiosonde

12 = Space Data Corporation (SDC) radiosonde.

WSUNITS is the units for the wind speed

ms = tenths of meters per second

kt = knots

PRESSURE is given in whole millibars (mb)

HEIGHT is given in meters (m)

TEMP is the temperature in tenths of degrees Celsius

DEWPT is the dew point temperature in tenths of a degree Celsius

WIND DIR is the wind direction in degrees

WIND SPD is the wind speed in either knots or tenths of a meter per second

An example of FORTRAN format statements necessary to read output rawinsonde data, according to the line type, is as follows:

```
254      (3i7,6x,a4,i7)
1        (3i7,2f7.2,2i7)
2        (7i7)
3        (i7,3x,a10)
4,5,6,7,8,9 (7i7)
```

Further information on these data files may be found in Reference [40].

B Numerical Method

Both the two-dimensional and the three-dimensional form of the nondimensionalized flow equations derived in Section 4 are very similar in structure, and indeed the algorithm that solves them is equally similar. This section contains a detailed description of both the two-dimensional algorithm used to calculate the plume rise, and the three-dimensional algorithm used to calculate the background wind field.

B.1 ALOFT-FT Algorithm (Plume Rise Calculation for ALOFT-CT)

Equations (27)–(30) constitute a mixed system of partial differential equations, *i.e.*, the equations for the temperature and velocity components are parabolic and the equation for the pressure (derived from the incompressibility condition) is elliptic. The equations and the associated boundary conditions are solved using a relatively simple finite difference technique. The computational domain spanning the crosswind plane is one unit in the vertical direction and (usually) four units in the horizontal direction, representing a physical domain fL units high and $4fL$ units wide. This area is divided into $J \times K$ uniformly sized rectangular cells (preferably square). The horizontal velocity v^* is assigned on the left and right boundaries of each cell, the vertical velocity w^* is assigned at the top and bottom, and the perturbation temperature \tilde{T}^* and pressure \tilde{p}^* are taken at cell centers. This placement of the flow variables leads to a very natural and efficient differencing scheme for the equations. Central differences are used to approximate all spatial derivatives, and the solution is advanced in time (*i.e.* the plume is tracked as it moves downwind) with a second order Runge-Kutta scheme. The particulate concentration (or any other non-reacting combustion product) may be represented by Lagrangian particles that are advected with the flow. Details of the entire procedure will be given in the following sections.

B.1.1 The Energy Equation

The nondimensionalized energy equation describing the evolution of the plume perturbation temperature \tilde{T}^* is given by

$$\frac{\partial \tilde{T}^*}{\partial t^*} + v^* \frac{\partial \tilde{T}^*}{\partial y^*} + w^* \frac{\partial \tilde{T}^*}{\partial z^*} + N^{*2} w^* = \frac{1}{\text{Re Pr}} \left(\frac{\partial^2 \tilde{T}^*}{\partial y^{*2}} + \frac{\partial^2 \tilde{T}^*}{\partial z^{*2}} \right) \quad (42)$$

In the jk th cell of the crosswind plane ($1 \leq j \leq J$ and $1 \leq k \leq K$), this equation is approximated by the discretized form

$$\frac{\partial \tilde{T}^*_{jk}}{\partial t^*} + F_{y^*,jk} + F_{z^*,jk} = \frac{1}{\text{Re Pr}} (\nabla^2 \tilde{T}^*)_{jk} \quad (43)$$

where

$$\begin{aligned} F_{y^*,jk} &= \frac{1}{2} \left(v^*_{jk} \frac{\tilde{T}^*_{j+1,k} - \tilde{T}^*_{jk}}{\delta y^*} + v^*_{j-1,k} \frac{\tilde{T}^*_{jk} - \tilde{T}^*_{j-1,k}}{\delta y^*} \right) \\ F_{z^*,jk} &= \frac{1}{2} \left(w^*_{jk} \frac{\tilde{T}^*_{j,k+1} - \tilde{T}^*_{jk}}{\delta z^*} + w^*_{j,k-1} \frac{\tilde{T}^*_{jk} - \tilde{T}^*_{j,k-1}}{\delta z^*} \right) + N^{*2} \frac{w^*_{jk} + w^*_{j,k-1}}{2} \\ (\nabla^2 \tilde{T}^*)_{jk} &= \frac{\tilde{T}^*_{j+1,k} - 2\tilde{T}^*_{jk} + \tilde{T}^*_{j-1,k}}{\delta y^{*2}} + \frac{\tilde{T}^*_{j,k+1} - 2\tilde{T}^*_{jk} + \tilde{T}^*_{j,k-1}}{\delta z^{*2}} \end{aligned}$$

The horizontal velocity component v_{jk}^* is assigned to the right edge of the jk th cell, $v_{j-1,k}^*$ to the left. Likewise, the vertical velocity component w_{jk}^* is assigned to the top, $w_{j,k-1}^*$ to the bottom. Due to the incompressibility condition the flux terms may be written more simply as

$$F_{y^*,jk} = \frac{v_{jk}^* \tilde{T}_{j+1,k}^* - v_{j-1,k}^* \tilde{T}_{j-1,k}^*}{2\delta y^*}$$

$$F_{z^*,jk} = \frac{w_{jk}^* \tilde{T}_{j,k+1}^* - w_{j,k-1}^* \tilde{T}_{j,k-1}^*}{2\delta z^*} + N_k^{*2} \frac{w_{jk}^* + w_{j,k-1}^*}{2}$$

The term N_k^{*2} is the nondimensionalized Brunt-Väisälä frequency. It is formed by the user specified input temperature profile, suitably interpolated onto the computational grid. The Reynolds number Re is of the order δz^{*-2} , the Prandtl number Pr is of order unity.

The energy equation is initialized by prescribing the perturbation temperature profile in the y - z plane a few fire diameters downwind of the fire. This may be prescribed in any way as long as

$$\sum_{j=1}^J \sum_{k=1}^K \tilde{T}_{jk}^{*0} \delta y^* \delta z^* = \frac{1}{f^3} \quad (44)$$

The superscript “0” indicates the initial distribution of temperature. A reasonable assumption is that \tilde{T}^{*0} assumes a Gaussian profile just downwind of the fire itself

$$\tilde{T}_{jk}^{*0} = \frac{1}{f^3 \beta_y \beta_z \pi} e^{-(y_j^* - y_{*0}^*)^2 / \beta_y^2} e^{-(z_k^* - z_{*0}^*)^2 / \beta_z^2} \quad (45)$$

where (y_{*0}^*, z_{*0}^*) is the center of the plume cross-section, (y_j^*, z_k^*) are the coordinates of the jk th cell, and β_y and β_z represent the cross-section half-widths. It has been observed that the downwind dispersion pattern is not very sensitive to the choice of these initial parameters. The width of the initial plume cross section is taken to be roughly that of the fire.

At the boundaries of the computational domain, the temperature perturbation boundary condition is adiabatic, that is, no temperature gradients are prescribed. This is a reasonable assumption as long as the plume stays well away from the edges of the computational domain.

The quantity \tilde{T}_{jk}^* is advanced in time through a simple second-order Runge-Kutta scheme. This technique is sometimes referred to as a predictor-corrector scheme because the solution is advanced from the n th to the $(n+1)$ th time step by the following two-step process

$$\tilde{T}_{jk}^{*n+1,est} = \tilde{T}_{jk}^{*n} - \delta t^* \left(F_{y^*,jk}^n + F_{z^*,jk}^n - (\nabla^2 \tilde{T}^*)_{jk}^n \right)$$

$$\tilde{T}_{jk}^{*n+1} = .5 \left[\tilde{T}_{jk}^{*n} + \tilde{T}_{jk}^{*n+1,est} - \delta t^* \left(F_{y^*,jk}^{n+1,est} + F_{z^*,jk}^{n+1,est} - (\nabla^2 \tilde{T}^*)_{jk}^{n+1,est} \right) \right]$$

The superscripts on each term indicate that all components of that term be evaluated at that particular time level, thus for example, $F_{y^*,jk}^n$ is evaluated with values of v^{*n} , w^{*n} , and \tilde{T}^{*n} . The superscript “ $n+1, est$ ” indicates that the term is an estimate of the value of that particular quantity at the $(n+1)$ th time step.

B.1.2 The Momentum Equations

The nondimensionalized momentum equations for the velocity components in the crosswind plane derived above for the plume rise approximation are as follows

$$\frac{\partial v^*}{\partial t^*} + v^* \frac{\partial v^*}{\partial y^*} + w^* \frac{\partial v^*}{\partial z^*} + \frac{\partial \tilde{p}^*}{\partial y^*} = \frac{1}{Re} \left(\frac{\partial^2 v^*}{\partial y^{*2}} + \frac{\partial^2 v^*}{\partial z^{*2}} \right) \quad (46)$$

$$\frac{\partial w^*}{\partial t^*} + v^* \frac{\partial w^*}{\partial y^*} + w^* \frac{\partial w^*}{\partial z^*} + \frac{\partial \tilde{p}^*}{\partial z^*} - \tilde{T}^* = \frac{1}{\text{Re}} \left(\frac{\partial^2 w^*}{\partial y^{*2}} + \frac{\partial^2 w^*}{\partial z^{*2}} \right) \quad (47)$$

These equations can be rewritten by making use of the vector identities

$$\nabla^2 \mathbf{u} = \nabla(\nabla \cdot \mathbf{u}) - \nabla \times (\nabla \times \mathbf{u}) \quad (48)$$

$$(\mathbf{u} \cdot \nabla) \mathbf{u} = \nabla \left(\frac{|\mathbf{u}|^2}{2} \right) - \mathbf{u} \times (\nabla \times \mathbf{u}) \quad (49)$$

The term $|\mathbf{u}|^2/2$ can be combined with the perturbation pressure \tilde{p}^* to form a total head $\mathcal{H}^* = |\mathbf{u}|^2/2 + \tilde{p}^*$. Also, the vorticity $\omega = \nabla \times \mathbf{u}$ is a scalar quantity because of the uniform flow in the downwind x direction. The reason for the application of these identities is merely to facilitate the numerical solution of the equations, which are now of the form

$$\begin{aligned} \frac{\partial v^*}{\partial t^*} - v^* \omega + \frac{\partial \mathcal{H}^*}{\partial y^*} &= -\frac{1}{\text{Re}} \frac{\partial \omega}{\partial z^*} \\ \frac{\partial w^*}{\partial t^*} + w^* \omega + \frac{\partial \mathcal{H}^*}{\partial z^*} - \tilde{T}^* &= \frac{1}{\text{Re}} \frac{\partial \omega}{\partial y^*} \end{aligned}$$

The finite differencing scheme for the spatial derivatives is given as

$$\frac{\partial v^*_{jk}}{\partial t^*} + F_{v^*,jk} + \frac{\mathcal{H}^*_{j+1,k} - \mathcal{H}^*_{jk}}{\delta y^*} = 0 \quad (50)$$

$$\frac{\partial w^*_{jk}}{\partial t^*} + F_{w^*,jk} + \frac{\mathcal{H}^*_{j,k+1} - \mathcal{H}^*_{jk}}{\delta z^*} = 0 \quad (51)$$

where

$$\begin{aligned} F_{v^*,jk} &= -\frac{w^*_{j+\frac{1}{2},k} \omega_{jk} + w^*_{j+\frac{1}{2},k-1} \omega_{j,k-1}}{2} + \frac{1}{\text{Re}} \frac{\omega_{jk} - \omega_{j,k-1}}{\delta z^*} \\ F_{w^*,jk} &= \frac{v^*_{j,k+\frac{1}{2}} \omega_{jk} + v^*_{j-1,k+\frac{1}{2}} \omega_{j-1,k}}{2} - \frac{1}{\text{Re}} \frac{\omega_{jk} - \omega_{j-1,k}}{\delta y^*} - \tilde{T}^*_{j,k+\frac{1}{2}} \\ \omega_{jk} &= \frac{w^*_{j+1,k} - w^*_{jk}}{\delta y^*} - \frac{v^*_{j,k+1} - v^*_{jk}}{\delta z^*} \end{aligned}$$

The inclusion of a half to a subscript indicates an average, thus

$$w^*_{j+\frac{1}{2},k} = \frac{w^*_{j+1,k} + w^*_{jk}}{2}$$

Free-slip conditions are prescribed for the tangential component of the velocity at all boundaries, consistent with the uniform wind assumption and spatial resolution of the grid. The boundary condition for the normal component of velocity is associated with the boundary condition for the pressure and will be described in the next section.

The velocity components are advanced from the n th to the $(n+1)$ th time step through the second-order Runge-Kutta scheme

$$v^{*n+1,est}_{jk} = v^{*n}_{jk} - \delta t^* \left(F_{v^*,jk}^n + \frac{\mathcal{H}^{*n}_{j+1,k} - \mathcal{H}^{*n}_{jk}}{\delta y^*} \right) \quad (52)$$

$$w_{jk}^{*n+1,est} = w_{jk}^{*n} - \delta t^* \left(F_{w^*,jk}^n + \frac{\mathcal{H}_{j,k+1}^{*n} - \mathcal{H}_{jk}^{*n}}{\delta z^*} \right) \quad (53)$$

$$v_{jk}^{*n+1} = .5 \left[v_{jk}^{*n} + v_{jk}^{*n+1,est} - \delta t^* \left(F_{v^*,jk}^{n+1,est} + \frac{\mathcal{H}_{j+1,k}^{*n+1,est} - \mathcal{H}_{jk}^{*n+1,est}}{\delta y^*} \right) \right] \quad (54)$$

$$w_{jk}^{*n+1} = .5 \left[w_{jk}^{*n} + w_{jk}^{*n+1,est} - \delta t^* \left(F_{w^*,jk}^{n+1,est} + \frac{\mathcal{H}_{j,k+1}^{*n+1,est} - \mathcal{H}_{jk}^{*n+1,est}}{\delta z^*} \right) \right] \quad (55)$$

The time step δt^* is allowed to vary from one time step to another, based on the CFL condition that roughly states

$$\delta t^* < \frac{\min(\delta y^*, \delta z^*)}{\sqrt{v^{*2} + w^{*2}}} \quad (56)$$

This condition essentially guarantees that a particle in the flow cannot travel more than the width of a grid cell in a single time step.

B.1.3 The Incompressibility Condition

Before the velocity components can be updated, it is necessary to determine the gradient of the total head at the n th time step, as seen in Eqs. (52) and (53), and then repeat the procedure for Eqs. (54) and (55). To see how this is done, consider the momentum equations in the vector-invariant form

$$\frac{\partial \mathbf{u}^*}{\partial t^*} + \mathbf{F}^* + \nabla \mathcal{H}^* = 0 \quad (57)$$

where \mathbf{F}^* denotes the non-linear convection, buoyancy and dissipative terms. Taking the divergence of this equation yields a Poisson equation for the total head

$$\nabla^2 \mathcal{H}^* = -\nabla \cdot \mathbf{F}^* \quad (58)$$

Notice that the incompressibility condition is asserted here because the time derivative of the velocity divergence is zero. In discretized form, the Poisson equation for the total head is given as

$$\begin{aligned} \frac{\mathcal{H}_{j+1,k}^* - 2\mathcal{H}_{jk}^* + \mathcal{H}_{j-1,k}^*}{\delta y^{*2}} + \frac{\mathcal{H}_{j,k+1}^* - 2\mathcal{H}_{jk}^* + \mathcal{H}_{j,k-1}^*}{\delta z^{*2}} = \\ - \frac{F_{v^*,jk} - F_{v^*,j-1,k}}{\delta y^*} - \frac{F_{w^*,jk} - F_{w^*,j,k-1}}{\delta z^*} \end{aligned} \quad (59)$$

Equation (58) is solved with a very efficient direct Poisson solver that exploits the uniform gridding of the computational domain through the use of Fast Fourier Transforms (FFTs) [48]. The lack of a superscript implies that all quantities are to be evaluated at the same time level. The boundary conditions for this elliptic equation are mixed. At the ground, the condition

$$\frac{\mathcal{H}_{j,1}^* - \mathcal{H}_{j,0}^*}{\delta z^*} = -F_{w^*,j,0}$$

is enforced, consistent with the fact that the vertical component of velocity w^* is zero at the ground. At the top and side boundaries, the pressure is assumed to be at its ambient value, thus the perturbation pressure is assumed to be zero. According to the steady state form of Bernoulli's theorem, the total head \mathcal{H}^* does not change along streamlines. Thus for outgoing flow, $\mathcal{H}^* = |\mathbf{u}^*|/2$, and for incoming flow, $\mathcal{H}^* = 0$.

B.1.4 Particle Tracking

As the velocity field evolves in the crosswind plane, the trajectories of the Lagrangian particles that are used to represent the particulate matter are computed. The particles are introduced into the flow at the start of the calculation and advected with the induced flow, given by the velocity field $(U, v + v', w + w')$, which has been suitably nondimensionalized. The initial distribution of particles in the crosswind plane mimics the initial temperature perturbation, where the particulate density ρ_p is prescribed so that

$$\int_{-\infty}^{\infty} \int_0^{\infty} U \rho_p dz dy = M \quad (60)$$

where M is the steady-state mass flux of particulate matter (or any other non-reacting combustion product). The quantity ρ_p is nondimensionalized

$$\rho_p = \frac{fM}{UL^2} \rho_p^* \quad (61)$$

so that Eq. (60) is now nondimensionalized

$$\sum_{j=1}^J \sum_{k=1}^K \rho_{p,jk}^* \delta y^* \delta z^* = \frac{1}{f^3} \quad (62)$$

Again the scale factor f indicates that it may be necessary to rescale the variables to contain the plume within the limits of the computational domain.

The total mass delivered to the jk th cell at the n th time level is given by the summation of the masses of all those particles within one cell width of the center of the cell. Thus, for the jk th cell a particle within one cell width of the center contributes a fraction of its mass to that cell, so that the particulate density of that cell may be expressed as the sum of the contributions of all particles in the neighborhood

$$\rho_{p,jk}^* = \sum (1 - r_{y^*})(1 - r_{z^*}) \frac{1/f^3}{N_p \delta y^* \delta z^*} \quad (63)$$

where N_p is the total number of particles representing the plume cross-section, and r_{y^*} and r_{z^*} are the lateral and vertical distances from the cell center, expressed as fractions of the cell dimensions.

The particles are advected with the flow according to the simple Runge-Kutta scheme that is used to advance the solution of the governing hydrodynamic equations. Briefly, the average of the velocity at the start and at the end of a time step is used to update the particle position. A random perturbation is applied to each particle position to mimic the temporal and spatial variation of the prevailing winds. This procedure has been described in Section 4.4.

B.2 ALOFT-CT Wind Field Calculation

The solution methodology introduced in the previous section applies equally well to the fully three-dimensional form of the governing equations (14)–(18). The scalings used to derive these nondimensionalized equations from the Boussinesq form of the governing equations are different, however. The length and time scales are no longer tied to the fire size, but rather to the background atmosphere. Indeed, the fire has no role at all in establishing the background atmosphere. The height of the computational domain is now fixed at some altitude well above the height to which

the plume is expected to loft, usually about 5 km. The longitudinal and latitudinal extent of the domain is usually set to about 30 km. This area is divided into $I \times J \times K$ rectangular cells, uniformly spaced in the horizontal directions, with the vertical spacing increasing with altitude so as to concentrate the grid near the terrain surface. The terrain is introduced into the flow field by “blocking” off cells that correspond to terrain features such as hills and mountains. The terrain data is available for Alaska at 3 arc second resolution, or roughly 100 m. In the three-dimensional calculations, the grid cells are on the order of several hundred meters in width, and tens of meters in height.

At the side boundaries of the domain, ambient winds are prescribed, based on sounding data. The x^* -axis is aligned with lines of constant latitude, the y^* -axis is aligned with lines of constant longitude, and the z^* -axis is aligned with the vertical. As before, velocity components are prescribed at their respective faces of each computational cell, while the scalar quantities defining the perturbation temperature and pressure are prescribed at cell centers. Central differences are used to approximate all spatial derivatives, and the solution is advanced in time with the same second order Runge-Kutta scheme as before. The solution is advanced in time until a wind field is established. Due to the periodic shedding of vortices from the terrain obstacles, a true “steady-state” is never achieved. However, after a few hours worth of simulated time advancement, the computed wind field certainly meets the criteria of a time-averaged solution to the equations.

B.2.1 The Energy Equation

The equation for the nondimensionalized temperature perturbation is as follows

$$\frac{\partial \tilde{T}^*}{\partial t^*} + u^* \frac{\partial \tilde{T}^*}{\partial x^*} + v^* \frac{\partial \tilde{T}^*}{\partial y^*} + w^* \frac{\partial \tilde{T}^*}{\partial z^*} + N^{2*} w^* = \frac{1}{\text{Re Pr}} \left(\frac{\partial^2 \tilde{T}^*}{\partial x^{*2}} + \frac{\partial^2 \tilde{T}^*}{\partial y^{*2}} + \frac{\partial^2 \tilde{T}^*}{\partial z^{*2}} \right) \quad (64)$$

The spatial terms of this equation are approximated at the ijk th cell center as follows

$$\begin{aligned} u^* \frac{\partial \tilde{T}^*}{\partial x^*} &\approx \frac{1}{2} \left[u^*_{ijk} \frac{\tilde{T}^*_{i+1,jk} - \tilde{T}^*_{ijk}}{\delta x^*} + u^*_{i-1,jk} \frac{\tilde{T}^*_{ijk} - \tilde{T}^*_{i-1,jk}}{\delta x^*} \right] \\ v^* \frac{\partial \tilde{T}^*}{\partial y^*} &\approx \frac{1}{2} \left[v^*_{ijk} \frac{\tilde{T}^*_{i,j+1,k} - \tilde{T}^*_{ijk}}{\delta y^*} + v^*_{i,j-1,k} \frac{\tilde{T}^*_{ijk} - \tilde{T}^*_{i,j-1,k}}{\delta y^*} \right] \\ w^* \frac{\partial \tilde{T}^*}{\partial z^*} &\approx \frac{1}{2} \left[w^*_{ijk} \frac{\tilde{T}^*_{i,j,k+1} - \tilde{T}^*_{ijk}}{\delta z^*} + w^*_{ij,k-1} \frac{\tilde{T}^*_{ijk} - \tilde{T}^*_{ij,k-1}}{\delta z^*} \right] \\ N^{2*} w^* &\approx N^{2*}_k \frac{w^*_{ijk} + w^*_{ij,k-1}}{2} \\ \frac{\partial^2 \tilde{T}^*}{\partial x^{*2}} + \frac{\partial^2 \tilde{T}^*}{\partial y^{*2}} + \frac{\partial^2 \tilde{T}^*}{\partial z^{*2}} &\approx \frac{\tilde{T}^*_{i+1,jk} - 2\tilde{T}^*_{ijk} + \tilde{T}^*_{i-1,jk}}{\delta x^{*2}} \\ &\quad + \frac{\tilde{T}^*_{i,j+1,k} - 2\tilde{T}^*_{ijk} + \tilde{T}^*_{i,j-1,k}}{\delta y^{*2}} + \frac{\tilde{T}^*_{ij,k+1} - 2\tilde{T}^*_{ijk} + \tilde{T}^*_{ij,k-1}}{\delta z^{*2}} \end{aligned}$$

The perturbation temperature at some time step n is advanced in time by δt^* to time step $n + 1$ with the two step predictor-corrector scheme (2nd order Runge-Kutta)

$$\tilde{T}^*_{ijk,n+1,est} = \tilde{T}^*_{ijk,n} - \delta t^* \left(\mathbf{u}^{*,n} \cdot \nabla \tilde{T}^{*,n} - \frac{1}{\text{Re Pr}} \nabla^2 \tilde{T}^{*,n} \right)$$

$$\tilde{T}_{ijk}^{*,n+1} = \frac{1}{2} \left(\tilde{T}_{ijk}^{*,n} + \tilde{T}_{ijk}^{*,n+1,est} - \delta t^* \left(\mathbf{u}^{*,n+1,est} \cdot \nabla \tilde{T}^{*,n+1,est} - \frac{1}{\text{Re Pr}} \nabla^2 \tilde{T}^{*,n+1,est} \right) \right)$$

Adiabatic boundary conditions are applied at solid surfaces (*i.e.* the ground), and also at the edges of the computational domain. This means that gradients in the perturbation temperature are set to zero at all computational boundaries.

B.2.2 The Momentum Equations

The nondimensionalized momentum equations are

$$\begin{aligned} \frac{\partial u^*}{\partial t^*} + u^* \frac{\partial u^*}{\partial x^*} + v^* \frac{\partial u^*}{\partial y^*} + w^* \frac{\partial u^*}{\partial z^*} + \frac{\partial \tilde{p}^*}{\partial x^*} &= \frac{1}{\text{Re}} \left(\frac{\partial^2 u^*}{\partial x^{*2}} + \frac{\partial^2 u^*}{\partial y^{*2}} + \frac{\partial^2 u^*}{\partial z^{*2}} \right) \\ \frac{\partial v^*}{\partial t^*} + u^* \frac{\partial v^*}{\partial x^*} + v^* \frac{\partial v^*}{\partial y^*} + w^* \frac{\partial v^*}{\partial z^*} + \frac{\partial \tilde{p}^*}{\partial y^*} &= \frac{1}{\text{Re}} \left(\frac{\partial^2 v^*}{\partial x^{*2}} + \frac{\partial^2 v^*}{\partial y^{*2}} + \frac{\partial^2 v^*}{\partial z^{*2}} \right) \\ \frac{\partial w^*}{\partial t^*} + u^* \frac{\partial w^*}{\partial x^*} + v^* \frac{\partial w^*}{\partial y^*} + w^* \frac{\partial w^*}{\partial z^*} + \frac{\partial \tilde{p}^*}{\partial z^*} - \tilde{T}^* &= \frac{1}{\text{Re}} \left(\frac{\partial^2 w^*}{\partial x^{*2}} + \frac{\partial^2 w^*}{\partial y^{*2}} + \frac{\partial^2 w^*}{\partial z^{*2}} \right) \end{aligned}$$

The vector identities given by Eqs. (48) and (49) are applied to these equations as before to simplify the spatial differencing. The momentum equations are rewritten

$$\begin{aligned} \frac{\partial u^*}{\partial t^*} - v^* \omega_{z^*}^* + w^* \omega_{y^*}^* + \frac{\partial \mathcal{H}^*}{\partial x^*} &= \frac{1}{\text{Re}} \left(\frac{\partial \omega_{y^*}^*}{\partial z^*} - \frac{\partial \omega_{z^*}^*}{\partial y^*} \right) \\ \frac{\partial v^*}{\partial t^*} + u^* \omega_{z^*}^* - w^* \omega_{x^*}^* + \frac{\partial \mathcal{H}^*}{\partial y^*} &= \frac{1}{\text{Re}} \left(\frac{\partial \omega_{x^*}^*}{\partial z^*} - \frac{\partial \omega_{z^*}^*}{\partial x^*} \right) \\ \frac{\partial w^*}{\partial t^*} + v^* \omega_{x^*}^* - u^* \omega_{y^*}^* + \frac{\partial \mathcal{H}^*}{\partial z^*} - \tilde{T}^* &= \frac{1}{\text{Re}} \left(\frac{\partial \omega_{y^*}^*}{\partial x^*} - \frac{\partial \omega_{x^*}^*}{\partial y^*} \right) \end{aligned}$$

Notice that the total pressure $\mathcal{H}^* = |\mathbf{u}^*|^2/2 + \tilde{p}^*$. The components of the vorticity are given by

$$\omega_{x^*}^* = \frac{\partial w^*}{\partial y^*} - \frac{\partial v^*}{\partial z^*} \quad \omega_{y^*}^* = \frac{\partial u^*}{\partial z^*} - \frac{\partial w^*}{\partial x^*} \quad \omega_{z^*}^* = \frac{\partial v^*}{\partial x^*} - \frac{\partial u^*}{\partial y^*}$$

The spatial differencing applied at each respective cell face is as follows

$$\begin{aligned} \frac{\partial u_{ijk}^*}{\partial t} + F_{x^*,ijk} + \frac{\mathcal{H}_{i+1,jk}^* - \mathcal{H}_{ijk}^*}{\delta x^*} &= 0 \\ \frac{\partial v_{ijk}^*}{\partial t} + F_{y^*,ijk} + \frac{\mathcal{H}_{i,j+1,k}^* - \mathcal{H}_{ijk}^*}{\delta y^*} &= 0 \\ \frac{\partial w_{ijk}^*}{\partial t} + F_{z^*,ijk} + \frac{\mathcal{H}_{ij,k+1}^* - \mathcal{H}_{ijk}^*}{\delta z^*} &= 0 \end{aligned}$$

where

$$F_{x^*,ijk} = -\frac{1}{2} (v_{i+\frac{1}{2},jk}^* \omega_{z^*,ijk}^* + v_{i+\frac{1}{2},j-1,k}^* \omega_{z^*,i,j-1,k}^*) + \frac{1}{2} (w_{i+\frac{1}{2},jk}^* \omega_{y^*,ijk}^* + w_{i+\frac{1}{2},j,k-1}^* \omega_{y^*,ij,k-1}^*)$$

$$\begin{aligned}
& -\frac{1}{\text{Re}} \left(\frac{\omega_{y^*,ijk}^* - \omega_{y^*,ijk}^*}{\delta z^*} - \frac{\omega_{z^*,ijk}^* - \omega_{z^*,ijk}^*}{\delta y^*} \right) \\
F_{y^*,ijk} &= \frac{1}{2} (u_{i,j+\frac{1}{2},k}^* \omega_{z^*,ijk}^* + u_{i-1,j-\frac{1}{2},k}^* \omega_{z^*,i-1,jk}^*) - \frac{1}{2} (w_{i,j+\frac{1}{2},k}^* \omega_{x^*,ijk}^* + w_{i,j+\frac{1}{2},k-1}^* \omega_{x^*,ijk-1}^*) \\
& -\frac{1}{\text{Re}} \left(\frac{\omega_{x^*,ijk}^* - \omega_{x^*,ijk-1}^*}{\delta z^*} - \frac{\omega_{z^*,ijk}^* - \omega_{z^*,i-1,jk}^*}{\delta x^*} \right) \\
F_{z^*,ijk} &= \frac{1}{2} (v_{ij,k+\frac{1}{2}}^* \omega_{x^*,ijk}^* + v_{i,j-1,k+\frac{1}{2}}^* \omega_{x^*,i,j-1,k}^*) - \frac{1}{2} (u_{ij,k+\frac{1}{2}}^* \omega_{y^*,ijk}^* + u_{i-1,j,k+\frac{1}{2}}^* \omega_{y^*,i-1,jk}^*) \\
& -\frac{\tilde{T}_{ij,k+1} + \tilde{T}_{ijk}}{2} - \frac{1}{\text{Re}} \left(\frac{\omega_{y^*,ijk}^* - \omega_{y^*,i-1,jk}^*}{\delta x^*} - \frac{\omega_{x^*,ijk}^* - \omega_{x^*,i,j-1,k}^*}{\delta y^*} \right) \\
\omega_{x^*,ijk}^* &= \frac{w_{i,j+1,k}^* - w_{ijk}^*}{\delta y^*} - \frac{v_{ij,k+1}^* - v_{ijk}^*}{\delta z^*} \\
\omega_{y^*,ijk}^* &= \frac{u_{ij,k+1}^* - u_{ijk}^*}{\delta z^*} - \frac{w_{i+1,jk}^* - w_{ijk}^*}{\delta x^*} \\
\omega_{z^*,ijk}^* &= \frac{v_{i+1,jk}^* - v_{ijk}^*}{\delta x^*} - \frac{u_{i,j+1,k}^* - u_{ijk}^*}{\delta y^*}
\end{aligned}$$

Again, the subscript $i + \frac{1}{2}$ indicates that the variable is an average of its values at the i th and the $(i + 1)$ th cell.

The advancement in time of the velocity components is identical to that of the temperature perturbation. In addition, free-slip boundary conditions are applied at solid surfaces. This choice of boundary condition reflects the relative coarseness of the numerical grid and the fact that atmospheric turbulence is introduced into the problem by randomly perturbing the Lagrangian particles that represent the combustion products rather than by directly simulating surface friction.

The time step δt^* is determined by the CFL condition

$$\delta t^* < \frac{1}{\max \left(\frac{u_{i-\frac{1}{2},jk}^*}{\delta x^*}, \frac{v_{i,j-\frac{1}{2},k}^*}{\delta y^*}, \frac{w_{ij,k-\frac{1}{2}}^*}{\delta z^*} \right)} \quad (65)$$

This condition essentially states that a particle cannot traverse more than the width of a grid cell in a single time step. In practice, the time step is on the order of about 10 seconds. The estimated velocity components are tested at each time step to ensure that the above condition is satisfied. If it is not, then the time step is reduced by 75% and the estimated velocity components are recomputed (and checked again).

B.2.3 The Incompressibility Condition

The incompressibility condition

$$\frac{\partial u^*}{\partial x^*} + \frac{\partial v^*}{\partial y^*} + \frac{\partial w^*}{\partial z^*} = 0 \quad (66)$$

when applied to the momentum equations yields a Poisson equation for the total pressure \mathcal{H}^*

$$\nabla^2 \mathcal{H}^* = -\nabla \cdot \mathbf{F} \quad (67)$$

which in discretized form is written

$$\begin{aligned} & \frac{\mathcal{H}^*_{i+1,jk} - 2\mathcal{H}^*_{ijk} + \mathcal{H}^*_{i-1,jk}}{\delta x^{*2}} + \frac{\mathcal{H}^*_{i,j+1,k} - 2\mathcal{H}^*_{ijk} + \mathcal{H}^*_{i,j-1,k}}{\delta y^{*2}} + \frac{\mathcal{H}^*_{ij,k+1} - 2\mathcal{H}^*_{ijk} + \mathcal{H}^*_{ij,k-1}}{\delta z^{*2}} \\ &= -\frac{F_{x^*,ijk} - F_{x^*,i-1,jk}}{\delta x^*} - \frac{F_{y^*,ijk} - F_{y^*,i,j-1,k}}{\delta y^*} - \frac{F_{z^*,ijk} - F_{z^*,ij,k-1}}{\delta z^*} \end{aligned}$$

The lack of a superscript implies that all quantities are to be evaluated at time level n . This equation is solved with a fast Poisson solver [48]. For external boundaries (for example at $x^* = 0$), the Poisson solver is given the boundary condition

$$\frac{\mathcal{H}^*_{1,jk} - \mathcal{H}^*_{0,jk}}{\delta x^*} = -F_{x^*,0,jk} - \left(\frac{\partial u_0(z, t)}{\partial t} \right)^*_{jk}$$

where the function $u_0(z, t)$ represents the latitudinal component of the prevailing wind profile, $U(z)$. It is given by

$$u_0(z, t) = -U(z) \tanh(t/\tau) \sin \alpha \quad (68)$$

where τ is a ramp-up time for the wind velocity, usually on the order of a few tens of seconds, and α is the prevailing wind direction. The reason for the ramp-up of the ambient winds is that the algorithm requires a zero-velocity initial condition throughout the domain because of the presence of the terrain obstacles. As the velocity at the boundaries ramps up to its prescribed value, the proper flow field is established throughout the domain.

At the terrain surface, the normal component of velocity is forced to remain zero by setting the normal component of the pressure gradient plus the flux term F equal to zero. Specifically, the normal component of F at the terrain surface takes on the value

$$F_n = -\frac{\partial \mathcal{H}^*}{\partial n} + \beta u_n$$

where $\beta = 0.8/\delta t^*$ and the total head is taken from the last iteration. This procedure ensures that the normal component of velocity at the ground (or mountain side) remains nearly zero. The error incurred by the relaxation scheme is several orders of magnitude less than the velocity itself. This accuracy is satisfactory, given the fact that the terrain is being approximated by rectangular blocks.

B.2.4 Particle Tracking

The Lagrangian particles representing combustion products that were introduced in the plume rise phase of the calculation continue to be tracked by the larger scale three-dimensional wind field. The position $\mathbf{x} = (x^*, y^*, z^*)$ of each particle is governed by the equation

$$\frac{d\mathbf{x}}{dt} = \mathbf{u} \quad (69)$$

The particle positions are updated according to the same Runge-Kutta scheme which is applied to the other flow quantities. The concentration of the pollutant in any given computational cell is simply given by the expression

$$\rho_{ijk} = \frac{M}{N_p} \frac{\sum t_p}{\delta V_{ijk}} \quad (70)$$

where M is the mass flux of the combustion product of interest, N_p is the number of particles representing that mass, t_p is the amount of time spent by each particle in the ijk th cell, δV_{ijk} is the volume of the cell, and the summation is over those particles which pass through the cell. An example of this procedure is as follows: Suppose that $N_p = 10,000$ particles are launched to represent $M = 1$ kg/s of smoke generated by the fire. If 100 of these particles pass through a volume which is 100 m on a side, and the residence time of each particle is $t_p = 20$ s, then the average concentration of particulate in that cell is given as

$$\frac{1 \text{ kg/s}}{10,000 \text{ part.}} \cdot \frac{100 \text{ part.} \times 20 \text{ s}}{1 \times 10^6 \text{ m}^3} = 2 \times 10^{-7} \text{ kg/m}^3$$

This, of course, is equivalent to $200 \mu\text{g/m}^3$.

C Additional Results and Flat Terrain Wind Speed/Lapse Rate Charts

On the following pages are the flat terrain wind speed/lapse rate diagrams for a variety of burn sizes and levels of atmospheric turbulence (*i.e.* land versus marine). In addition, ALOFT-CT calculations are included for some of the areas studied above, but with a variety of different meteorological conditions applied.

- Figures 42–44 present flat terrain wind speed/lapse rate diagrams for fires consuming 1,000, 2,000, and 500 bbl/h, respectively.
- Figures 45–56 present footprints of twelve simulated smoke plumes originating in the Valdez Narrows. These simulations are intended to demonstrate the effect of various meteorological conditions on downwind dispersion.
- Figures 57–62 present footprints of six simulated smoke plumes originating at the Trans-Alaska Pipeline just west of Fairbanks. The fires each consume 1,000 bbl/h ANS crude. Again, these demonstrate the effect of different meteorological conditions.
- Figures 63–68 present the results of six simulations of burns involving six distinct fires, each fire consuming 1,000 bbl/h ANS crude and originating near the Valdez Marine Terminal.

FLAT TERRAIN, GROUND LEVEL PARTICULATE CONCENTRATION FOR VARIOUS METEOROLOGICAL CONDITIONS

BURN SIZE 1336 MW

SMOKE GENERATION RATE 4.5 kg/s

LATERAL VELOCITY STANDARD DEVIATION 1.2 m/s

VERTICAL VELOCITY STANDARD DEVIATION 1.0 m/s

CRITICAL CONCENTRATION 150 $\mu\text{g}/\text{m}^3$

SOLID LINES INDICATE DOWNWIND DISTANCE (km); SHORT DASHES MAXIMUM CONCENTRATION ($\mu\text{g}/\text{m}^3$); LONG DASHES EXTENT OF CRITICAL CONCENTRATION (km)

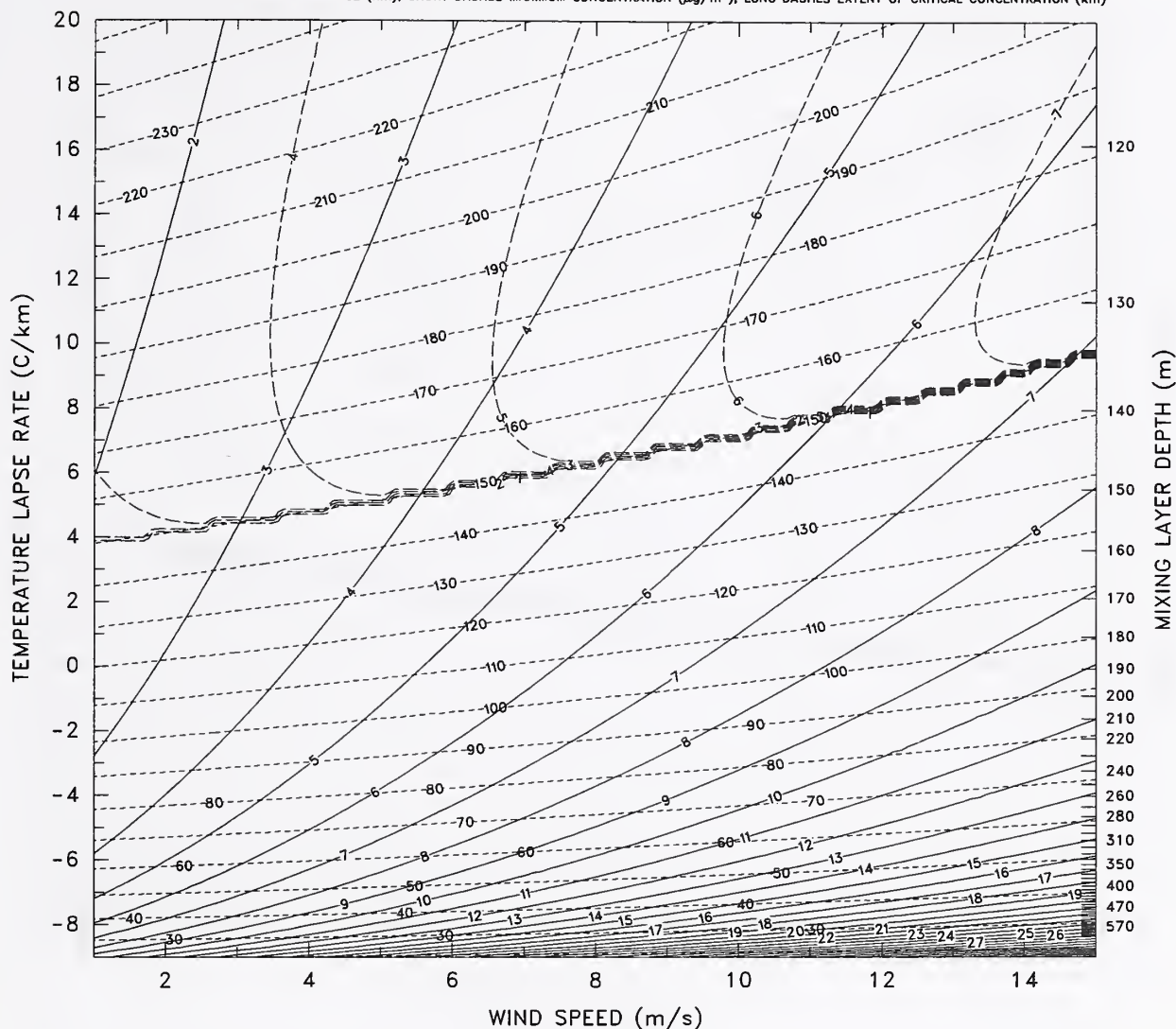


Figure 42: Correlated ALOFT-FT results for a fire generating 1336 MW with typical over-land wind fluctuations. This fire size corresponds to a 760 m² burn of ANS crude consuming 1,000 bbl/h. This single fire has been used as a base line case for many of the simulations in this report.

FLAT TERRAIN, GROUND LEVEL PARTICULATE CONCENTRATION FOR VARIOUS METEOROLOGICAL CONDITIONS

BURN SIZE 2672 MW

SMOKE GENERATION RATE 9.0 kg/s

LATERAL VELOCITY STANDARD DEVIATION 1.2 m/s

VERTICAL VELOCITY STANDARD DEVIATION 1.0 m/s

CRITICAL CONCENTRATION $150 \mu\text{g}/\text{m}^3$

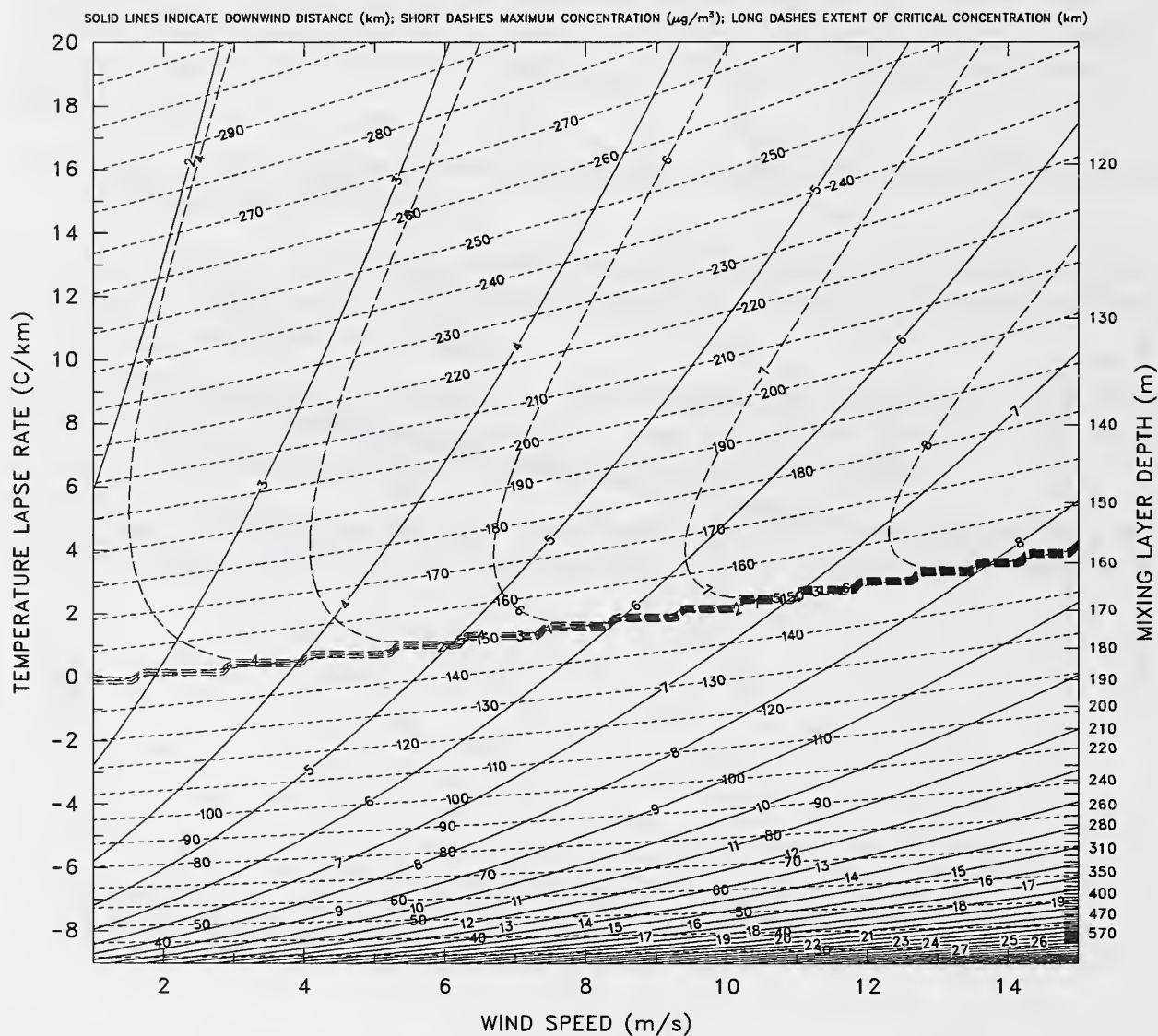


Figure 43: Correlated ALOFT-FT results for a fire generating 2672 MW with typical over-land wind fluctuations. This fire size corresponds to a $1,520 \text{ m}^2$ burn of ANS crude consuming 2,000 bbl/h.

FLAT TERRAIN, GROUND LEVEL PARTICULATE CONCENTRATION
FOR VARIOUS METEOROLOGICAL CONDITIONS

BURN SIZE 668 MW

SMOKE GENERATION RATE 2.2 kg/s

LATERAL VELOCITY STANDARD DEVIATION 1.2 m/s

VERTICAL VELOCITY STANDARD DEVIATION 1.0 m/s

CRITICAL CONCENTRATION $150 \mu\text{g}/\text{m}^3$

SOLID LINES INDICATE DDWNWIND DISTANCE (km); SHORT DASHES MAXIMUM CONCENTRATION ($\mu\text{g}/\text{m}^3$); LONG DASHES EXTENT OF CRITICAL CONCENTRATION (km)

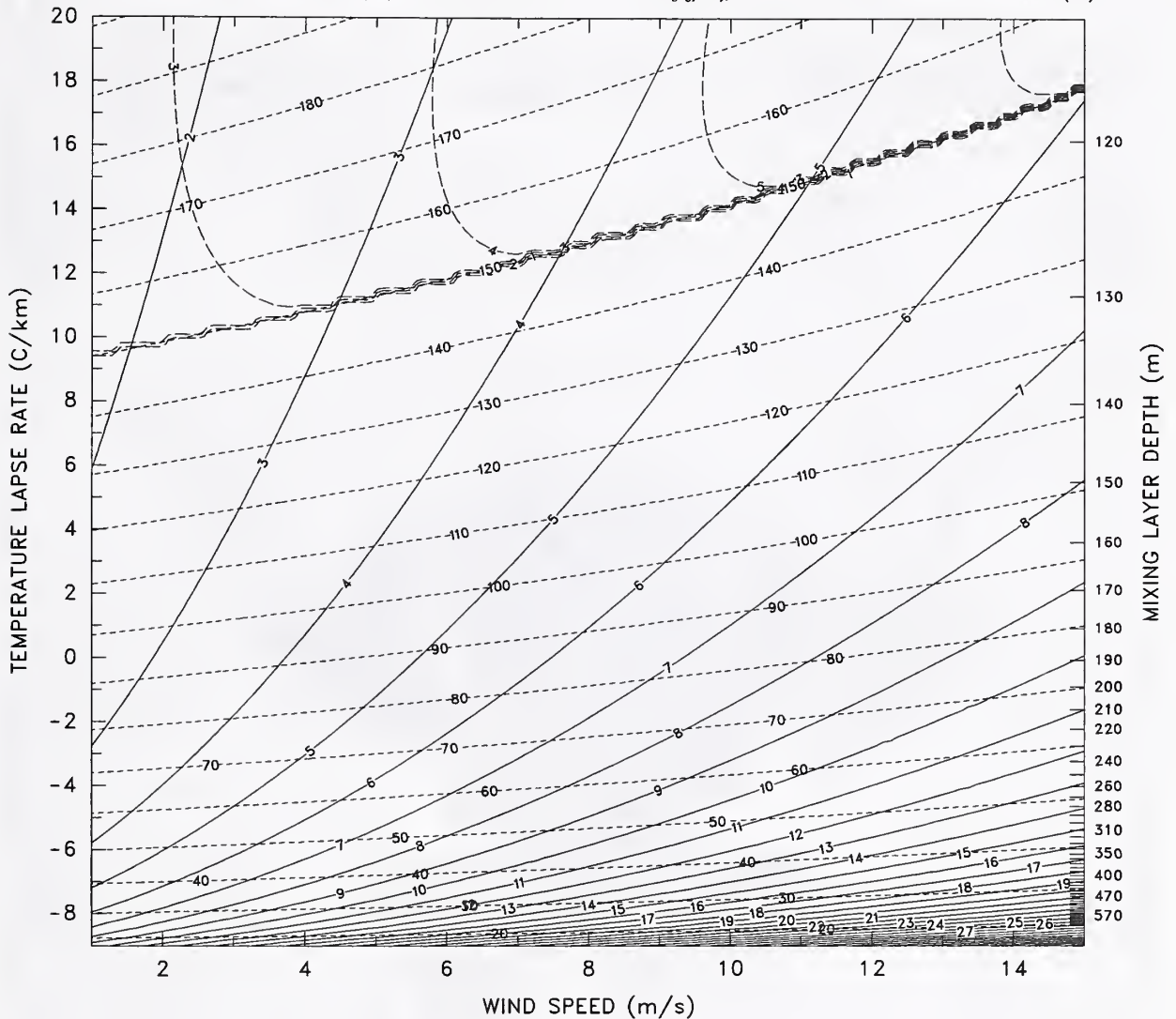


Figure 44: Correlated ALOFT-FT results for a fire generating 668 MW with typical overland wind fluctuations. This fire size corresponds to a 380 m^2 burn of ANS crude consuming 500 bbl/h.

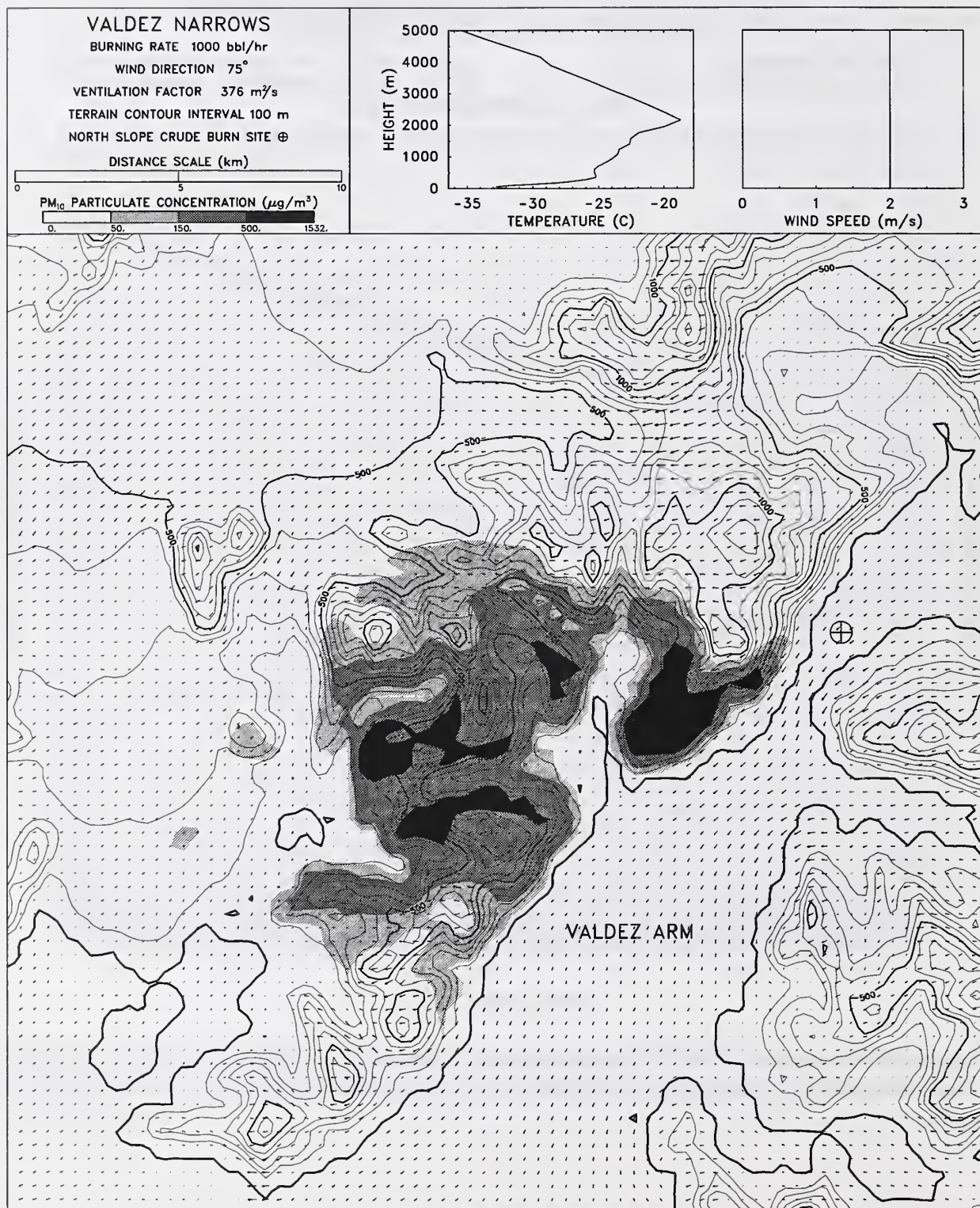


Figure 45: Footprint of simulated smoke plume originating in the Valdez Narrows. This simulation is first in a series of twelve to evaluate the role of different meteorological conditions on downwind dispersion.

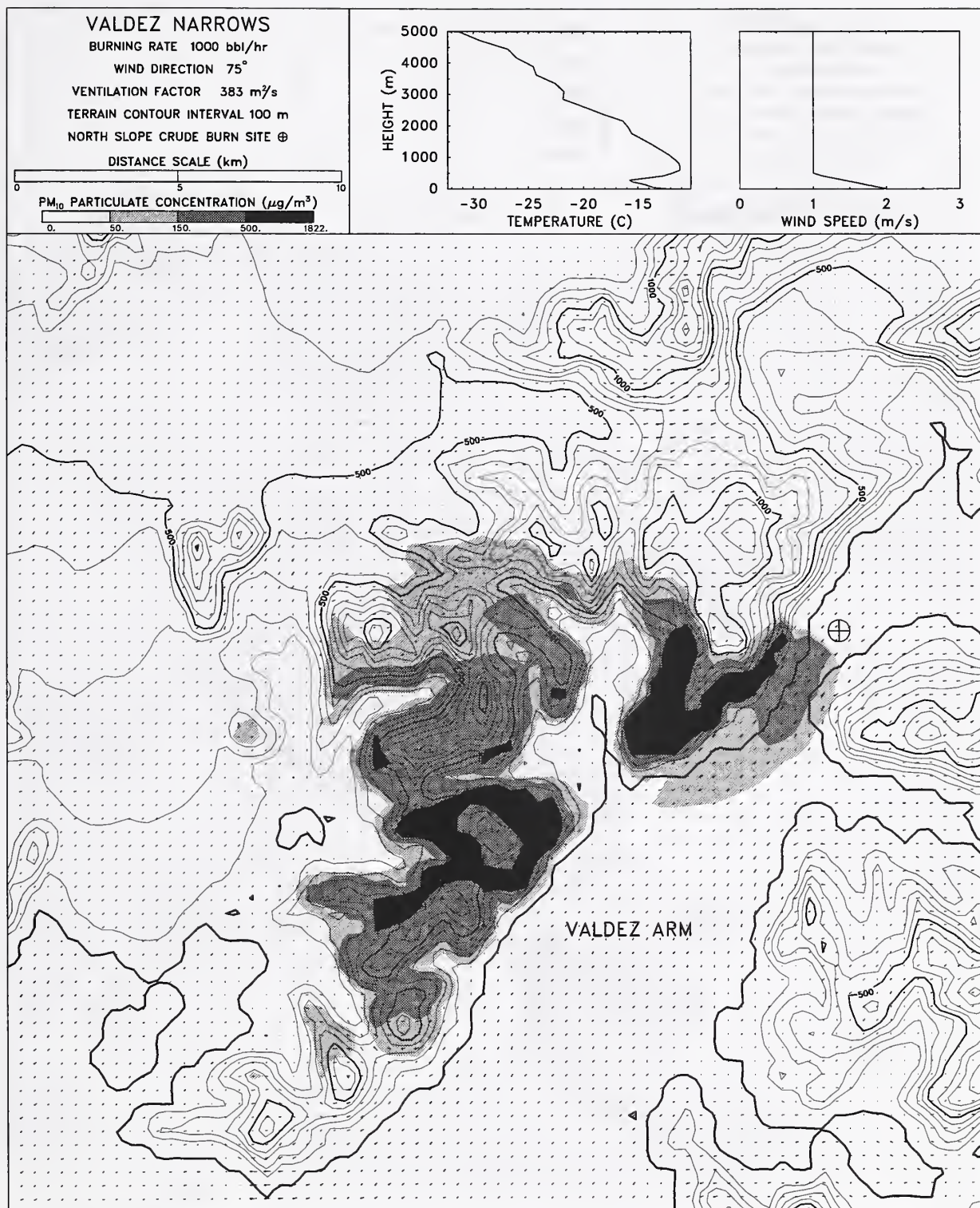


Figure 46: Footprint of simulated smoke plume originating in the Valdez Narrows. This simulation is second in a series of twelve to evaluate the role of different meteorological conditions on downwind dispersion.

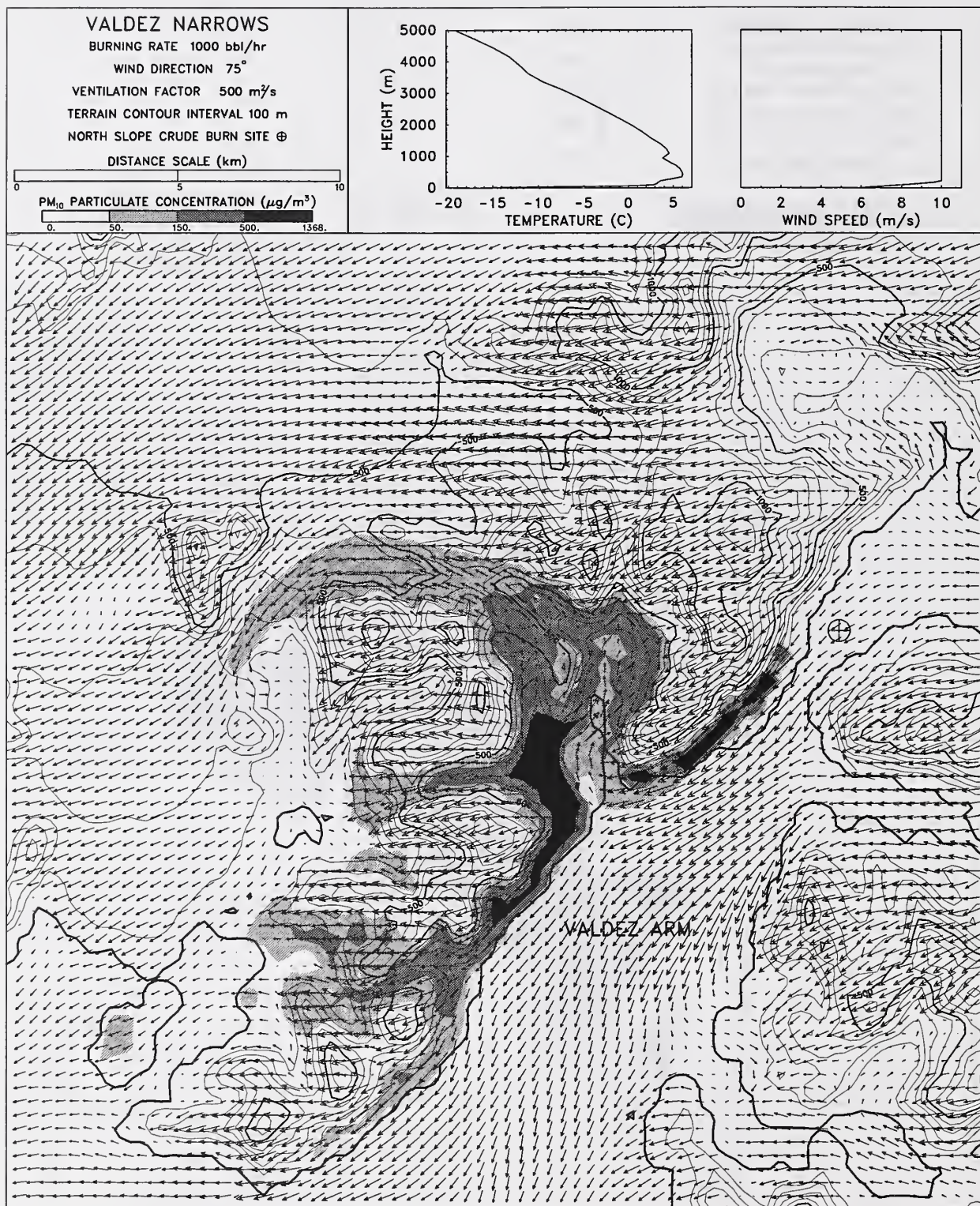


Figure 47: Footprint of simulated smoke plume originating in the Valdez Narrows. This simulation is third in a series of twelve to evaluate the role of different meteorological conditions on downwind dispersion.

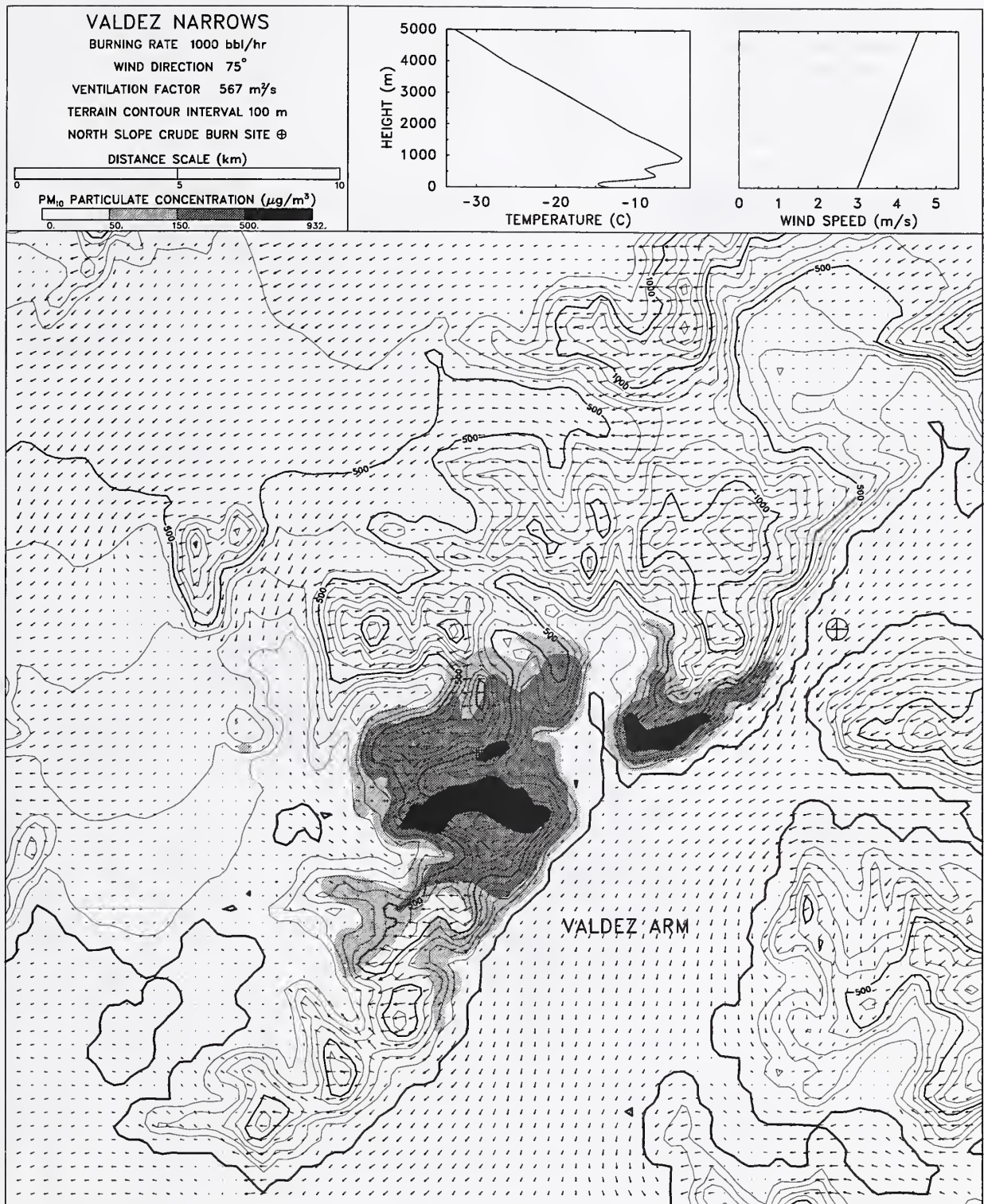


Figure 48: Footprint of simulated smoke plume originating in the Valdez Narrows. This simulation is fourth in a series of twelve to evaluate the role of different meteorological conditions on downwind dispersion.

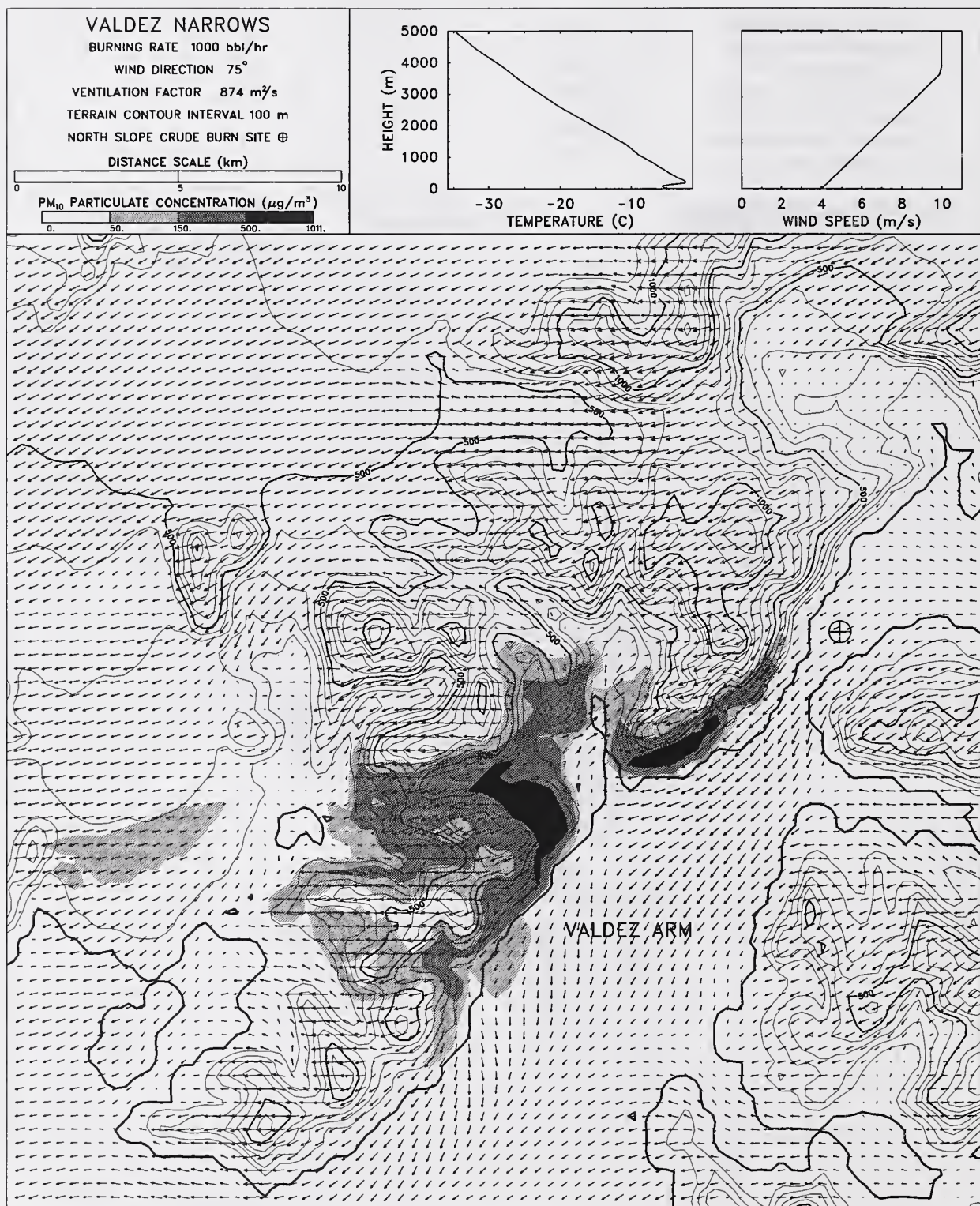


Figure 49: Footprint of simulated smoke plume originating in the Valdez Narrows. This simulation is fifth in a series of twelve to evaluate the role of different meteorological conditions on downwind dispersion.

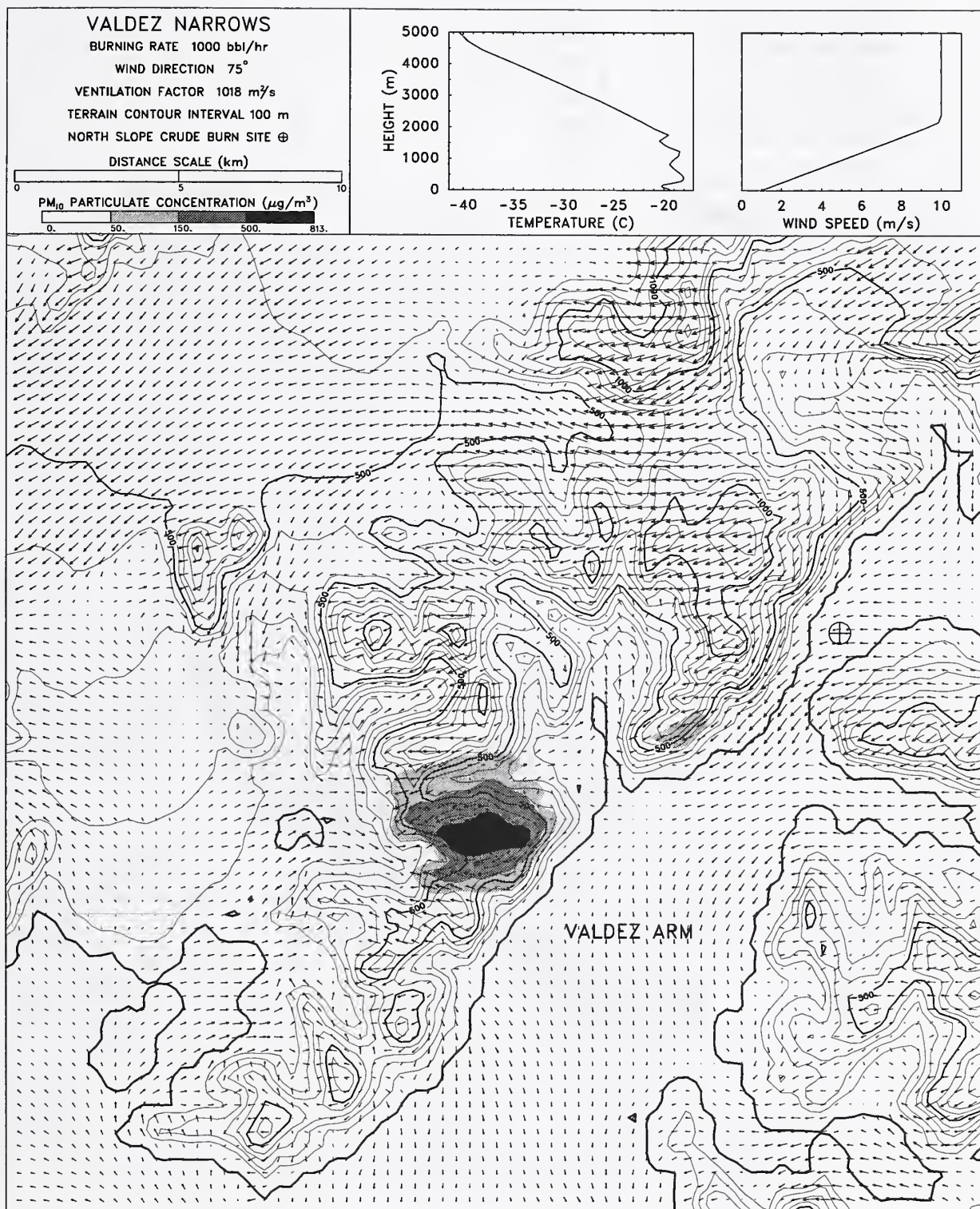


Figure 50: Footprint of simulated smoke plume originating in the Valdez Narrows. This simulation is sixth in a series of twelve to evaluate the role of different meteorological conditions on downwind dispersion.

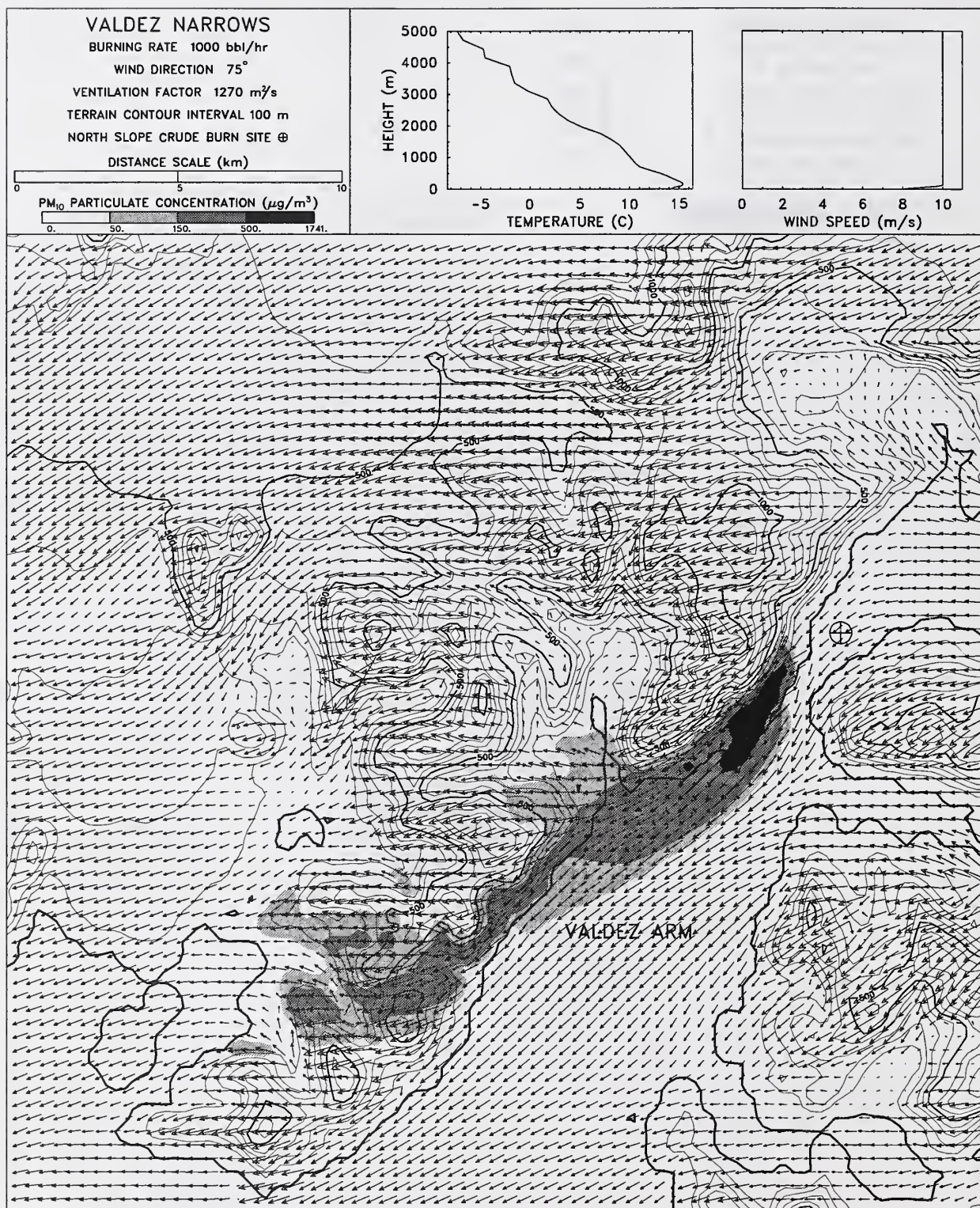


Figure 51: Footprint of simulated smoke plume originating in the Valdez Narrows. This simulation is seventh in a series of twelve to evaluate the role of different meteorological conditions on downwind dispersion.

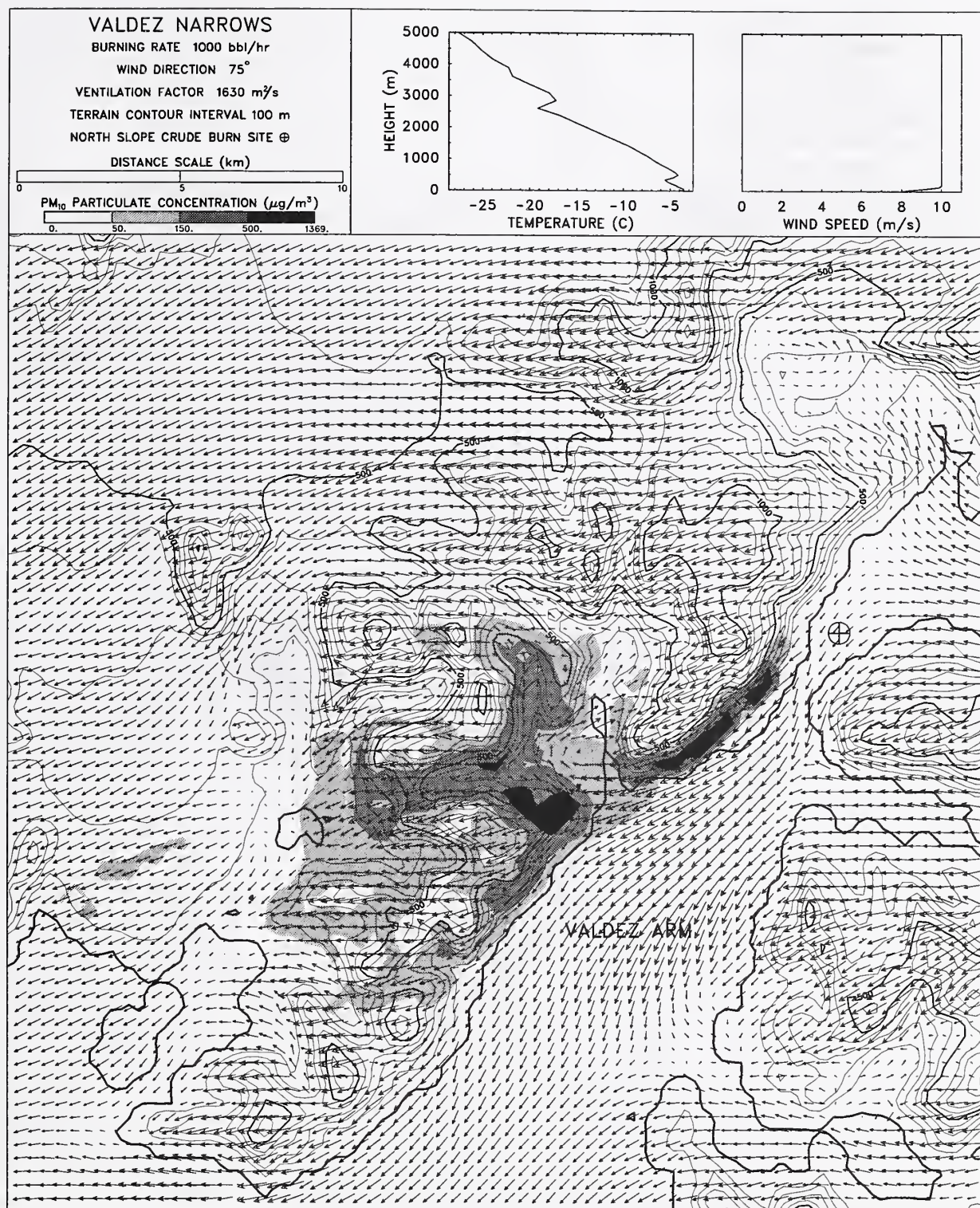


Figure 52: Footprint of simulated smoke plume originating in the Valdez Narrows. This simulation is eighth in a series of twelve to evaluate the role of different meteorological conditions on downwind dispersion.

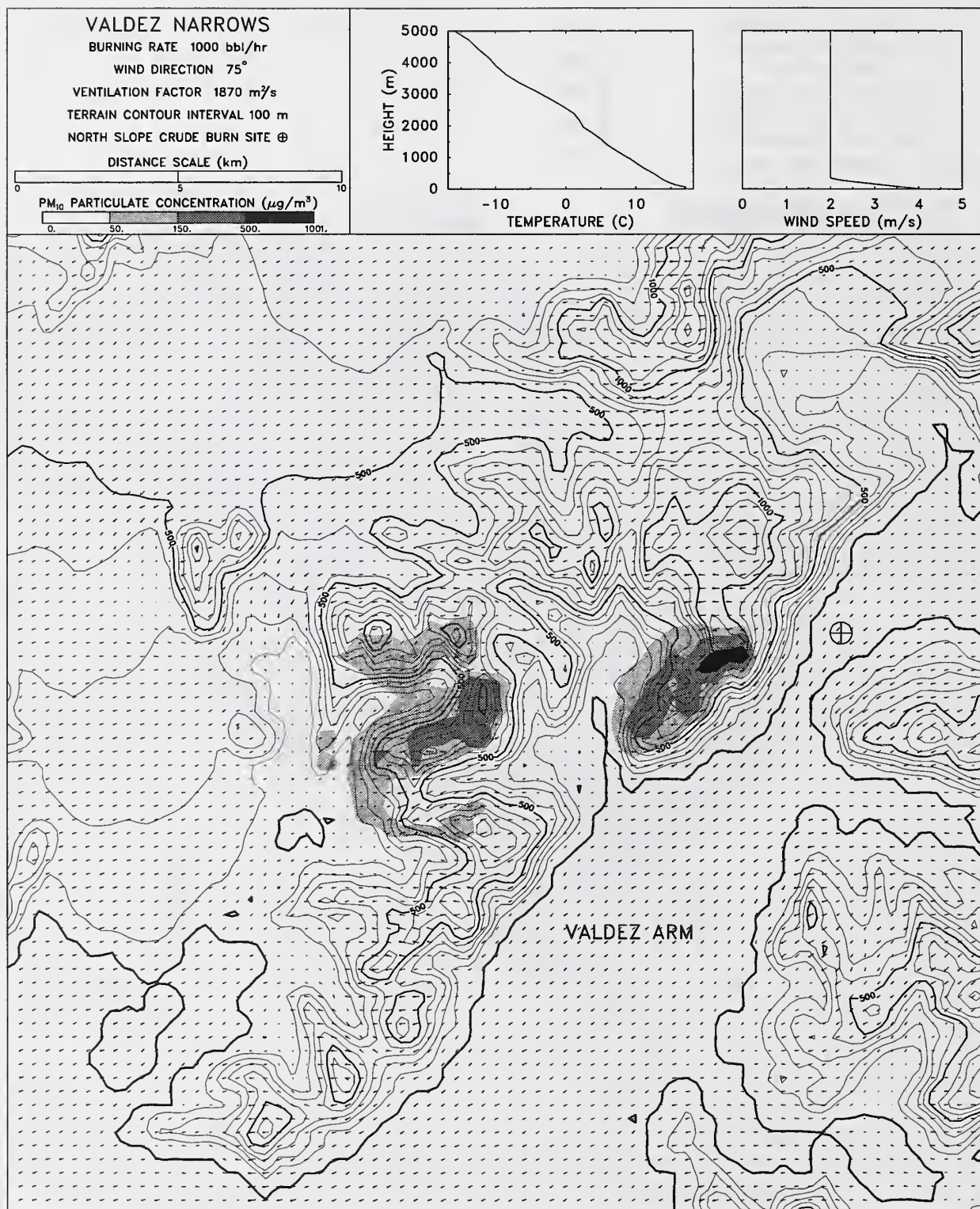


Figure 53: Footprint of simulated smoke plume originating in the Valdez Narrows. This simulation is ninth in a series of twelve to evaluate the role of different meteorological conditions on downwind dispersion.

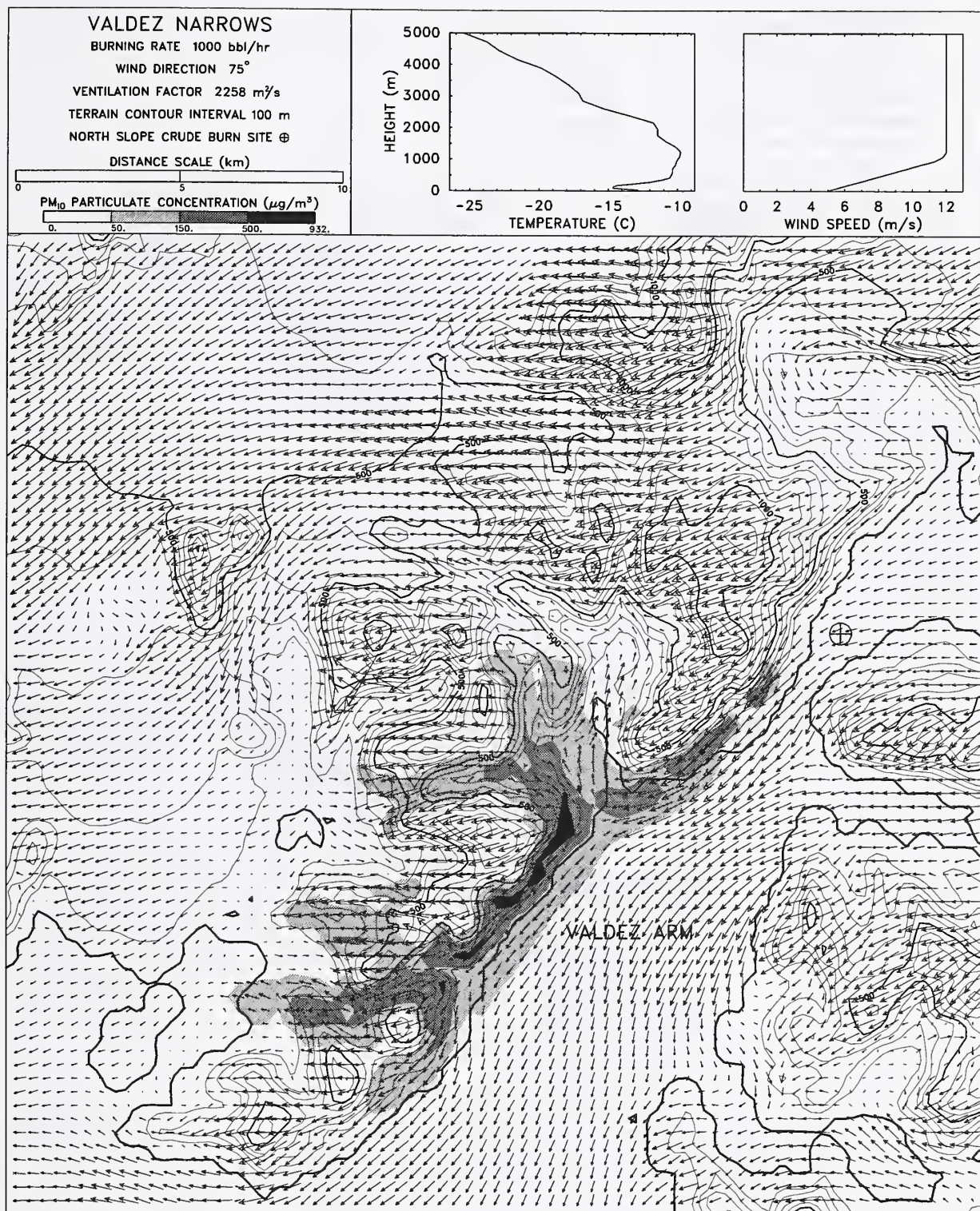


Figure 54: Footprint of simulated smoke plume originating in the Valdez Narrows. This simulation is tenth in a series of twelve to evaluate the role of different meteorological conditions on downwind dispersion.

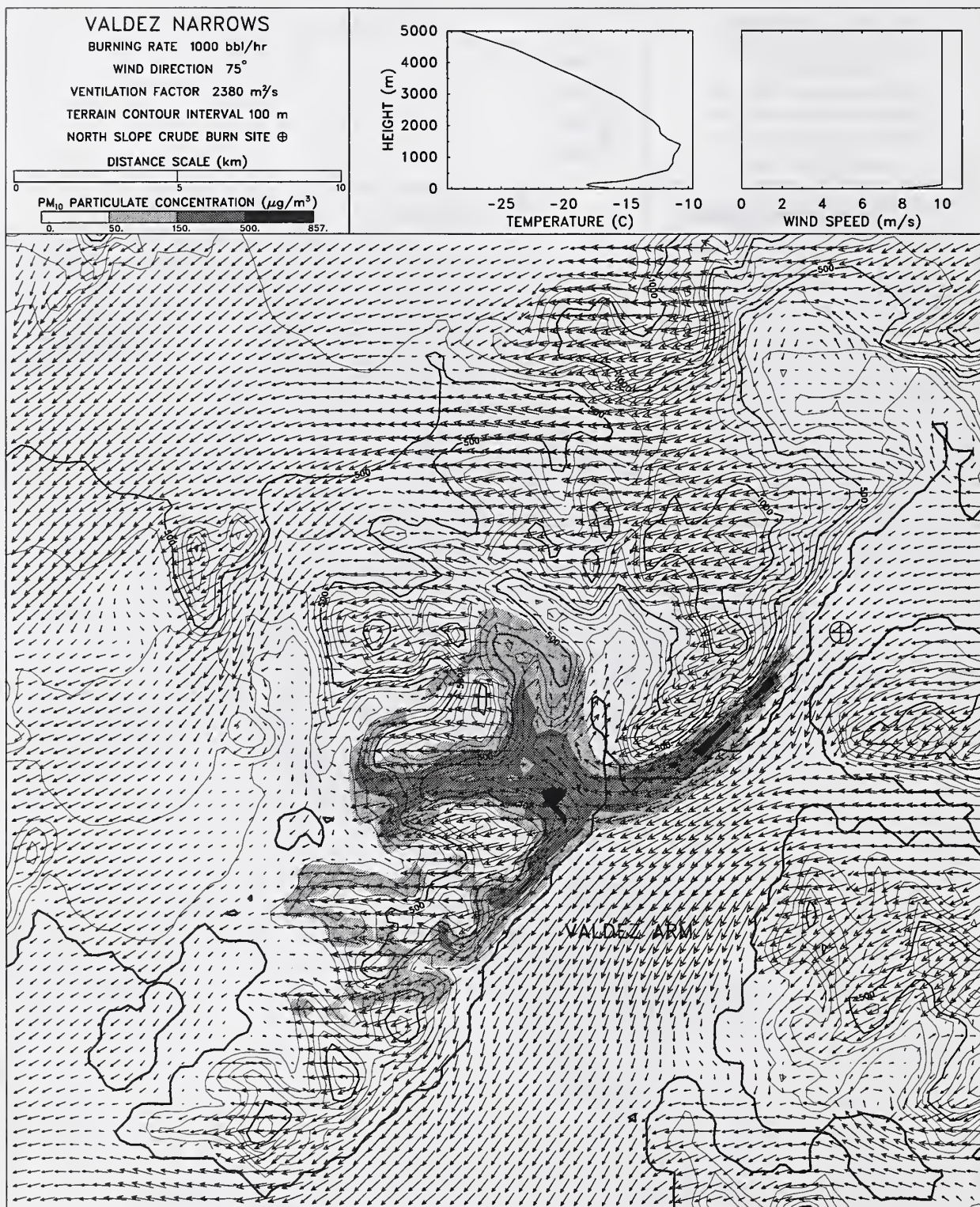


Figure 55: Footprint of simulated smoke plume originating in the Valdez Narrows. This simulation is eleventh in a series of twelve to evaluate the role of different meteorological conditions on downwind dispersion.

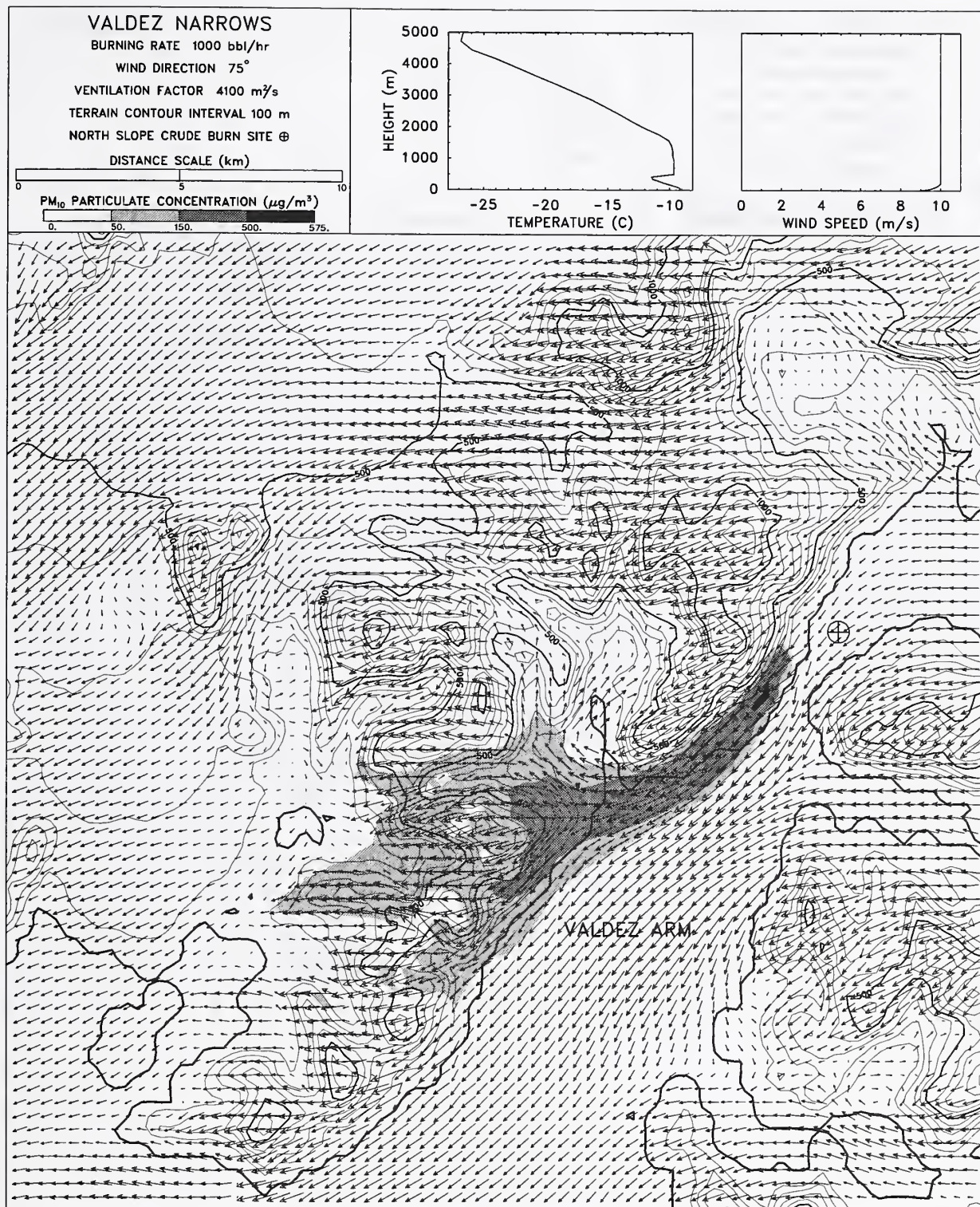


Figure 56: Footprint of simulated smoke plume originating in the Valdez Narrows. This simulation is twelfth in a series of twelve to evaluate the role of different meteorological conditions on downwind dispersion.

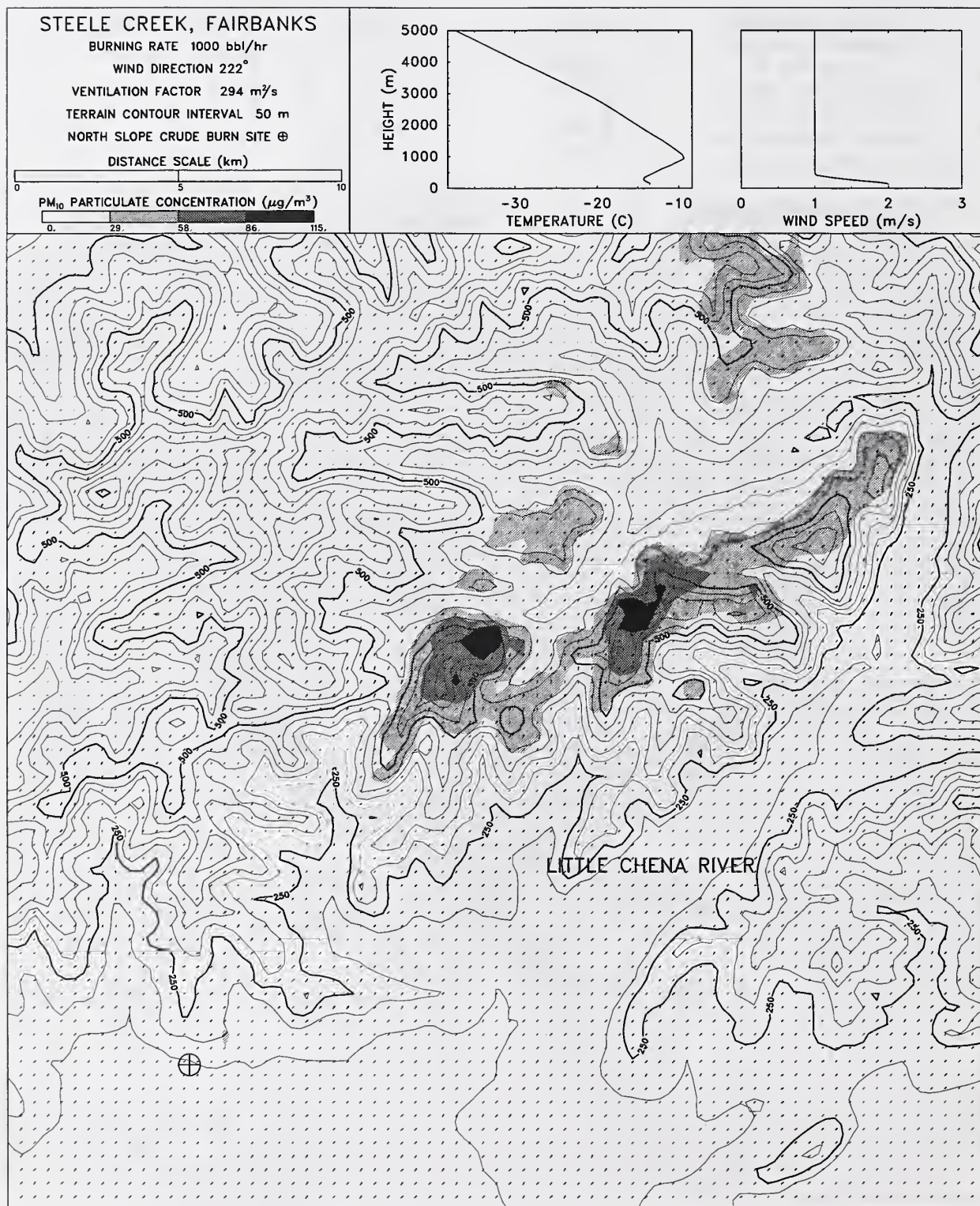


Figure 57: Footprint of simulated smoke plume originating at the Trans-Alaska Pipeline just west of Fairbanks. The fire consumes 1,000 bbl/h ANS crude. First in a series of six.

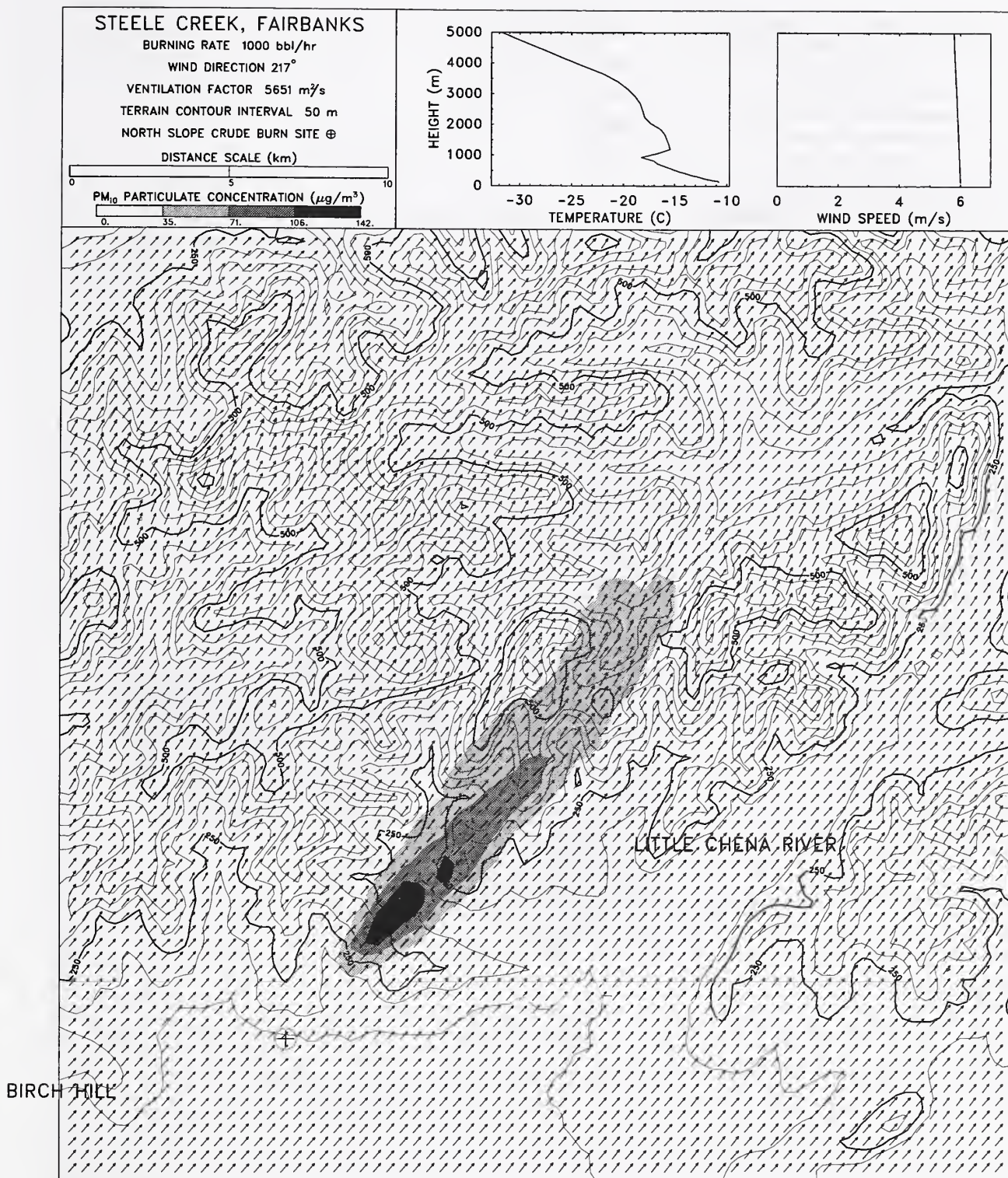


Figure 58: Footprint of simulated smoke plume originating at the Trans-Alaska Pipeline just west of Fairbanks. The fire consumes 1,000 bbl/h ANS crude. Second in a series of six.

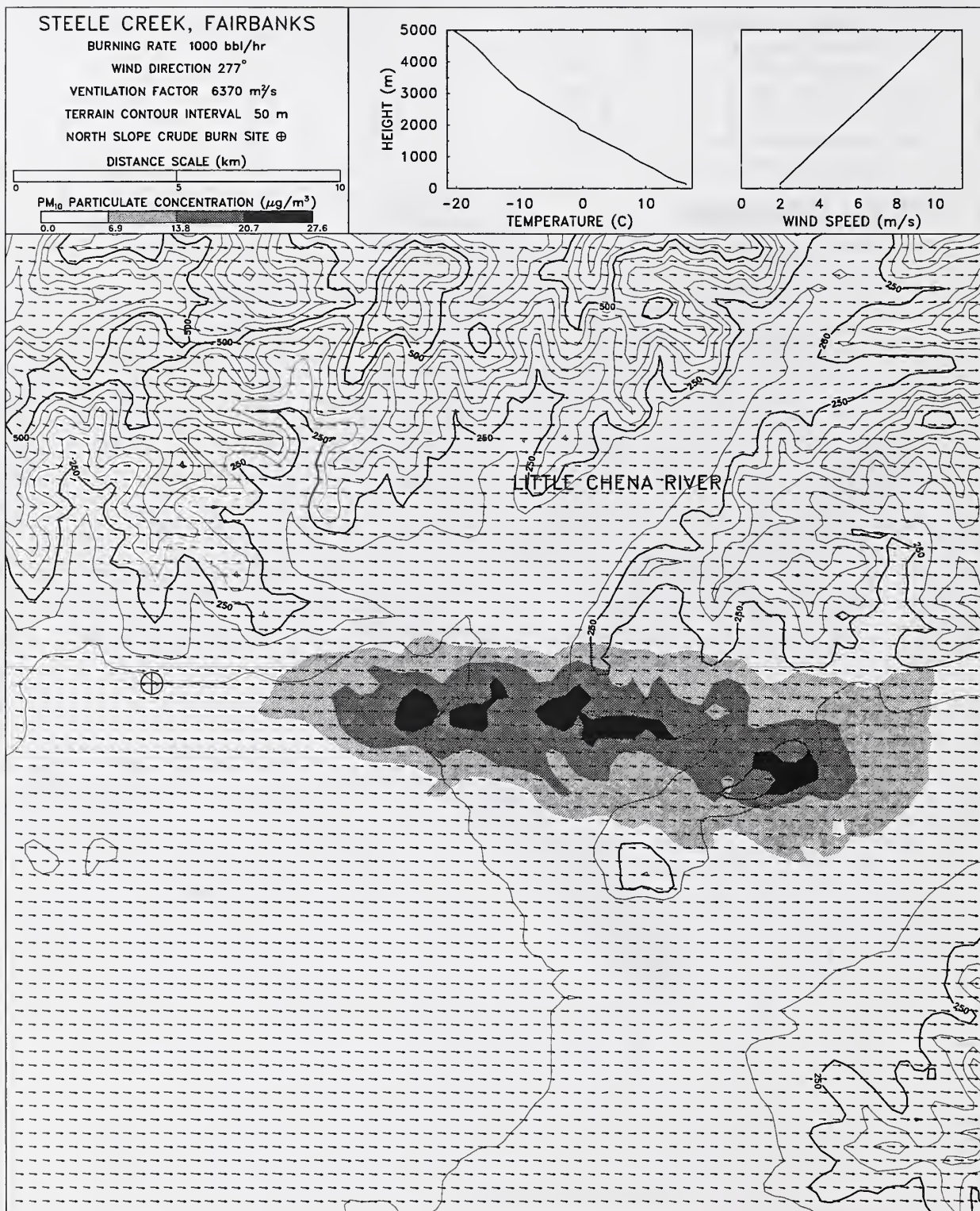


Figure 59: Footprint of simulated smoke plume originating at the Trans-Alaska Pipeline just west of Fairbanks. The fire consumes 1,000 bbl/h ANS crude. Third in a series of six.

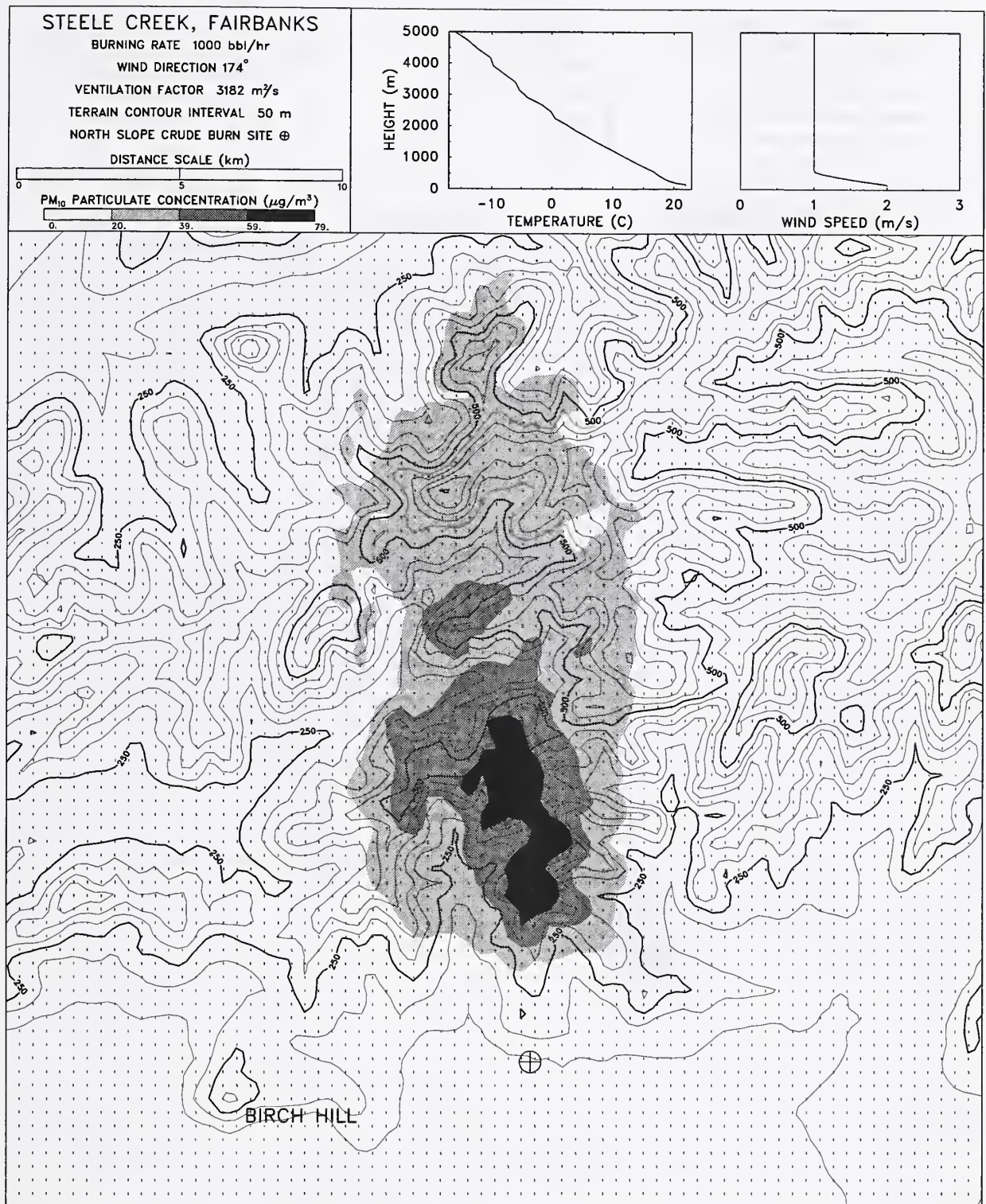


Figure 60: Footprint of simulated smoke plume originating at the Trans-Alaska Pipeline just west of Fairbanks. The fire consumes 1,000 bbl/h ANS crude. Fourth in a series of six.

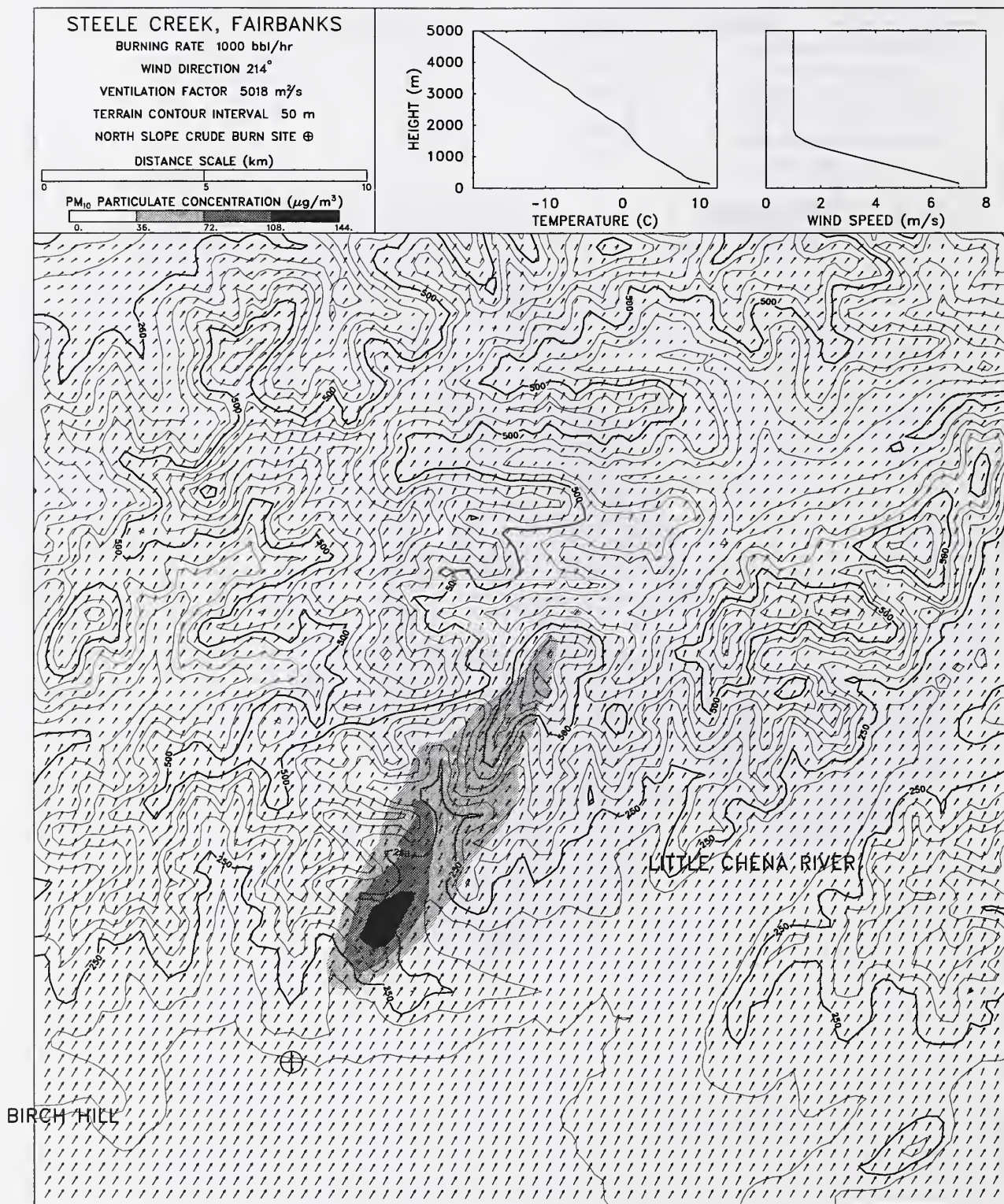


Figure 61: Footprint of simulated smoke plume originating at the Trans-Alaska Pipeline just west of Fairbanks. The fire consumes 1,000 bbl/h ANS crude. Fifth in a series of six.

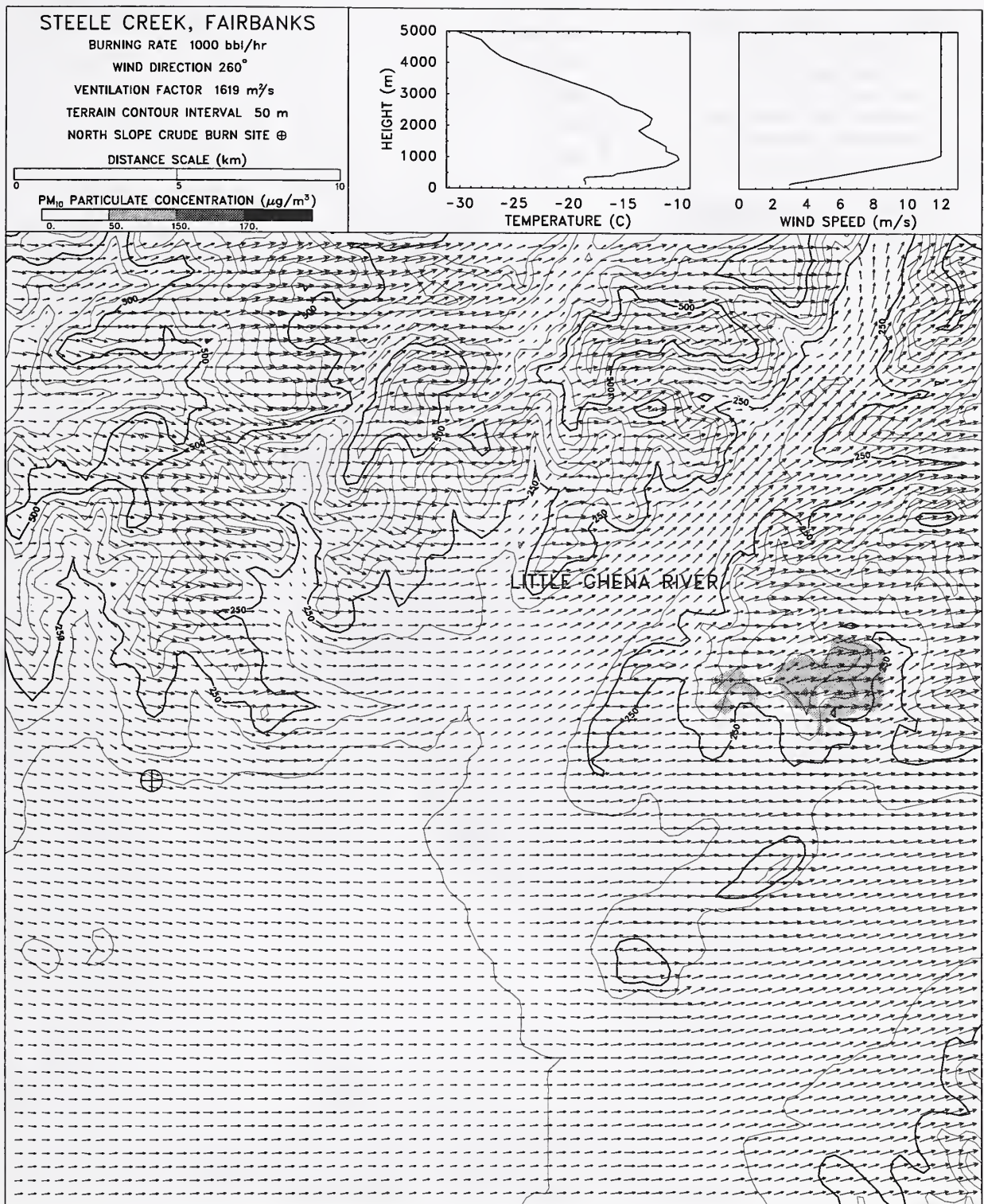


Figure 62: Footprint of simulated smoke plume originating at the Trans-Alaska Pipeline just west of Fairbanks. The fire consumes 1,000 bbl/h ANS crude. Sixth in a series of six.

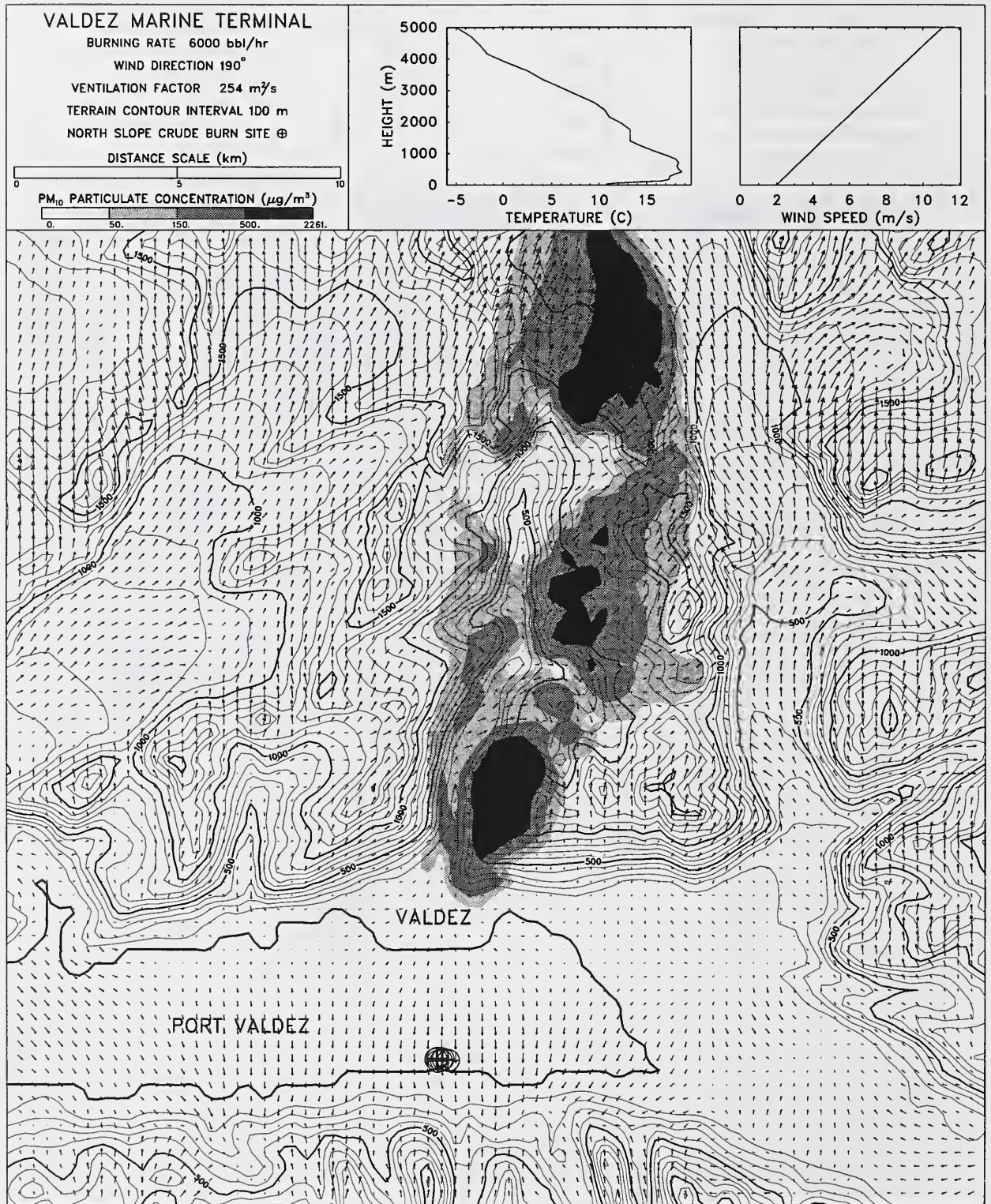


Figure 63: Footprint of six smoke plumes originating at the Valdez Marine Terminal. Each fire consumes 1,000 bbl/h ANS crude. First in a series of six.

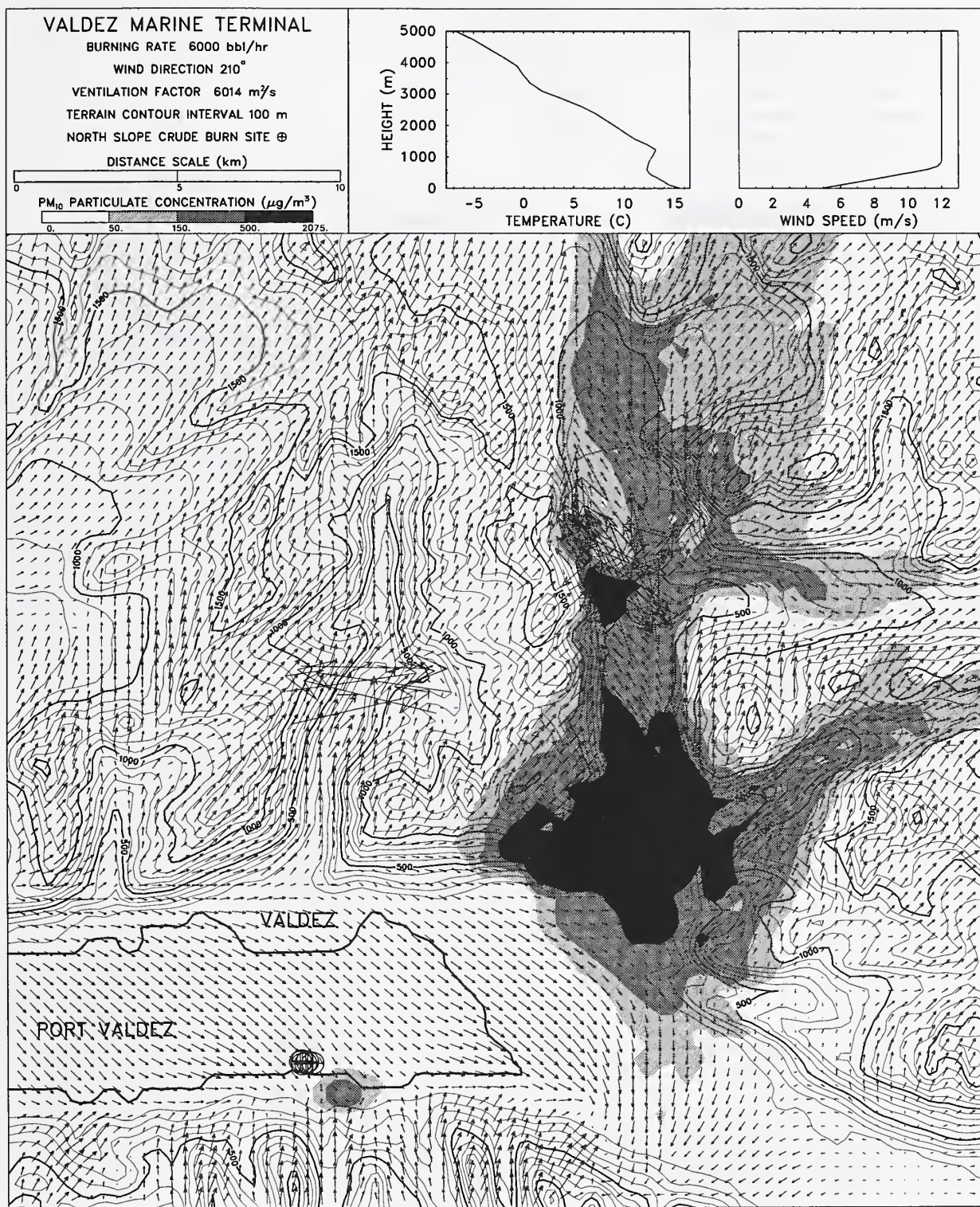


Figure 64: Footprint of six smoke plumes originating at the Valdez Marine Terminal. Each fire consumes 1,000 bbl/h ANS crude. Second in a series of six.

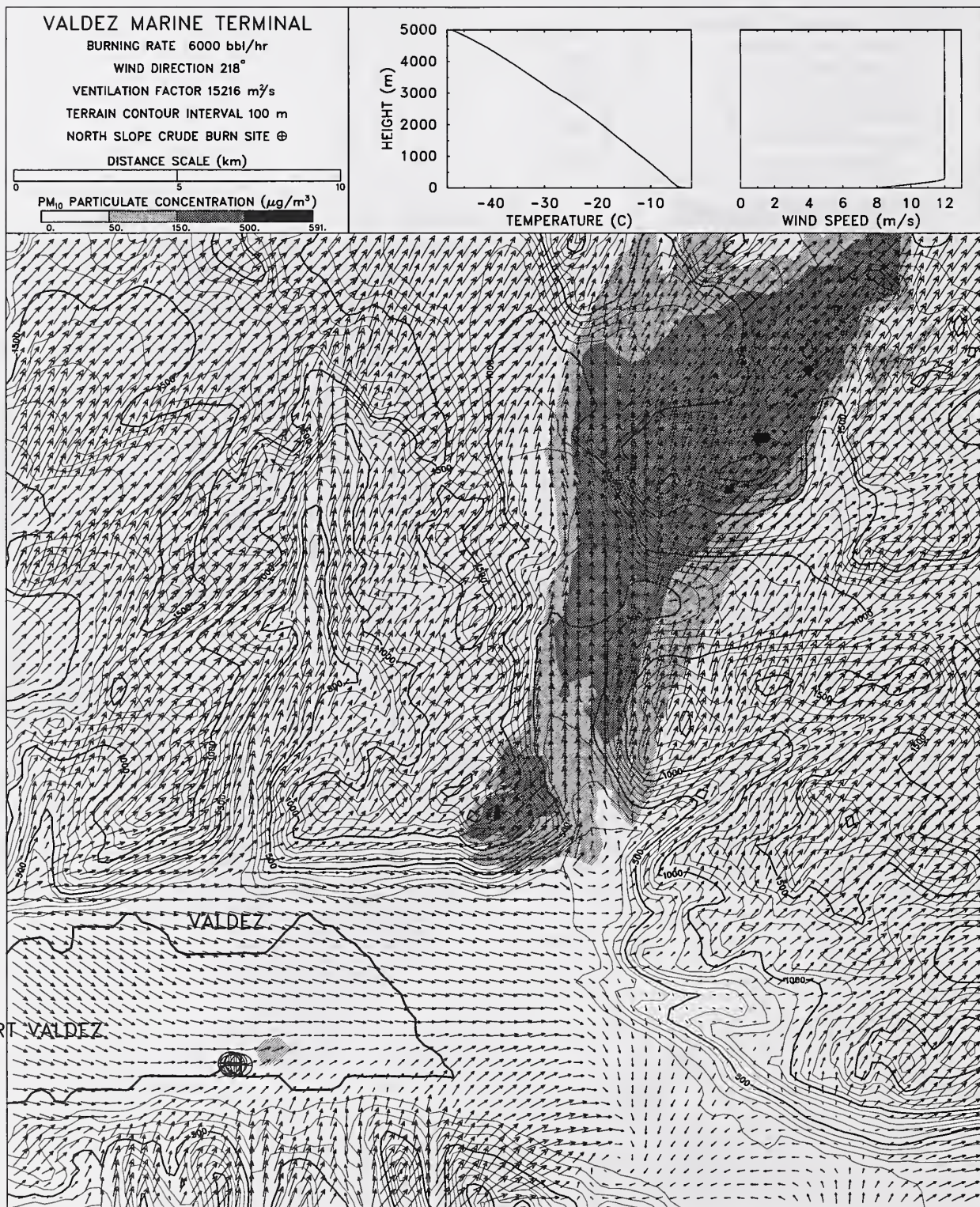


Figure 65: Footprint of six smoke plumes originating at the Valdez Marine Terminal. Each fire consumes 1,000 bbl/h ANS crude. Third in a series of six.

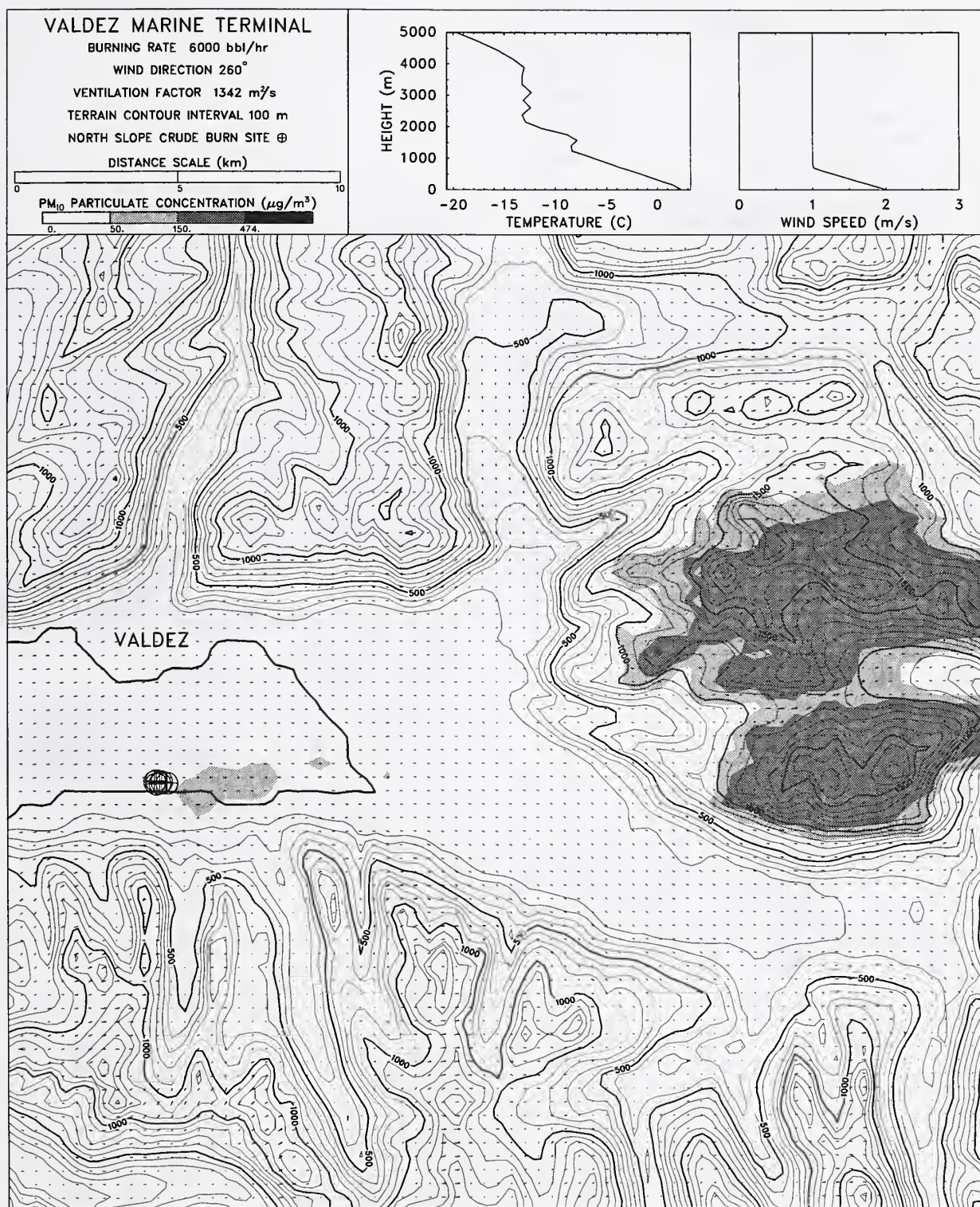


Figure 66: Footprint of six smoke plumes originating at the Valdez Marine Terminal. Each fire consumes 1,000 bbl/h ANS crude. Fourth in a series of six.

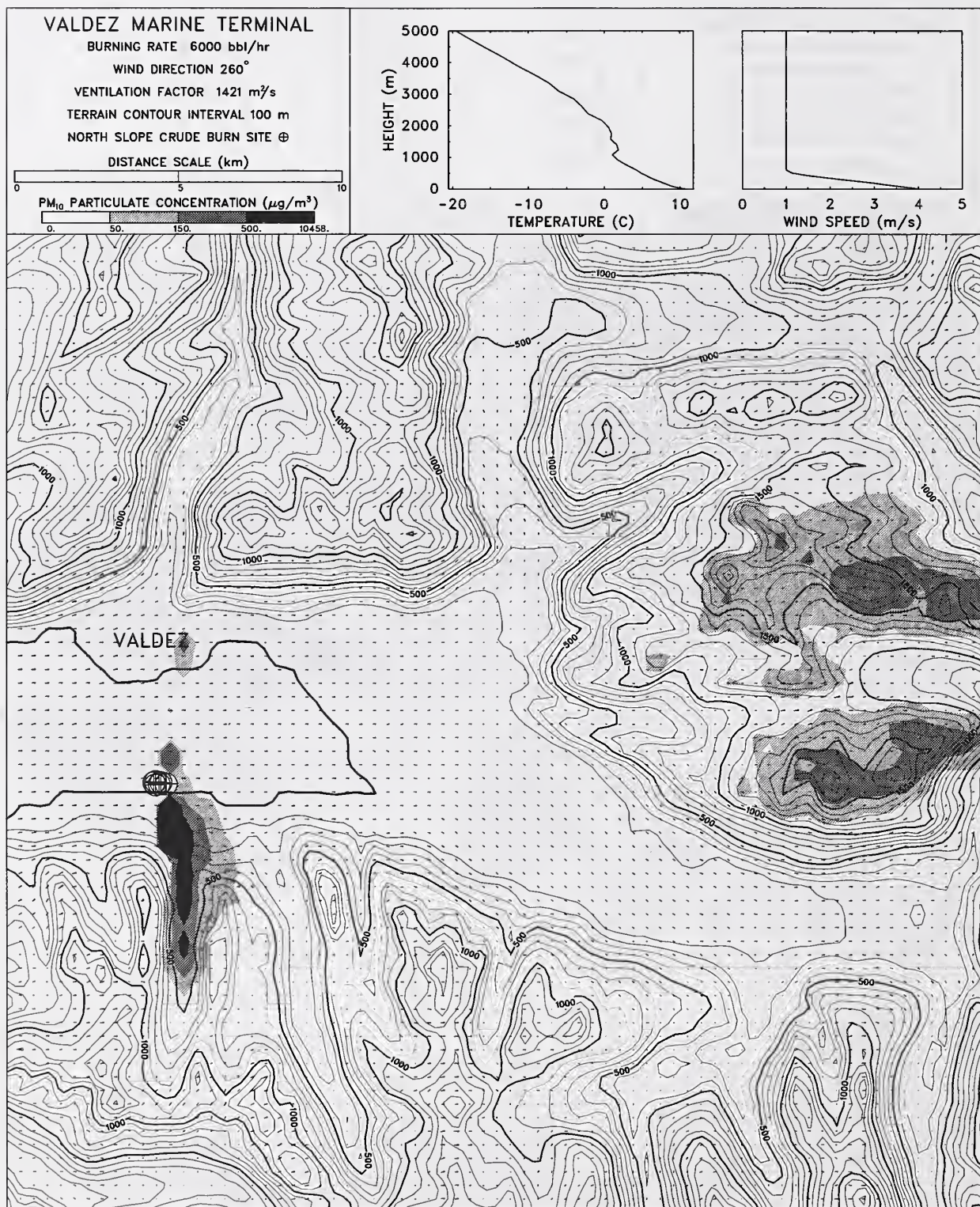


Figure 67: Footprint of six smoke plumes originating at the Valdez Marine Terminal. Each fire consumes 1,000 bbl/h ANS crude. Fifth in a series of six.

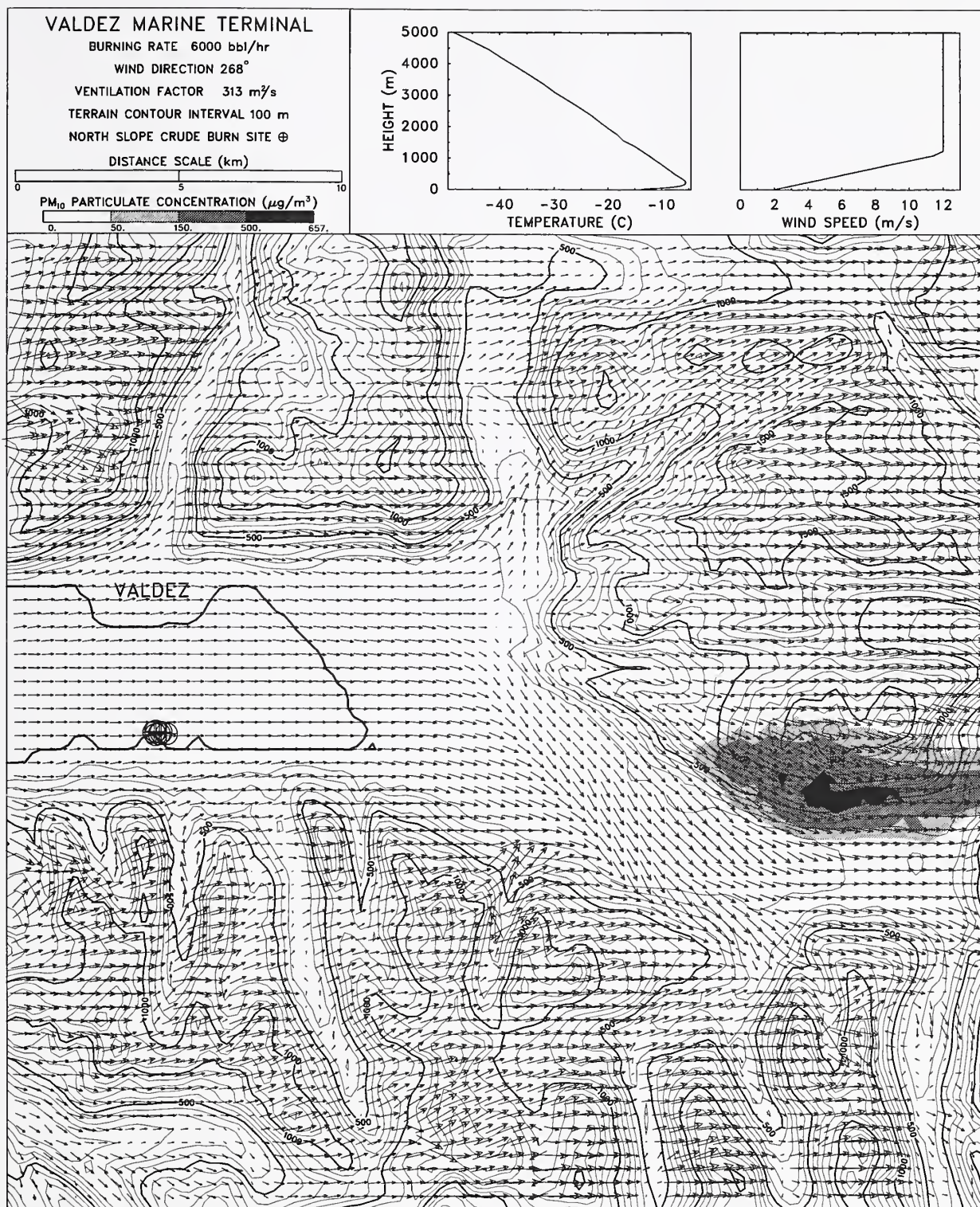


Figure 68: Footprint of six smoke plumes originating at the Valdez Marine Terminal. Each fire consumes 1,000 bbl/h ANS crude. Sixth in a series of six.

